Nanoindentation characterisation of carbon fibre reinforced plastic microstructures

Mark Hardiman

Publication date

01-01-2016

Licence

This work is made available under the CC BY-NC-SA 1.0 licence and should only be used in accordance with that licence. For more information on the specific terms, consult the repository record for this item.

Document Version
1

Citation for this work (HarvardUL)

Hardiman, M. (2016) 'Nanoindentation characterisation of carbon fibre reinforced plastic microstructures', available: https://hdl.handle.net/10344/5227 [accessed 12 Oct 2022].

This work was downloaded from the University of Limerick research repository.

For more information on this work, the University of Limerick research repository or to report an issue, you can contact the repository administrators at ir@ul.ie. If you feel that this work breaches copyright, please provide details and we will remove access to the work immediately while we investigate your claim.

UNIVERSITY of LIMERICK
OLLSCOIL LUIMNIGH

Nanoindentation Characterisation of Carbon Fibre Reinforced Plastic Microstructures

Mark Hardiman

This thesis is submitted in fulfilment of the requirements for the Degree of Doctor of Philosophy at the Faculty of Science and Engineering, University of Limerick

Submitted to the University of Limerick, May 2016.

ABSTRACT

The increasing use of fibrous composite materials in the automotive and aerospace industries has led to increased demand for predictive analysis tools that require careful measurement of the fibre and matrix constituent properties in order to accurately predict the macroscopic deformation and failure response of the materials. Recent developments in nanoindentation testing have enabled accurate property measurements to be carried out at the scale required to probe the individual fibrous composite constituents in situ. However, quantitative characterisation of the matrix constituent has proven challenging due to the inhomogeneity of the composite microstructure and the non-linear time-dependent polymer matrix properties. Hence, a detailed experimental and numerical investigation was carried out into the use of nanoindentation to determine the in situ properties of the polymer matrix constituent in an aerospace grade carbon fibre reinforced epoxy composite (Hexcel HTA/6376).

An experimental comparison of the bulk and in situ 6376 matrix properties was carried out using a state-of-the-art Nanoindenter G200, supplied by Agilent. The bulk matrix and composite material were co-cured to produce specimens ideal for matrix characterisation. It is found that the unconstrained in situ indentation modulus increased with a decrease in matrix pocket size, and was up to 19% greater than the bulk matrix modulus. However, a clear discrepancy was noted between the bulk matrix elastic modulus values derived from indentation testing and those determined using traditional macroscopic tensile tests, with the indentation modulus being consistently larger by approximately 40%. Thus, an investigation into the effects of pile-up, viscoelasticity and hydrostatic stress on the polymer indentation modulus was carried out and experimental and analytical techniques were developed to account for viscous and hydrostatic stress effects that systematically reduced the calculated modulus to within 3% of the macroscopic value. The proposed techniques move towards addressing the well-known disparity between nanoindentation and macroscopic measured moduli.

Numerical studies using non-linear Finite Element Analysis were carried out to provide insight into the experimental observations and to help decouple highly interdependent variables, such as fibre constraint and residual stress effects on matrix properties. The apparent indentation modulus was found to increase by up to 47% due to the added constraint of the surrounding discrete fibre regions. A two-step modelling approach was used to determine the effect of residual stress states in two regions of interest, namely, the pocket and interfacial matrix regions following thermal cool-down of the composite from cure temperature. It is found that the hardness property decreased for the majority of the residual stress states, whereas the modulus property was found to be insensitive to residual stress.

Declaration

The substance of this thesis is the original work of the author and due reference and acknowledgement has been made, where necessary, to the work of others. No part of this thesis has already been submitted for any other degree.

Mark Hardiman

Signature

Date

Examination Board

Chairman: Dr. Jeremy Robinson

External Examiner: Dr. Saurav Goel

Internal Examiner: Dr. Ronan O'Higgins

Acknowledgements

I would like to acknowledge the support of my supervisor Dr. Conor McCarthy and thank him for all his help throughout the project. I would also like to thank Dr. Ted Vaughan for his advice and support, and for laying the micromechanical groundwork for the project.

I would like to acknowledge the funding provided by the Irish Research Council (IRC) and all of the staff and students at the Irish Centre for Composites Research (IComp) who have provided me with invaluable advice, friendship and entertainment over the years. I would like to thank Dr. Holger Pfaff, formally of Keysight/Agilent technologies, who provided critical technical support when needed and assisted with the experimentation. I would also like to thank Mike Keeble from Beuhler, for his technical advice regarding sample preparation.

Finally, I would like to thank my family, Mom and Dad, Gary and Jacqueline, who have supported me all the way in the good times and the bad.

Contents

List of Figures **xv**

List of Tables **xxv**

Nomenclature **xxvii**

1 Introduction **1**

1.1 Background 1

1.2 Motivation 2

1.3 Problem description and objectives 4

1.4 Thesis outline 7

2 Literature Review **9**

2.1 Introduction 9

2.2 Fibrous composite micromechanisms 9

2.3 Micromechanics 10

2.3.1 Thermal residual stress 12

2.3.2 Constituent material behaviour 14

2.4 Nanoindentation 16

2.4.1 Theory 18

2.4.2 Continuous stiffness measurement (CSM) 23
2.4.3 Pile-up and residual stress effects 25
2.4.4 Numerical simulation of nanoindentation 29
2.5 Nanoindentation of composite materials 32
2.5.1 Bulk vs in situ properties 32
2.5.2 Interphase characterisation 33
2.5.3 Effect of neighbouring constituents 35
2.6 Nanoindentation of polymeric materials 37
2.6.1 Elastic characterisation 37
2.6.2 Viscoelasticity 40
2.6.3 Hydrostatic stress 42
2.7 Summary of literature review 45

3 Numerical Characterisation of Fibre Constraint Effects on Matrix Constituent Characterisation 49

3.1 Introduction 49
3.2 Model description 50
3.2.1 2D axisymmetric model 51
3.2.2 3D models 53
3.2.3 Material properties 56
3.3 Results and discussion 58
3.3.1 Model validation 58

3.3.2 Effect of friction coefficient 60

3.3.3 Comparison of indentation stress fields 60

3.3.4 Fibre constraint results 61

3.4 Concluding remarks 69

4 The Effect of Microscale Residual Stress on in situ Matrix Characterisation 71

4.1 Introduction 71

4.2 Model development 73

4.2.1 Modelling strategy 73

4.2.2 Thermal cooldown models 73

4.2.3 3D indentation models 76

4.2.4 Material behaviour 78

4.3 Results and discussion 79

4.3.1 Matrix pocket region 79

4.3.2 Interfacial region 82

4.4 Concluding remarks 91

5 Experimental Nanoindentation of Fibrous Composite Microstructures 93

5.1 Introduction 93

5.2 Sample preparation 94

5.2.1 Lay-up and curing process 94

5.2.2 Surface preparation 97
5.2.3 Resulting microstructure 99
5.3 Testing and analysis procedures 104
5.3.1 Express test property mapping 105
5.3.2 Characterisation of bulk 6376 106
5.3.3 Characterisation of in situ 6376 107
5.4 Results and discussion 107
5.4.1 Express test results 107
5.4.2 Bulk 6376 matrix results 109
5.4.3 Experimental investigation of fibre constraint 112
5.4.4 Bulk versus in situ matrix properties 115
5.4.5 Statistical analysis of nanoindentation results 119
5.5 Concluding remarks 120

6 Investigation of Pile-Up, Viscoelasticity and Hydrostatic Stress Effects on Polymer Matrix Indentation 123

6.1 Introduction 123
6.2 Characterisation of 6376 matrix material 125
6.3 Investigation of material pile-up 127
6.4 Investigation of viscoelastic effects 130
6.4.1 Maximum load hold segment time (t_{hold}) 131
6.4.2 Indentation strain-rate ($\dot{\varepsilon}$) 133

6.4.3 Point of contact stiffness evaluation ($h_{\frac{dP}{dh}}$) 134
6.4.4 Analysis of non-linear curve-fitting procedure 138
6.5 Influence of hydrostatic stress 141
6.6 Concluding remarks 143

7 Conclusions and Recommendations for Future Work 145

7.1 Conclusions 145
7.1.1 Fibre constraint 145
7.1.2 Thermal residual stress 146
7.1.3 Bulk versus in situ properties 147
7.1.4 Elastic characterisation of polymers 148
7.2 Future work 149
7.2.1 Matrix and interphase characterisation 149
7.2.2 Residual stress effects 152
7.2.3 Nanoindentation of polymers 153
7.2.4 Push-out testing 155

References 159

Bibliography 159

A Publication Summary 177

B Aluminium pile-up correction 179

B.1 Experimental setup 179

B.2 Results 179

List of Figures

1.1 (a) Berkovich indenter geometry, (b) Typical load-displacement curve 2

1.2 Nanoindentation of carbon fibre/epoxy composite matrix constituent (a) Micrograph and (b) Scanning Probe Microscopy (SPM) image of residual indentation 3

2.1 Fibrous composite failure mechanisms under various loading conditions (Llorca et al., 2011) 10

2.2 In situ SEM observation of (a) shear bands in the matrix constituent under transverse compression loading (Llorca et al., 2011) and (b) interface damage and matrix cracking under transverse tension loading (Zhang et al., 2010) 11

2.3 Micromechanical models of HTA/6376 composite (a) RVE subjected to transverse tension loading (Vaughan and McCarthy, 2011*a*), (b) RVE subjected to shear loading (Vaughan and McCarthy, 2011*b*) . . 13

2.4 Contour plot of the maximum principal residual stress (kPa) for (a) microstructure with 60% fibre volume fraction (b) microstructure with 50% fibre volume fraction (Yang et al., 2013) 14

2.5 Yield surfaces (a) von Mises, (b) Mohr-Coulomb 15

2.6 Commonly used indenter tip shapes 17

2.7 (a) SEM image of a Berkovich indenter tip (b) Residual impression left by a Berkovich tip on a fused silica substrate (Fischer-Cripps, 2009) 18

2.8 (a) Schematic of indenter and specimen surface at full load for a conical indenter (b) Schematic of indenter and specimen surface at full unload for a conical indenter, (c) Typical load-displacement curve highlighting the parameters used in the nanoindentation analysis . . . 20

2.9 (a) Small oscillating load applied to primary indentation force, (b) A schematic of dynamic system during sample testing 24

2.10 Pile-up and sink-in material behaviour at maximum indentation depth (a) side profile of indentation, (b) geometry of projected contact areas for each case 26

2.11 Effect of residual stress on contact area (a) indentation schematic, (b) Real vs Oliver and Pharr calculated contact area (Mann, 2005) . 27

2.12 Contact boundary of indentation carried out on Zr_{55} to a maximum load of 8 mN (a) Surface tilt corrected by linear least-squares fitting, (b) Line-scan profiles, (c) Contact boundary determined by two highest point sets, (d) Three-dimensional topography of the indentation (Zhang et al., 2015) 28

2.13 (a) Geometry and boundary conditions for 2D axisymmetric indentation model, (b) Detailed view of finite element mesh under indenter tip (Bhattacharya and Nix, 1988) 30

2.14 3D Berkovich indentation model (Larsson et al., 1996) 31

2.15 Schematic diagram of the nanoindentation MD simulation model (Goel et al., 2014) 32

2.16 Neat and in situ modulus and hardness values for Cytec 977-3 epoxy resin measured by nanoindentation (Gregory and Spearing, 2005). . . 34

2.17 Nanoindentation of glass fibre/vinylester composite (a) load displacement curves for fibre, ‘interphase’ and matrix regions, (b) variations in elastic modulus across fibre-matrix interface (Kim et al., 2001) . . 35

2.18 Variation of the stiffness measured from the FEA with position from the interface (Lee et al., 2007). 37

2.19 Elastic moduli evaluated by Oliver and Pharr procedure from force curves obtained by nanoindentation, E_N, vs macroscopic moduli, E_M, for a broad range of polymer samples and polymer morphologies. (Tranchida et al., 2007) 38

2.20 Examples of poor power-law curve fits from (a) VanLandingham et al. (2001) indentation carried out on benzocyclobutene (BCB) polymer and (b) Beyaoui et al. (2009) indentation carried out on polycarbonate (PC) 40

2.21 Load–displacement data at the loading–unloading peak for two indentations on PMMA performed under similar loading conditions. The introduction of a hold segment (10 s) at the peak load reduces the creeping effect upon the unloading set of data (Briscoe et al., 1998). 42

2.22 Indentation elastic modulus and hardness of PMMA as a function of holding time (Jin et al., 2015) 43

2.23 Dependence of elastic moduli, evaluated by Oliver and Pharr procedure, on loading rate in a broad range of conditions for three morphologies: amorphous PC and two semicrystalline iPP. Results are compared with macroscopic bulk moduli (Tranchida et al., 2007) . . . 44

2.24 Elastic modulus ratio vs hydrostatic pressure for various amorphous polymers (Pae and Bhateja, 1975). 44

3.1 Berkovich indenter tip geometry 51

3.2 Magnified view of indentation region of the 2D axisymmetric model along with boundary conditions 52

3.3 Six-fold symmetry of Berkovich indenter tip geometry 54

3.4 3D finite element models used to represent a nanoindentation in the vicinity of fibres, (a) fibres represented as a rigid boundary, (b) fibres represented by a circular pattern of closely packed fibres and (c) fibres represented by a less dense packing arrangement 55

3.5 A plan view showing the section assignments of the models containing discrete fibre regions: (a) closely packed ring of fibres, (b) sparse array of three surrounding fibres 56

3.6 Optical microscope image of the HTA/6376 microstructure showing the matrix-rich regions between the laminae 57

3.7 Elastic response of the (a) 2D axisymmetric model compared with Sneddon's theory and (b) 3D nanoindentation model compared with Larsson's expression 59

3.8 Variation of indentation modulus and hardness with friction coefficient (μ) 60

3.9 Comparison of von Mises stress fields produced by (a) 2D and (b) 3D models 61

3.10 Size comparison of stress fields produced by 2D and 3D models 62

3.11 3D Nanoindentation simulation load-displacement curves for three different values of r 63

3.12 Ratio of Young's Modulus to unconstrained Young's modulus plotted against r for all four model-types 64

3.13 Illustration showing the projected contact area of an unconstrained indentation when r = 20 µm 65

3.14 Development of stress in the fibre sections throughout the loading step when $r = 10$ µm 66

3.15 Load displacement curves for 3D model with fibres for the unconstrained case and for $r = 10$ µm 67

3.16 Ratio of contact area extracted from the finite element models (A_{FEA}) to contact area calculated from Oliver and Pharr method (A_{OP}), plotted against different values of r 68

3.17 Ratio of Young's Modulus to unconstrained Young's modulus plotted against r for all four model-types where the contact area was extracted directly from the models 69

4.1 Finite element modelling strategy 74

4.2 Schematic and mesh of plane-strain thermal cooldown finite element model for a matrix pocket of 15 µm radius 75

4.3 Single fibre unit cell with periodic boundary conditions and example mesh for inter-fibre spacing (*Sp*) of 5 µm 76

4.4 3D finite element indentation model showing detail of the indentation site and the boundary conditions used to apply a biaxial stress state prior to indentation 78

4.5 (a) Maximum and (b) Minimum in-plane principle stress state following thermal cooldown for the 6376 matrix pocket with a radius of 5.97 µm 80

4.6 Equibiaxial stress versus size of matrix pocket 81

4.7 Stress state under indenter at maximum indentation depth for 8.5 µm matrix pocket residual stress state model 82

4.8 Load versus displacement data extracted from the finite element simulations for various pocket residual stress states 83

4.9 Normalised indentation parameters plotted versus matrix pocket size 84

4.10 Stress state following thermal cooldown for periodic unit cell with inter-fibre spacing of 2 µm 84

4.11 The variation of radial and tangential interfacial region stresses for an inter-fibre spacing of 0.25 µm 85

4.12 The evolution of radial and tangential stresses with increasing inter-fibre spacing 86

4.13 Radial and tangential residual stress values for points A and B for the range of investigated inter-fibre spacings 87

4.14 Load-displacement data for a number residual stress states determined at (a) Point A and (b) Point B 88

4.15 Normalised indentation parameters plotted versus inter-fibre spacing for (a) point A and (b) point B 89

4.16 The 1% equivalent plastic strain (PEEQ) boundary for the non-prestressed substrate and the stress states at point A and point B for 0.25 µm inter-fibre spacing 90

5.1 Schematic of lay-up applied to create ‘hybrid’ samples 95

5.2 Schematic of the bagging arrangement used to cure the hybrid panels in the autoclave 96

5.3 LBBC TC1000HTPT Thermoclave 97

5.4 Hybrid samples mounted in clear epoxy 97

5.5 Buehler Phoenix 4000 sample preparation system 98

5.6 Resulting microstructure of the hybrid sample at the composite/epoxy interface 101

5.7 SPM scans of bulk matrix region (a) 10×10 µm area contact mode AFM scan, (b) 50×50 µm area tapping mode AFM scan and (c) 50×50 µm area scanned using Berkovich indenter tip and Nanovision stage 102

5.8 3D scan of composite regions, (a) high fibre volume region following surface preparation procedure A, (b) isolated fibre following surface preparation procedure A, (c) high fibre volume region following surface preparation procedure B, (d) isolated fibre following surface preparation procedure B 103

5.9 The Agilent Nano Indenter G200 and a cross-sectional diagram of the XP-NMAT (Agilent, 2009). 105

5.10 Micrograph of the 12 × 12 µm region of microstructure mapped using express testing 106

5.11 Express test quantitative property maps of indentation (a) hardness (b) modulus 108

5.12 (a) Load displacement curves for 30 bulk 6376 matrix indentations (b) Young's modulus versus indentation depth for the basic and CSM indentations 110

5.13 (a) Parametrised load-displacement curve (b) Resulting non-linear curve-fit 111

5.14 Optical microscope image (1000X) of a residual impression from an indentation carried out into a matrix pocket with a radius of 5.71 µm 113

5.15 Modulus versus indenter displacement data for indentations into bulk 6376 resin and two resin pockets determined using the CSM Nanoindentation technique 114

5.16 Normalised Modulus plotted against Fibre Constraint Factor (FCF) for all 50 pocket indentations and FE models 116

5.17 The unconstrained modulus for each matrix pocket indentation plotted versus the radius of the matrix pocket (lower x-axis) and the unconstrained depth of the indentation (upper x-axis). The bulk matrix mean and SD variance corresponding with the indentations depths on the upper x-axis are also shown. 117

5.18 The unconstrained hardness for each matrix pocket indentation plotted versus the radius of the matrix pocket (lower x-axis) and the unconstrained depth of the indentation (upper x-axis). The bulk matrix mean and SD variance corresponding with the indentations depths on the upper x-axis are also shown. 118

6.1 Pile-up and sink-in material behaviour at maximum indentation depth (a) side profile of indentation, (b) geometry of projected contact areas for each case 124

6.2 (a) load-displacement curves, (b) Indentation modulus and hardness versus target indentation depth 126

6.3 (a) Micrograph and SPM image of 5 µm indentation, highlighting locations of line scans, (b) Line scans A, B and C 127

6.4 Normalised (a) Contact area and (b) Indentation modulus determined using each of the pile-up correction methods 129

6.5 Comparison of residual depths calculated from load-displacement curves and scanning probe microscopy (SPM) 130

6.6 Comparison of load-displacement curves for a 2 µm displacement target and peak load hold times of 0, 10, 60, 120 600 and 3600 seconds. . 132

6.7 The long term creep response of the 2 µm indentation with a hold time of 3600 s: (a) Hold time versus indenter displacement, (b) Hold time versus creep rate. 132

6.8 Indentation modulus versus hold time for the six hold times and four different indentation depths tested 133

6.9 The effect of indentation strain rate on the 6376 epoxy loading curves 134

6.10 Indentation modulus versus strain rate for five repeats at four different strain rates 135

6.11 Schematic of load displacement data highlighting the areas of positive and negative unloading drift, the point of inflection for the drift, and the original and new unload data to be fitted 136

6.12 Unloading curve creep-relaxation profiles detailing the (a) Drift displacement and (b) Normalised drift displacement, measured from the unloading curves, plotted against the percentage of the maximum load 137

6.13 Indentation modulus results for the original and new unloading curves for the four indentation depths tested 138

6.14 Comparison between the non-linear curve fits and unloading data: (a) Hold time of 0 seconds (b) Hold time of 3600 seconds (c) Strain rate of 0.001 /s (d) Strain rate of 1 /s (e) Original unloading data (f) New unloading data. 140

6.15 Schematic of an indentation, highlighting the contributions of the materials yield stress and the hydrostatic stress to the overall measured material hardness 142

7.1 10×10 µm dynamic mechanical map of CFRP using dynamic nanoscale imaging (a) fibre-matrix topography, (b) storage modulus map, (c) storage modulus variation across interface (Gu et al., 2010) 151

7.2 Finite element simulations of nanoindentation: (a) Thin film applied to substrate (adapted from Pandure et al. 2014) (b) Interphase region of fibrous composite (adapted from Li et al. 2012) 152

7.3 SEM indentation made on thin TiN/SiNx coating deposited on Si (Rabe et al., 2004). 155

7.4 SEM image of (a) upper surface of the composite slice after the push-out test, (b) lower surface of the composite slice after the push-out test.(Canal et al., 2012) 156

B.1 Results from indentations carried out on Aluminium Alloy 6082T6: (a) load-displacement curves for 5 µm indentations (b) modulus results from CSM and basic indentations 180

B.2 The residual impression of a 5 µm indentation carried out on Aluminium Alloy 6082: (a) Optical microscope image (1000X), (b) SPM image 181

B.3 (a) Top view of Aluminium Alloy 6082 SPM image, highlighting locations of line scans, (b) Line scans A, B and C 182

B.4 Normalised (a) Contact area and (b) Indentation modulus determined using each of the pile-up correction methods for Aluminium alloy 6082 182

List of Tables

3.1 Constituent and composite elastic properties (Vaughan and McCarthy, 2011*b*; O'Higgins et al., 2008) 57

4.1 Constituent and composite material elastic and thermal properties (Vaughan and McCarthy, 2011*a*; O'Higgins et al., 2008; Telford et al., 2014) 79

5.1 Sample Preparation Procedure A 99

5.2 Sample Preparation Procedure B 100

5.3 The best choice of curve-fitting constraints for the best fit constants of the Oliver and Pharr non-linear curve-fit 111

5.4 Student-t test parameters 120

6.1 Analysis of non-linear curve fitting parameters 139

6.2 Summary of results 144

Nomenclature

Uppercase Roman Symbols

A	Contact Area
A_{FEA}	Finite element contact area
A_{OP}	Contact Area determined using Oliver and Pharr procedure
A_{PROJ}	Projected contact area measured using SPM
A_{PU}	Projected contact area corrected for pile-up
B	Curve-fitting constant
C	Indentation constraint factor
C_n	Area calibration constants
$E(0)$	Elastic modulus under atmospheric pressure
$E(P)$	Elastic modulus under hydrostatic pressure
E	Young's modulus
E^r	Reduced modulus
E_i	Young's modulus of indenter
E_M	Macroscopic modulus
E_N	Indentation modulus
E_{PROJ}	Modulus corrected using projected contact area
E_{PU}	Modulus corrected using pile-up height
E_r	Reduced modulus
E_s	Young's modulus of sample
E_{un}	Unconstrained modulus

F_0	Amplitude of CSM oscillating force
H	Hardness
K_f	Load frame stiffness
K_s	Support spring stiffness
M	Harmonic oscillator mass
N_B	Number of bulk material indentations
N_I	Number of in situ material indentations
P	Indentation load
P_{max}	Maximum indentation load
R^2	Coefficient of variation
R_a	Arithmetic average roughness
R_c	Paraboloid radius of curvature
R_{FM}	Fibre-matrix relief
R_p	Radius of matrix pocket
S	Contact stiffness
Sp	Inter-fibre spacing
X_B	Mean of bulk material properties
X_I	Mean of in situ material properties
Z	Value for the test statistic
Z_{crit}	Critical value of the test statistic

Lowercase Roman Symbols

$\frac{dP}{dh}$	Slope of unloading curve/Contact stiffness

df	Degrees of freedom
h	Indentation depth
$h_{\frac{dP}{dh}}$	Point of contact stiffness evaluation
h_{creep}	Indentation creep displacement
h_c	Contact depth
h_{max}	Maximum indentation depth
h_{PU}	Pile-up height
h_{PU}	Pile-up height
h_p	Residual indentation depth
h_{SP}	Indentation depth setpoint
m	Curve-fitting exponent
r	Distance from initial point of indentation to outside fibre region
t	Time
t_{hold}	Max load holding segment time
th	Interfacial region thickness
z	CSM oscillating displacement
z_0	Amplitude of CSM oscillating displacement

Greek Symbols

υ	Poissons ratio
α	Conical indenter half-angle
δ	CSM phase angle
$\dot{\varepsilon}$	Indentation strain rate

γ	Hay et al. (1999) correction factor
μ	Coefficient of friction
ν_i	Poisson’s ratio of indenter
ν_s	Poisson’s ratio of sample
ω	Frequency of CSM oscillating force
ϕ	Angle of internal friction
σ_1	Maximum principal stress
σ_2	Middle principal stress
σ_3	Mimimum principal stress
σ_B	Standard deviation of bulk material properties
σ_C	Compressive strength
σ_I	Standard deviation of in situ material properties
σ_n	Normal stress
σ_T	Tensile strength
σ_{YC}	Yield stress in compression
σ_Y	Yield stress
τ	Shear stress
τ_c	Cohesion stress
υ_s	Poisson’s ratio of specimen
ε	Intercept correction
$d\Theta$	Angular increment

Abbreviations

AFM	Atomic Force Microscopy
BCB	Benzocyclobutene
CFRP	Carbon Fiber Reinforced Plastic
CSM	Continuous Stiffness Measurement
DCM-II	Dynamic Contact Module II
DMA	Dynamic mechanical analysis
DSI	Depth-sensing indentation
FCF	Fibre Constraint Factor
FEA	Finite Element Analysis
FRP	Fibre-Reinforced Plastics
HTE	High Throughput Experimentation
iPP	Isotactic polypropylene
ISO	International Organization for Standardization
MD	Molecular dynamics
MMC	Metal matrix composite
NMAT	Nanomechanical Actuating Transducer
PC	Polycarbonate
PMCs	Polymer Matrix Composites
PMMA	Poly(methyl methacrylate)
PS	Polystyrene
RVE	Representative Volume Element
SEM	Scanning Electron Microscope
SPM	Scanning Probe Microscopy
TEM	Transmission Electron Microscopy

1 Introduction

1.1 Background

The use of composite materials in structural applications has increased significantly in recent decades due to the higher specific stiffness and strength of the materials in comparison to metallic materials. Composite materials are commonly used in the automotive, aerospace and marine industries, as well as in a number of consumer products such as golf clubs and tennis rackets. Much of the recent developments in composite materials have been driven by the aerospace industry, where composite materials initially were used in the design of military aircraft, as increased performance and manoeuvrability could be achieved due to their lightweight nature. In recent years, the increase in fuel prices and requirement to reduce CO_2 emissions from commercial aircraft has prompted the use of composite materials in primary aircraft structures. Composite material use in commercial aircraft has increased from 5-6% of the aircraft structure by weight in the early 1990s, to up to 50% in today's advanced aircraft programs such as the Boeing 787 and Airbus 350, with further increase expected in the coming years (Mazumdar, 2015).

The increasing industrial demand for composite structures has been mirrored by an increase in demand for predictive analysis tools, required to gain a greater understanding into the behaviour of composite materials under various types of loading. Fibre-reinforced plastics (FRP) are the most common type of composite material used in industry. The fibre constituents are made from glass or carbon in most cases, and exhibit very high strength and stiffness. The fibre diameters are generally in the order of a few microns. This small fibre size is advantageous, as smaller diameter fibres decrease the likelihood that failure-inducing flaws will exist in the material, while also increasing the interfacial surface area with the surrounding matrix material. The binding matrix material is generally more compliant, but also more ductile than the fibres. The matrix material adheres the fibres together and defines the shape of the composite part, while also serving to protect the structural fibres from external damage and environmental attack.

Nanoindentation is a non-destructive testing technique that can be used to determine the properties of materials at the micro and nano scales. During the test a small diamond tip of pyramidal geometry, such as the Berkovich tip shown in Fig. 1.1a, is brought in contact with the sample surface and allowed to penetrate into the surface to a preset maximum indenter load or displacement. The indenter load and displacement response is continuously measured throughout the test (Fig. 1.1b) and can be used to infer the mechanical properties of the small localised region of material, such as hardness and elastic modulus. The technique has been successfully used to determine the properties of thin film materials applied to a substrate, and has been recently used in an attempt to determine the properties of fibrous composite materials since the indentations operate on a scale that allows the individual composite constituents to be characterised. Fig. 1.2 shows an example of a residual nanoindentation impression carried out in a region of matrix material between the fibres in an aerospace carbon fibre/epoxy composite material.

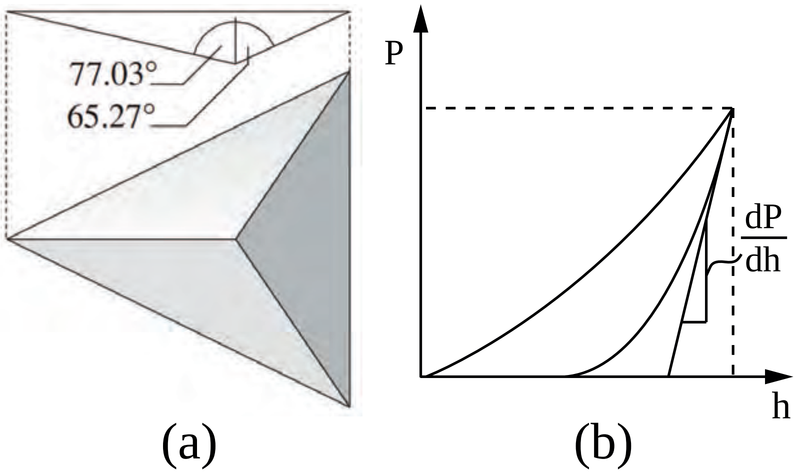

Figure 1.1: (a) Berkovich indenter geometry, (b) Typical load-displacement curve

1.2 Motivation

Much of the structural analysis of the composite parts used in primary aircraft structures relies on design practices and strength predictions which are based on ply-level analysis and macroscale testing. Macroscopic stress and strain criteria are often used to predict the response of composite materials to various loading scenarios, as opposed to criteria based on the actual physical mechanisms of failure. Local microscale failure events such as fibre breakage/kinking, matrix cracking,

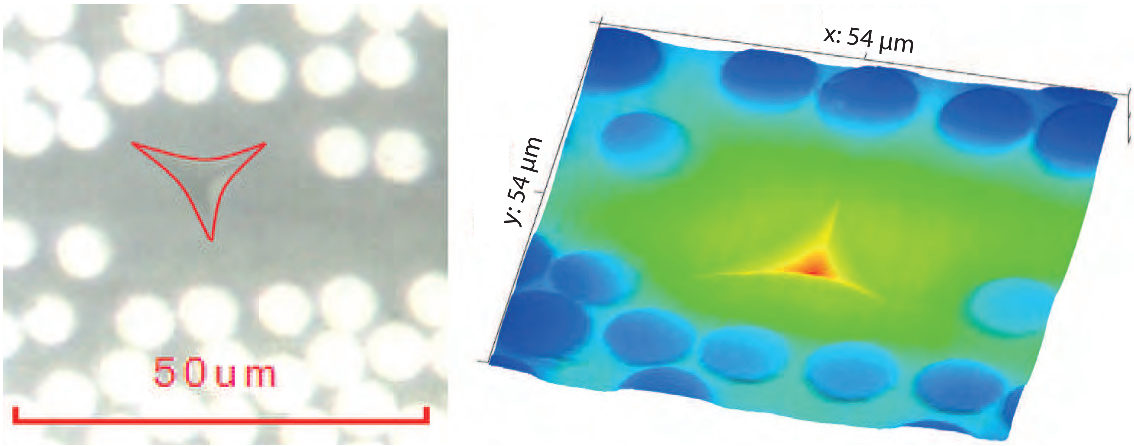

Figure 1.2: Nanoindentation of carbon fibre/epoxy composite matrix constituent (a) Micrograph and (b) Scanning Probe Microscopy (SPM) image of residual indentation

fibre-matrix debonding and inter-ply delamination initiate failure in composite materials. These intraply micromechanical events eventually lead to the macroscopic failure of the material. Currently, there is a distinct lack of agreement between the predictions made by numerous failure theories when compared to the experimental response of different composite lay-ups and loading arrangements (Kaddour and Hinton, 2013). This predictive uncertainty adversely affects the design of composite structures, with larger factors of safety employed than those used for traditional metallic materials, whose failure mechanisms are better understood. This overdesign of composite structures somewhat negates the weight-saving advantages of the materials. As a result, a significant amount of research has been carried out in order to gain a greater understanding of the link between the damage at the composite microscale and that experienced by the larger composite structure. Micromechanical finite element models of composite microstructures have successfully been used to predict the macroscopic stress-strain behaviour of composite materials. These models analyse the response of composite to loading, based on the constituent material properties in their bulk form, and the strength and toughness of the fibre-matrix interface. Micromechanical modelling could potentially prove to be a useful tool in future composite structure design projects by limiting the amount of costly coupon and structural testing required in order to validate the strength of composite structural elements. However, in order to ensure the accurate simulation of microscale deformation and damage, quantitatively accurate properties of the in situ constituents must be determined.

The microscale properties of the matrix constituent influences the macroscale properties of a composite structure when the material is loaded transversely to the fibre direction in tension or compression, while also influencing the in-plane shear response and fibre-direction compressive strength (Llorca et al., 2011). The properties of the matrix constituent can be approximated using conventional mechanical testing of coupon specimens fabricated from the material in its bulk form. However, the degree to which the cross-linking process and properties of the in situ polymer matrix are affected by the intensive thermal, mechanical and chemical processes taking place during the consolidation of the constituent phases is not well understood. The nanoindentation technique presents the most viable approach to experimentally determine the properties of the in situ matrix constituent, and gain a greater insight into the effect of the composite manufacturing process on the microscale behaviour of the materials. However, there is a distinct lack of quantitative experimental comparisons between the bulk and in situ composite matrix properties in the current literature. Such comparisons provide critical input data to micromechanical simulations of composite materials.

1.3 Problem description and objectives

This thesis outlines a combined experimental and numerical investigation into the application of the nanoindentation technique to characterise the matrix material of a carbon fibre/epoxy composite material. The theory used by the nanoindentation technique in order to calculate the material properties of the substrate assumes that the substrate is a single phase, homogeneous medium. Therefore, the application of this theory to inhomogeneous composite materials which are composed of discrete regions of different material properties can be problematic. The sub-surface deformation field produced by the indentation loading could potentially overlap into the neighbouring material phases, leading to erroneous characterisation of the target material. During the indentation of thin films, it is common practice to restrict the maximum indentation depth to no more than 10% of the film thickness in order to minimize the influence of the substrate on the film indentation properties. However, no such generalised rule exists for indentations carried out on the constituents of fibrous composite materials.

Furthermore, carbon fibre/epoxy composite materials undergo a high temperature curing process in order to consolidate the final part geometry and cure the polymer matrix material. It has been previously shown that this process leads to the development of significant residual stress in microstructure of the final part post-cure, especially for materials with a large thermal gradient following cure and high volume fraction of fibre reinforcement. The nature and magnitude of the residual stress state varies throughout the composite microstructure and could potentially skew or add bias to the indentation properties of the in situ constituents. While the effects of equibiaxial residual stress states on the nanoindentation load-displacement data and properties has been previously investigated, no study exists which examines the effect of the complex residual stress states which exist in the fibrous composite microstructure post-cure.

In the majority of micromechanical simulations of composite failure, the discrete constituent regions are modelled using the properties of each material in their bulk form. This may not be the case after the composite manufacturing and high temperature curing process. Thus, an important comparison can be made between the indentation properties of the bulk and in situ matrix material. Property changes are more likely to occur in the matrix constituent as the material is in a molten state during the curing process. This could potentially lead to chemical interactions between the molten matrix material and fibre treatments, while the surrounding fibres could also affect the cross-linking of the matrix material during the curing process. While low-depth indentations are required in order to characterise the small pockets of matrix material within the high fibre volume fraction composite microstructure, low-depth indentations can also be influenced by bias or scatter due to tip blunting, surface roughness and size-scale effects. Therefore, a careful experimental study is required to find the correct balance between the various sources of error associated with indentation studies on inhomogeneous materials, in order to calculate the in situ properties of the matrix material.

In micromechanical simulations of the composite failure process, the elastic behaviour of the composite matrix constituent is defined using the Young's modulus of the material. While this property is readily determined using the nanoindentation technique, the ability of the technique to correctly quantify the true elastic modulus of polymeric materials has been called into question by a number of authors, with the modulus being overestimated in the vast majority of cases (Kranenburg et al., 2009; Tranchida et al., 2007). The failure of the nanoindentation theory to correctly quantify the elastic modulus of polymeric materials has often been attributed to material pile-up, viscoelastic deformation and the effect of the hydrostatic stress.

The above open questions have led to the formation of the following objectives for this thesis:

1. To develop a finite element model of the indentation process applied to the matrix constituent of a fibrous composite microstructure. This will allow the constraining effect of the surrounding fibres to be characterised, and the potential error due to the constraint to be quantified and compared with experimental variations reported in literature.
2. To carry out a numerical study to determine the nature and magnitude of the various residual stress states which exist in the microstructure of a carbon-fibre epoxy composite post-cure and to analyse the effect of the residual stress states on the nanoindentation test.
3. To carry out a robust experimental comparison between bulk and in situ polymer matrix material, ensuring that the results are free from the influence of the surrounding fibre constraint and statistically significant relative to the scatter associated with low-depth indentations. Also, to determine any trend between the in situ matrix properties and the vicinity of the surrounding fibre reinforcement.
4. To investigate the residual impressions of bulk polymer matrix indentations for evidence of pile-up. Also, to alter experimental indentation settings and theoretical treatment of the load-displacement data to nullify any time-dependent effects on the calculation of the material's elastic modulus. Finally, to theoretically measure the magnitude of the sub-surface hydrostatic stress and characterise the effect of this stress state on the calculated value of the polymer indentation modulus.

1.4 Thesis outline

Following this introduction, Chapter 2 presents a review of the literature relevant to the nanoindentation of fibrous composite microstructures. The importance of the experimental technique to micromechanical simulations of composite failure is highlighted. The review summarises the experimental and numerical work previously carried out on composite nanoindentation, as well as highlighting the potential issues related to applying the technique to inhomogeneous composite and polymeric materials.

In Chapter 3, a finite element approach is presented which models the nanoindentation process applied to an in situ matrix pocket. The effect the surrounding fibre constraint on the calculated indentation modulus is determined and comparisons are made between 2D and 3D modelling approaches.

In Chapter 4, a two-step finite element framework is presented that examines the effect of thermal residual stress on the nanoindentation of in situ matrix material. A micromechanical modelling approach is used to determine the state of residual stress at the composite microscale, while a three-dimensional nanoindentation model is used to characterise the effect of the residual stress on the properties determined using nanoindentation.

In Chapter 5, the variation of the in situ matrix properties has been investigated using nanoindentation experiments. A method of specimen manufacture is presented which involves co-curing of the composite material and bulk matrix to produce specimens ideal for microscale characterisation. The fibre constraint effect is characterised experimentally, which allows valid comparisons to be made between the bulk and in situ properties of the matrix material, independently of the constraint.

In Chapter 6, the effects of pile-up, viscoelasticity and hydrostatic stress on the indentation modulus of the carbon-fibre composite epoxy matrix are investigated experimentally. Scanning Probe Microscopy (SPM) is used to investigate the residual impressions for evidence of pile-up. Also, alterations are made to the experimental setup and theoretical treatment of the resulting data in order to negate viscous and hydrostatic stress effects on the calculation of the specimen indentation modulus.

Finally, Chapter 7 summarises the main conclusions from the work described in the thesis. This chapter also includes some further discussion of the main results, and recommendations are outlined for future work.

2 Literature Review

2.1 Introduction

In this chapter, a review of the literature relevant to the characterisation of polymer matrix composites using the nanoindentation technique is presented. The effect of the in situ properties and thermal residual stress on the micromechanical behaviour of fibrous composite materials is outlined. A description of the nanoindentation method and theory is included, and previous work on the application of the method to composite materials is highlighted. The review addresses the numerous issues associated with the application of the technique to the inhomogeneous fibrous composite microstructure. The effects of neighbouring constituents, pile-up, residual stress and time-dependent deformation on the important nanoindentation parameters and properties are highlighted. The review also details the use of numerical finite element modelling to gain a greater insight into the stress and deformation fields produced during a nanoindentation experiment.

2.2 Fibrous composite micromechanisms

While the failure behaviour of most structural materials is largely controlled by a single failure mechanism, the macroscopic deformation and failure behaviour of fibre-reinforced composite materials is controlled by a number of local mechanisms which occur at the microscale. The initiation and propagation of these micromechanisms are dependent on the constituent materials properties, the local distribution of the reinforcing fibres, and the direction of the applied load relative to the direction of the unidirectional reinforcing fibres, as highlighted in Figure 2.1. When the material is loaded longitudinally parallel to the fibres, the failure is dominated by the strength of the fibre material. When the fibres begin to fail, the load is quickly transferred to the other surrounding fibres. This leads to rapid damage propagation after initial failure until the matrix is unable to support the stress redistributed by the failed fibres, and final failure occurs. The failure process under longitudinal compressive loading generally occurs by fibre-kinking due to slight off-axis orientations of the unidirectional reinforcement. This failure process is also affected by the elastic properties of the matrix constituent, as the buckling deformation will be restricted by the surrounding matrix material (Herakovich, 2012).

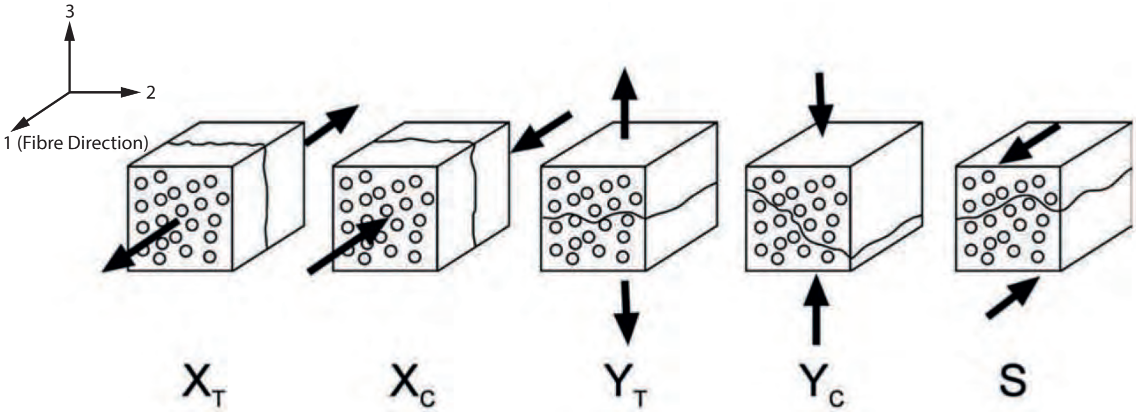

Figure 2.1: Fibrous composite failure mechanisms under various loading conditions (Llorca et al., 2011)

In general, composite structures are designed in order to have the orientation of the fibres parallel to the direction of the externally applied mechanical loads. However, it is almost impossible to avoid situations where the structure is loaded transversely to the fibres. Often, the first local failures in composite structures are observed in transverse plies, and can potentially lead to premature failure of the composite structure. Tensile failure of transverse plies is brittle and highly dependent on the properties of the matrix constituent, where failure is attributed to matrix cracking and fibre-matrix debonding. In contrast, under transverse compression or shear loading, large deformation occurs prior to failure due to the non-linear behaviour of the matrix constituent under these loadings. It is clear that the large number of failure micromechanisms which can occur at the composite microscale complicates failure predictions for composite structures. As more accurate strength predictions are required, the field of micromechanics has grown in order to gain a greater insight into the microscale damage process, and relate the observed processes to the macroscopic stress-strain response.

2.3 Micromechanics

Recent advancements in experimental and numerical analysis techniques have allowed for more extensive research to be carried out at the composite microscale.

Modern experimental equipment such as microtest machines allow tensile, compression and bending tests to be carried out in the chamber of an SEM, allowing for unparalleled observation of composite micromechanical deformation and damage. An SEM micrograph showing a composite microstructure subjected to transverse compression loading is shown in Fig. 2.2a (Llorca et al., 2011). The large strain response of the composite under this type of loading was apparent, where strain localisation in the matrix constituent is observed, as well as the onset of fibre-matrix interface damage. Fig. 2.2b shows the in situ observation a composite microstructure under transverse tension loading (Zhang et al., 2010). The failure sequence is much more brittle, with matrix and interface cracking clearly shown. Experimental micromechanical analysis provides a qualitative understanding of the microscale composite failure process. However, quantitative insight into the effects of local fibre distribution, constituent properties and interface strength through experimentation has proven difficult.

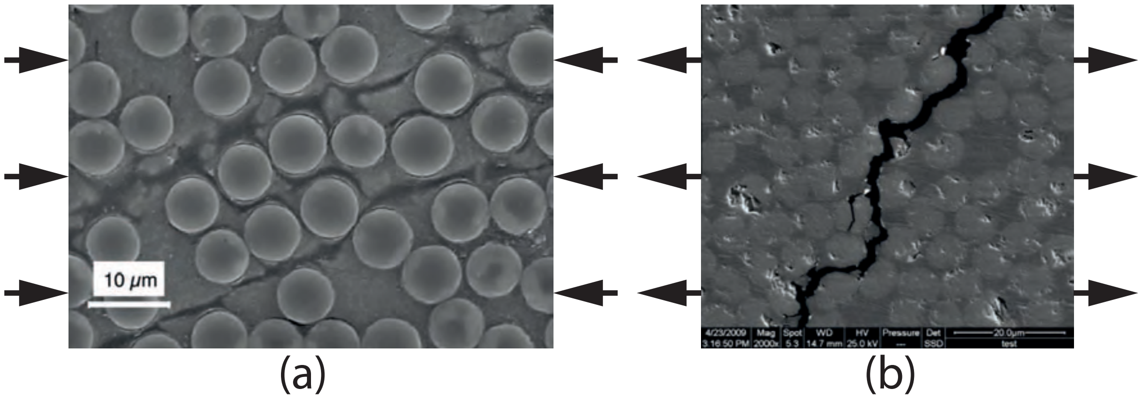

Figure 2.2: In situ SEM observation of (a) shear bands in the matrix constituent under transverse compression loading (Llorca et al., 2011) and (b) interface damage and matrix cracking under transverse tension loading (Zhang et al., 2010)

In recent decades, computers have become much more efficient at carrying out numerical finite element calculations, allowing for more complex multiscale problems to be analysed. Micromechanical finite element modelling has become a popular method of linking the various composite failure processes between the micro and macro scales. These models provide an insight into the material's micromechanical behaviour based on applied macroscopic stress states and the properties of the individual composite constituents. Periodic unit cells or representative volume elements (RVEs) are generally used to represent the whole microstructure of the composite with a repeating array of fibres in a polymer matrix. Another less common approach is embedded cell modelling where only a small microstructural section of interest is represented by the composite microstructure, while the rest of the model is represented by the macroscopic properties of the composite (González and Llorca, 2006). Vaughan and McCarthy (2011*a*; 2011*b*) carried out two separate micromechanical studies of the HTA/6376 carbon-fibre epoxy composite utilising the periodic unit cell approach. The first investigated the response of the microstructure to transverse loadings using a finite element micromechanics damage model and the second, using a similar model, investigated the effect of shear loadings on the composite microstructure. The models assume the properties of each constituent remain the same as the properties of the material in its bulk form. The microstructural array of fibres within the matrix was created using an algorithm which generates statistically equivalent fibre distributions of actual experimental fibrous composite microstructures (Vaughan and McCarthy, 2010). These models provide a quantitative insight into the failure process of the composite at the microscale, and can be used to relate the damage behaviour observed in the model to the macroscopic experimental stress-strain behaviour of the composite. The response of the micromechanical models to transverse and shear loadings are shown in Figures 2.3a and 2.3b respectively.

2.3.1 Thermal residual stress

In order to consolidate a final composite part and cure the epoxy matrix material, composite parts are cured in a vacuum assisted, high temperature and pressure autoclave process. Once the part is fully cured at this high temperature, it is subsequently cooled down to room temperature. At the macroscale, thermal contraction can cause the shape and dimension of a composite panel to be different than those of the uncured panel and tool, leading to significant warpage in curved parts (Tseng and Osswald, 1994). At the microscale, it has been shown that significant residual stress develops as a result of the mismatch in thermal expansion coefficients between the fibre and matrix phases. The nature and magnitude of this stress varies spatially throughout the microstructure and is dependent on the fibre volume fraction and inter-fibre spacings (Hojo et al., 2009). A post-cure stress distribution from a finite element study carried out by Yang et al. (2013) is shown in Fig. 2.4, where the post-cure stress states for two different microstructures are

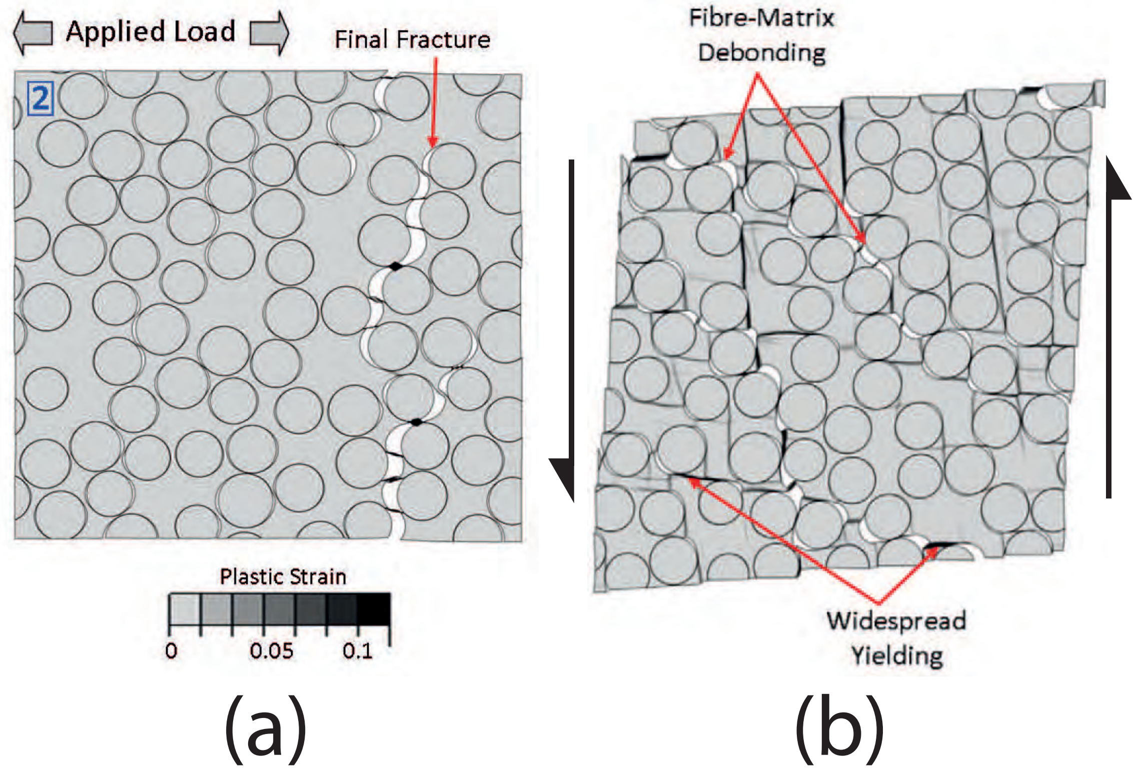

Figure 2.3: Micromechanical models of HTA/6376 composite (a) RVE subjected to transverse tension loading (Vaughan and McCarthy, 2011*a*), (b) RVE subjected to shear loading (Vaughan and McCarthy, 2011*b*)

shown. Fig. 2.4a shows a microstructure with a fibre volume fraction of 50% and an inter-fibre spacing of 0.8 µm, while Fig. 2.4b shows microstructure with a fibre volume fraction of 60% and an inter-fibre spacing of 0.1 µm. It is clear from the resulting stress contours that the constituent and interface stress states are highly dependent on the fibre distribution. The magnitude of the residual stress is often large enough to play a role in the micromechanical failure process under transverse loadings. Vaughan and McCarthy (2011*a*) showed that the transverse strength of the HTA/6376 composite was increased by the existence of large compressive residual stress at the fibre-matrix interface, which served to offset the interfacial debonding induced by the tensile loading. However, other studies have shown that interfacial and matrix material damage can be produced due to the cooldown stresses, prior to the application of any external load. This residual damage has been observed in numerical simulations (Maligno et al., 2009; Yang et al., 2013) as well as experimentally (Gentz et al., 2004). In these cases, the existence of residual stress has a detrimental effect on the transverse strength of the ply, depending on the constituent properties and the strength of the fibre matrix interface.

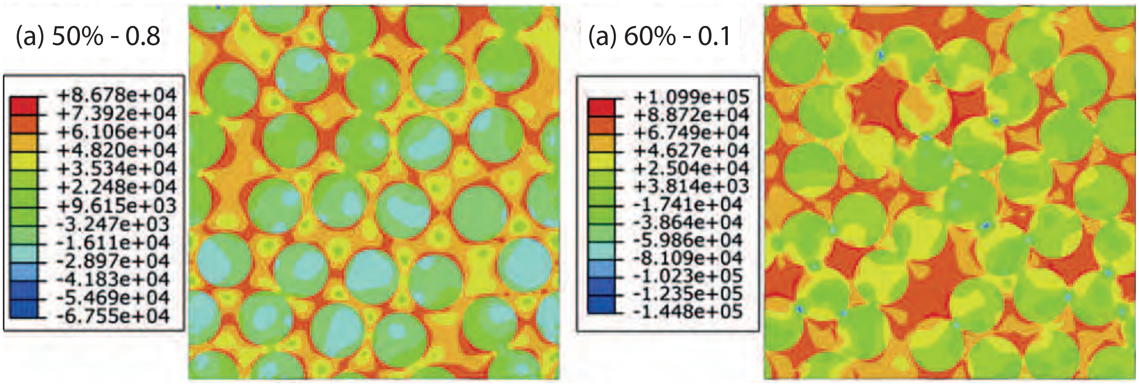

Figure 2.4: Contour plot of the maximum principal residual stress (kPa) for (a) microstructure with 60% fibre volume fraction (b) microstructure with 50% fibre volume fraction (Yang et al., 2013)

2.3.2 Constituent material behaviour

In order to ensure realistic micromechanical modelling of the composite deformation and failure processes, accurate definition of the constituent material behaviour is required. The reinforcing fibre materials generally exhibit a brittle failure response, and can simply be modelled as an elastic material in the absence of fibre damage. Glass fibres generally exhibit isotopic elastic behaviour, whereas carbon fibres are transversely isotropic, and are an order of magnitude stiffer in their longitudinal direction than the transverse direction. The behaviour of the binding matrix material is dependent on the applied stress state. Epoxy is often used as the matrix phase in aerospace composites due to its good adhesion properties and resistance to moisture absorption. The elastic behaviour of polymers can vary slightly depending on whether they are loaded in tension or compression (Tranchida et al., 2007), while the yielding behaviour varies more significantly due to the influence of the hydrostatic component of stress (Fiedler et al., 2001). Two commonly used classical yield criteria for isotropic ductile materials are the Tresca and von Mises yield criteria, which are described in Equations 2.1 and 2.2, respectively:

$$\sigma_1 - \sigma_3 = \sigma_Y \tag{2.1}$$

$$(\sigma_1 - \sigma_2)^2 + (\sigma_2 - \sigma_3)^2 + (\sigma_3 - \sigma_1)^2 = 2\sigma_Y^2 \tag{2.2}$$

where σ_1, σ_2 and σ_3 are the three principal stresses and σ_Y is the uniaxial yield stress of the material. It is clear from the above formulae that a hydrostatic increase in the stress state ($\sigma_1 = \sigma_2 = \sigma_3$) has no effect on the yielding behaviour of the material. This is apparent in the 3D yield surface plot for the von Mises criterion shown in Fig. 2.5a. These criteria are only dependent on the deviatoric component of stress, and thus, cannot be used to accurately predict yielding the polymers. The plasticity theories for geological materials such as soil and concrete include consideration of the hydrostatic stress component and, thus, can be conveniently applied to epoxy materials. The Mohr-Coulomb criterion induces yield in the material when the combined normal (σ_n) and shear (τ) stress on a plane reaches a critical level according Equation 2.3:

$$\tau_c = \tau + \sigma_n \tan\phi \tag{2.3}$$

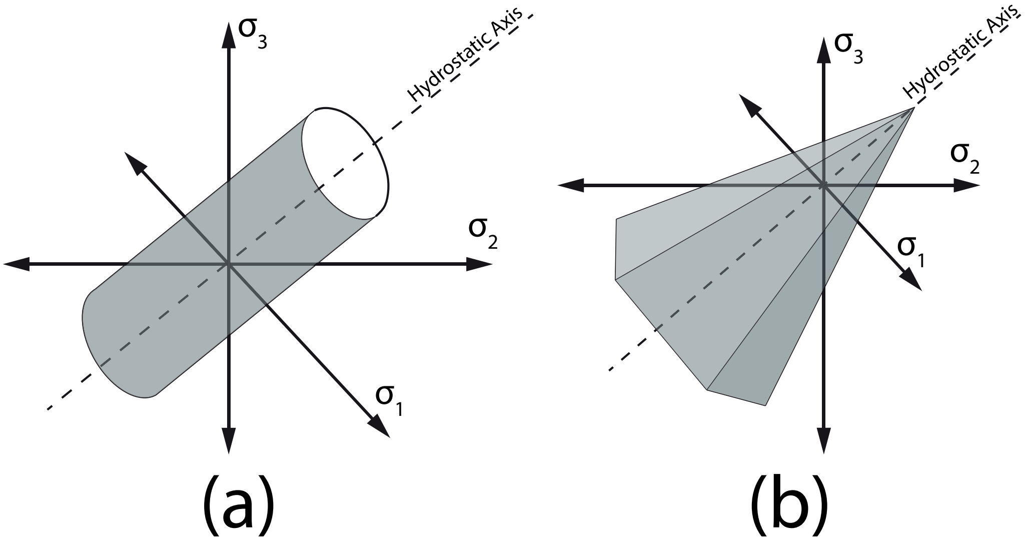

Figure 2.5: Yield surfaces (a) von Mises, (b) Mohr-Coulomb

where τ_c is the cohesion stress (yield stress in pure shear) and ϕ is the angle of internal friction. The yield criterion can be expressed in terms of the maximum and minimum principal stresses, as shown in Equation 2.4:

$$f(\sigma_1, \sigma_3) = (\sigma_1 - \sigma_3) + (\sigma_1 + \sigma_3)\sin\phi - 2\tau_c\cos\phi = 0 \tag{2.4}$$

The yield surface for the Mohr-Coulomb criterion is shown in Fig. 2.5b, where it is clear than an increase in stress along the hydrostatic axis will affect the yielding behaviour of the material. Yielding also occurs in tension at a lower stress than in compression. Experimental studies have shown that the linear dependence of the yield stress on the hydrostatic pressure, assumed by the Mohr-Coulomb criterion, provides a good prediction for polymer behaviour (Altenbach and Tushtev, 2001). The criterion has been successfully applied to micromechanical simulations of FRP materials subjected to tensile, compressive and combined loading regimes (Vaughan and McCarthy, 2011*a*; González and Llorca, 2007; Totry et al., 2008).

One major limitation of the current micromechanical analysis techniques is the assumption that the properties of each constituent remain the same as the properties of the material in its bulk form, which may not be the representative of the material behaviour after the complex composite manufacturing and curing processes. Thus, the nanoindentation technique has recently been employed by a number of authors in an effort to experimentally characterise of the in situ constituent materials at the microscale.

2.4 Nanoindentation

Nanoindentation is a non-destructive testing technique which can be used to determine the mechanical properties of materials at small scales. A sharp indenter tip, usually made from diamond, is driven into the surface of the material under either load or displacement control, allowing material properties of the substrate material, such as elastic modulus and hardness, to be determined. The technique developed as an evolution from traditional Vickers hardness testing. Both methods are based around the concept of loading a pyramidal indenter into a material in an attempt to determine properties of that material. In a Vickers hardness test, the hardness is calculated by dividing the maximum load reached during the indentation by the projected area of the residual impression, which is directly measured post-hoc using an optical microscope. Technological improvements to the transducer sensitivity of indentation devices allowed for the continuous monitoring of the load and displacement throughout the indentation cycle. The technique was first used at the micron scale by Fröhlich et al. (1977) and shortly thereafter became commonly used as a technique for determining the surface properties of materials. Further development of the technique eventually allowed the tests to be carried out on the nanometre scale, hence forming a new field of study known as nanoindentation. This allowed the load and displacement to be measured within the millinewton and nanometre ranges, respectively. The theoretical treatment of the load-displacement data has been the topic of extensive research, with the most commonly used method being that developed by Oliver and Pharr in (1992).

The four-sided pyramidal Vickers tip, shown in Fig. 2.6a, is the most commonly used indenter geometry for traditional hardness testing at the macro and micro-scales. However, for nanoscale measurements, the three-sided pyramid shape of the Berkovich indenter (Fig. 2.6b) is preferred for property measurement. This tip shape was invented by Russian scientist E.S. Berkovich in the USSR (Berkovich, 1950), and has the same area to depth ratio as the Vickers tip. The three-sided pyramidal shape of the tip means that it is more easily manufactured at small scales due to lack of a 'chisel' edge defect at the indenter tip, which can occur when manufacturing a Vickers shaped tip at small scales. An SEM image of a Berkovich tip is shown in Figure 2.7a and the residual plastic impression from a Berkovich indentation into a fused silica substrate material is shown in Figure 2.7b (Fischer-Cripps, 2009).

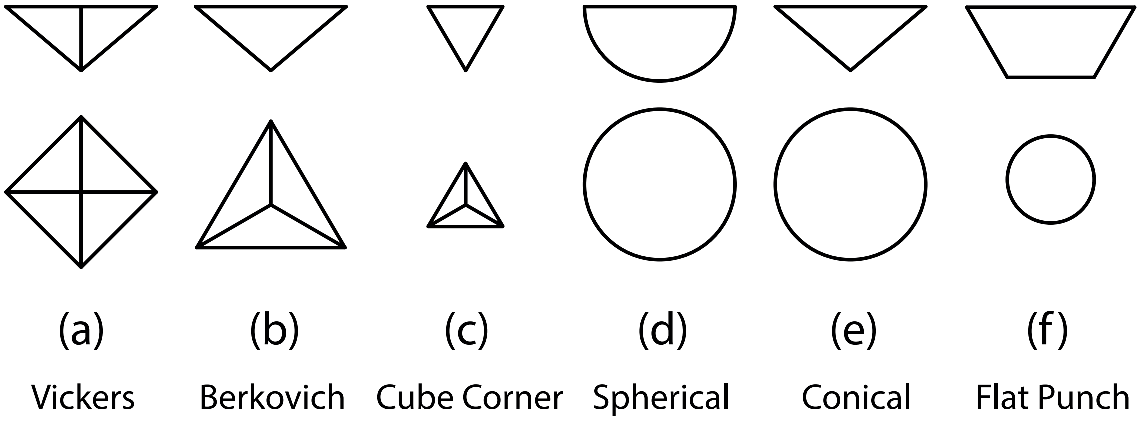

Figure 2.6: Commonly used indenter tip shapes

A selection of the other commonly used indenter geometries are shown in

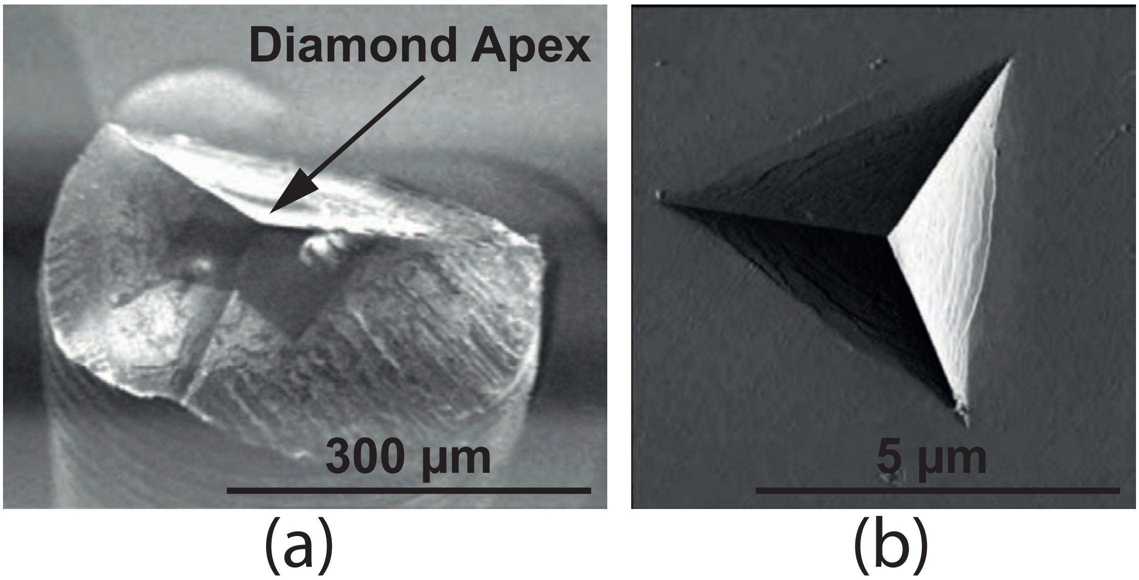

Figure 2.7: (a) SEM image of a Berkovich indenter tip (b) Residual impression left by a Berkovich tip on a fused silica substrate (Fischer-Cripps, 2009)

Figure 2.6. Spherical indenters can be used to gain information about the elastic-plastic transition of a substrate, which can theoretically be used to examine yielding and work hardening, and to recreate the entire uniaxial stress-strain curve from data obtained in a single test. This is not possible with a sharp indenter tip as plasticity occurs almost instantaneously after the initiation of contact. Conical indenters have the advantage of an axisymmetric geometry facilitating the use of analytical models in the analysis of their nanoindentation response. Indentations carried out by pyramidal indenter tips are conveniently analysed using the theory for an equivalent conical geometry, but are much easier to manufacture, and less prone to wear than conical tips. Flat punch indenters offer a useful alternative to pyramidal indenters as the determination of the contact area is less ambiguous and constant with indentation depth.

2.4.1 Theory

The nanoindentation technique uses elastic contact theory in order to derive the mechanical properties of the sample using continuous measurements of force and displacement. The first relationship between force, displacement and elastic properties was developed by Hertz (1881), who analysed the case of elastic contact between two curved surfaces. The determination of stress and deformation fields in a flat substrate loaded by an axisymmetric indenter was first analysed by Boussinesq (1885). However, this work did not include a closed-form solution. A solution for contact between a cone and a flat surface was derived by Love (1939), while later, Sneddon (1965) published a general solution governing contact between any axisymmetric body and a flat surface. It was shown that the solutions derived using Sneddon's general expressions were in agreement with the solutions derived by Hertz and Love specifically for paraboloid and conical indenter geometries, respectively. The derived relationship between the indenter load and displacement for a paraboloid is given in Equation 2.5:

$$P = \frac{4}{3} E_r R_c^{\frac{1}{2}} h^{\frac{3}{2}} \tag{2.5}$$

where P is the indenter load, h is the indenter displacement, R_c is the radius of the paraboloid, and E_r is the effective modulus of the contact, which accounts for deformation in both the indenter and the substrate. The relationship between the indenter load and displacement for a conical indentation is given in Equation 2.6:

$$P = \frac{2}{\pi} E_r \tan \alpha h^2 \tag{2.6}$$

where α is the half-angle of the cone, as illustrated in Fig. 2.8a. The force-displacement relations given in Equations 2.5 and 2.6 can be generalised for any axisymmetric geometry, as shown in Equation 2.7:

$$P = Bh^m \tag{2.7}$$

where B is a constant which depends on the indenter geometry and substrate properties, while the exponent m is equal to 1 for elastic indentations with a flat punch indenter, equal to 1.5 for elastic indentations by a paraboloid, and equal to 2 for elastic indentations with a conical indenter. In order to apply this elastic theory developed by Sneddon to indentations where both elastic and plastic deformation

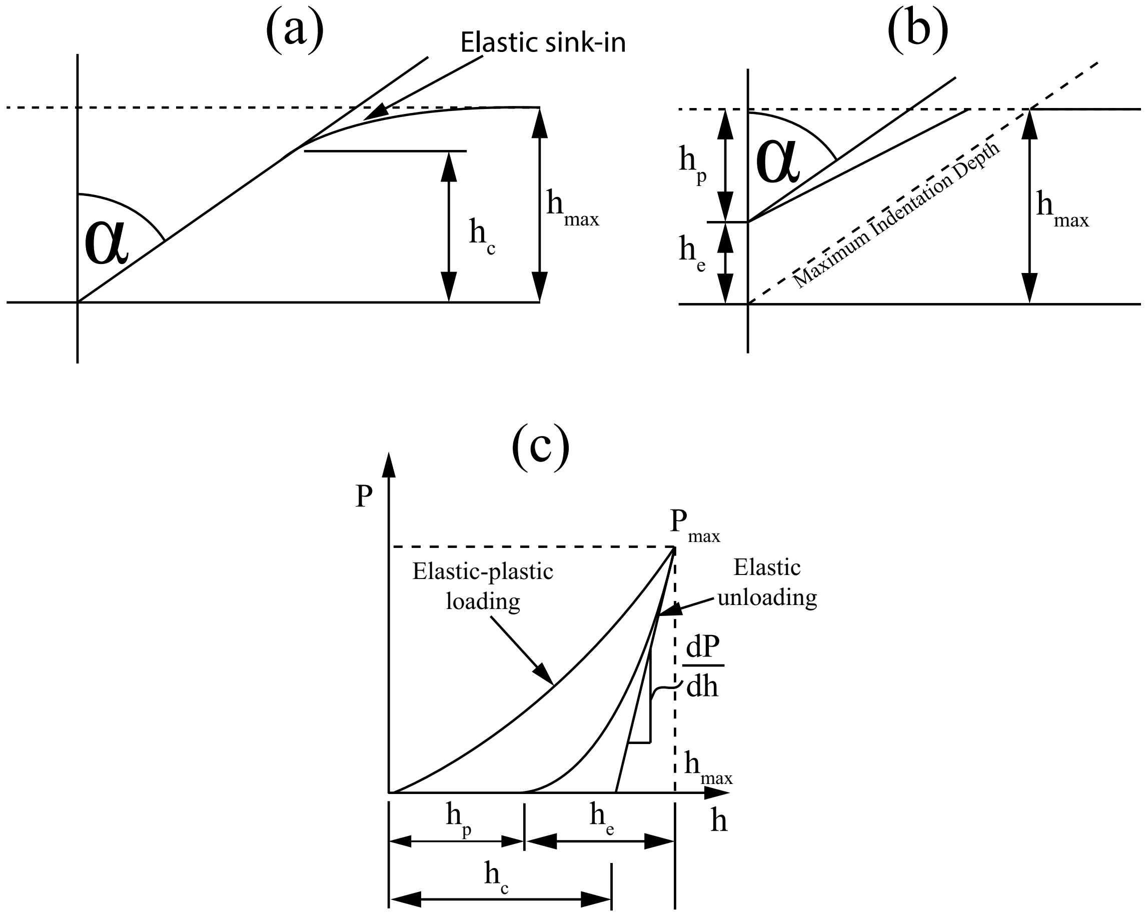
(a)
Elastic sink-in
α
h_c
h_{max}
(b)
h_p
α
h_e
Maximum Indentation Depth
h_{max}
(c)
P
P_{max}
Elastic-plastic loading
Elastic unloading
$\frac{dP}{dh}$
h_{max}
h
h_p
h_e
h_c

Figure 2.8: (a) Schematic of indenter and specimen surface at full load for a conical indenter (b) Schematic of indenter and specimen surface at full unload for a conical indenter, (c) Typical load-displacement curve highlighting the parameters used in the nanoindentation analysis

occurs during loading, the theory is applied to the recoverable unloading portion of the data. According to ISO 14577, at least 50% of the unloading data should be fitted. Therefore, Equation 2.7 can be re-written as:

$$P(h) = B\,(h - h_p)^m \tag{2.8}$$

where h_p is the residual depth of the indentation following complete unloading, as illustrated in Fig. 2.8b. The stiffness of the contact (S) can be determined by differentiating these force-displacement relations with respect to displacement ($\frac{dP}{dh}$), as shown in Fig. 2.8c. It was shown by Pharr et al. (1992) that the relationship between the stiffness (S), reduced modulus (E_r) and the contact area (A) is not dependent on the geometry of the indenter. This relation is given in Equation 2.9.

$$S = \frac{dP}{dh} = \frac{2\gamma E_r \sqrt{A}}{\sqrt{\pi}} \tag{2.9}$$

where γ is a correction factor proposed by Hay et al. (1999), who discovered that the application of Sneddon's elastic solution to conical indentations lead to a slight error, as it improperly accounted for radial material displacement into the contact region for conical indentations. For a conical indenter it was shown that γ is dependent on the sample Poisson's ratio (υ_s) and the half-angle of the conical indenter (α) according to Equation 2.10:

$$\gamma = 1 + \frac{\pi(1 - 2\upsilon_s)}{4(1 - \upsilon_s)} \cot \alpha \tag{2.10}$$

Equation 2.9 can be used to determine the reduced modulus of the indentation. The elastic modulus of the substrate can then be calculated by accounting for the effect of the non-rigid indenter on the measured load-displacement, using Equation 2.11:

$$\frac{1}{E_r} = \frac{1 - {\nu_s}^2}{E_s} + \frac{1 - {\nu_i}^2}{E_i} \tag{2.11}$$

where E_s and υ_s are the elastic modulus and Poisson's ratio of the specimen, while E_i and υ_i are the values corresponding to the indenter material. For cases where the indenter is assumed to be rigid, Equation 2.11 can be reduced down to Equation 2.12 by assuming E_i is infinite:

$$\frac{1}{E_r} = \frac{1 - {\upsilon_s}^2}{E_s} \tag{2.12}$$

It should be noted that in order to determine the modulus of the specimen using Equations 2.11 or 2.12, a decent estimate of the sample's Poisson's ratio (υ_s) is required. However, the dependence of the calculated specimen modulus value on the chosen value of specimen Poisson's ratio is weak. Uncertainty analysis shows that an uncertainty of 40% in the Poisson's ratio leads to only 5% uncertainty in the calculated Young's modulus (Philip, 2009).

The calculation of the hardness property of the specimen is much more straightforward, simply defined as the load on the indenter tip (P) divided by the projected contact area (A):

$$H = \frac{P}{A} \tag{2.13}$$

The hardness property is useful as experiments show that the measured hardness value is proportional to the specimen material's yield stress in compression according to Equation 2.14:

$$H \approx C\sigma_{YC} \tag{2.14}$$

where σ_{YC} is the material's yields stress in compression and C is a constant called the 'constraint factor'. The contact pressure in an indentation test required to induce flow in the material is higher than that of a uniaxial compression test due to the confined nature of the indentation stress field. During an indentation test, the stressed material is confined by the surrounding non-stressed material, leading to a significant build-up of sub-surface hydrostatic stress, which contributes to the overall measured contact pressure or hardness. The value of C is dependent on the specimen material and type of indenter used.

It is clear from Equations 2.9 and 2.13 that in order to calculate the elastic modulus and hardness of the specimen, an accurate determination of the contact area is required. Traditionally, the contact area was determined by examining the impression of the residual indentations after the experiment using optical or electron microscopy. However, these methods of area determination are time-consuming, cumbersome and prone to human error. The methods developed by Oliver and Pharr in 1992 provide an expression which allows the contact area to be inferred using only the measured load-displacement data. This method assumes that the surface in the region of contact deforms elastically and uses elastic contact mechanics to determine the contact depth (h_c) in terms of the maximum indentation depth (h_{max}), the maximum contact load (P_{max}) and the contact stiffness (S), according to Equation 2.15:

$$h_c = h_{max} - \varepsilon \frac{P_{max}}{S} \tag{2.15}$$

where ε is referred to as the 'intercept correction', which for a conical indenter is equal to 0.72, for a paraboloid indenter is equal to 0.75, and for a flat punch is equal to 1. Oliver and Pharr found that a value of 0.75 best accounts for material behaviour during experiments, and thus, is the most widely accepted value. Once the contact depth has been calculated, the contact area can easily be determined since the geometry of the indenter tip is known. For a Berkovich indenter the relationship between the projected contact area and contact depth (h_c) is given by Equation 2.16:

$$A(h_c) = 24.56{h_c}^2 + C_1{h_c}^1 + C_2{h_c}^{1/2} + C_3{h_c}^{1/4} + C_4{h_c}^{1/8} ... + C_8{h_c}^{1/128} \tag{2.16}$$

where the constants C_n are used to account for any experimental deviation of the tip geometry from that of the perfect Berkovich geometry. The development of a technique to infer the contact area from the measured load-displacement data was highly valuable as it allowed for high throughput experimentation (HTE) using indentation experiments by removing the time-consuming area determination step. The method also allows material properties from indentations carried out at the nanoscale to be determined, where accurate area determination by direct means is difficult.

2.4.2 Continuous stiffness measurement (CSM)

As an alternative to analysing the unloading curve, the contact stiffness can be determined using the Continuous Stiffness Measurement (CSM) technique (Asif et al., 1999). A load is applied to the indenter tip as normal, in order to carry out the indentation. However, an oscillating force with a force amplitude several orders of magnitude smaller than the indentation load is superimposed on to the primary load, as illustrated in Fig. 2.9a. This method provides an accurate determination of the point of initial contact, while also allowing for continuous measurement of the contact stiffness (S) as a function of indentation depth. This makes the technique a powerful tool when analysing the in situ properties of composite materials, where depth dependent effects can add erroneous bias or scatter to the unloading contact stiffness.

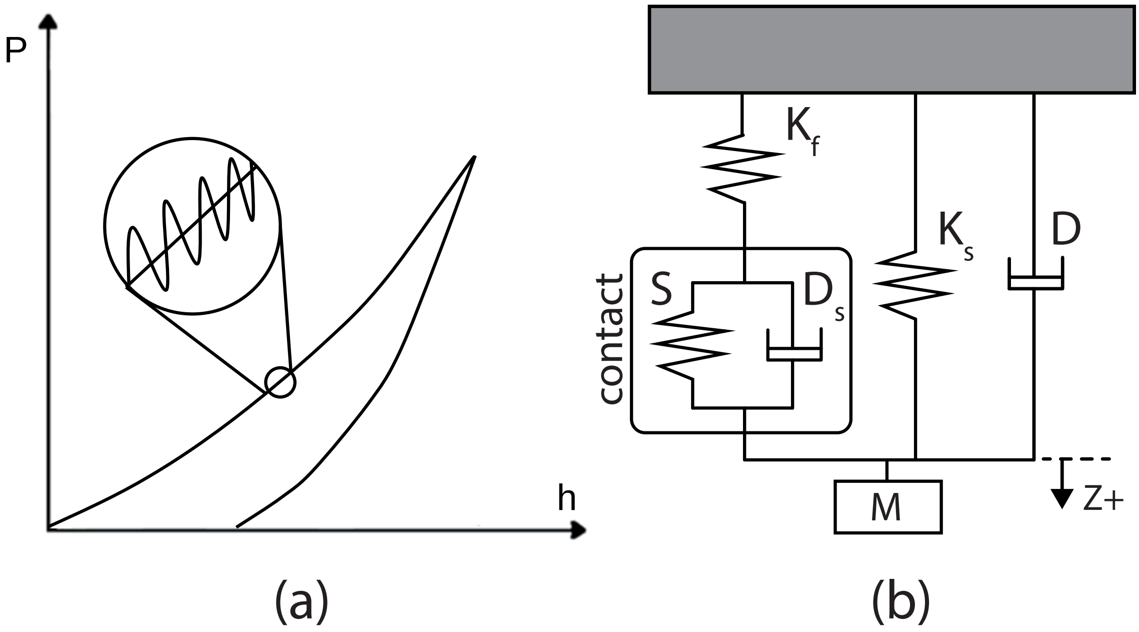

Figure 2.9: (a) Small oscillating load applied to primary indentation force, (b) A schematic of dynamic system during sample testing

The oscillating sinusoidal force signal is applied to the loading with an angular frequency ω and an amplitude of F_0 according to Equation 2.17:

$$F(t) = F_0 e^{i\omega t} \tag{2.17}$$

The corresponding displacement oscillation is then monitored using a lock-in amplifier, and lags behind the force signal by a phase angle δ according to Equation 2.18:

$$z(t) = z_0 e^{i\omega t + \delta} \tag{2.18}$$

An analysis of the dynamic system (shown in Fig. 2.9b) allows the contact stiffness to be calculated using Equation 2.19:

$$S = \left[\frac{1}{\frac{F_0}{z_0}\cos\delta - (K_s - M\omega^2)} - \frac{1}{K_f} \right]^{-1} \tag{2.19}$$

where K_s is the support spring stiffness and K_f is the load frame stiffness of the instrument. This continuously measured stiffness can then be used to calculate the material properties using the relations in Section 2.4.1, as a function of the indentation depth.

2.4.3 Pile-up and residual stress effects

According to Sneddon's elastic contact theory, the surface of the specimen is drawn downward into the sample during elastic indentations. This is known as 'sink-in' behaviour and this assumption is used to infer the projected contact area from the load-displacement data and, subsequently, calculate hardness and modulus of the substrate material. In the vast majority of sharp indentations, plasticity will occur in the substrate. When plastic deformation occurs, the material may sink-in or pile-up around the indenter, as illustrated in Fig. 2.10a. If the material piles up, the contact area will be underestimated by the nanoindentation theory, leading to overestimation of the calculated properties. A finite element study carried out by Bolshakov and Pharr (1998) showed that the contact areas can be underestimated by as much as 60% when pile-up occurs, and that the behaviour is dependent on the ratio of the reduced modulus to the yield stress (E_r/σ_Y), and the material's work-hardening behaviour.

The effects of pile-up can be exacerbated for indentations carried out on inhomogeneous materials. During the indentation of soft metal films on a hard substrate, it has been reported that pile-up is significantly enhanced due to the constraints imposed by the substrate on the indentation's plastic deformation field

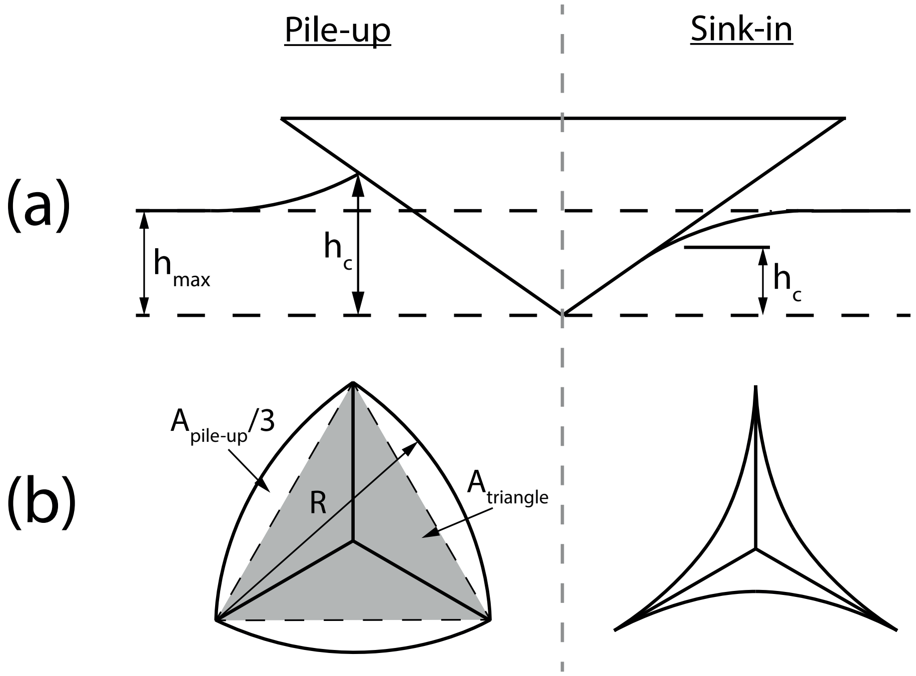

Figure 2.10: Pile-up and sink-in material behaviour at maximum indentation depth (a) side profile of indentation, (b) geometry of projected contact areas for each case

(Zhou et al., 2008). The presence of a residual stress state in the substrate can also affect the pile-up and sink-in behaviour. Experimental indentations carried out on pre-stressed substrates have also been investigated by Khan et al. (2011) for aluminium alloys, Breuils et al. (2011) for steel, Huang et al. (2009) for SiN thin films, and Bai et al. (2000) for thin hard carbon nitride films. The experiments show that tensile residual stress leads to a reduction of the indentation modulus and hardness, while compressive residual stress leads to an increase in the apparent properties for the same materials.

Wei and Yang (2011) determined the effect of residual stress on the characterisation of diamond-like carbon films using a two-step finite element analysis that simulated the pre-stress induced by a thermal process followed by nanoindentation. It was found that the residual stress state in the film was dependent on the substrate material and surface roughness. Similar to the experimental results, compressive residual stress increased the hardness and modulus, and tensile residual stresses lead to a reduction in the properties. Other finite element studies have been carried out to determine the effect of residual stress on the indentation properties of nickel films (Ling et al., 2010) and general elastic–plastic strain-hardening materials (Xu and Li, 2005), with similar trends in resulting properties reported. While the vast majority of these investigations assume an equibiaxial stress state and use an asymmetric modelling approach, Breuils et al. (2011) carried out full 3D finite element simulations, allowing the effects of non-equibiaxial stress states to be determined. Modelling results from Bolshakov and Pharr (1998) showed that tensile residual stress leads to excessive sink-in behaviour and compressive residual stress causes material pile-up, as illustrated in Fig. 2.11. The results also show that when the contact area is measured directly, the hardness and elastic modulus are not significantly affected by the residual stress.

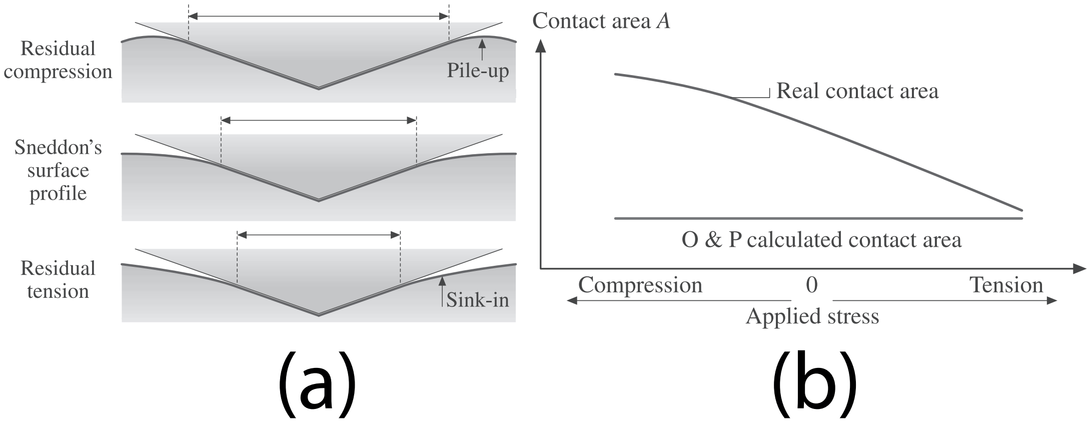

Figure 2.11: Effect of residual stress on contact area (a) indentation schematic, (b) Real vs Oliver and Pharr calculated contact area (Mann, 2005)

While the use of optical, electron and spanning probe microscopy to measure the true contact area is often recommended for cases where pile-up occurs during an indentation (ISO, 2015; Oliver and Pharr, 2004), there is no standard procedure or consensus regarding the methods of measurement of the corrected contact area. A number of authors have estimated the projected contact area based on the curvature of the arc from the residual impression observed using optical or scanning probe microscopy (SPM), as illustrated in Fig. 2.10b (Cabibbo et al., 2013; Beegan et al., 2003, 2005; Kese and Li, 2006; Saha and Nix, 2001; Zhou et al., 2008). Scanning probe microscopy techniques can also be used to measure the height of the material pile-up based on the measured 3D surface profile. Zhang et al. (2015)

recently investigated the effects of pile-up on the indentation modulus of Zr-based bulk metallic glasses. The nanoindenter tip was used to generate a 3D SPM image of the impressions using a scanning force of 2 µN. Line scans starting from the centre of the impression were examined and it was assumed that the highest points of the cross-sections were the summit of the residual pile-up, and formed the contact boundary, as illustrated in Fig. 2.12. Another approach taken by authors to correct for pile-up was to measure the pile-up height from SPM scans, and add this height to the overall contact depth (h_c). This corrected contact depth can be used in combination with the indenter tip's area function (2.16) to calculate the corrected contact area (Cao et al., 2006; Zhou et al., 2008).

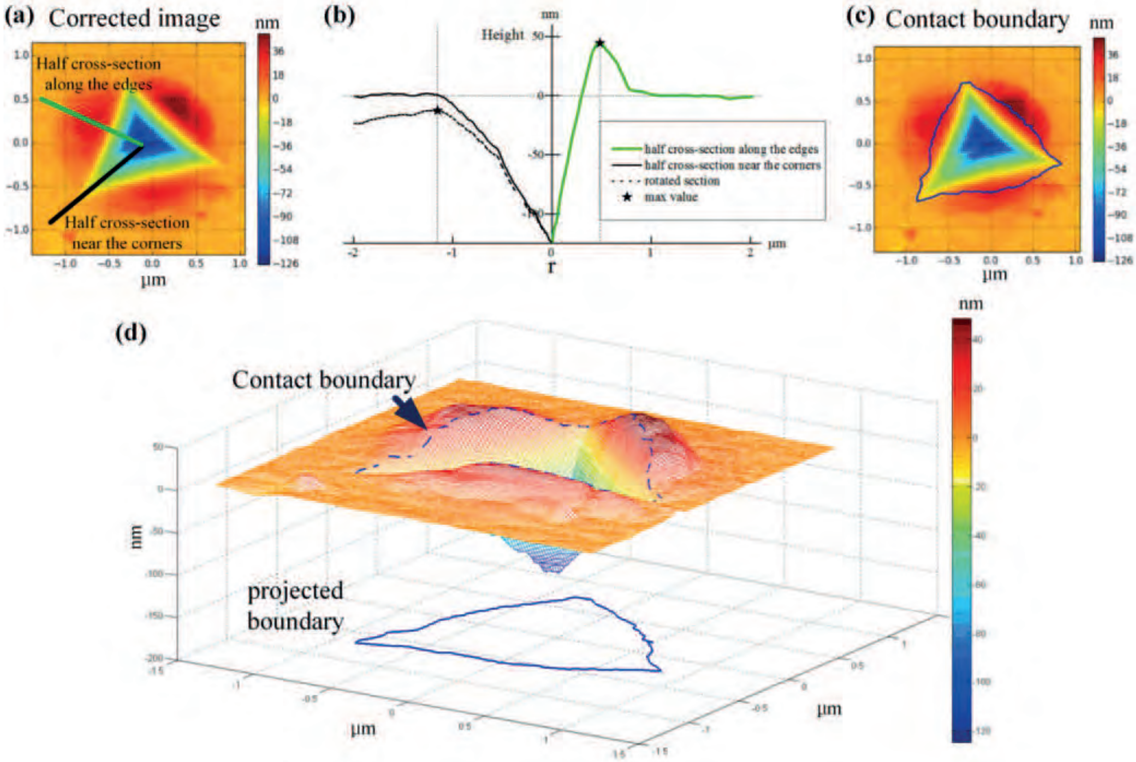

Figure 2.12: Contact boundary of indentation carried out on Zr_{55} to a maximum load of 8 mN (a) Surface tilt corrected by linear least-squares fitting, (b) Line-scan profiles, (c) Contact boundary determined by two highest point sets, (d) Three-dimensional topography of the indentation (Zhang et al., 2015)

2.4.4 Numerical simulation of nanoindentation

In recent years, the theoretical models used to establish the nanoindentation theory have been complimented by numerical modelling of the nanoindentation process applied to various substrate materials. The most popular computational modelling method used is the finite element method. Though solutions exist which define the relationship between the indenter load and displacement for elastic indentations, plasticity occurs during the vast majority of nanoindentation tests and is difficult to analyse analytically. Many authors have turned to finite element methods to accurately model this complex elastic-plastic behaviour. The first ever comparison between load-displacement data simulated from Finite Element Analysis (FEA) and experimental load-displacement data was carried out by Bhattacharya and Nix (1988), where it was shown that the finite element method could be used as an effective tool for simulating nanoindentation experiments. The geometry and boundary conditions of the model are shown in Fig. 2.13a, where the indentation problem is represented by a simplified axisymmetric model. The finite element mesh around the indentation site is shown in Figure 2.13b where the three-sided pyramidal Berkovich indenter geometry has been modelled as an axisymmetric rigid cone with the same projected contact area to indenter depth ratio as the Berkovich indenter. It has been shown that this conical representation produces the same load-displacement response as the pyramidal Berkovich indenter, even though the stress fields differ (Marteau et al., 2014). This simplified 2D approach has been used for the vast majority of nanoindentation finite element simulations (Panich and Sun, 2004; Gregory and Spearing, 2005; Khan et al., 2010; Bressan et al., 2005; Pelegri and Huang, 2008).

While the simplifying assumption of 2D axisymmetric indentation modelling is useful due to the computational efficiency offered by such simulations, the impact of this assumption on the simulation results must be questioned for pyramidal indentations. A number of authors have shown that the load-displacement data from 2D conical and 3D Berkovich indentations are almost identical (Lichinchi et al., 1998; Ruan et al., 2010). However, Warren and Guo (2006) noted noticeable differences between the stress fields and the shape of the indentation impression produced by each model, hinting that the conical and pyramidal geometries may not be interchangeable for every scenario. In such cases, three-dimensional analyses have been

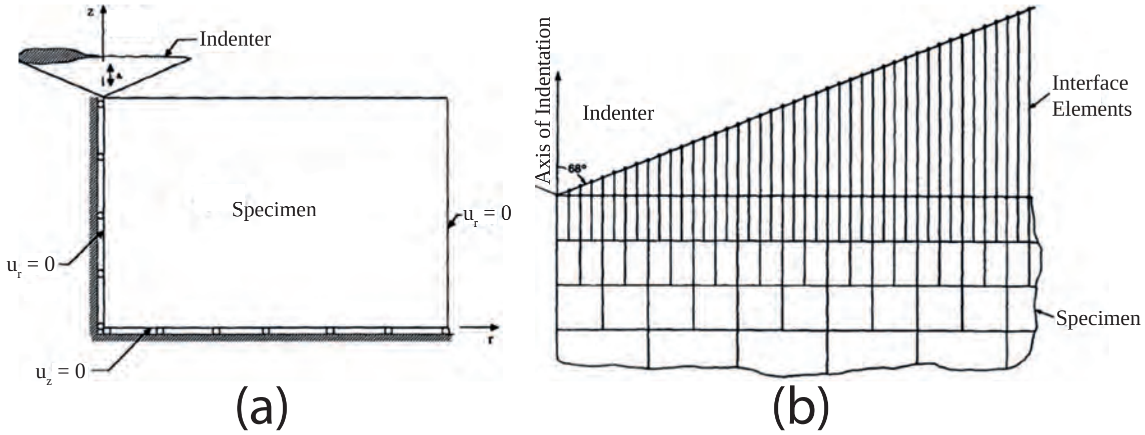

Figure 2.13: (a) Geometry and boundary conditions for 2D axisymmetric indentation model, (b) Detailed view of finite element mesh under indenter tip (Bhattacharya and Nix, 1988)

carried out where the actual geometry of the pyramidal indenter has been fully taken into account. An example of a three-dimensional model created by Larsson et al. (1996) is shown in Fig. 2.14. When modelling the Berkovich geometry, the six-fold symmetry of the indenter tip shape can be used to simplify the model by only making it necessary to model one-sixth of the indenter and specimen geometries. The indenter has been represented as a rigid plane with an angular offset from the surface of the material being indented. Lichinchi et al. (1998) used a similar approach to investigate the nanoindentation of hard films on a softer substrate, while Tho et al. (2006) studied the indentation size effect on copper and aluminium using a full 3D model. Both authors noted that the load-displacement data extracted from the models was in good agreement with experimental data.

The insight that finite element models give into the mechanics of the nanoindentation test can also be used to determine the validity of the assumptions used in nanoindentation theory. Mata and Alcalá (2004) examined the influence of friction on sharp indentations carried out on strain hardening solids. It was concluded that the effects of friction on the indentation properties were dependent on whether pile-up or sink-in occurred during the indentation and the material's strain-hardening behaviour. Rodríguez et al. (2006) and Pelletier et al. (2008) used numerical indentation methods to estimate the effect of material pile-up on the indentation of an aluminium matrix composite constituent and glassy polymers, respectively. Rather than estimate the projected contact area using the Oliver and Pharr method, the

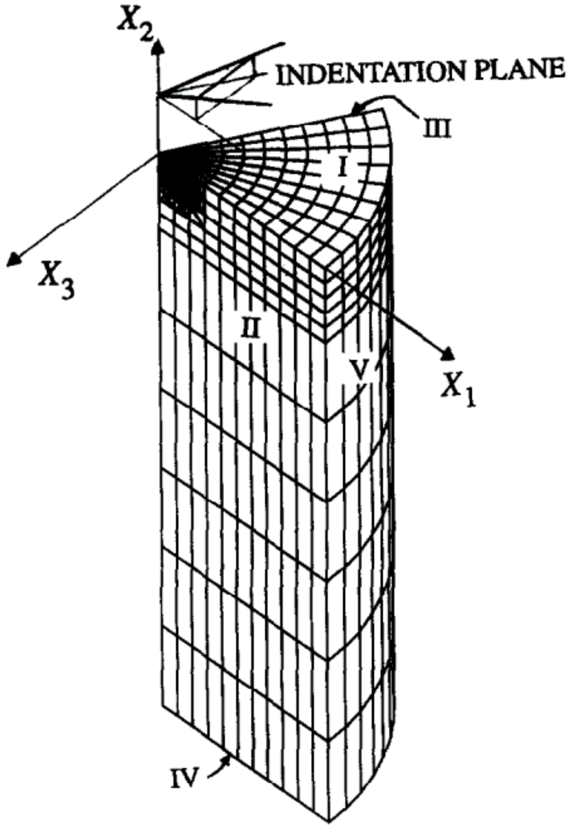

Figure 2.14: 3D Berkovich indentation model (Larsson et al., 1996)

contact area was calculated by identifying the last point of contact at maximum load in the 2D axisymmetric finite element mesh. This allowed the authors to apply an area correction to all their experimental indentation test data, leading to more accurate determination of the indentation properties.

Finite element modelling of nanoindentation is based on the assumption that the indented material can be modelled as an elastic-plastic continuum. This continuum description appears to work well for indentation measurements down to depths as shallow as 10–20 nm (Knapp et al., 1999). However, this assumption is no longer valid when the maximum indentation depth is only a few nanometres. At this scale, the load-displacement response measured is dependent on the interatomic interactions of the nanostructure. Molecular Dynamics (MD) is a numerical modelling tool in which the forces between individual molecules of a system are governed by a set of mathematical equations which are based on Newton's laws of motion. These equations are solved to compute the position, velocity and acceleration of each molecule in the system for each time increment. Verkhovtsev et al. (2013) carried out large-scale MD simulations of the nanoindentation process of a titanium crystal substrate. The effect of square, conical and spherical indenter geometries on the load-displacement response was investigated to a maximum penetration depth of 3 nm. It was shown that the hardness and reduced modulus were dependent on the indenter geometry. Goel et al. (2014) studied the nanoindentation response of iron carbides using the MD simulation model shown in Fig. 2.15. The results provided an insight into the cohesive dynamics of iron and carbon, as atoms from the substrate were found to cling to the indenter upon unloading, causing a negative depth hysteresis in the load-displacement data. The results also highlighted the formation of a new phase of iron-carbide formed due to deviatoric strain, as opposed to the high temperature induced in the substrate during nanoindentation.

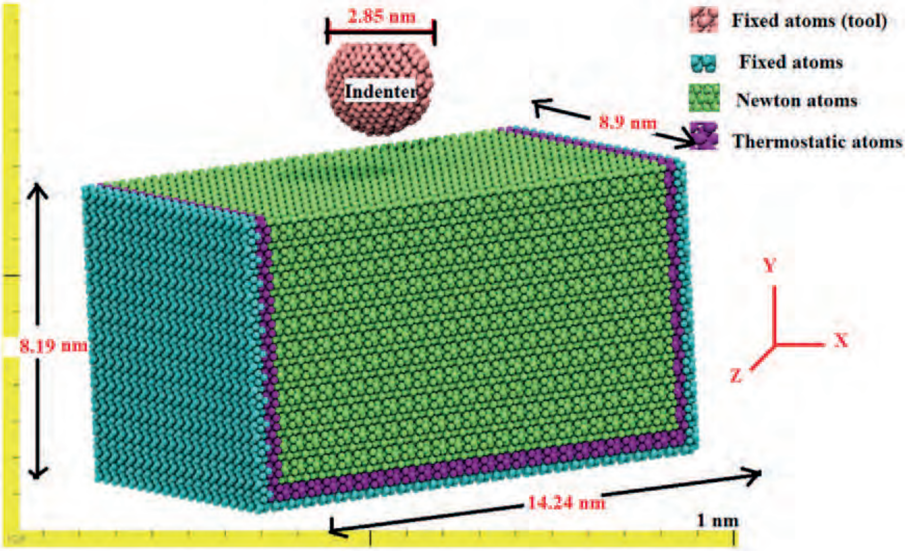

Figure 2.15: Schematic diagram of the nanoindentation MD simulation model (Goel et al., 2014)

2.5 Nanoindentation of composite materials

2.5.1 Bulk vs in situ properties

The bulk properties of the fibre and matrix constituents are often used in fibrous composite micromechanical simulations to predict the composite properties and failure behaviour. However, these bulk properties may differ from the post-cure in situ properties. Nanoindentation has emerged as one of the few techniques which allows direct measurement of the constituent properties, where the technique has been widely used to determine the elastic-plastic properties of film-composite materials where one constituent is deposited as a thin film onto a substrate material (Bec et al., 2006). Nanoindentation has also been used to determine the in situ constituent properties of fibrous composites. Gregory and Spearing (2005) carried out nanoindentation tests on both the neat and in situ resins for two composite material systems, one with a thermoplastic matrix (PEEK) and one with a thermosetting matrix (epoxy). The results for the modulus and hardness of the bulk and in situ epoxy resin is shown in Fig. 2.16, where it is clear that the in situ properties are consistently higher than those of the bulk material. The in situ hardness and modulus values were up to 30% larger than the values of the bulk resin. Rodríguez et al. (2006) investigated the properties of an aluminium metal matrix reinforced with 15 vol.% SiC particles using nanoindentation. Once the results had been corrected for pile-up, it was found that the hardness of the in situ matrix was higher than that of the unreinforced alloy, while the values increased slightly as the distance to the nearest reinforcement was decreased. However, the in situ matrix properties are not always larger than the corresponding bulk material properties. Guicciardi et al. (2008) compared the indentation properties of particle-reinforced ceramic composites and showed that, depending on the constituents used, the in situ matrix properties can be lower, higher or the same as the material in its bulk form.

2.5.2 Interphase characterisation

The nanoindentation technique has also been used to determine the properties of the 'interphase' region, a phase located between the fibre and matrix constituents formed during curing which has properties which differ to those of either constituent. A number of authors have carried out shallow grid indentations leading from one constituent to the other in an attempt to measure the properties and thickness of this region. Kim et al. (2001) carried out grid nanoindentation across a glass-fibre/vinylester composite interface. The resulting load displacement curves for the fibre, matrix and interphase regions are shown in Fig. 2.17a, while the variation of

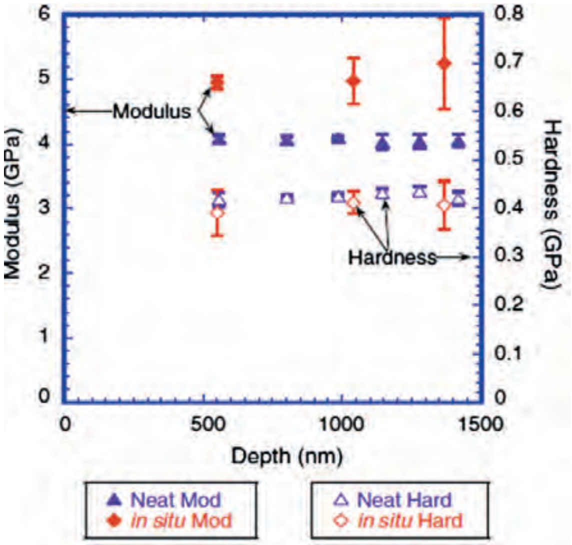

Figure 2.16: Neat and in situ modulus and hardness values for Cytec 977-3 epoxy resin measured by nanoindentation (Gregory and Spearing, 2005).

the indentation modulus across the fibre-matrix interface is shown in Fig. 2.17b. It was concluded that the interphase thickness was approximately equal to 1 µm, where the measured properties were intermediate between that of the fibre and matrix constituents. Khanna et al. (2003a) attempted to determine the properties of the interphase region of a glass-fibre/polyester composite using an Atomic Force Microscope (AFM) as an indentation device. The resulting interphase thickness was approximately 4 µm, with the measured modulus being higher or lower than the matrix modulus, depending on the fibre treatments applied pre-cure. The author's also noted that accurate quantitative characterisation of the region was difficult due to the effects of pile-up, viscoelasticity and surface preparation issues (Khanna et al., 2003b). Hodzik et al. (2001; 2004) investigated the effect of water-aging on the interphase properties of glass-fibre/phenolic and glass-fibre/polyester composites and detected an increase in the interphase thickness with increased exposure to water. While the widths of the interphase for glass-fibre reinforced materials have been in the order of microns, the size of the interphase for a carbon-fibre epoxy composite was determined by Wu et al. (2014) using Transmission Electron Microscopy (TEM) to be approximately 200 nm for a 7 µm diameter fibre.

The measured differences between the bulk and in situ matrix properties and the variation of the in situ properties at different microstructural regions is often

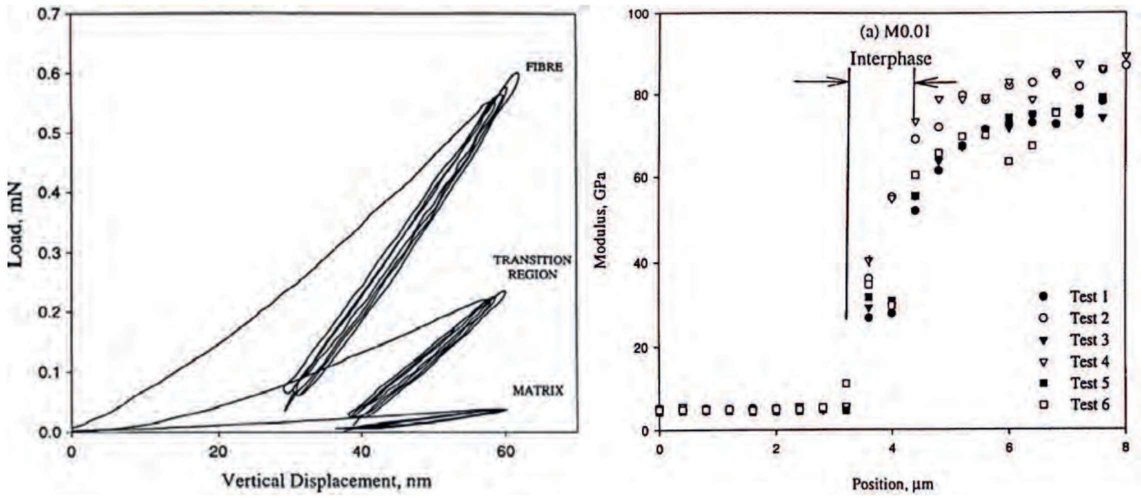

(a) (b)

Figure 2.17: Nanoindentation of glass fibre/vinylester composite (a) load displacement curves for fibre, ‘interphase’ and matrix regions, (b) variations in elastic modulus across fibre-matrix interface (Kim et al., 2001)

attributed to a change in the chemical constitution of the matrix material due to reactions with fibre treatment agents (Kim et al., 2001; Gregory and Spearing, 2005; Hobbiebrunken et al., 2006). It has also been postulated that the fibre reinforcement leads to partial immobilisation of the polymer matrix which alters the curing conditions and polymer cross-linking process, leading to a change in the resulting in situ matrix properties (Jones, 2010). Kim and Hodzic (2003) also speculated that volumetric changes and the generation of residual stress from thermal and chemical sources may also play a role.

2.5.3 Effect of neighbouring constituents

Nanoindentation theory assumes that the substrate material is a homogeneous continuum. Erroneous constituent characterisation can occur when neighbouring phases in the vicinity of the indentation site influence the mechanics of the indentation. This is especially apparent when attempting to determine the properties of thin film materials applied to substrates. In this case a general rule of thumb is to ensure that the indentation depth is no more than 10% of the thickness of the thin layer (Oliver and Pharr, 1992). A similar stress transfer between constituents is also possible for fibrous composites. Gregory and Spearing (2005) carried out a simple 2D finite element analysis to determine the minimum size of the resin pocket necessary to produce nanoindentation results for the matrix constituent which were free from the influence of the surrounding fibres. The matrix material was defined as an elastic-perfectly plastic material using classical von Mises plasticity. It was concluded that the diameter of the resin pocket was required to be at least 50 times the maximum depth of indentation. This meant a large amount of the reported experimental data was not suitable for matrix property characterisation and highlighted an inherent difficulty in the characterisation of the matrix constituent in high fibre volume fraction composite materials. Lee et al. (2007) also carried out a simple 3D finite element analysis of flat punch indentations carried out across a fibre-matrix interface. The fibre and matrix constituents were defined using basic elastic properties. Figure 2.18 shows the variation of the contact stiffness calculated from the load displacement data across the interface. A region where the contact stiffness varies between the bulk fibre and matrix properties was determined. Interestingly, the size of this region was similar to that determined from the experiments, and thus, it was concluded that the results for indentation modulus in these region are convoluted by the mechanical constraint of the surrounding fibres and also any true change in material properties. VanLandingham et al. (1999) noted a large increase in the contact stiffness from AFM indentations measured within 200 nm of a carbon-fibre epoxy composite interface, but noted that this was likely due to the effect of fibre constraint. It was concluded that the responses measured within 200 nm of the fibre cannot be considered as representative of an ‘interphase’ effect. Downing et al. (2000) measured a gradient in the elastic modulus across the interface of a glass fibre-reinforced epoxy material. However, once the fibre had been removed by etching, the gradient reversed itself. Thus, it was concluded that interphase characterisation using the nanoindentation technique was not possible due to fibre bias in this case. These studies highlight the significant effect of fibre constraint on the nanoindentation results of fibrous composite microstructures.

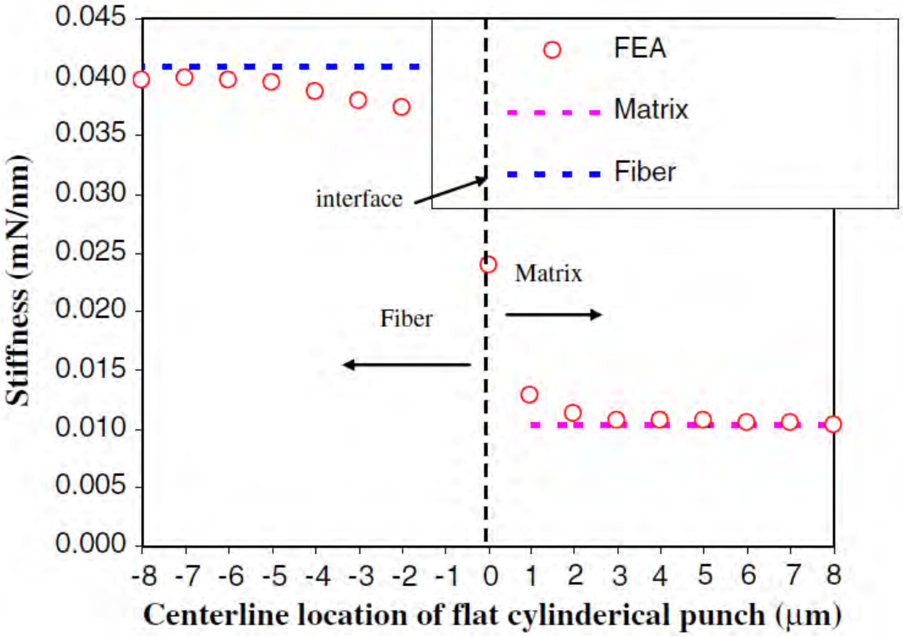

Figure 2.18: Variation of the stiffness measured from the FEA with position from the interface (Lee et al., 2007).

2.6 Nanoindentation of polymeric materials

2.6.1 Elastic characterisation

The nanoindentation theory developed by Sneddon (1965) and Oliver and Pharr (1992) has been applied to experiments carried out on polymeric materials by a number of authors. However, quantitative characterisation of the elastic modulus of polymeric materials has proven to be a challenge using these methods. For soft polymers, difficulties have arisen in regards to determining the point of initial contact due to the compliance of the materials systems (Deuschle, 2008). Even for harder glassy polymers, doubts have arisen over whether the nanoindentation theory, with its roots an elastic contact mechanics, can be used to correctly analyse force-displacement curves arising from tests carried out on polymeric materials (VanLandingham et al., 1999). One of the predominant issues arising from the nanoindentation of polymers has been the large difference between elastic moduli determined from nanoindentation testing and those determined from the more conventional macroscopic tension and compression tests (Kranenburg et al., 2009). For polymers, the reported values of indentation modulus tend to be consistently larger than those determined from conventional testing. Modulus increases have been reported in the order of 70% for polystyrene (PS) and 64% for polycarbonate (PC) (Tranchida et al., 2007), while a 67% increase has been reported for poly(methyl methacrylate) (PMMA) (Lu et al., 2003). VanLandingham et al. (2001) reported an increase of 20% for poly(benzocyclobutene). The elastic moduli obtained by nanoindentation (E_N) have been plotted against their respective macroscopic moduli (E_M) for a selection of polymers in Fig. 2.19 (Tranchida et al., 2007).

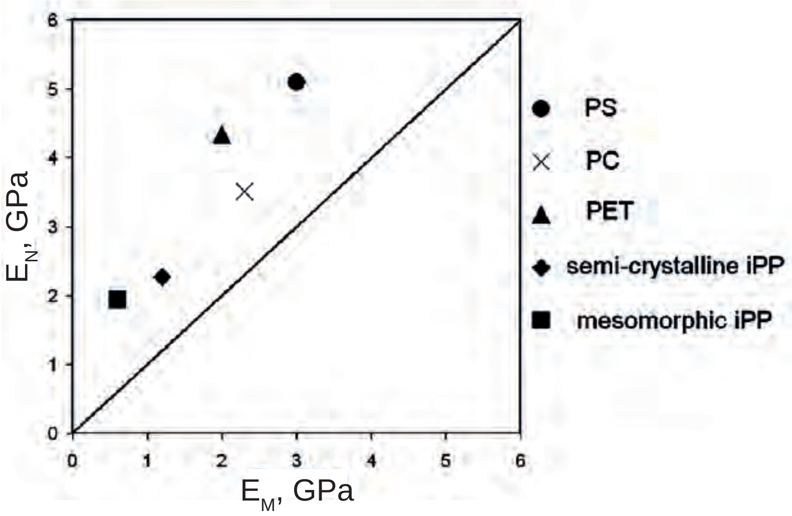

Figure 2.19: Elastic moduli evaluated by Oliver and Pharr procedure from force curves obtained by nanoindentation, E_N, vs macroscopic moduli, E_M, for a broad range of polymer samples and polymer morphologies. (Tranchida et al., 2007)

More recently, De Silva et al. (2013) carried out both tensile and nanoindentation testing on Poly(lactic acid)/natural halloysite nanotubes films in order to determine the effect of nanotube concentration on strength and stiffness. While the relative changes in modulus with nanotube concentration were similar for both tests, the authors noted that the values of elastic modulus inferred from the nanoindentation tests were many times larger those determined from the tensile testing. Similarly, King et al. (2013) analysed the effect of adding graphene nanoplatelets to bulk epoxy through the use of conventional macroscopic testing and nanoindentation. The moduli determined from nanoindentation testing were 33% greater than those determined from tensile tests, while the relative trends of modulus increase with increase in nanoplatelet concentration remained the same for both techniques. These recent studies show that the nanoindentation technique can be successfully applied to comparative studies between polymeric materials, while also highlighting distinct limitations in the ability of the theory to quantitatively determine the true elastic modulus of these materials.

The apparent failing of the nanoindentation technique to correctly characterise elastic behaviour of polymeric materials has been evidenced through analysis of the non-linear curve fit which is applied to the unloading data according to Equation 2.20.

$$P(h) = B\left(h - h_p\right)^m \tag{2.20}$$

According to Sneddon's elastic theory (Sneddon, 1948) and the concept of an "effective indenter" (Pharr and Bolshakov, 2002), the value of the curve-fitting exponent (m) in Equation 2.20 should fall somewhere between the value for an elastic flat punch indentation ($m = 1$) and that of an elastic conical indentation ($m = 2$). However, a number of authors have noted that the application of the non-linear curve-fit to the unloading curves of polymeric materials often leads to poor curve-fits and values of the curve-fitting exponent which are greater than the upper limit of 2. VanLandingham et al. (2001) carried out indentations on a benzocyclobutene (BCB) polymer and noted that the power law fits using both the commercial DSI system software and commercially available statistics software did not converge for any of the experimental data sets, but results were output based on the values of the fitting parameters for the final iteration. An example of a resulting curve-fit is shown in Fig. 2.20a where it can be seen that the fit is a very poor representation of the actual unloading data. The power law exponents from the curve fits were all greater than 2, ranging from 2.2 to 2.7. Beyaoui et al. (2009) also noted a poor fit when Equation 2.20 was fit to unloading data from indentations carried out on PC (Fig. 2.20b) and PMMA. The exponents from the curve fits were also found to fall outside the expected range with values of 3.7 and 2.2 reported for PMMA and PC respectively. Interestingly, the authors noted that if the materials were loaded and unloaded a large number of times, the exponent from the fitting procedure was found to decrease rapidly and tend to values of 1.8 for PMMA and 1.5 for PC, i.e. within the expected range for elastic-plastic materials. The values of modulus however, were found to be insensitive to the number of unloading and reloading cycles.

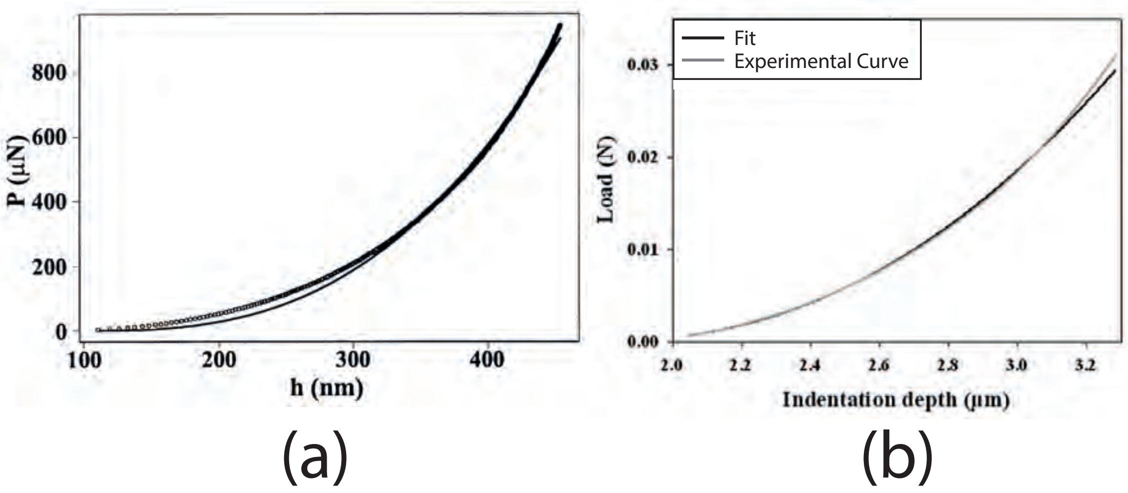

Figure 2.20: Examples of poor power-law curve fits from (a) VanLandingham et al. (2001) indentation carried out on benzocyclobutene (BCB) polymer and (b) Beyaoui et al. (2009) indentation carried out on polycarbonate (PC)

In summary, at the very least, elastic modulus determination using nanoindentation data has been shown to be problematic for polymer materials. At worst, the Oliver and Pharr procedure, as well as any other procedure derived from elastic contact mechanics, is incorrect from a theoretical point of view and cannot be applied to the nanoindentation unloading curves obtained for polymeric materials (Tranchida et al., 2007). A number of authors have postulated that the polymer indentation modulus overestimation could be due to the effects of material pile-up, described in Section 2.4.3 (King et al., 2013; Kranenburg et al., 2009). However, based on the ratio of final depth to maximum indentation depth, Tranchida et al. (2007) expected the influence of pile-up to be modest for glassy polymers.

2.6.2 Viscoelasticity

A number of authors have expressed concern over the use of elastic contact theory in the analysis of materials which exhibit time-dependent viscoelastic and viscoplastic behaviour. The overestimation of the sample elastic modulus, as well as the poor non-linear curve fits associated with polymeric materials have often been attributed to this peculiar material behaviour (VanLandingham et al., 2001; Tranchida et al., 2007; Lagoudas et al., 2006; Oyen, 2007; King et al., 2013; Beyaoui et al., 2009). The most obvious evidence of the effect of this time-dependent behaviour occurs when viscoelastic creep dominates the initial unloading response of the load-displacement data. In this case, the initial decrease in the applied load does not lead to a decrease in the indenter displacement. This is often described as a 'nose' and leads to a negative initial unloading slope. This negative value for the contact stiffness makes the calculation of the sample elastic modulus impossible. An example of a "nose" occurring during the nanoindentation unloading segment is shown in Fig. 2.21 for an indentation carried out on PMMA (Briscoe et al., 1998).

In order to reduce to effect of indentation creep on the unloading data of nanoindentation experiments, Hochstetter et al. (1999) proposed the addition of a constant load hold segment between the loading and unloading segments of a nanoindentation test. This method of minimising viscoelastic effects has been shown to remove the 'nose' from unloading data where it had existed in the absence of a hold time. The effect of a 10 second hold segment on the unloading data from Briscoe et al. (1998) is also shown in Fig. 2.21. The hold segment has since become an intrinsic part of standard nanoindentation testing for all materials (Agilent, 2009), while for materials which exhibit time-dependent deformation, it is recommended to determine an optimum hold time which sufficiently diminishes the effect of this time dependent deformation on the initial unloading data (Lagoudas et al., 2006). In order the determine the effect of hold segment time on the indentation modulus predicted for polymers, Tranchida et al. (2007) carried out experiments with holding segment times which varied from 1 to 100 seconds. However, only a 5% reduction in elastic modulus was reported for the longest hold time of 100 seconds. Jin et al. (2015) compared the results for indentations carried out on PMMA with holding time segments ranging from 10 seconds to 1000 seconds. As the holding time was increased, the elastic modulus and hardness both drastically decreased as shown in Fig. 2.22, while keeping both the maximum load and loading rate constant. Beake and Leggett (2002) also determined the effect of varying hold times on the hardness and elastic modulus of poly(ethylene terephthalate) films. Much less drastic reductions in hardness (15%) and modulus (8%) were reported over a range of holding times varying between 10-600s.

Another method to minimize the effect of time-dependent deformation on the nanoindentation results is to vary the loading and unloading rates of the indenta-

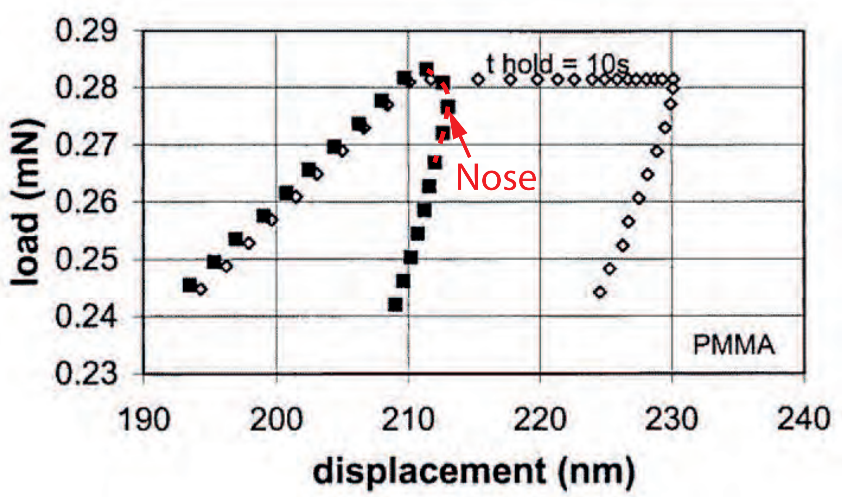

Figure 2.21: Load–displacement data at the loading–unloading peak for two indentations on PMMA performed under similar loading conditions. The introduction of a hold segment (10 s) at the peak load reduces the creeping effect upon the unloading set of data (Briscoe et al., 1998).

tions. Tranchida et al. (2007) carried out experiments with varying loading/unloading rates ranging between 1 to 100 µN/s for indentations carried out on amorphous Polycarbonate (PC) and two semicrystalline isotactic polypropylene (iPP) samples. The elastic modulus was unaffected by changing loading rates and deviated more from the macroscopic test value as the rate increased as shown in Fig. 2.23. Beake and Leggett (2002) also found that the modulus was relatively insensitive to changes in loading/unloading rates between 0.01 and 1 mN/s, while hardness decreased slightly with increasing loading rate. Conversely, Jin et al. (2015) reported that the indentation modulus of PMMA was sensitive to unloading rate across a range of 0-3 mN/s. The modulus decreased with increase in unloading rate, while the hardness remained constant. The author's concluded that a high unloading rate was required to obtain reasonable measurements free from the influence of viscous deformation.

2.6.3 Hydrostatic stress

It has been shown that the macroscopic stiffness and strength of polymeric materials is dependent on the hydrostatic stress state surrounding the specimen

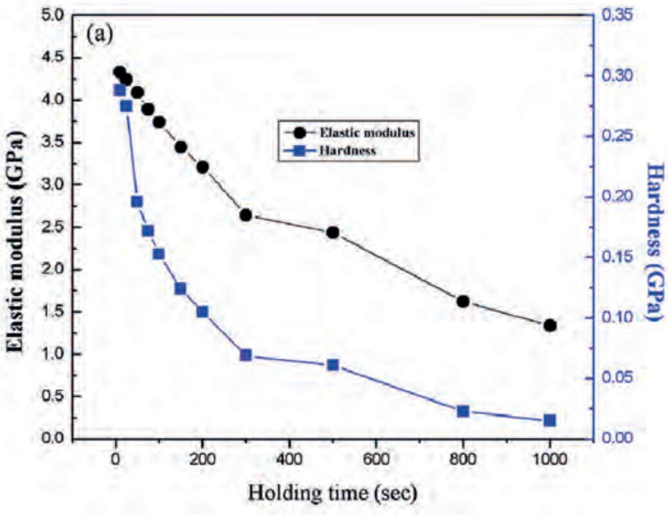

Figure 2.22: Indentation elastic modulus and hardness of PMMA as a function of holding time (Jin et al., 2015)

during the test. In general, the elastic modulus of polymers increases with increasing hydrostatic pressure when tensile tests are performed in a thick-walled cylindrical pressure chamber (Pae and Bhateja, 1975). The ratio of elastic modulus under hydrostatic pressure ($E(P)$) to the modulus at atmospheric pressure ($E(0)$) for several amorphous polymers is shown in Fig. 2.24. It was proposed by Birch (1938) that the increase in modulus due to the presence of hydrostatic pressure is described by Equation 2.21:

$$E = E(0) + 2\sigma_H(5 - 4\upsilon)(1 - \upsilon) \tag{2.21}$$

where $E(0)$ is the elastic modulus at atmospheric pressure, σ_H is the applied hydrostatic pressure, and υ is the Poisson's ratio of the material. It is clear from Equation 2.21, that the pressure dependence of the elastic modulus is greater for materials that have a lower modulus at atmospheric pressure, such as polymers. This expression was experimentally verified and shown to correctly predict the change in the tensile modulus of polymers with increasing hydrostatic pressure by Silano et al. (1974) and Pae and Bhateja (1975). During a nanoindentation test, the stressed material below the indentation tip becomes constrained by the surrounding unstressed material, leading to a build-up of large compressive hydrostatic stress in the substrate (Atkins and Tabor, 1965). It has been postulated by a number of authors

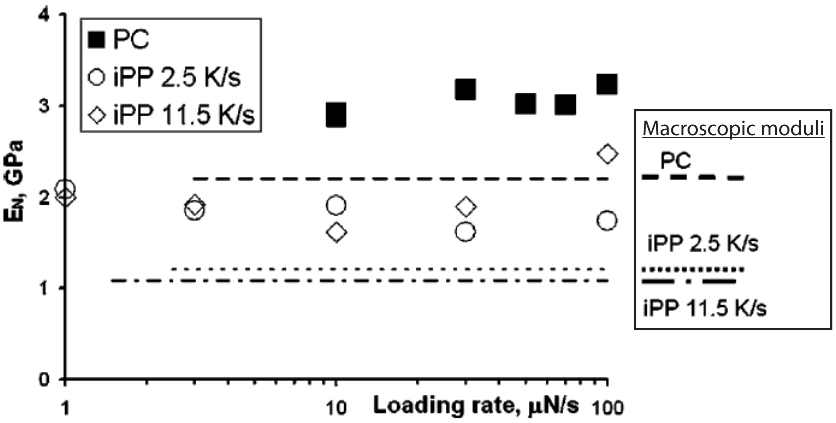

Figure 2.23: Dependence of elastic moduli, evaluated by Oliver and Pharr procedure, on loading rate in a broad range of conditions for three morphologies: amorphous PC and two semicrystalline iPP. Results are compared with macroscopic bulk moduli (Tranchida et al., 2007)

that for polymers, the existence of this hydrostatic stress state could play a role in the overestimation of the indentation modulus for the materials (VanLandingham et al., 2001; Briscoe and Sebastian, 1996; Doerner and Nix, 1986).

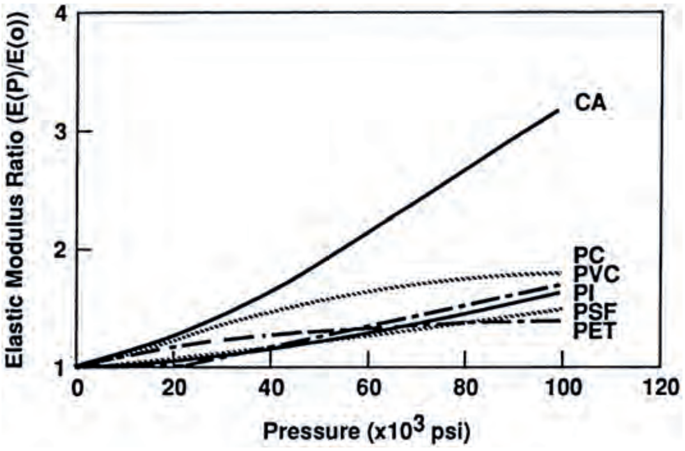

Figure 2.24: Elastic modulus ratio vs hydrostatic pressure for various amorphous polymers (Pae and Bhateja, 1975).

2.7 Summary of literature review

In this chapter a comprehensive literature review has been carried out on the work relevant to the application of the nanoindentation technique to carbon fibre reinforced plastic composite materials. In Section 2.2, it is shown that the macroscopic deformation and failure of composite materials is linked to mechanisms which occur at the microscale. The deformation and final failure mechanisms at this scale are intrinsically linked to the microscale properties of the composite constituents. Experimental micromechanical analyses, such as those carried out by Zhang et al. (2010) and Llorca et al. (2011), provide a qualitative insight into the deformation and failure mechanisms, while the results from micromechanical finite element models, such as those created by González and Llorca (2006) and Vaughan and McCarthy (2011*a*; 2011*b*), have provided a quantitative insight into the effects of constituent properties, interface strength and the distribution of reinforcement on these mechanisms. However, the accuracy of these models is highly dependent on the inputs used to define the properties of the constituents. Thus, experimental methods to determine these properties in situ are required if virtual mechanical tests of composite materials are to become more widely used as an alternative to expensive coupon and structural testing (Llorca et al., 2011).

The nanoindentation technique and theory are described in Section 2.4, where it is shown that the theory is based on elastic deformation of a homogeneous medium, with the most commonly used analysis technique being that developed by Oliver and Pharr in 1992. While this theory is valid in most cases, the underlying analysis assumptions are invalidated when the theory is applied to certain materials, and can lead to bias or error in their analysis. Section 2.4.4 highlights a number of finite element studies of the nanoindentation process, such as that carried out by Bhattacharya and Nix (1988), and shows that the numerical technique is useful for providing an insight into analytical or material issues associated with the nanoindentation technique in certain experimental scenarios. Finite element methods have often been used to examine the mechanics of indentations carried out on thin films, where the characterisation of the thin film material can be influenced by the substrate properties (Bressan et al., 2005). This scenario is analogous to the effect of fibre constraint on the characterisation of the matrix constituent in fibrous composite materials. Section 2.5.3 describes numerical studies carried out by Gregory and Spearing (2005) and Lee et al. (2007) who investigated the effect of fibre constraint on the indentation properties of matrix pockets and the 'interphase' region, respectively. While both studies conclude that the effect is significant, these studies simplify the microscale geometry and matrix material properties, and acknowledge that more accurate modelling is required to fully understand the phenomenon.

Section 2.3.1 details the effect of thermal cooldown on the microscale residual stress state for fibrous composites. Numerical modelling techniques employed by Vaughan and McCarthy (2011*a*) and Yang et al. (2013) show that the post-cure stress distribution varies in nature and magnitude throughout the composite microstructure and is highly dependent on the fibre reinforcement volume fraction and distribution. Vaughan and McCarthy (2011*a*) found that the large compressive residual stress at the fibre-matrix interface is beneficial for transverse tensile loading scenarios, as it offsets the initiation of fibre-matrix debonding. However, thermal residual stress can also lead to microscale damage prior to loading, adversely affecting the strength of the ply, as shown by Maligno et al. (2009) and Yang et al. (2013). These studies highlight the significant magnitude of the residual stress state which exists in the composite microstructure post-cure. Section 2.4.3 highlights finite element studies, such as work carried out by Bolshakov and Pharr (1998), which show that residual stress in a nanoindentation substrate can affect the pile-up and sink-in behaviour, affecting the calculation of nanoindentation properties. While the effect of thermal residual stress on the composite mechanical performance has been analysed previously, the degree to which the constituent material properties of long-fibre reinforced composite materials, measured through nanoindentation, are affected has not yet been investigated, and will be examined in this thesis.

Bulk properties are often used in micromechanical models to predict the properties of the composite. However, the high-temperature curing process associated with composite manufacture leads to intensive thermal, mechanical and chemical processes taking place during the consolidation of the constituent phases, which may alter the in situ properties. For this reason a number of authors have attempted to determine the in situ properties of the matrix constituent using nanoindentation, as described in Section 2.5.1. However, very few studies exist comparing the bulk and in situ properties of polymer-matrix composites, the most extensive comparison being carried out by Gregory and Spearing (2005). While it was shown that the in situ properties of an epoxy resin were larger than that of the bulk, the study also highlighted the difficulty in obtaining valid nanoindentation measurements from high fibre volume fraction composites microstructures. The variation of the in situ properties relative to the matrix pocket radius was also not investigated. The bulk and in situ materials were cured separately for the study which may have affected the comparison, and while the CSM technique (described in Section 2.4.2) was used, the values failed to converge until a large indentation depth was reached, limiting its usefulness. The CSM technique is a very powerful tool for examining the properties of composite constituents. However this potential has not been fulfilled for polymer matrix composite materials, and will be used to further examine the composite matrix in-situ properties in this thesis.

Section 2.6 describes attempts made by authors to determine the elastic modulus of polymeric materials using nanoindentation. The results from investigations carried out by VanLandingham et al. (1999) and Tranchida et al. (2007) clearly highlight a disparity between the values of elastic moduli determined from nanoindentation in comparison with those determined from tensile tests, with the indentation moduli being consistently larger. This limits studies of polymer composite matrix constituents to comparative studies between bulk and in situ properties, without an accurate quantitative determination of the elastic modulus. While a number of authors have turned to analysing polymer indentations with viscoelastic and viscoplastic models (Fischer-Cripps, 2004; Oyen, 2005; Odegard et al., 2003), the Young's modulus is the parameter used to define the elastic matrix material behaviour in composite micromechanical analyses (González and Llorca, 2006; Totry et al., 2008; Romanowicz, 2010; Vaughan and McCarthy, 2011*a*). Thus, the incorrect determination of polymer elastic moduli by nanoindentation remains a predominant issue preventing the accurate quantitative characterisation of the in situ matrix in polymer composite materials. The effects of pile-up, viscoelasticity and hydrostatic stress on the calculation of polymer indentation modulus using the standard Oliver and Pharr methods of analysis are not well understood and will be investigated as part of this thesis.

3 Numerical Characterisation of Fibre Constraint Effects on Matrix Constituent Characterisation

3.1 Introduction

In recent years, a large amount of research has been focused on analysing the response of a fibrous composite material's constituent phases and their interfaces under various loading conditions. Analysis of this type involves carefully examining the microstructure of the composite material and relating the observed behaviour to macroscopic failure mechanisms. To facilitate this type of analysis, micromechanical models have been developed which model each constituent as a discrete material and allow for stress distribution, damage and eventual failure of the composite to be simulated at the microscale (Vaughan and McCarthy, 2011*a*; González and Llorca, 2007). However, these models assume that the properties of each constituent remain the same as the properties of the material in its bulk form. This may not be the case after the composite manufacturing and curing processes. The nanoindentation technique can be employed to determine these constituent properties in situ, in an attempt to more accurately model the microscale behaviour.

The theory on which the nanoindentation technique is based assumes that the substrate material is a homogeneous continuum. This assumption can lead to a number of issues when the technique is applied to multi-phase composite materials. One such issue is the potential for neighbouring phases in the vicinity of the indentation site to influence the mechanics of the indentation. This can occur when the indentation's stress field is constrained or promoted, depending on the relative properties of the constituent materials. Thus, special analysis is required to ascertain the effect of neighbouring constituents on the nanoindentation load-displacement data, based on the geometry and properties of the material constituents in question. Previous work has shown that the load-displacement data from nanoindentation tests carried out into the resin region of a fibrous composite can be influenced by the reinforcing effect of the surrounding fibres (Gregory and Spearing, 2005; Lee et al., 2007). This leads to results which are convoluted due to the mechanical constraint effect of the fibres, which hinders the ability of the technique to accurately characterise potential differences in mechanical properties of the bulk and in situ material. Accurate characterisation of the fibre constraining effect is essential in order to understand the experimental limitations imposed by this phenomenon, and deduce accurate matrix material properties from nanoindentation testing.

In this chapter, finite element models of the indentation test applied to the high fibre volume fraction HTA/6376 composite microstructure have been generated. The constraining effect of the surrounding fibres on the indentation of in situ matrix has been analysed in detail, using both 2D and 3D finite element modelling. The effect of surrounding fibre volume fraction and sub-surface stress fields have been analysed, while the influence of fibre constraint on the calculation of the contact area has also been studied.

3.2 Model description

The material under investigation is HTA/6376, a high strength carbon fibre reinforced polymer used in the aerospace industry. The material has a high fibre volume fraction of approximately 60% with a mean fibre diameter of 6.6 µm (Vaughan and McCarthy, 2010). The commercial finite-element code Abaqus v6.10 (ABAQUS-Inc., 2013) was used to create the models and carry out the analyses. The assumptions made in the finite element models were as follows:

- No debonding occurs between fibre and matrix due to the indentation stress fields
- The 6376 matrix material properties are constant throughout the region (i.e. no ‘interphase’ region with a property gradient exists)
- The fibres are unidirectional and perfectly straight
- No creep or damage has been modelled in the matrix or the fibres
- The indenter tip is rigid and representative of perfectly sharp 2D cone or 3D Berkovich geometry (Fig. 3.1)
- No pre-existing stress state existed after the composite curing process (The effect of microscale residual stress is examined in detail in Chapter 4)
- Contact between the indenter and the specimen is assumed to be frictionless

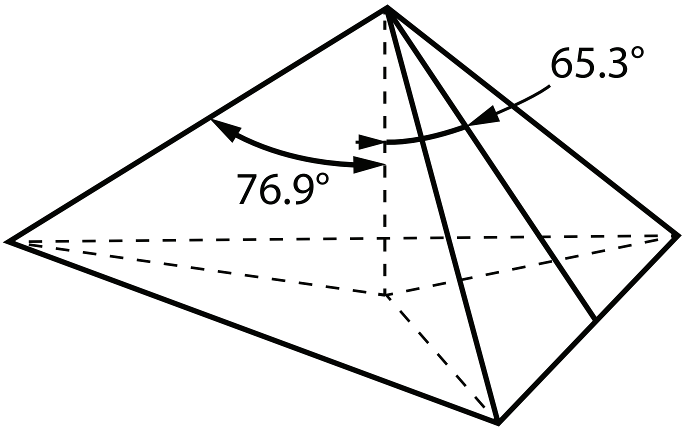

Figure 3.1: Berkovich indenter tip geometry

3.2.1 2D axisymmetric model

The first modelling approach assumes that the problem could be simplified by the 2D axisymmetric representation of the indentation process. This is the analytical geometry on which the nanoindentation theory is based, and the simplified modelling approach is consistent with previous finite element investigations of the nanoindentation process (Panich and Sun, 2004; Gregory and Spearing, 2005; Khan et al., 2010; Pelegri and Huang, 2008). The mesh and boundary conditions used for the 2D models are illustrated in Figure 3.2. Here, the specimen and the indenter were treated as revolution bodies. Four-noded antisymmetric solid (CAX4) elements were used to model the 6376 resin, while it was assumed that the indenter could be modelled as a rigid cone with a half-angle of 70.3°. This simplified representation gives the same projected area to depth ratio as the three-sided Berkovich pyramid tip geometry generally used in nanoindentation experiments. A fine mesh was used in the indentation region, as large local deformation takes place in this zone, and the mesh became gradually coarser further afield from this region. This ensured that around 30 elements were in contact with the indenter at full load. The left and bottom regions of the model where constrained from movement in the X and Z directions respectively. Infinite elements in Abaqus were also experimented with in an attempt to replicate the infinite boundary at the bottom and right sides of the model. However, as the boundary effect was of interest in this investigation, the dimensions in the X and Z directions (Figure 3.2) were initially set to a value 300 times the maximum indentation depth in order to ensure far-field effects were negligible.

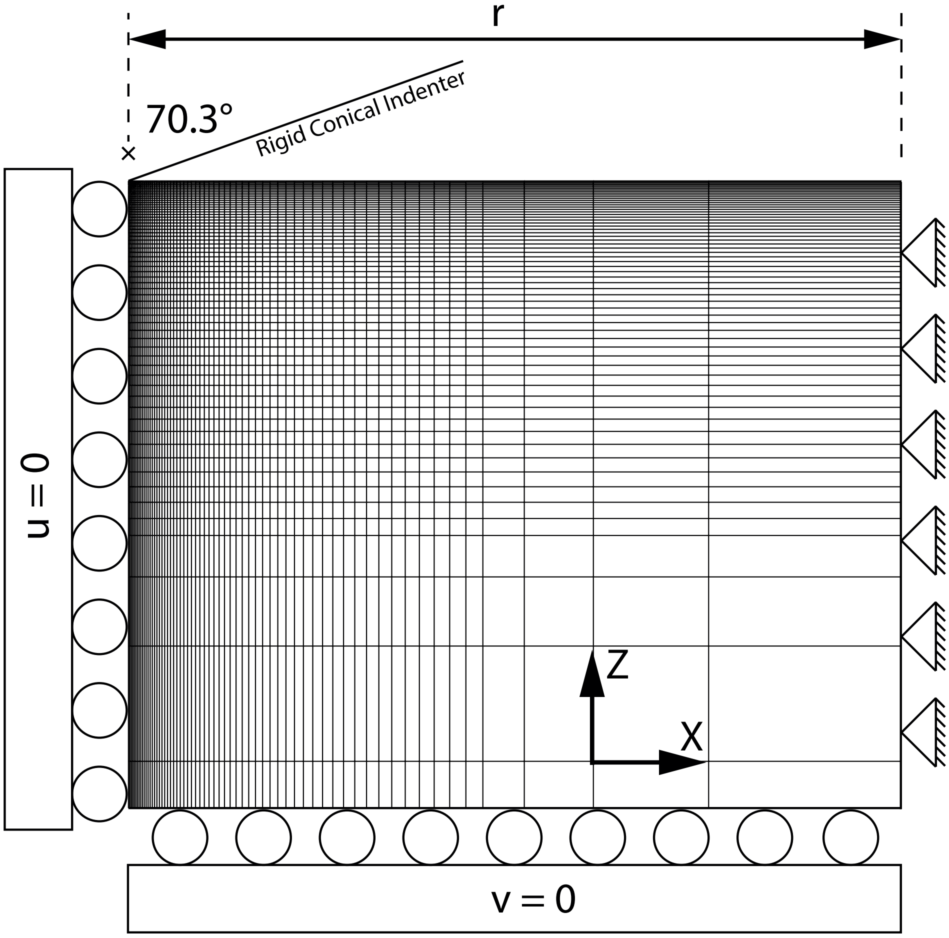

Figure 3.2: Magnified view of indentation region of the 2D axisymmetric model along with boundary conditions

The 2D models were used to examine the effect of the surrounding fibres on indentations of the matrix constituent. The deformation of the right-hand end of the model was restricted from movement in all directions (i.e. $u = v = w = 0$) to represent a rigid fibre constraint. The value of r shown in Figure 3.2 represents the distance from the initial contact point of indentation to the outside rigid ‘fibre’ region. This value of r was gradually reduced, while the indentation depth held constant at 1 µm in order to determine the change in indentation response closer to the rigid boundary.

3.2.2 3D models

In order to model the three-sided pyramidal geometry of the actual Berkovich indenter, a 3D model is required. The 3D model also allows the microstructure of the fibrous composite to be defined more realistically than with the 2D axisymmetric model. The three-sided Berkovich indenter geometry contains two planes of symmetry which allows accurate simulations of the indentation test to be produced using only one sixth of the substrate and indenter geometries. This is illustrated in Figure 3.3 where the modelled geometry has been highlighted. The substrate part was meshed with a combination of linear hexahedral elements (C3D8) and linear wedge elements (C3D6) available in Abaqus. Similar to the 2D models, a refined mesh was used in the central region at the indentation site, and gradually became coarser away from this region. Due to the six-fold symmetry employed, the Berkovich indenter geometry could be modelled using a single rigid plane with an angular offset of 24.7° from the surface as shown on the right of Figure 3.4a. This perfectly represents the Berkovich indenter geometry when the symmetry is taken into account. The use of the Mohr-Coulomb yield criterion to define the elastic-plastic behaviour of the 6376 material led to convergence issues, largely due to the extreme distortion experienced by the elements initially contacted by the rigid indenter. It was found that the models would not converge when a structured meshing algorithm was used. Thus, an advancing front sweep meshing algorithm was employed for the 3D models described herein, which facilitated convergence of the simulations.

Three different 3D substrate geometries were used to investigate the fibre constraint effect on the nanoindentation response of the resin. The first model shown in Figure 3.4a represents the constraint of the fibres as a rigid boundary similar to the 2D model described earlier. This is achieved by constraining the displacement of the nodes on the whole of the outside curved surface in every direction. The rest of the boundary conditions are similar to those used in the 2D model. This model geometry was used to highlight any difference in the fibre constraint response between the indentations carried out using a 2D cone and the accurate 3D Berkovich geometry.

The second 3D model shown in Figure 3.4b contains discrete cylindrical regions which represent the HTA fibres. These sections were added to the bulk speci-

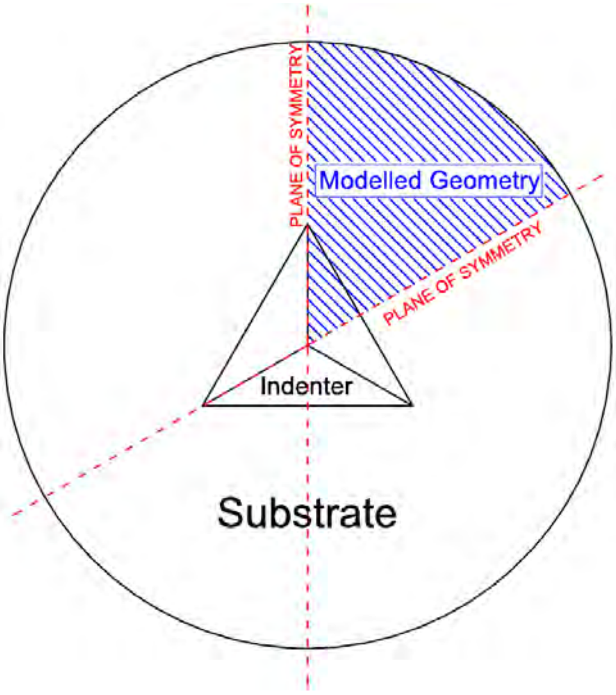

Figure 3.3: Six-fold symmetry of Berkovich indenter tip geometry

men in order to realistically represent cylindrical fibres surrounding the indentation zone. The diameter of the HTA fibres was 6.6 µm and the inter-fibre spacing was between 0.4 and 0.6 µm. These values were chosen based on average results determined in a previous study which characterised the fibre distribution of the HTA/6376 composite microstructure (Vaughan and McCarthy, 2010). Beyond this first layer of surrounding fibres, the material has been assigned the homogenised properties of the HTA/6376 composite through an embedded cell approach, as illustrated in Fig. 3.5a. Models were also developed which included further discretised layers of fibres beyond the first layer, however the results from these models did not vary significantly from the results from the embedded cell models. The variable r has been defined as the distance from the initial point of indentation to the closest point on the edge of the fibre, as shown in Fig. 3.4b.

The final 3D model shown in Figure 3.4c represents a situation where the fibre packing arrangement around the indentation region is less dense. It is useful to compare results for this model with the results for the closely packed fibres model as often in fibrous composites, like HTA/6376, the large resin pockets are located at the interply regions, as shown in Figure 3.6. This often leads to matrix rich regions

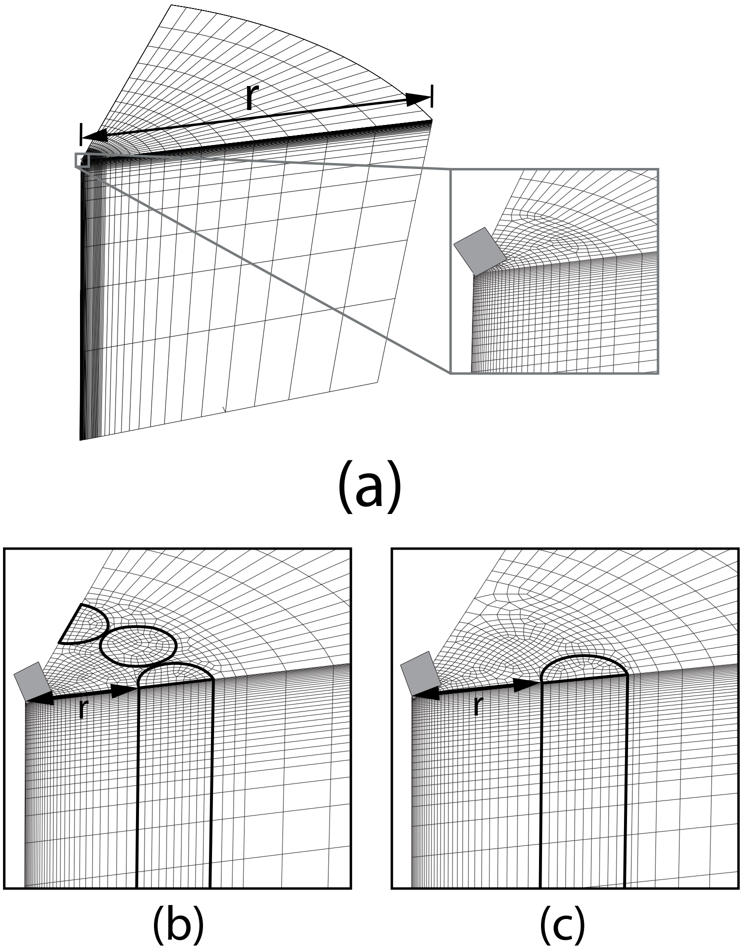

Figure 3.4: 3D finite element models used to represent a nanoindentation in the vicinity of fibres, (a) fibres represented as a rigid boundary, (b) fibres represented by a circular pattern of closely packed fibres and (c) fibres represented by a less dense packing arrangement

which are longer in one direction than the other. Thus, when indentation is carried out in these regions, the constraint effect will only be due to a few fibres initially. Due to the nature of the six-fold symmetry, adding one fibre to the model is equivalent to a less dense ring of three fibres surrounding the indentation region. Again, the embedded cell approach was used for these models and a plan view outlining the various section assignments for the models is illustrated in Figure 3.5b.

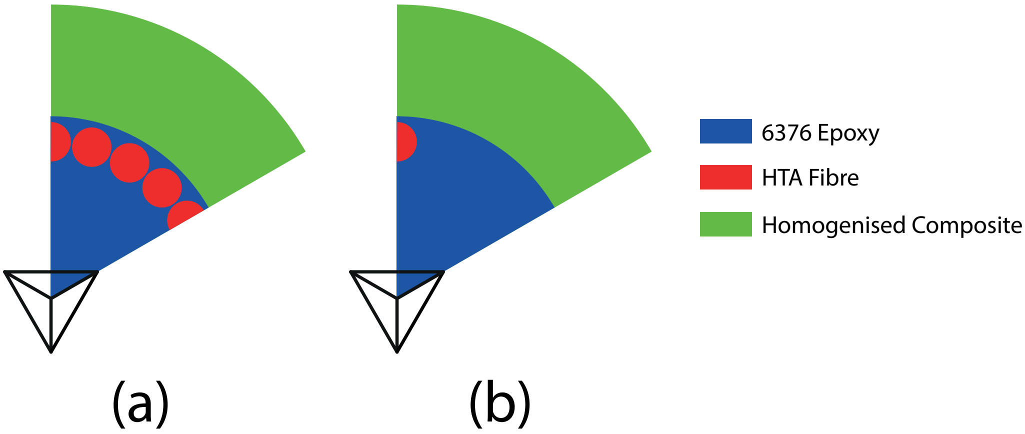

Figure 3.5: A plan view showing the section assignments of the models containing discrete fibre regions: (a) closely packed ring of fibres, (b) sparse array of three surrounding fibres

3.2.3 Material properties

A large strain solution was used in the analysis and both constituent materials were defined using the elastic properties shown in Table 3.1. The HTA fibre was assumed to exhibit transversely isotropic linear elastic behaviour, while the 6376 resin's elastic-plastic behaviour was modelled using the pressure-sensitive Mohr-Coulomb yield criterion. This yield criterion is capable of taking into account the hydrostatic pressure sensitivity of the 6376 resin and has been previously used to predict yielding in polymers associated with fibrous composite materials (González and Llorca, 2007; Vaughan and McCarthy, 2011*a*; Totry et al., 2008). The Mohr-Coulomb criterion induces yield in the material when the combined normal (σ_n) and shear (τ) stress reach a critical level on a plane according to Equation 3.1:

$$\tau_c = \tau + \sigma_n \tan\phi \tag{3.1}$$

where τ_c is the cohesion stress (yield stress in pure shear) and ϕ is the angle of internal friction. The yield criterion can be expressed in terms of the maximum and minimum principal stresses, as shown in Equation 3.2:

$$f(\sigma_1, \sigma_3) = (\sigma_1 - \sigma_3) + (\sigma_1 + \sigma_3)\sin\phi - 2\tau_c \cos\phi = 0 \tag{3.2}$$

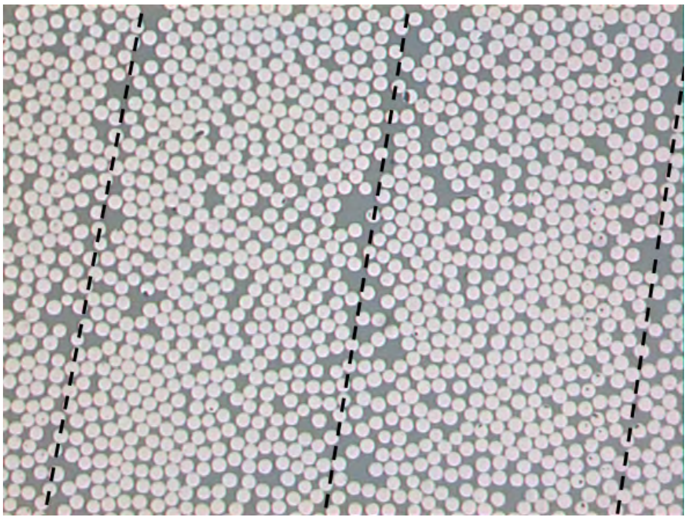

Figure 3.6: Optical microscope image of the HTA/6376 microstructure showing the matrix-rich regions between the laminae

Table 3.1: Constituent and composite elastic properties (Vaughan and McCarthy, 2011*b*; O'Higgins et al., 2008)

	Fibre (HTA)	Matrix (6376)	Composite (HTA/6376)
E_{11}(GPa)	238	3.63	139
E_{22}/E_{33}(GPa)	28	3.63	10
υ_{12}	0.25	0.34	0.32
υ_{23}	0.33	0.34	0.5
υ_{31}	0.02	0.34	0.32
G_{12}/G_{31} (GPa)	24	1.34	5.2
G_{23} (GPa)	7.2	54×10^{-6}	3.6

The cohesion stress and friction angle used to describe the yield behaviour using the Mohr-Coulomb model can be related to the tensile (σ_T) and compressive (σ_C) strengths of the material using Equations 3.3 and 3.4 respectively:

$$\sigma_T = 2\tau_c \frac{\cos\phi}{1+\sin\phi} \tag{3.3}$$

$$\sigma_C = 2\tau_c \frac{\cos\phi}{1-\sin\phi} \tag{3.4}$$

Using these expressions combined with experimental data from tension and compression tests carried out on specimens of 6376 epoxy resin by Fiedler et al. (2005), the friction angle (ϕ) and cohesion stress (τ_c) were determined as 26° and 82 MPa respectively. The homogenised properties of the composite used in the embedded cell approach are also given in Table 3.1 (O'Higgins et al., 2008).

3.3 Results and discussion

3.3.1 Model validation

In order to verify the mesh and boundary conditions used for the finite element models, the load-displacement data from simulated indentations carried out on elastic substrates defined using the 6376 material's elastic properties was compared with expressions from the literature. The load-displacement curves from the elastic 2D axisymmetric simulations have been compared with the elastic load-displacement response predicted by Sneddon's theory for elastic indentation by a conical-shaped indenter given in Equation 3.5:

$$P = \frac{2\gamma}{\pi} E_r (\tan\alpha) h^2 \tag{3.5}$$

where P is the indenter load, h is the indenter displacement, α is the half-angle of the conical indenter and E_r the reduced modulus of the contact. The correction factor γ was proposed by Hay et al. (1999), who discovered that the application Sneddon's elastic solution to conical indentations lead to a slight error, as it improperly accounted for radial material displacement into the contact region for conical indentations. As shown in Figure 3.7a, the two curves show good correlation, verifying the mesh and boundary conditions used in the 2D model.

In order to verify the mesh and boundary conditions used in the generation of the 3D models, the nanoindentation of a substrate defined with the 6376 material's elastic properties was simulated using the 3D models. The load-displacement curves from the model were then compared with the expected load-displacement curves according to the expression given in Equation 3.6, derived numerically by Larsson et al. (1996).

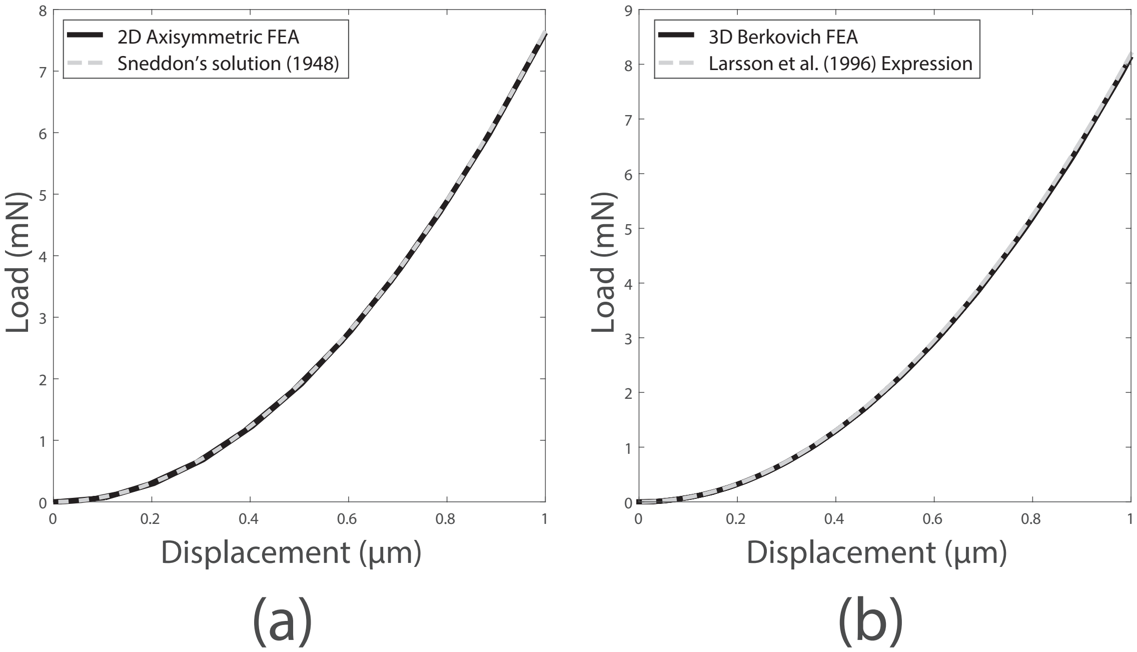

Figure 3.7: Elastic response of the (a) 2D axisymmetric model compared with Sneddon's theory and (b) 3D nanoindentation model compared with Larsson's expression

$$P = 2.1891(1 - 0.21\upsilon_s - 0.01\upsilon_s^2 - 0.41\upsilon_s^3)\frac{E}{1-\upsilon_s^2}h^2 \tag{3.6}$$

The load-displacement data has been compared in Fig. 3.7b. and shows good agreement between the curves. The elastic modulus used as an input to define the elastic substrates (3.63 GPa) has been compared with the indentation moduli determined using the simulated elastic unloading data and Equation 3.7 based on the Oliver and Pharr analysis.

$$E = \frac{1}{2\gamma\sqrt{A}}\frac{dP}{dh}\sqrt{\pi}(1 - {\upsilon_s}^2) \tag{3.7}$$

where A is the contact area, $\frac{dP}{dh}$ is the unloading contact stiffness and υ_s is the sample Poisson's ratio. The output indentation moduli were 3.68 GPa and 3.70 GPa for the 2D and 3D models respectively which show reasonable agreement with the input value of 3.63 GPa.

3.3.2 Effect of friction coefficient

In order to verify the validity of the frictionless contact assumption used in the finite element contact definition, the 3D nanoindentation of bulk 6376 matrix material was simulated with coefficients of friction (μ) ranging from 0 to 1. Figure 3.8 shows the variation of the normalised indentation modulus and hardness values for all the simulations. Based on the tight Y-axis limits, it is clear that the dependence of the indentation parameters on friction coefficient was negligible. This result is in line with previous studies into the effects of friction on nanoindentation testing (Liao et al., 2009; Wang et al., 2007). Thus, the friction coefficient was assumed to be zero for the remaining simulation results presented herein.

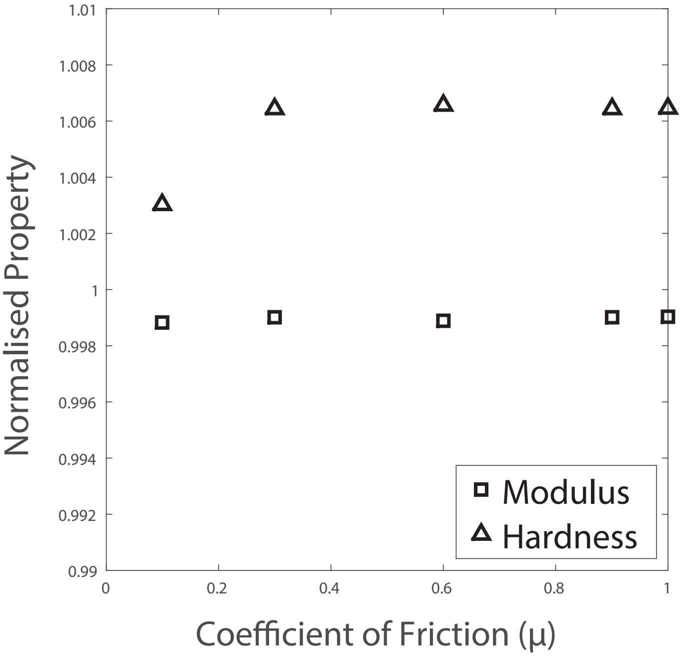

Figure 3.8: Variation of indentation modulus and hardness with friction coefficient (μ)

3.3.3 Comparison of indentation stress fields

It has been shown experimentally and numerically that conical and pyramidal indenter geometries with the same projected area to depth ratio produce the same load displacement data (Lichinchi et al., 1998; Ruan et al., 2010). This allows the nanoindentation theory which is based on axisymmetric conical indentations to be applied to indentations carried out with a pyramidal Berkovich tip, but has been shown produce different stress fields in certain cases (Warren and Guo, 2006). The stress fields produced by the 2D and 3D indentation models are shown in Figs. 3.9a and 3.9b, respectively. The near field stress states located directly under the sharp indenter tip are different for both models. However, the size of the stress fields perpendicular to the indentation direction is of interest to this study, as the constraining fibre reinforcement is parallel to the indentation direction. It is clear from Fig. 3.9 that the far field stresses produced by each indentation geometry are quite similar, and are reasonably axisymmetric, even for the non-axisymmetric 3D Berkovich indenter geometry. The size of the stress fields for the 2D conical and 3D Berkovich indentations are directly compared in Fig. 3.10, where the lines represent the regions where the stress was equal to 26.4 MPa, i.e. 10% of the 6376 material's compressive yield strength (σ_{YC}). The size of the stress fields are very similar for both indenter geometries, with the 2D stress field extending slightly farther from the point of indentation than that produced by the 3D Berkovich geometry.

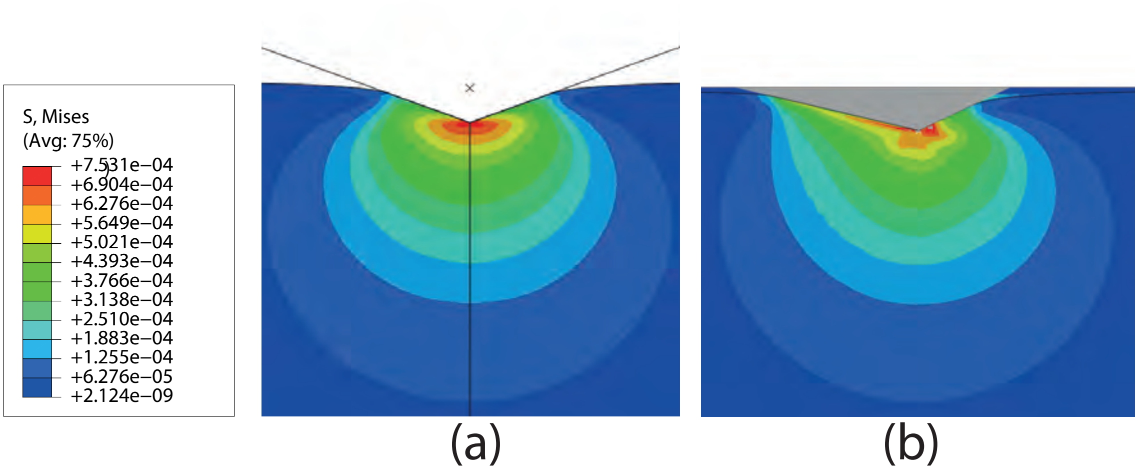

Figure 3.9: Comparison of von Mises stress fields produced by (a) 2D and (b) 3D models

3.3.4 Fibre constraint results

The indentation modulus was determined from the nanoindentation load-displacement curves at each value of r for all of the models considered. When r

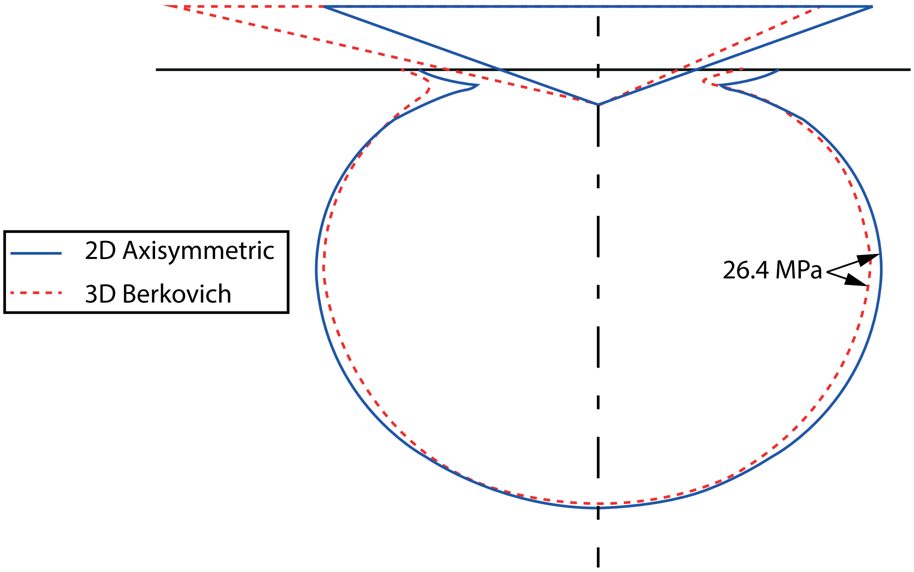

Figure 3.10: Size comparison of stress fields produced by 2D and 3D models

was made sufficiently large and the indentation was unaffected by any boundary, the models reproduced the correct elastic modulus value of the resin for both the 2D and 3D unconstrained models. The 2D model predicts a modulus value of 3.68 GPa while the 3D model predicts a modulus value of 3.70 GPa, which both compare well with the value of 3.63 GPa used to define the material properties in the model. Since the maximum indentation depth was held constant at 1 µm, the r value gave an indication as to how constrained the indentations were by the rigid boundary and discrete fibre sections. In all the models, it was found that as the value of r decreased, the maximum load required to achieve the maximum indentation depth increased, as shown in Figure 3.11 for four different values of r in the 3D model where the fibre constraint was represented by a rigid boundary condition. This also results in a steeper slope in the initial part of the unloading curve which indicates an increase in contact stiffness with decreasing distance to the fibre regions.

The values of Young's modulus obtained for each value of r were compared with the unconstrained value of Young's modulus obtained from the same model. This gave an indication as to the degree to which the constraints were affecting the value of indentation modulus calculated using the nanoindentation simulation's load-displacement data. The ratio of Young's Modulus to unconstrained Young's modulus is plotted against values of r in Figure 3.12 for all four model-types. Both

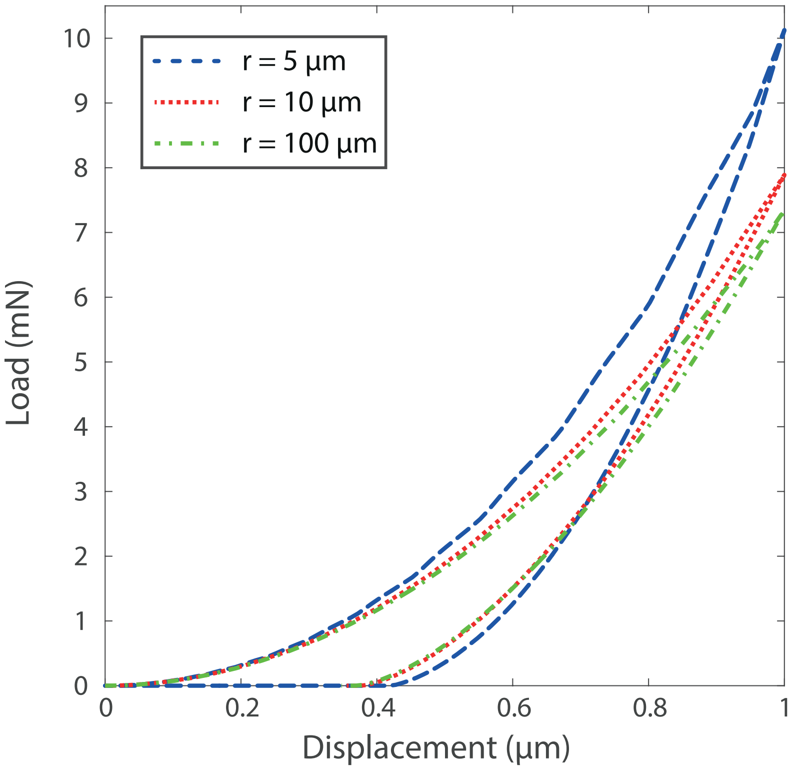

Figure 3.11: 3D Nanoindentation simulation load-displacement curves for three different values of r

the 2D and 3D models with fibre constraint represented by a rigid boundary produced similar results, with the 2D axisymmetric cone assumption slightly overconstraining the indentation compared to the more realistic 3D Berkovich geometry. This is due to the slightly larger stress field produced by the conical indentation in comparison to the Berkovich indentation, highlighted in Fig. 3.10. The 3D model of the indentation site surrounded by densely packed fibres produced results with significantly lower values of E/E_{un} than both the 2D and 3D models with the rigid boundary. This shows that representing the fibre constraint as a rigid boundary severely over-constrains the indentation compared to the realistic composite microstructure. This is most likely due to the cylindrical shaped fibres imposing a less significant mechanical constraint on the indentation, as stress can also flow through the inter-fibre spacing while also in the non-rigid fibre sections. Fig. 3.12 shows that for this realistic microstructural geometry, the indentations remain relatively unconstrained for values of r equal to 20 or greater. A sharp increase in modulus is observed for lesser values of r. Fig. 3.13 illustrates the approximate size of the projected contact area relative to the surrounding microstructure for this limiting indentation ($r = 20$ µm). Visually, the projected area appears quite small in comparison with the size of the pocket. In an experimental scenario, the indentation could easily be assumed to be completely unconstrained, despite being right on the limit of what can be considered an unconstrained indentation. This highlights the importance of characterising the fibre constraint effect prior to carrying out indentations into the in situ matrix pockets of high fibre volume fraction composite materials.

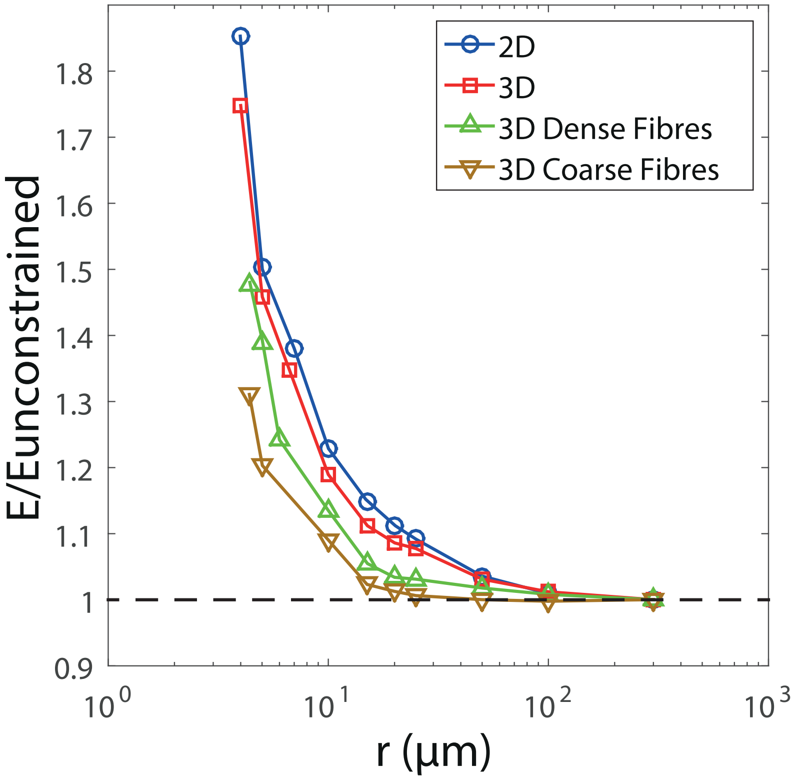

Figure 3.12: Ratio of Young's Modulus to unconstrained Young's modulus plotted against r for all four model-types

The final 3D model with just three immediate fibres around the indentation site region showed lower values of E/E_{un} than both other 3D models. This shows that the density of the fibre distribution is also a significant factor which should also be considered when selecting a suitable indentation site. The orientation of the Berkovich indenter tip relative to the surrounding microstructure had little impact on the results. This is due to the axisymmetric shape of the sub-surface indentation stress imposed by the Berkovich indenter tip, highlighted in Fig. 3.10. A closer look

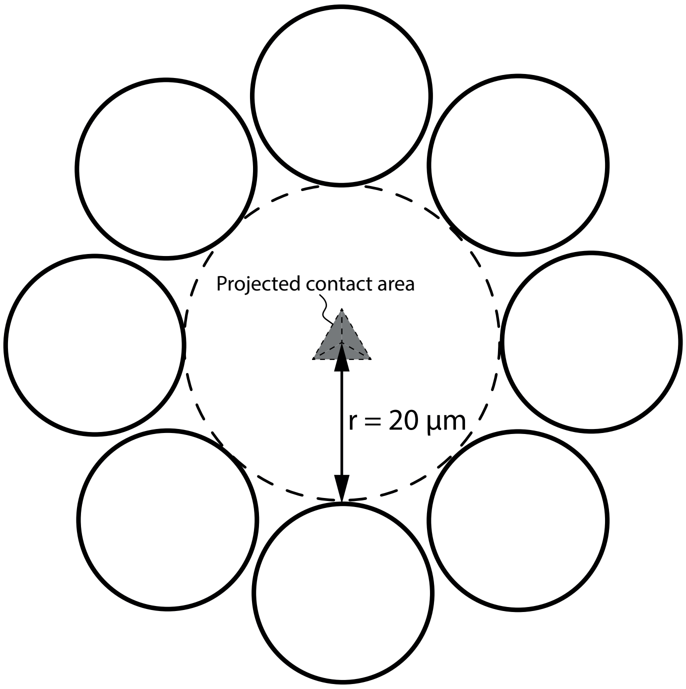

Figure 3.13: Illustration showing the projected contact area of an unconstrained indentation when r = 20 µm

at the stress distribution in the 3D models with fibre sections provides an interesting insight into the mechanics of the fibre constraint in these indentations. The stress distribution at three different indentation depths is shown in Figure 3.14 for the 3D model with closely-packed fibres where $r = 10$ µm . The stress limits for the contours have been limited to a range of $0.1\sigma_{YC} \leq \sigma \leq \sigma_{YC}$ where σ_{YC} is the yield stress of the 6376 resin in compression (264 MPa). Figure 3.14 shows that as the indentation depth increases, significant compressive stress develops in the fibre section, despite the fact that the indent was located in what would initially appear to be a large resin pocket within the composite microstructure. The load-displacement curve for this nanoindentation simulation is shown in Figure 3.15 along with the load-displacement curve for the unconstrained indentation. Initially, for low values of indenter displacement, both sets of data exhibit a similar response as the fibre constraint is not prevalent at these depths. As the indentation depth increases, stress is transferred to the surrounding fibres, as shown in Figure 3.14, and this effect leads to a divergence in the load displacement curves.

The finite element models have also been used to investigate the validity of

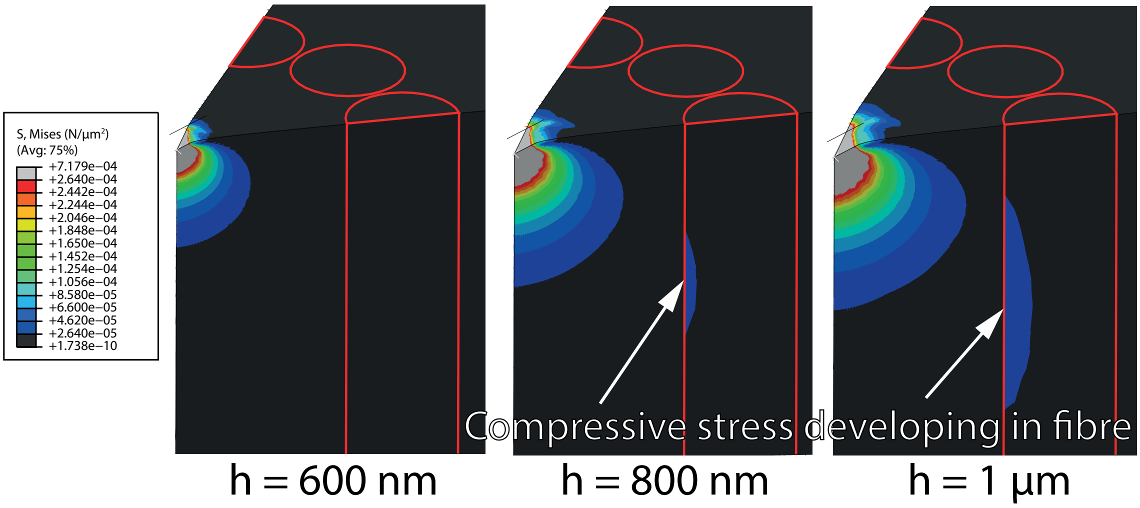
S, Mises (N/μm²)
(Avg: 75%)
+7.179e−04
+2.640e−04
+2.442e−04
+2.244e−04
+2.046e−04
+1.848e−04
+1.650e−04
+1.452e−04
+1.254e−04
+1.056e−04
+8.580e−05
+6.600e−05
+4.620e−05
+2.640e−05
+1.738e−10
Compressive stress developing in fibre
h = 600 nm
h = 800 nm
h = 1 μm

Figure 3.14: Development of stress in the fibre sections throughout the loading step when $r = 10$ μm

the Oliver and Pharr model for determining the correct contact area for indentations carried out on the in situ 6376 resin. The projected contact areas inferred using this nanoindentation theory can be compared to the areas measured directly from the finite element model contact area. The contact area was extracted directly from the simulations by summing the total area of the nodes in contact at the maximum indentation load. This contact area was then converted to the projected contact area using Equation 3.8, based on the geometry of the Berkovich tip:

$$A_{PROJ} = 0.929 A_{ABAQUS} \tag{3.8}$$

where A_{PROJ} is the projected contact area and A_{ABAQUS} is the contact area extracted from Abaqus. Figure 3.16 shows the ratio of the contact areas extracted from the finite element models (A_{FEA}) to those determined by the Oliver and Pharr method (A_{OP}), plotted against different values of r for the 3D models with a dense array of surrounding fibres. For the higher values of r the contact areas are within 10% of each other showing that the Oliver and Pharr approximation is reasonably accurate in determining the true correct contact area for the unconstrained 6376 material. However for lower values of r, the contact area determined from the finite element models becomes increasingly larger than those determined from the Oliver and Pharr method. This is due to the fibre constraint effect and becomes prevalent

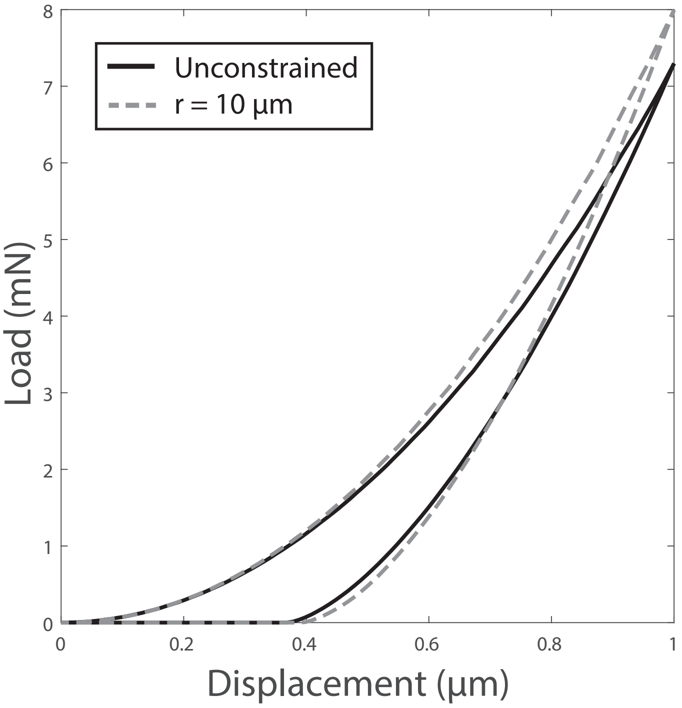

Figure 3.15: Load displacement curves for 3D model with fibres for the unconstrained case and for $r = 10$ µm

at similar values of r to the increased modulus values shown in Figure 3.12 ($r <$ 20 µm). The surrounding fibres cause the indented matrix to pile-up around the indenter to a larger degree than that predicted by the Oliver and Pharr theory, which increases the contact area, and causes error in the results. This behaviour is analogous to the pile-up error which is observed during the indentation of soft thin films on hard substrates (Zhou et al., 2008). The values of indentation modulus determined using the true projected contact area extracted directly from the finite element models are plotted in Fig. 3.17, where it can be seen that while the effect of the sub-surface fibre constraint is still prevalent, the relative increase in the modulus property is much less than that determined using the theoretically deduced contact areas of Fig. 3.12.

The results presented highlight the inherent difficulty in quantitatively characterising the in situ matrix material of fibrous composites due to the effects of the fibre constraint. It has been previously shown that these effects hinder the ability of the nanoindentation technique to accurately characterise the 'interphase' regions surrounding the fibre matrix interface (Lee et al., 2007; Gao and Mäder, 2002). An

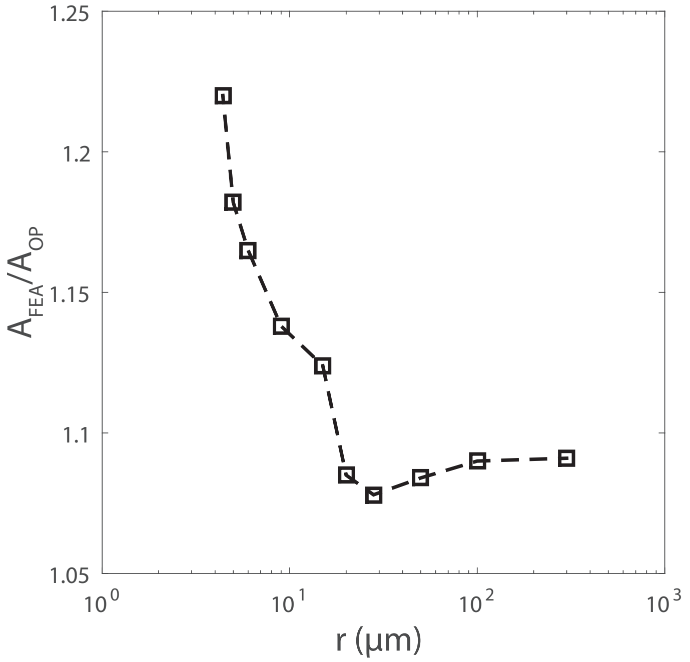

Figure 3.16: Ratio of contact area extracted from the finite element models (A_{FEA}) to contact area calculated from Oliver and Pharr method (A_{OP}), plotted against different values of r

interesting comparison can be made between the magnitude of the property increase determined from the finite element models and those reported from previous experimental characterisations. It is clear from the data presented in Fig. 3.12 that the fibre constraint effect leads to a less than two-fold increase in the value of the property, even for the most severe case of 2D indentations constrained by an adjacent rigid boundary. Therefore, experimental measurements of property variations in the interphase region which are several times larger than the properties of the matrix material (Kim et al., 2001) cannot be fully attributed to the fibre constraint effect based on the results of the finite element analysis presented in this work. Accurate three-dimensional finite element modelling with combined experimentation could potentially be used to deconvolute the effects of the fibre constraint from the true property change of the matrix material in cases where the effects of the constraining fibre boundary are unavoidable due to experimental limitations.

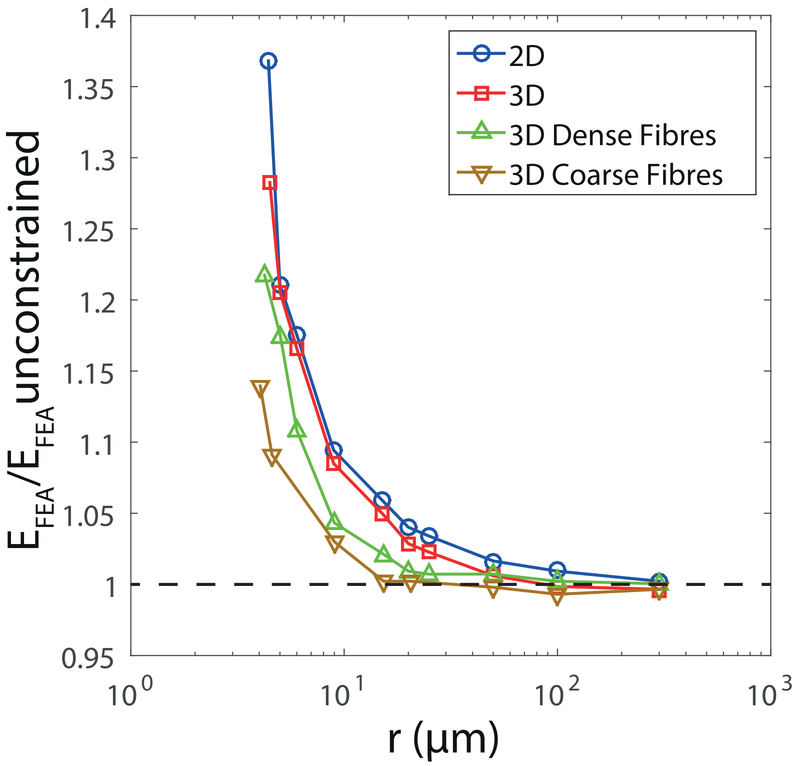

Figure 3.17: Ratio of Young's Modulus to unconstrained Young's modulus plotted against r for all four model-types where the contact area was extracted directly from the models

3.4 Concluding remarks

The effect of surrounding fibre constraint on the nanoindentation response of the matrix constituent of a fibrous composite has been characterised using both simplified 2D and realistic 3D finite element models of the indentation process. The results demonstrate that care should be taken when determining a suitable nanoindentation site when attempting to determine the in situ properties of the matrix region. The 2D conical and 3D Berkovich indenter geometries produced very similar axisymmetric stress fields, with the 2D field being slightly larger. This lead to a slight overestimation of the fibre constraint effect when this simplifying assumption was employed. Simplifying the analysis by assuming the fibre constraint can be modelled as a rigid boundary leads to a very conservative overestimation of the fibre constraining effect, and so should be avoided in future studies.

The 3D embedded cell models, with included discrete fibre sections, highlight the stress transfer which across the fibre-matrix interfaces during the indentation of the matrix pocket. This occurs even in relatively large resin pockets where, in an experimental scenario, it would likely be assumed than the indentation is free from the constraint of the surrounding fibres. The effect of surrounding fibres also leads to an increase in the projected contact area for the indentations as the size of the matrix pockets became smaller. This effect is not accounted for by the nanoindentation analysis techniques and contributes significantly to the artificial increase in the measured indentation modulus. The finite element methodology described in this work could be applied to any fibre–matrix material system to determine the composite microstructure's susceptibility to this phenomenon and the size of the matrix pocket necessary in order to carry out a valid unconstrained nanoindentation of the resin material.

4 The Effect of Microscale Residual Stress on in situ Matrix Characterisation

4.1 Introduction

In recent years the nanoindentation technique has seen increasing use in the characterisation of composite materials and their constituents (Gibson, 2014). This research has been mainly focused on the characterisation of two regions within the microstructure, namely, the matrix constituent regions (Gregory and Spearing, 2005; Canal et al., 2012; Rodríguez et al., 2006) and the "interphase" region which lies adjacent to the fibre-matrix interface (Kim and Hodzic, 2003; Gao and Mäder, 2002; Khanna et al., 2003a; Hodzic et al., 2004; Yedla et al., 2008). Indentations carried out into the in situ matrix material have shown an apparent increase in hardness and modulus compared to the material properties in bulk form (Gregory and Spearing, 2005). Meanwhile the measured properties of the interphase region have been found to be both softer than the matrix constituent in some cases, and harder in other cases, depending on the material system being investigated and the adhesion-promoting fibre surface treatments used (Kim and Hodzic, 2003). While these apparent microstructural property changes have generally been attributed to chemical interactions between constituents and fibre treatments, or altering curing conditions due to the surrounding microstructure (Gao and Mäder, 2002; Yedla et al., 2008), it has also been proposed that thermal and/or chemical residual stress could also contribute to the variation of measured properties (Kim and Hodzic, 2003).

Several micromechanical models of fibrous composite materials have shown the significance of the residual stress states generated in the material microstructure following material processing (Vaughan and McCarthy, 2011*a*; Zhao et al., 2006). This residual stress develops in the material microstructure as a result of the mismatch in thermal expansion coefficients between the fibre and matrix phases, and varies spatially throughout the microstructure (Hojo et al., 2009). In general it has been shown that a combination of compressive and shear stress can develop close to the fibre-matrix interface, whose magnitude depends upon proximity of neighbouring fibres, while further away from fibre-matrix interfaces, e.g. in matrix pockets, tensile stress dominates (Asp et al., 1996; Zhao et al., 2006; Vaughan and

McCarthy, 2011*b*). Interestingly, a number of experimental and numerical studies have indicated that the magnitude of the stress can sometimes be large enough to cause post-cure microscale damage initiation in the material, prior to any mechanical loading (Yang et al., 2013). While the effects of this residual stress on the mechanical performance of composite material has been characterised previously (Asp et al., 1996; Zhao et al., 2006; Yang et al., 2013), their effect on constituent material properties measured using nanoindentation in fibrous composites has yet to be investigated, and so forms the main topic of investigation herein.

Contact finite element models of the nanoindentation process have provided insight into the various mechanisms related to the nanoindentation technique and analysis of data (Bhattacharya and Nix, 1988; Lichinchi et al., 1998; Knapp et al., 1997; Khan et al., 2011; Xu and Li, 2005). The effect of pre-existing residual stress in a nanoindentation substrate has also been an area of interest for many researchers. The sensitivity of nanoindentation properties to the magnitude and nature of such residual stress has previously been successfully investigated through the use nanoindentation experiments and modelling on aerospace aluminium alloys (Khan et al., 2011; Bolshakov et al., 1996), steel (Breuils et al., 2011) and thin-film materials (Chuang et al., 2008; Huang et al., 2009; Bai et al., 2000; Wei and Yang, 2011; Ling et al., 2010). In these material systems, the material properties measured using nanoindentation technique are dependent on the residual stress-state, with compressive stress generally leading to an increase in the calculated properties, and a decrease in properties observed for cases where tensile residual stress was present. However, the degree to which the constituent material properties of long-fibre reinforced composite materials, measured through nanoindentation, are affected has not yet been investigated.

In this chapter, a combined micromechanical and contact finite element modelling approach has been used to characterise the effect of microscale residual stress on the nanoindentation of a fibrous composite microstructure. Section 4.2 provides a detailed description of the finite element modelling strategy and construction. The results from the finite element models are presented and discussed in detail in Section 4.3. Finally, Section 4.4 summarises the main findings from the numerical investigation as well as providing some concluding remarks.

4.2 Model development

4.2.1 Modelling strategy

An overview of the modelling strategy employed in this investigation is illustrated in Fig. 4.1, which consists of two stages of modelling. Firstly, plane strain micromechanical modelling was implemented to determine the state of residual stress in the HTA/6376 composite microstructure following thermal cooldown from the cure temperature (448 K) to room temperature (298 K). Additional residual stress induced due to matrix chemical shrinkage and through the process of specimen planing have not been considered in this analysis. To determine the effect of the microstructural residual stress states on the nanoindentation of the 6376 matrix material, the in-plane stress state at the regions of interest to nanoindentation studies have been extracted from the micromechanical plane strain models. In order to isolate the effects of these residual stress states, free from any boundary or fibre constraint effects (Chapter 3), these stress states were then applied to a separate three-dimensional substrate material. A finite element simulation of the indentation process was then carried out to predict the indentation response of the pre-stressed 6376 matrix material. The load-displacement history of the rigid indenter tip was recorded throughout the loading and unloading steps. This data was then exported and analysed using the nanoindentation theory to determine the effect of the various microstructural residual stress states in the regions of interest on the parameters and properties determined from nanoindentation tests.

4.2.2 Thermal cooldown models

The two main fibrous composite microstructural regions of interest to nanoindentation studies are the large matrix pockets and the interfacial matrix regions adjacent to the fibre-matrix interface. Separate model geometries have been devised for each of these regions in order to investigate the nature and magnitudes of the residual stress which exist in these regions in a parametric manner. The fibre and matrix regions were meshed using a quad dominated mesh which consisted of mostly four-noded (CPEG4) elements with a smaller number of three-noded (CPEG3) plane strain elements also included.

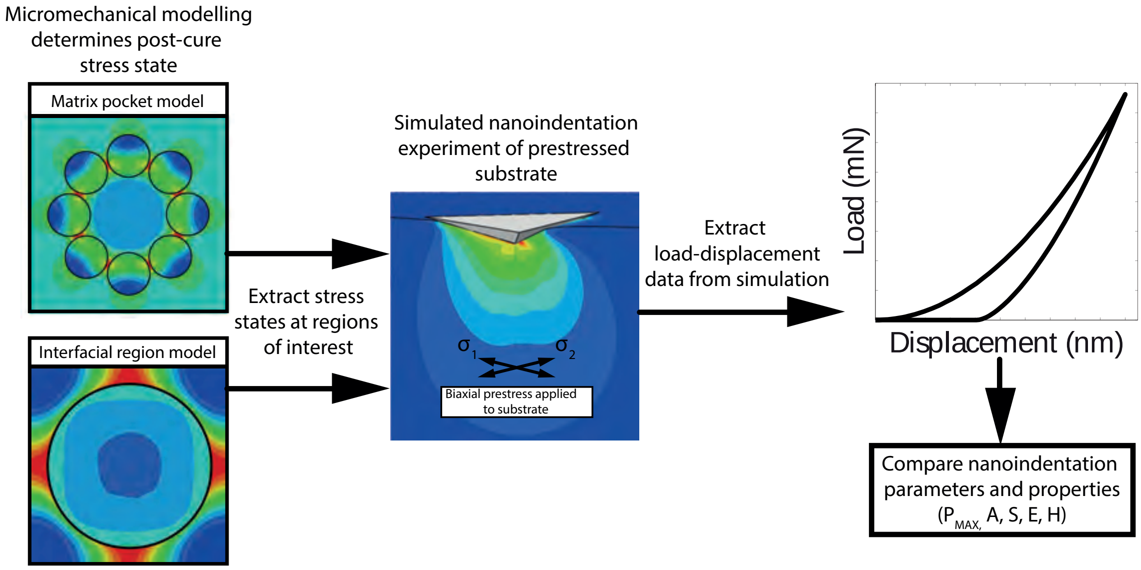
Micromechanical modelling determines post-cure stress state
Matrix pocket model
Interfacial region model
Extract stress states at regions of interest
Simulated nanoindentation experiment of prestressed substrate
σ1
σ2
Biaxial prestress applied to substrate
Extract load-displacement data from simulation
Load (mN)
Displacement (nm)
Compare nanoindentation parameters and properties (P MAX, A, S, E, H)

Figure 4.1: Finite element modelling strategy

The plane strain modelling approach was used to determine the residual stress state in the large open regions of matrix following thermal cooldown of the HTA/6376 composite. The modelling approach was designed to determine the residual stress state which exists in matrix pocket regions which were surrounded by a circular array of fibres, with an internal radius of R, following thermal cooldown. The models were built in accordance with the schematic shown in Fig. 4.2. The diameter of the HTA fibres was 6.6 µm and the inter-fibre spacing was between 0.4-0.6 µm based on the average results determined from a previous study which characterised the HTA/6376 composite microstructure (Vaughan and McCarthy, 2010). An embedded cell approach was used, where the homogenised HTA/6376 composite properties have been assigned to the material beyond the fibres. Symmetric boundary conditions were applied to the left and bottom sides of the models (as highlighted in Fig. 4.2), while the total size of the model was set to 300×300 µm. The radius of the matrix pocket (R) was varied over a range from 3.86 µm to 23.9 µm based on the range of matrix pocket sizes observed through microscopy studies of the HTA/6376 microstructure, which is examined in more detail in Chapter 5. A detailed example of the mesh used for the model with a matrix pocket radius of 15 µm is also shown in Fig. 4.2.

To investigate the nature and magnitude of the residual stress in the inter-

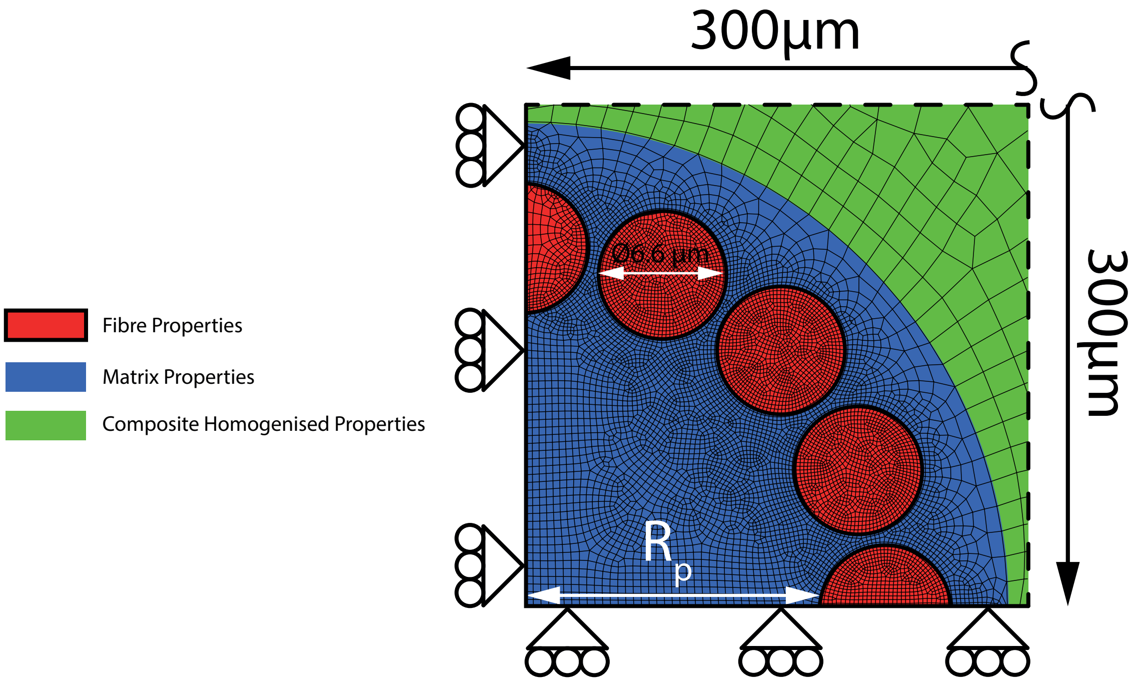

Figure 4.2: Schematic and mesh of plane-strain thermal cooldown finite element model for a matrix pocket of 15 µm radius

facial regions post-cure, a single fibre periodic square unit cell has been used. A schematic of its Representative Volume Element (RVE) is shown in Fig. 4.3. Periodic boundary conditions, similar to those described by van der Sluis et al. (2000), were applied to the RVE to ensure a macroscopically uniform stress/displacement field existed across the boundaries of the RVE. These consist of a series of tie constraints which require corresponding nodes on each opposing face of the RVE to undergo identical displacements. The periodic boundary conditions can be expressed in terms of the nodal displacement vector, u, such that

$$u_{North} - u_{n4} = u_{South} \tag{4.1}$$

$$u_{East} - u_{n2} = u_{West} \tag{4.2}$$

where the subscripts North, South, East and West correspond to nodes situated on each edge of the RVE and subscripts, n_2 and n_4 correspond to the control nodes which are located at each corner of the RVE, as shown in Fig. 4.3. Again, the fibre has been assigned a constant diameter of 6.6 µm, while the total square size of the RVE was varied to examine the effect of different fibre spacing (Sp) on the interfacial region matrix stress state. The inter-fibre spacings were varied over a range of 0.25 to 50 µm. The finite element mesh for the model with the inter-fibre spacing of 5 µm is shown in Fig. 4.3. In order to determine whether fibre-matrix interface damage occurred as a result of the thermal residual stress, the fibre-matrix interface has been modelled using cohesive elements available in ABAQUS (ABAQUS-Inc., 2013). A linear-elastic traction-separation law has been used with a very high initial stiffness (10^5 GPa/m), in order to ensure displacement continuity prior to any damage at the interface. The normal and shear strengths of the elements were set to 60 MPa, while the total fracture value in each of the fracture directions was assumed to be 10 J/m^2 (Vaughan and McCarthy, 2011a,b).

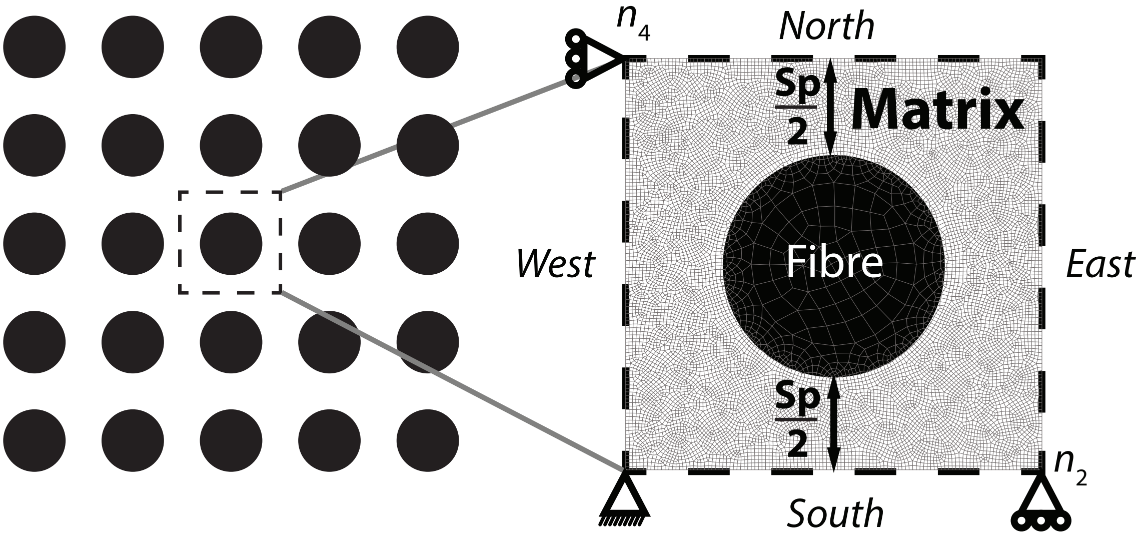

Figure 4.3: Single fibre unit cell with periodic boundary conditions and example mesh for inter-fibre spacing (Sp) of 5 µm

4.2.3 3D indentation models

To determine the effect the microstructural residual stress states on the nanoindentation of the 6376 matrix material, the in-plane stress state at regions of interest to nanoindentation studies have been extracted from the plane strain models. These stress states were then applied to a three-dimensional substrate material and a finite element simulation of the indentation process carried out to predict the indentation response of the pre-stressed 6376 matrix material. The use of full 3D modelling allows the effects of both equibiaxial and non-equibiaxial stress states to be determined (Breuils et al., 2011). The bulk 6376 epoxy has been modelled as a 400×400×200 µm 3D deformable solid in order to ensure that far-field boundary effects on the indentation were negligible. A single plane of symmetry has been applied to the mid-plane of the nanoindentation substrate under the point of the Berkovich indentation, as shown in Fig. 4.4. The substrate part was meshed with a combination of linear hexahedral elements (C3D8) and linear wedge elements (C3D6) available in Abaqus. A refined mesh was used in the central region at the indentation site, as large local strain gradients were expected in this region. The mesh gradually became coarser further afield from this region. Prior to the indentation step, the substrate geometry was pre-stressed in a separate step through the use of a biaxial combination of tensile or compressive surface displacement boundary conditions on the outer faces of the substrate geometry, as highlighted in Fig. 4.4. The basic constitutive equations of linear elasticity were used in combination with the elastic properties of the 6376 matrix material, in order to determine the biaxial combination of outer surface displacement boundary conditions required to produce the required residual stress state.

The Berkovich indenter tip has been modelled as a 3D discrete rigid solid. The indenter part was meshed using a combination of 3D rigid four-node (R3D4) and three-node (R3D3) elements. Details of the finite element model's indentation site are also shown insert to Fig. 4.4, where it was ensured that the tip of the indenter remained coincident with the midpoint of the substrate's upper surface prior to indentation. The load-displacement data for frictionless indentations was compared with data where the coefficient of friction varied between 0 and 0.9. The hardness and modulus were found to vary by a maximum of 1.3% when comparing the models with friction with the frictionless models for all residual stress cases. Therefore an assumption of frictionless contact was deemed valid, and results from frictionless models are presented herein. After the application of the substrate displacements, the indenter was then pushed into the substrate to a maximum depth of 1 µm and then withdrawn back to its original position. This indentation depth was chosen for convenience and the results are representative of an indentation of any depth given

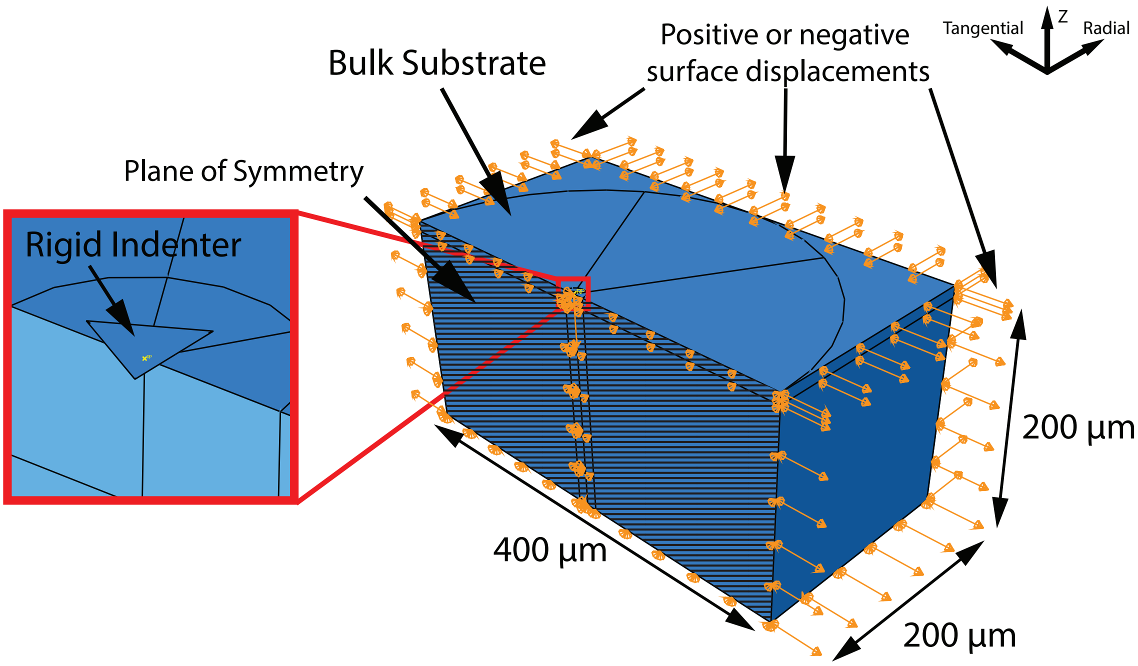
Bulk Substrate
Positive or negative surface displacements
Tangential
Z
Radial
Plane of Symmetry
Rigid Indenter
200 µm
400 µm
200 µm

Figure 4.4: 3D finite element indentation model showing detail of the indentation site and the boundary conditions used to apply a biaxial stress state prior to indentation

that the substrate material is large enough to prevent any boundary effects on the indentation response.

4.2.4 Material behaviour

The matrix and fibre constituents and homogenised composite regions were modelled using the elastic properties in Table 4.1. The HTA fibres and composite regions were assumed to exhibit transversely isotropic linear elastic behaviour. The 6376 epoxy resin was assumed to exhibit isotropic linear elastic behaviour while its non-linear plastic behaviour was modelled using the pressure-sensitive Mohr-Coulomb yield criterion, as described previously in Chapter 3. The friction angle (ϕ) and cohesion stress (τ_c) were assigned the predetermined values of 26° and 82 MPa, respectively. In order to determine the residual stress state following thermal cooldown from cure temperature, the constituents were assigned the thermal expansion coefficients (α) listed in Table 4.1.

Table 4.1: Constituent and composite material elastic and thermal properties (Vaughan and McCarthy, 2011*a*; O'Higgins et al., 2008; Telford et al., 2014)

	Fibre (HTA)	Matrix (6376)	Composite (HTA/6376)
E_{11}(GPa)	238	3.63	139
E_{22}/E_{33}(GPa)	28	3.63	10
υ_{12}	0.25	0.34	0.32
υ_{23}	0.33	0.34	0.5
υ_{31}	0.02	0.34	0.32
G_{12}/G_{31} (GPa)	24	1.34	5.2
G_{23} (GPa)	7.2	$54{\times}10^{-6}$	3.6
$\alpha_{11}(K^{-1})$	$-0.1{\times}10^{-6}$	$54{\times}10^{-6}$	$-0.1{\times}10^{-6}$
$\alpha_{22}/\alpha_{33}(K^{-1})$	$10{\times}10^{-6}$	$54{\times}10^{-6}$	$28.6{\times}10^{-6}$

4.3 Results and discussion

4.3.1 Matrix pocket region

The distributions of the maximum and minimum principle stresses for the 6376 matrix pocket of 5.97 µm radius are shown in Fig. 4.5a and Fig. 4.5b, respectively. A relatively homogeneous stress state was observed across the vast majority of the matrix pocket except in the regions very close to the fibre matrix interface. The homogeneous region is highlighted by the hatched central regions in Fig. 4.5. Based on the results of the fibre constraint investigation in Chapter 3, the projected contact area of an unconstrained Berkovich indentation has been superimposed onto Fig. 4.5. This shows that the indentation was carried out entirely into this region of homogeneous stress-state and any influence from the stress gradients closer to the fibre matrix interfaces is assumed to be negligible. Similar stress states were observed for all the different values of R investigated. The in-plane principal stresses within the homogeneous stress regions were found to be in a state of equibiaxial tension for the full range of matrix pocket sizes investigated. The values of the equibiaxial principle stresses for the pockets are plotted against the size of the matrix pocket in Fig. 4.6. It can be seen that the magnitude of equibiaxial tensile stress decreases almost linearly with increase in matrix pocket size. Interestingly, despite this trend and the wide range of matrix pocket sizes investigated, the magnitude of the equibiaxial stress only varies between 19.9 and 26.2 MPa for the largest and smallest pocket radii respectively. None of the stress states determined for the investigated range of matrix pocket sizes caused plastic deformation in the 6376 matrix material according to the Mohr-Coulomb yield criterion.

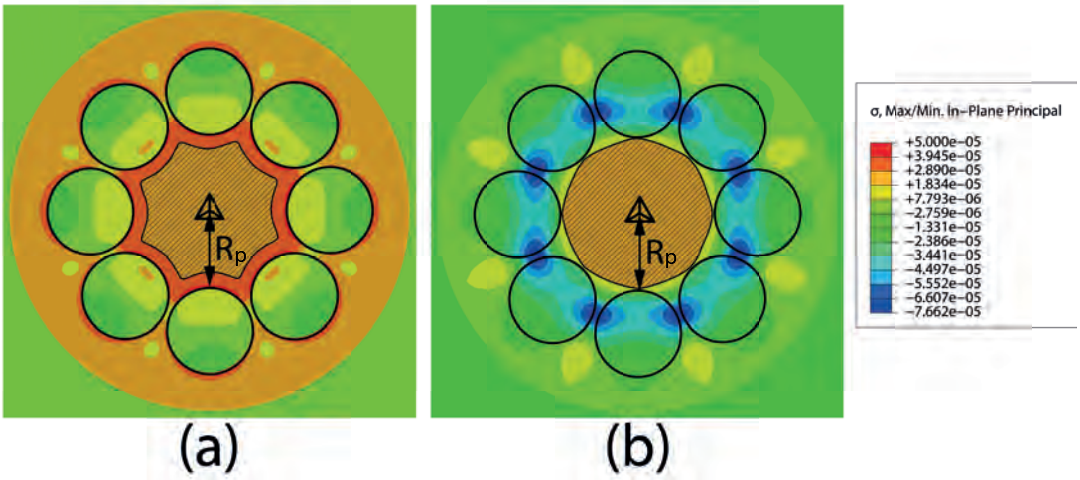

Figure 4.5: (a) Maximum and (b) Minimum in-plane principle stress state following thermal cooldown for the 6376 matrix pocket with a radius of 5.97 µm

The stress state under the indenter tip at maximum indentation displacement is shown in Fig. 4.7 for the model containing the pre-applied stress state corresponding to a matrix pocket of 8.5 µm radius. Both the localised indentation stress and homogeneous region of residual stress that exists throughout the rest of the substrate are shown. The simulated load-displacement curves for some of the residual stress states considered are shown in Fig. 4.8 and compared with the simulated load-displacement curve for the case with no residual stress applied. The residual stress has a noticeable effect on the load-displacement data, most markedly, the load required to reach the constant 1 µm indentation depth reduces with decreasing pocket size due to the larger residual stress present. The effect of the residual stress states from each pocket size on the nanoindentation parameters (P_{max}, A and S) and calculated properties (H and E) is shown in Fig. 4.9, where the values have been normalised against those from the non-prestressed substrate indentation. The hardness (H) property is influenced to a much greater degree than the indentation modulus (E) property, decreasing by up to 11.9%, in comparison with the non-prestressed substrate. This decrease in hardness is due to the decrease in indentation load required to reach the maximum displacement and the increase of 7.3% in the estimated contact area according to Fig. 4.9. Another interesting finding is that the value of the in situ hardness changes by only 3.4% across the full

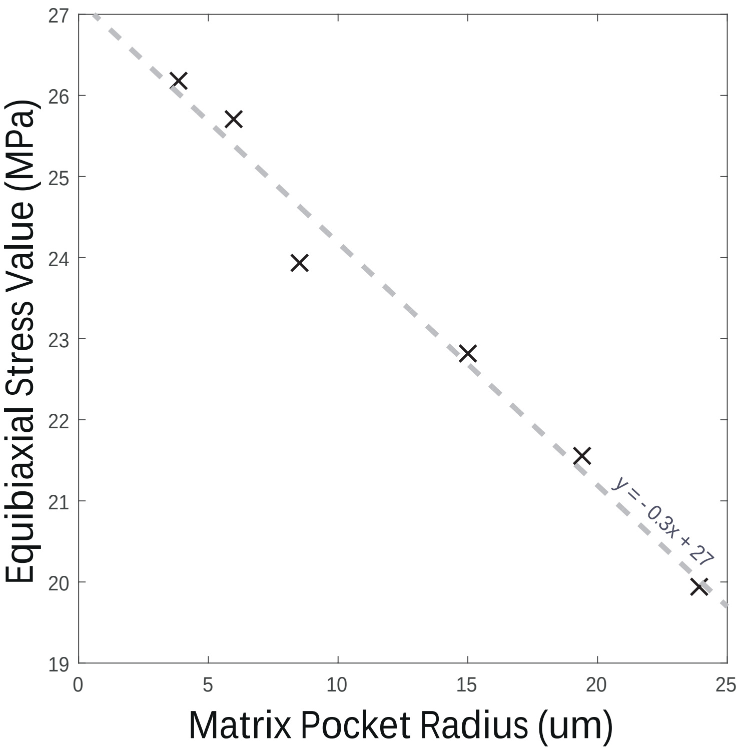

Figure 4.6: Equibiaxial stress versus size of matrix pocket

range of in situ matrix pocket sizes. This indicates that while the residual stress is clearly an important factor when comparing the response of bulk material with in situ material, the effect is much less substantial when comparing the response of just the in situ pockets across a wide range of sizes.

Previous finite element investigations have shown that the presence of residual stress in a substrate can lead to errors when determining the true projected contact area using the Oliver and Pharr methods of analysis due to the effects of material pile-up or excessive sink-in behaviour (Bolshakov et al., 1996). For comparison, the true projected contact areas have also been extracted directly from the 3D finite element models and the values of indentation hardness and modulus recalculated using these directly determined areas. These values were then normalised by their respective values from the non-prestressed substrate indentation, and plotted in Fig. 4.9. These projected contact areas are still up to 4.5% greater than those extracted from the stress-free model resulting in calculated values of hardness which are up to 9.5% smaller than that of the initially stress-free substrate. This indicates that the stress state has a greater influence on the areas calculated using the Oliver

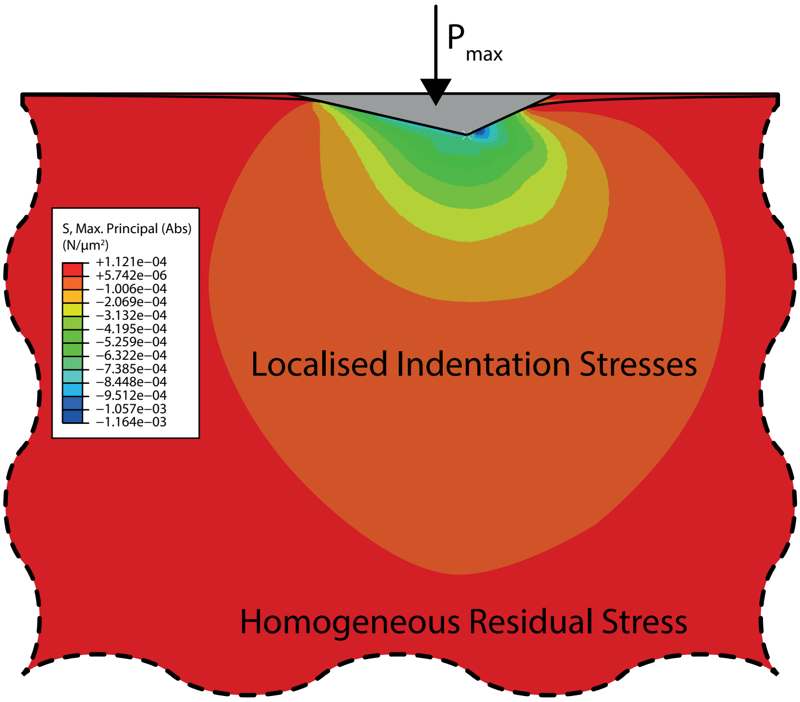
P max
S, Max. Principal (Abs) (N/µm²)
+1.121e−04
+5.742e−06
−1.006e−04
−2.069e−04
−3.132e−04
−4.195e−04
−5.259e−04
−6.322e−04
−7.385e−04
−8.448e−04
−9.512e−04
−1.057e−03
−1.164e−03
Localised Indentation Stresses
Homogeneous Residual Stress

Figure 4.7: Stress state under indenter at maximum indentation depth for 8.5 µm matrix pocket residual stress state model

and Pharr method, while also having a substantial effect on the actual contact areas extracted directly from the finite element analysis. Thus, the change in the measured properties, plotted in Fig. 4.9, is not solely due to pile-up or excessive sink-in inducing error in the Oliver and Pharr area prediction. The values for indentation modulus do not deviate by more than 1.2% from that of the stress-free value, and therefore shown to be insensitive to the equibiaxial tensile stress state which is present in the matrix pockets.

4.3.2 Interfacial region

The stress state that exists in the single-fibre periodic unit cell model with an inter-fibre spacing of 2 µm following thermal cooldown is shown in Fig. 4.10. It is clear that the stress state of the matrix material close to the fibre-matrix interface varies greatly around the circumference of the fibre and is highly dependent on the vicinity of the surrounding fibres. The residual stresses in the first element of matrix material adjacent to the fibre-matrix interface have been resolved in the radial and

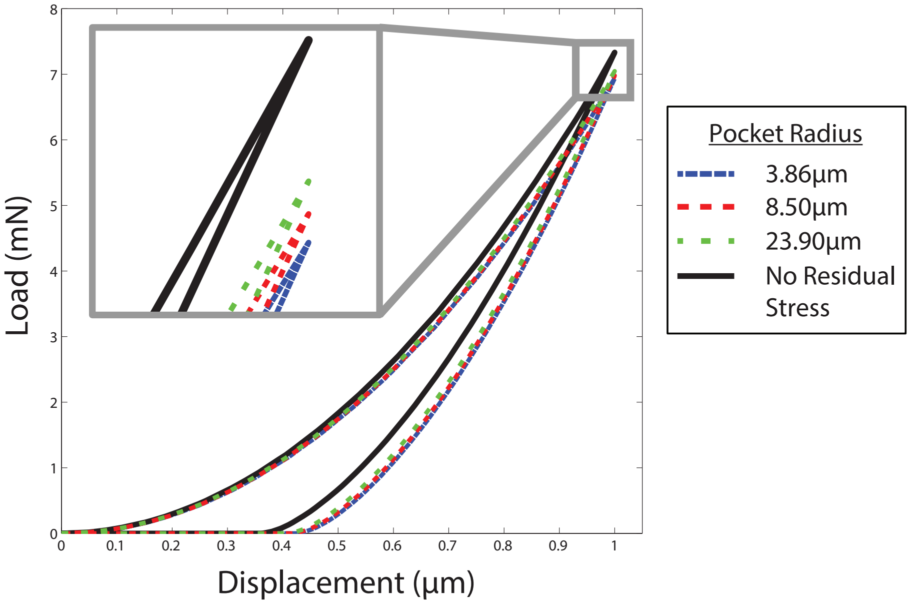

Figure 4.8: Load versus displacement data extracted from the finite element simulations for various pocket residual stress states

tangential directions relative to the centre of the fibre. The variation of both the radial and tangential residual stresses for the case where the inter-fibre spacing was 0.25 µm is shown in Fig. 4.11. The stresses in each direction have been plotted separately on a polar plot. The circumference of the central fibre represents the axis of zero stress, with positive (tensile) stresses protruding out of the fibre and negative (compressive) stresses plotted inside the fibre's dashed boundary.

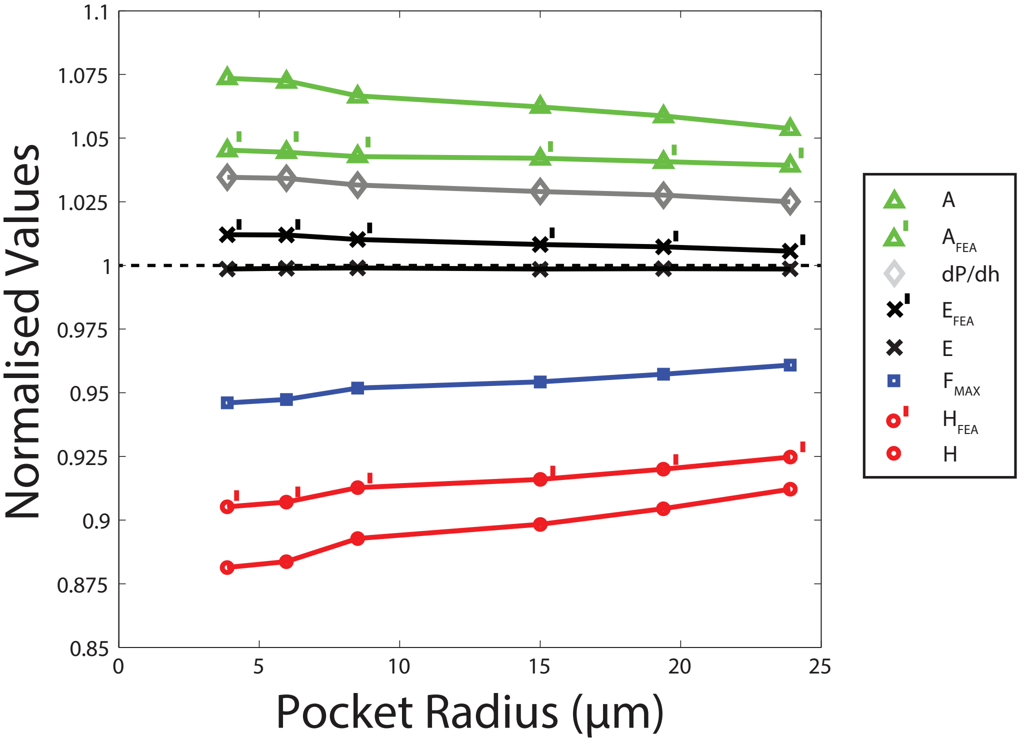

Figure 4.9: Normalised indentation parameters plotted versus matrix pocket size

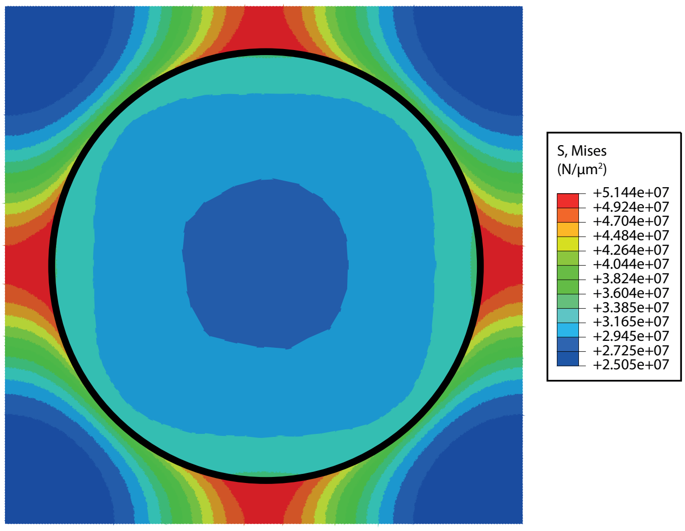
S, Mises
(N/μm²)
+5.144e+07
+4.924e+07
+4.704e+07
+4.484e+07
+4.264e+07
+4.044e+07
+3.824e+07
+3.604e+07
+3.385e+07
+3.165e+07
+2.945e+07
+2.725e+07
+2.505e+07

Figure 4.10: Stress state following thermal cooldown for periodic unit cell with inter-fibre spacing of 2 μm

The evolution of radial and tangential stresses with increasing inter-fibre spacing is shown in Fig. 4.12, where a large variation in the nature and magnitude

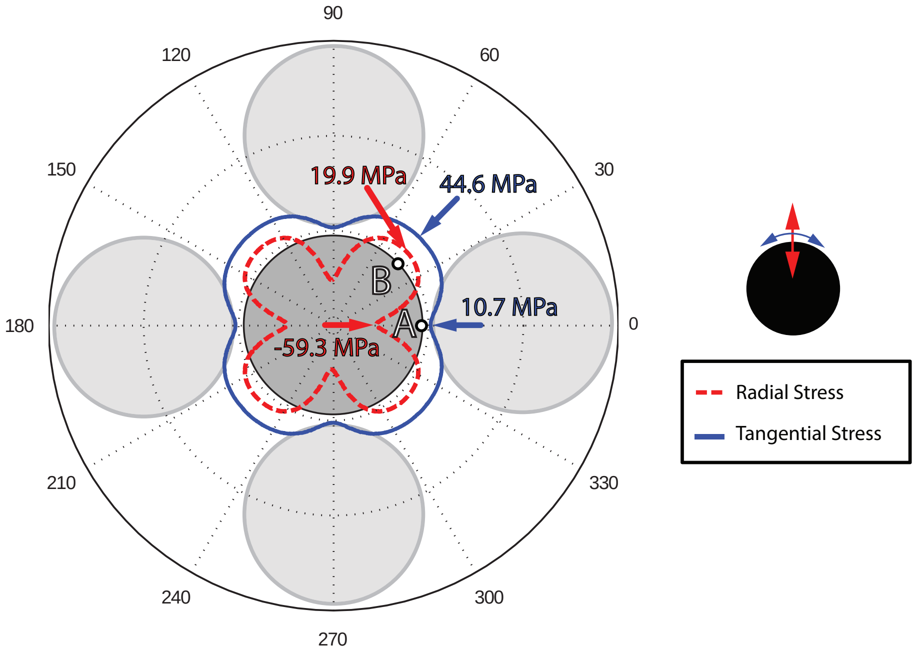

Figure 4.11: The variation of radial and tangential interfacial region stresses for an inter-fibre spacing of 0.25 µm

of the stress around the circumference of the fibre is evident for small inter-fibre spacings. This variability of stress around the fibre circumference decreases as this spacing increases, eventually converging to constant compressive radial and tensile tangential stress states of similar magnitude as the inter-fibre spacing increases. For the initial small inter-fibre spacings, the plotted stress states form a quatrefoil shape (Fig. 4.12a and 4.12b), where the lowest values of radial and tangential stress are located at the point of minimal inter-fibre spacing, while the peak tensile stress is located at 45° to the axis joining the fibre centres, adjacent to the surrounding matrix rich regions. These points on the fibre have been marked as points A and B on Fig. 4.11. At the points A and B, the direction of the radial and tangential stresses correspond to the in-plane principal stress directions, and thus, these two points were used as the main points of interest for the interfacial region residual stress investigation.

The values of the radial and tangential residual stresses for points A and B are plotted in Fig. 4.13 for the range of inter-fibre spacings (Sp) investigated. The residual stress at the point A is a combination of compressive radial and tensile tangential stress over the full range of inter-fibre spacings. The radial stress at the

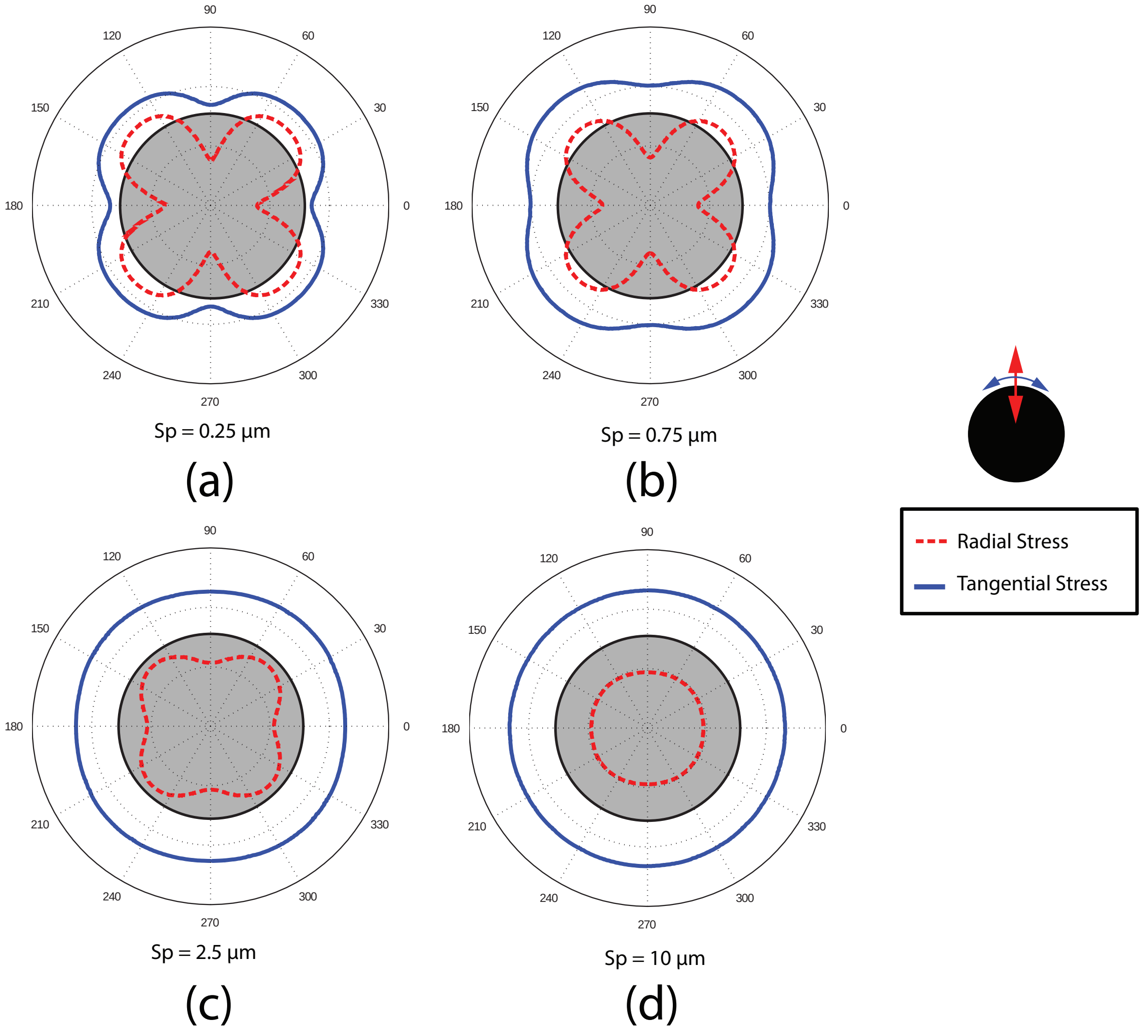

Figure 4.12: The evolution of radial and tangential stresses with increasing inter-fibre spacing

point B undergoes considerable change as the inter-fibre spacing increases, changing from a tensile (20 MPa) to a compressive (-21.3 MPa) state over the range of spacings investigated. The tangential stress at point B remains tensile throughout, with a reasonably linear decrease in tensile stress magnitude as the inter-fibre spacing increases. None of the examined stress states described in this section caused plastic deformation in the matrix material according to the Mohr-Coulomb yield criterion, or fibre-matrix interface damage in the cohesive elements.

The various interfacial region stress states determined from the cooldown models for the regions of interest A and B were applied to the bulk nanoindentation

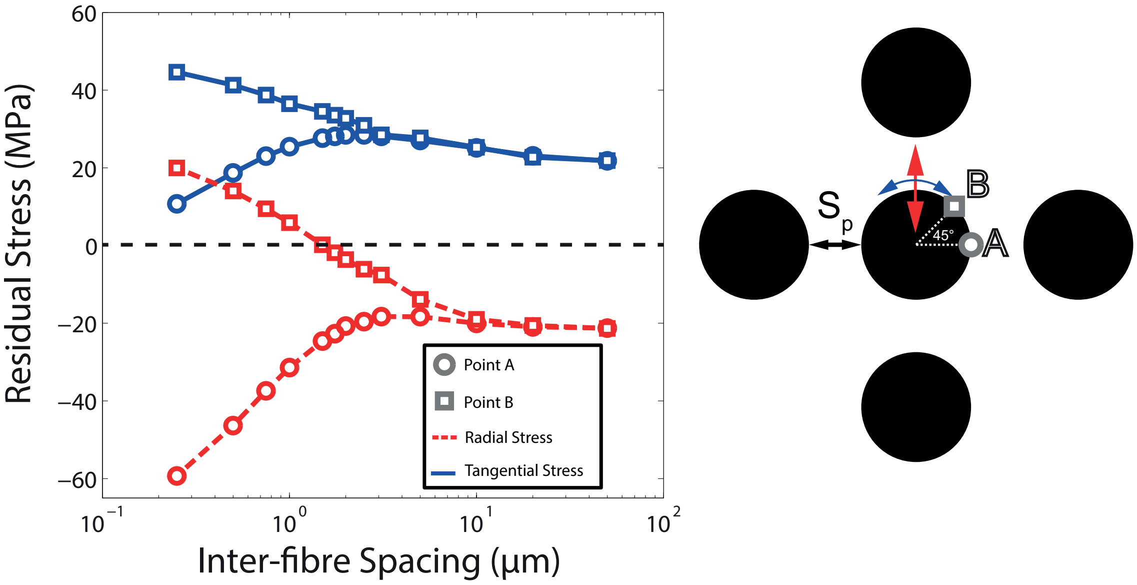

Figure 4.13: Radial and tangential residual stress values for points A and B for the range of investigated inter-fibre spacings

substrate through a combination of tensile and/or compressive outer boundary substrate displacements. The radial stresses were applied perpendicular to the plane of symmetry while the tangential stresses were applied parallel to this plane as highlighted by the coordinate system in Fig. 4.4. The calculated indentation properties were found to be largely insensitive to the Berkovich tip orientation relative to the radial and tangential directions, with hardness and modulus varying by a maximum of 2% and 1.5%, respectively, across the full range of stress states investigated when the indenter orientation was rotated by 90 degrees. This is likely due to the axisymmetric stress field produced in the substrate during the Berkovich indentation.

The nanoindentation load-displacement curves predicted for a selection of the residual stress states are shown in Fig. 4.14a and Fig. 4.14b for the points of interest A and B respectively. The load-displacement data for the stress states at point A does not deviate largely from the load-displacement data for the non pre-stressed substrate. The data lacked any distinctive trends in relation to the inter-fibre spacing. However, it is noticeable that the peak load for the 0.25 µm spacing stress state was larger than the peak load for the unstressed substrate. The deviation of the load-displacement data from that of the stress-free substrate is more apparent for the stress states determined at point B. There is also a clear trend in this data, manifesting as a positive shift along the displacement axis that increases as the inter-fibre spacing decreases. This results in an observed decrease of peak load and increase of final plastic indentation depth as the inter-fibre spacings become smaller.

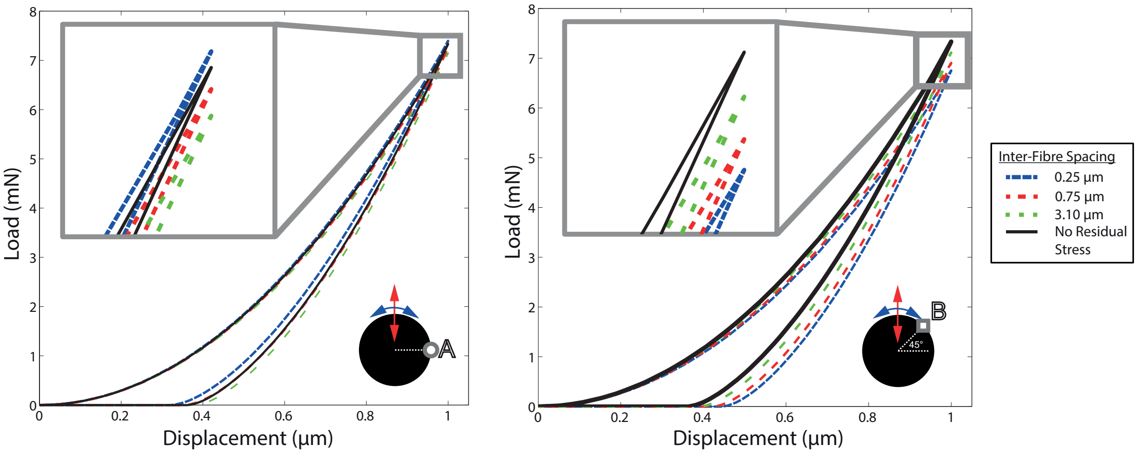

(a) (b)

Figure 4.14: Load-displacement data for a number residual stress states determined at (a) Point A and (b) Point B

The effect of the residual stress states determined at point A on nanoindentation parameters is shown in Fig. 4.15a. The substantial change in stress state at point A over the range of inter-fibre spacings from 0.25-3 μm leads to a substantial shift in the normalised indentation parameters over the same range of spacings. For the smaller inter-fibre spacings, the compressive radial stress was the dominant component of the in-plane stress state. This results in an increase in normalised hardness by up to 4.9% for an inter-fibre spacing of 0.25 μm. This due to the increase in peak load required to reach the constant indentation depth, seen in Fig. 4.14a, and a decrease in the normalised contact areas for the small inter-fibre spacings. As the inter-fibre spacing increases, these trends in peak load and area begin to reverse, leading to a reduction in the normalised hardness values. This change in the normalised parameters is as a result of the large decrease in magnitude of the radial compressive stress magnitude at point A as the inter-fibre spacing increases, reducing the overall constraint on the indentation stress field. For inter-fibre spacings greater than 3.1 μm, the normalised indentation parameters begin to approach the values of the non-prestressed model, and eventually converge to final values as the effect of surrounding fibre microstructure becomes negligible.

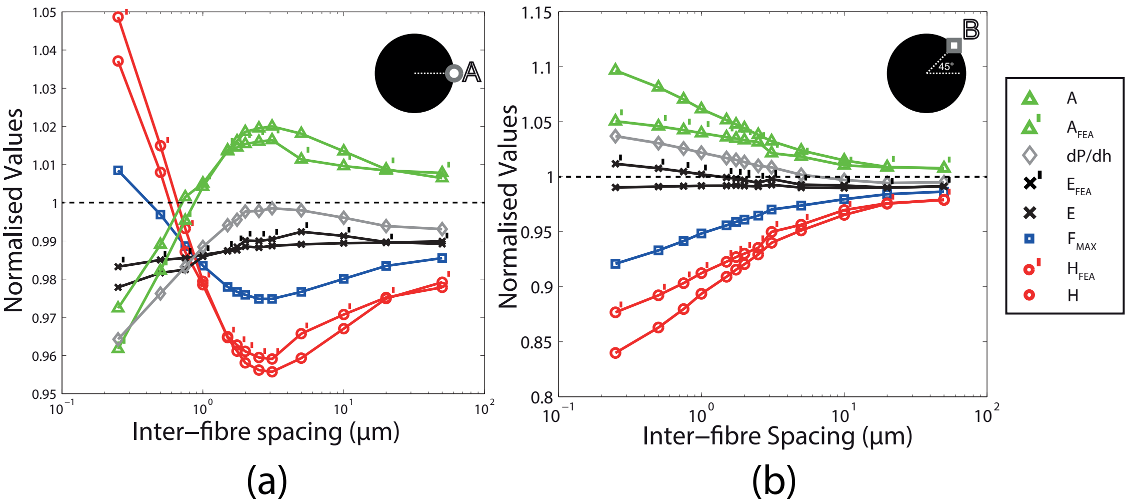

Figure 4.15: Normalised indentation parameters plotted versus inter-fibre spacing for (a) point A and (b) point B

The normalised nanoindentation parameters for the stress states at point B are plotted in Fig. 4.15b. For the very small values of inter-fibre spacing (< 2 µm), the radial and tangential stresses at the point B are in biaxial tension. The largest deviation of the normalised nanoindentation parameters is also shown to occur over this range of inter-fibre spacings in Fig. 4.15b. As the inter-fibre spacing increases, the radial stress at the point B becomes compressive and the values of the normalised nanoindentation parameters begin to converge to the same values as those determined at point A for large inter-fibre spacings.

The results for the points A and B indicate that the effect of the residual stress is minimised for the cases when the radial and tangential stresses are roughly equal and opposite in magnitude, for example, at the point of interest A with an inter-fibre spacing of approximately 1 µm, and for the homogenised stress state at large inter-fibre spacings. It is also interesting that the variation of the normalised nanoindentation parameters was much larger for the stress states at the point B than for those determined at the point A. This is due to the combination of compressive radial and tensile tangential stresses found at the point A over the full range of inter-fibre spacings. This is an important finding, as the point B is adjacent to a matrix-rich region, and therefore would likely be an advantageous region for carrying out experimental grid indentations travelling from one constituent to the other. However, despite these trends in the hardness property, the normalised indentation modulus values were largely insensitive to the interfacial stress states, only deviating by 2.2% and 1.1% from those of the non-prestressed substrate for points A and B respectively.

The plastic strain fields below the indenter tip for the pre-stressed substrates corresponding to an inter-fibre spacing of 0.25 µm are shown in Fig. 4.16 for the points A and B. These have then been compared with the plastic strain field for the non-prestressed substrate. It can be clearly seen that the large in-plane radial compressive stress at point A for this inter-fibre spacing has a noteworthy effect on the size of the plastic strain field below the indenter tip at the maximum indentation depth. This compression increases the constraint effect of the surrounding material on the indentation stress field and reduces the overall volume of plastically deformed material in the substrate substantially. This sub-surface constraint directly increases the material's resistance to permanent plastic deformation and is the underlying mechanism responsible for the apparent increase in indentation hardness values shown in Fig. 4.15a for very small inter-fibre spacings at point A. Conversely, the biaxial tensile stress state at point B reduces the bulk matrix constraint on the indentation stress field, allowing a greater volume of plastic flow in the material as shown in Fig. 4.16 at the maximum indentation depth.

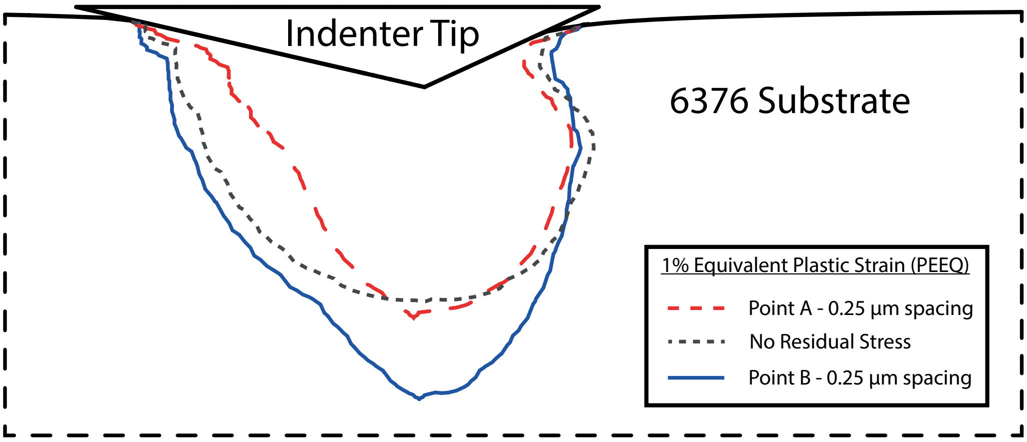
Indenter Tip
6376 Substrate
1% Equivalent Plastic Strain (PEEQ)
Point A - 0.25 µm spacing
No Residual Stress
Point B - 0.25 µm spacing

Figure 4.16: The 1% equivalent plastic strain (PEEQ) boundary for the non-prestressed substrate and the stress states at point A and point B for 0.25 µm inter-fibre spacing

4.4 Concluding remarks

The effect of the residual stress states that exist in the HTA/6376 carbon-fibre composite microstructure following cure on nanoindentation testing of the matrix constituent has been fully characterised using a finite element approach. An important comparison can be made between the trends determined in this numerical analysis and those previously reported from experimental observations. The results indicate an apparent decrease in hardness of the matrix pockets with the existence of residual stress due to the presence of equibiaxial tension following thermal cool-down. Previous experimental work carried out by Gregory and Spearing (2005) has reported an increase in the in situ hardness of the matrix in comparison with the bulk matrix material which is inverse to the trend reported in this numerical analysis. Thus, this experimentally reported change in in situ material behaviour cannot be attributed to the existence of residual stress in the in situ matrix material. While this reduction in hardness was somewhat expected due to the tensile nature of the residual stress in these regions, the quantitative reduction of the property is of interest. The existence of residual stress in these regions could in fact lead to underestimation of the true variation due to factors such as changes to the in situ polymer matrix cross-linking process during curing, and interfacial reactions with fibre treatments. This underestimation is more likely to occur when comparing bulk and in situ material, as opposed to comparing different in situ microstructural regions.

The effect of residual stress in the interfacial region on measured nanoindentation parameters is more complex due to the varying stress states that exist in these regions post-cure. The effect of these stress states on the nanoindentation parameters has been shown to be highly dependent on the position of the indentation around the circumference relative to the surrounding microstructural topology. For the vast majority of interfacial region stress states considered in this analysis, the hardness decreased as a result of the residual stress. The only cases that lead to an increase in indentation hardness was at the point of interest A for very small inter-fibre spacings (≤ 0.5 µm). As this point of interest is located between fibres at the point of minimal inter-fibre spacings, it is highly unlikely that these regions would be considered suitable for experimental grid indentations due to other experimental problems such as fibre-matrix relief (Khanna et al., 2003b) and the sub-surface fibre constraint effects investigated in Chapter 3. Importantly, the results show that the potential for the large compressive residual stresses present at the fibre-matrix interface to increase the indentation properties is nullified by perpendicularly acting tensile stresses in these regions. Thus, similar to the matrix pocket results, there is a potential for hardness of the interfacial regions (or 'interphase' material) to be underestimated due to dominant tensile stress which exists in the majority of experimentally suitable interfacial regions. These underestimations of the hardness property occur whether the contact area is inferred using the Oliver and Pharr analysis, or directly from the simulation's contact.

While the trends for the hardness property show it to be sensitive to the existence of residual stress in the substrate, as highlighted by the observed change in subsurface plastic strain fields, it was found that the indentation modulus was largely insensitive to the state of residual stress in the substrate. This property only varied by a maximum of 2.2% for the stress states investigated. Therefore, the indentation modulus is the recommended indentation property to be determined when carrying out a comparative parametric analysis between microstructural regions which are affected by the existence of thermal residual stress. The use of the hardness property for comparative investigations of this nature may add some unnecessary bias or variation to the already problematic scatter associated with experimental nanoindentation. The methodology outlined in this chapter could be used to characterise residual stress effects of other composite materials, and identify the microstructural regions where the effects are negated and allow the true stress-independent constituent properties to be determined using the standard nanoindentation testing protocols.

5 Experimental Nanoindentation of Fibrous Composite Microstructures

5.1 Introduction

In order to predict microscopic damage accumulation and its effect on the macroscopic structure, multiscale modelling approaches have emerged that enable detailed predictions of local deformation mechanisms in fibrous composite materials. Such studies have shown that the load-bearing capacity and failure behaviour of fibrous composite materials are governed by the local microstructure and in situ constituent material properties (Vaughan and McCarthy, 2011*a*,*b*; Totry et al., 2008; Llorca et al., 2011). While such models have provided insight into the role of the material microstructure on physical properties at higher length scales, the vast majority have assumed that the behaviour of individual constituents are equivalent to those in bulk form. However, the high-temperature curing process associated with composite manufacture leads to intensive thermal, mechanical and chemical processes taking place during the consolidation of the constituent phases. This could lead to significant variations in the mechanical properties in the small matrix pockets of high volume fraction composite materials, and close to fibre-matrix interfaces (Gregory and Spearing, 2005; Gao and Mäder, 2002). Nanoindentation is an extremely useful technique for determining the hardness and Young's modulus of extremely small localised regions and is ideally suited for the determination of the in situ mechanical properties of fibrous composites. It has been shown that the characterisation of in situ composite matrix material is not trivial due to the effect of the surrounding fibre constraint, which was examined in Chapter 3. While the effects of fibre constraint may be avoided in experiments by using shallow indentation depths in the order of tens of nanometres (Lee et al., 2007; Hodzic et al., 2000), evaluating mechanical properties at such a small length scale presents its own difficulties, as results are highly sensitive to factors such as tip blunting, surface roughness and size-scale effects (Tranchida et al., 2007; Tatiraju et al., 2008; Tho et al., 2006; Voyiadjis and Peters, 2010; Han, 2010). It has proved difficult to find the correct balance between these potential sources of error when carrying out indentations on the matrix constituent of fibrous composites. It is possible that large differences could exist between the in situ and bulk properties within highly confined matrix regions, but characterising such effects to determine local material properties requires that mechanical constraint be effectively decoupled from the indentation response. Recent advances in experimental techniques and more precise characterisation of material responses at shallow penetration depths, in combination with FE models of the indentation process provide a framework to accurately characterise the in situ mechanical properties of high volume fraction composites.

In this chapter, an experimental investigation of the microscale properties of the HTA/6376 composite material is carried out using the nanoindentation technique. A unique specimen preparation procedure which facilitates micromechanical characterisation using the nanoindentation technique has been developed and is described. The resulting microstructure has been analysed using optical and scanning probe microscopy to determine the suitability of the samples for indentation studies. Express test property mapping was used to determine a general overview of the microscale properties of the composite material. The continuous stiffness measurement (CSM) technique was then used to indent a large number of in situ resin pockets over a wide range of pocket sizes. This allowed the effect of the neighbouring fibre constraint on the nanoindentation experiments to be characterised experimentally and the results are compared with those from the previous finite element investigation of Chapter 3. Once this effect has been characterised, the unconstrained in situ matrix properties are compared with the properties determined from nanoindentation tests carried out on the bulk resin. The influence of resin pocket size of the in situ indentation modulus has also been investigated.

5.2 Sample preparation

5.2.1 Lay-up and curing process

The HTA/6376 composite material was manufactured by laying up prepreg material which was supplied on a roll from suppliers Hexcel. Each composite ply was approximately 0.125 mm thick and all the composite plies were oriented unidirectionally. The composite lay-up process was carried out in a dedicated clean room in accordance with ASTM standard D5687 / D5687M - 95. In order to make comparisons between the bulk 6376 epoxy and the material in situ, bulk 6376 resin was also supplied by the composite supplier Hexcel. The bulk uncured resin was supplied on a roll in thin film form. The resin was coated onto backing paper at nominally 72 g/m^2, making the film approximately 0.05 mm in thickness. The material was made bulk by cutting segments from the roll and laying up in the normal manner associated with composite prepreg materials. For the nanoindentation tests, a composite/epoxy 'hybrid' specimen was cured by consolidating the bulk 6376 resin material on top of a unidirectional composite HTA/6376 lay-up. Firstly, a unidirectional HTA/6376 composite panel measuring 80 x 50 x 1 mm was laid up following a $[0]_8$ lay-up sequence. Roughly 2 mm of bulk uncured 6376 resin (i.e. 40 layers of the supplied film) was then laid up on top of the composite lay-up as illustrated in Figure 5.1. The resin was applied on top to allow easier degassing of the bulk material to occur during curing.

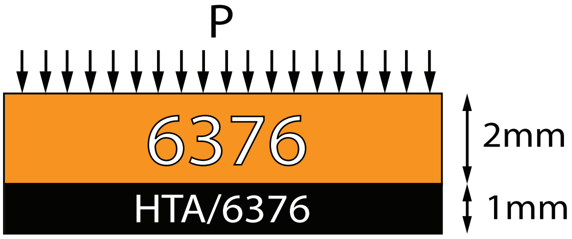

Figure 5.1: Schematic of lay-up applied to create 'hybrid' samples

Adjustments had to be made to the bagging procedure such that resin did not flow over the tool plate in the autoclave and to ensure that the air trapped in the bulk resin region of the panels (due to the awkward process of laying up thin films of material) was degassed from the samples during the curing cycle. A schematic of the modified bagging arrangement is shown in Figure 5.2. The plaque was contained within a released aluminium frame in order to prevent the resin flowing across the tool while in its molten state. The inner dimensions of the frame were 80 x 50 x 3 mm. A layer of glass-fibre bleeder was inserted just above the resin plaque to give air being degassed from the resin a path to the vacuum port while also stopping the flow of resin over the top of the aluminium frame by absorbing a finite amount of resin. Other attempts to simultaneously cure and degas the resin using regular and vacuum ovens were tested, however these led to extremely porous cured bulk resin regions.

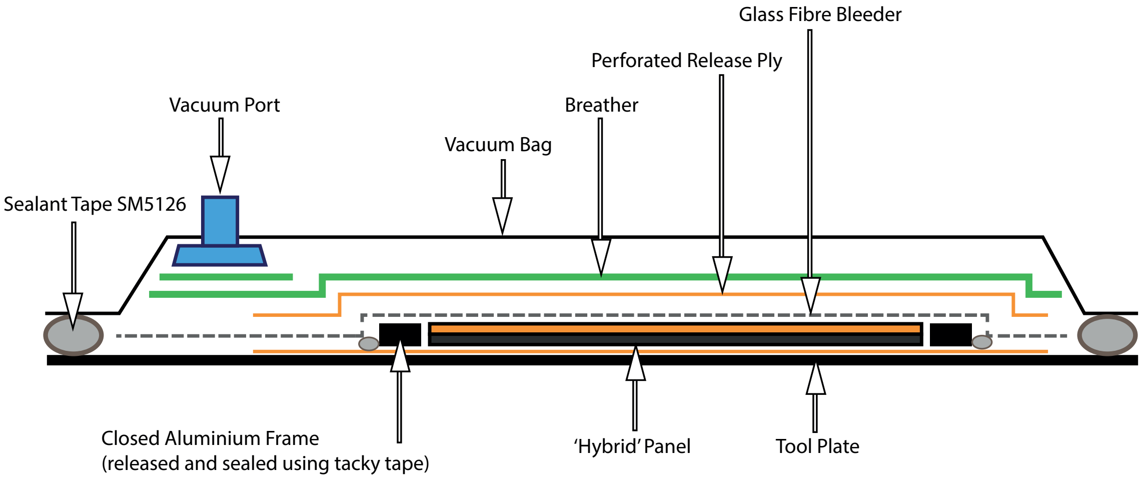

Figure 5.2: Schematic of the bagging arrangement used to cure the hybrid panels in the autoclave

The bagged up lay-ups were cured in an LBBC TC1000THPT Thermoclave system, shown in Figure 5.3. The hybrid plaques were cured in the vacuum-assisted process where the plaques were heated at 2 °C/min and consolidated for two hours at 175 °C. The panels were then cooled down to room temperature at 2 °C/min. A maximum pressure of 0.7 MPa was applied by the thermoclave for the duration of curing, with pressure ramping rates of 0.1 kPa/min applied at the start and end of the curing cycle. The autoclave method of simultaneous composite and bulk matrix curing was deemed the most successful, with only a small number of voids forming in the bulk matrix material due to trapped air during curing. The voids accumulated near the top surface and could be easily removed during the subsequent grinding and polishing processes. The autoclave process also allowed greater control over the curing temperatures and pressures, while also insuring that the curing process was identical for both the composite and the bulk matrix. This facilitated the best experimental comparison between bulk and in situ properties. Small pieces measuring roughly 15 x 10 x 3 mm were cut from the hybrid plaques using a dedicated composite diamond coated cutting wheel. These small samples were then mounted in 31.75 mm (1.25") diameter clear epoxy cylinders with the fibre direction facing toward the top face of the cylinder. An example of the mounted specimen is shown in Figure 5.4. The cured bulk 6376 resin had an orange colour as opposed to the black colour of the HTA/6376 composite.

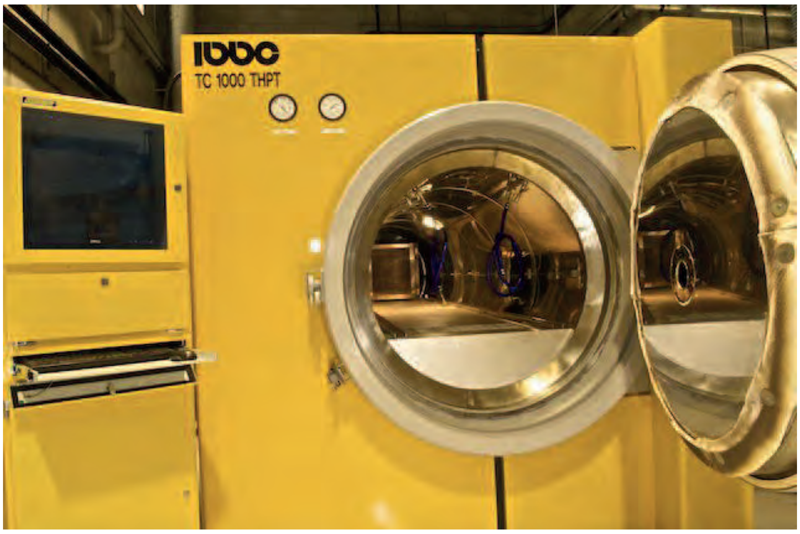

Figure 5.3: LBBC TC1000HTPT Thermoclave

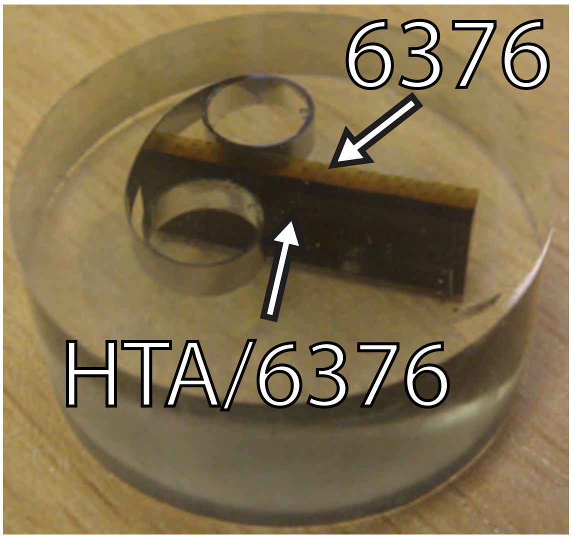

Figure 5.4: Hybrid samples mounted in clear epoxy

5.2.2 Surface preparation

In order to obtain consistent reliable data from nanoindentation experiments, the roughness of the substrate sample surface must be minimized at the scale at which the measurements are taken. The general rule of thumb is that the surface roughness should be no more than 5% of the depth at which results are required

(Agilent, 2009). This is especially important for the characterisation of composite constituents as shallow indentations are often required in order to minimize the effects of the neighbouring constituents. In order to reduce the surface roughness of the specimens, grinding and polishing procedures were carried out on the specimens using the Buehler Phoenix 4000 sample preparation system shown in Fig. 5.5. As there is no standard procedure for the surface preparation of composite specimens for nanoindentation experiments, the procedures devised were based on the ASTM standard E3-11, which deals with the preparation of metallographic specimens (ASTM, 2011). All the necessary consumables for polishing were supplied by Buehler.

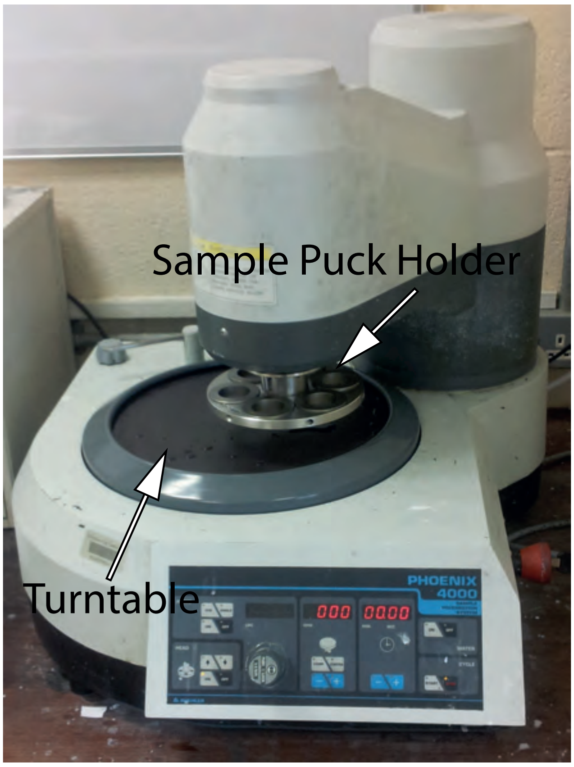

Figure 5.5: Buehler Phoenix 4000 sample preparation system

Initially, lower grit SiC paper was used in order to remove the layer of epoxy between the sample and the platen, and to plane the cylindrical sample surface. This is followed by further grinding stages with incrementally finer grades of SiC paper. Following the grinding stages, the specimens were polished using a combination of diamond and alumina polishing suspensions on a cloth surface. The effect of two surface preparation procedures are outlined below. The first surface preparation procedure (A) is outlined in Table 5.1. This procedure utilised high individual specimen loads with diamond suspensions, and was previously used to prepare samples of the HTA/6376 composite for microscopy studies (Vaughan and McCarthy, 2010). The second procedure (B) is outlined in Table 5.2. This procedure is notably less aggressive than procedure A, where the specimen loads and platen rotational speeds have been reduced, and the time on the aggressive SiC paper grinding stages has also been limited to 45 seconds for each grinding stage. The Microcloth surface was replaced by TexMet C cloth in an effort to reduce the difference in height (relief) between the fibre and matrix constituents based on communications with consumable suppliers Buehler (Mike Keeble, 2013). The samples were quickly rinsed with water between each grinding/polishing stage and lubricants and suspensions with a neutral pH value were chosen in order to minimize any reaction between the polishing agents and the constituent materials.

Table 5.1: Sample Preparation Procedure A

Surface	Lubricant Extender	Time (min:sec)	Force per Specimen (lbs)	Speed (RPM)	Relative Motion
SiC - P240	Water	Until Plane	25	250	Contra
SiC - P600	Water	2:00	25	250	Contra
SiC - P1200	Water	2:00	25	200	Contra
Microcloth	Diamond Suspension 6 µm	5:00	25	200	Comp
Microcloth	Diamond Suspension 1 µm	5:00	20	200	Comp
Microcloth	Alumina Suspension 0.05 µm	02:00	15	150	Comp

5.2.3 Resulting microstructure

Both sample preparation methods produced very clear micrographs of the composite microstructure. The microstructure of the hybrid samples near the composite/epoxy interface is shown in Figure 5.6. Interestingly, there are now distinct

Table 5.2: Sample Preparation Procedure B

Surface	Lubricant Extender	Time (min:sec)	Force per Specimen (lbs)	Speed (RPM)	Relative Motion
SiC - P240	Water	0:45	5	200	Comp
SiC - P600	Water	0:45	5	200	Comp
SiC - P1200	Water	0:45	5	150	Comp
TexMet C	Alumina Suspension 0.3 µm	5:00	4	150	Contra
TexMet C	Alumina Suspension 0.05 µm	5:00	3	150	Contra

regions within the microstructure. At the top of Figure 5.6, there is the bulk resin region which contains no fibres. It can also been seen that no bubbles or voids have formed at the microscale, which were prominent at the macroscale during the preliminary attempts of curing the bulk resin material. The high fibre volume-fraction region of the sample is shown at the bottom of Figure 5.6, where there are very few large resin pockets due to the high fibre volume fraction of the HTA/6376 composite material. In the middle region of the micrograph, there is a region of matrix containing fibres which have migrated into the resin region during the curing process. This region contains fibre arrangements of varying density which produces resin pockets of many different sizes and a number of fibres which are completely isolated from the rest of the composite microstructure. This region of the microstructure makes the hybrid specimens advantageous for indentation studies. The specimens greatly increase the range of the matrix pocket sizes which can be studied and ensures that both the bulk and in situ matrix material have undergone identical curing conditions. The specimens also allow for experimental comparison to be carried out between indentations which were positioned just micrometres apart. This allows the indentations to be carried out in the same sample holder which ensures that the calibrated machine compliance remains constant for the bulk and in situ indentations.

Surface roughness measurements of the bulk matrix regions of the samples were carried out using an Atomic Force Microscope (AFM) and Scanning Probe

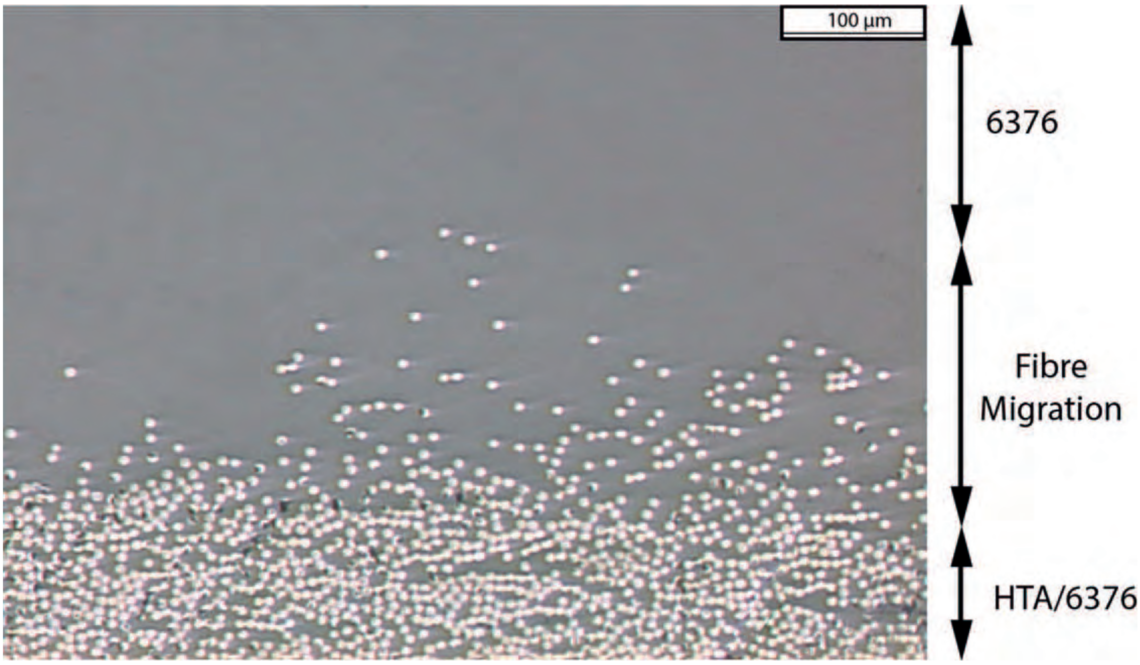

Figure 5.6: Resulting microstructure of the hybrid sample at the composite/epoxy interface

Microscopy (SPM) using the indenter tip in order to determine if the resulting surface was suitable for nanoindentation studies. The AFM measurements were carried out using an Agilent 5500 AFM. Two separate 10×10 µm areas of the bulk matrix surface were scanned in contact mode, one of which is shown in Fig. 5.7a. Two 50×50 µm areas of the bulk matrix surface were then scanned in tapping mode, one of which is shown in Fig. 5.7b. The mean surface roughness (R_a) measured from the AFM scans was 2.2 ± 0.6 nm. The Berkovich tip of the nanoindenter was also used to measure the surface roughness of the matrix material following sample preparation. The Agilent G200 nanoindenter system includes a closed-loop nanopositioning stage with a resolution of 0.5 nm, known as the Nanovision stage. This stage generates surface images by raster scanning the sample beneath the indenter tip, and applying a small contact force to the surface. Three separate 50×50 µm areas of the bulk matrix were scanned using a scanning force of 1 mN, one of which is shown in Fig. 5.7c. The mean surface roughness (R_a) measured using this data was 2.9 ± 0.3 nm. Similar values of surface roughness were measured for both surface preparation procedures and the surfaces were deemed sufficient for nanoindentation experiments.

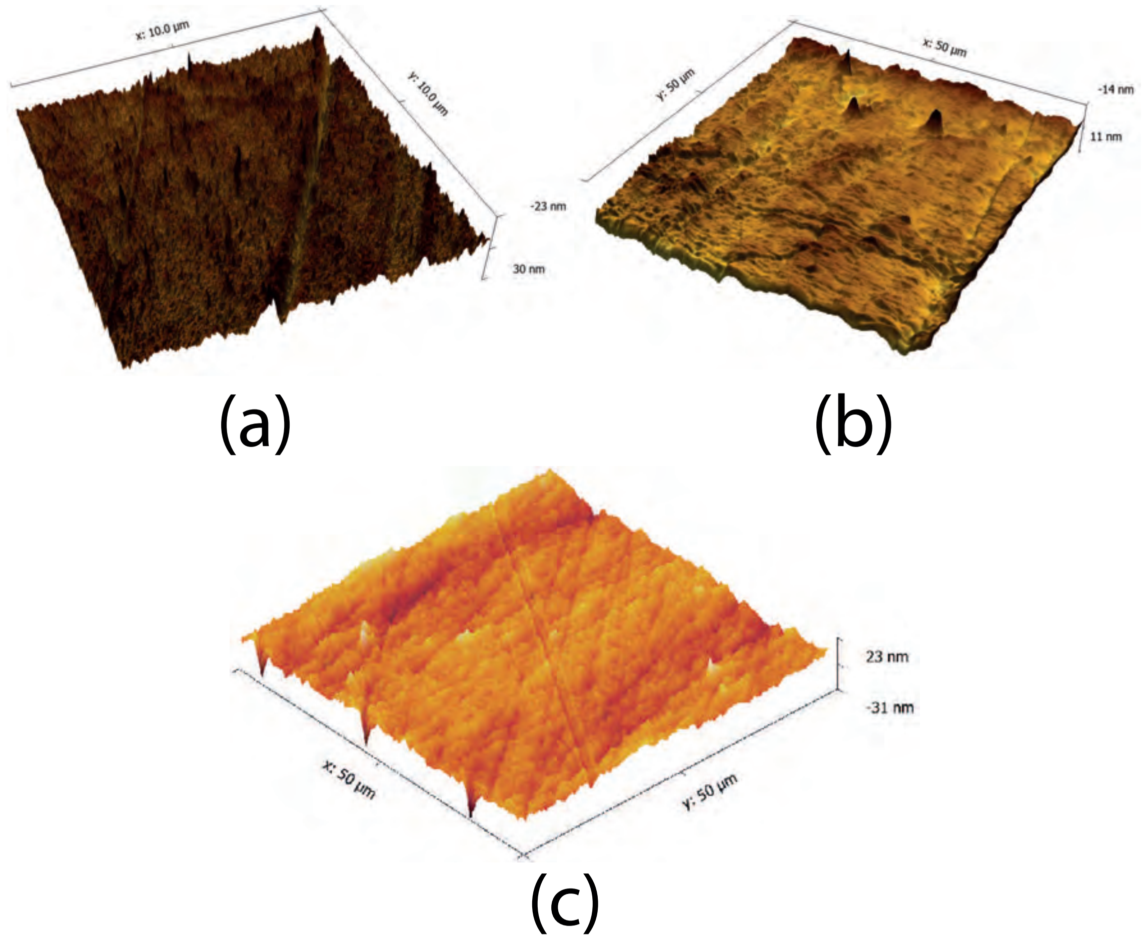

Figure 5.7: SPM scans of bulk matrix region (a) 10×10 µm area contact mode AFM scan, (b) 50×50 µm area tapping mode AFM scan and (c) 50×50 µm area scanned using Berkovich indenter tip and Nanovision stage

While the different surface preparation procedures did not impact significantly on the optical microscopy or matrix region roughness of the samples, the same could not be said for the composite regions of the sample. Figs 5.8a and 5.8b show 3D nanovision scans of the composite regions of the sample prepared using surface preparation procedure A. A cube corner indenter tip geometry was used to carry out the scans due to the added sharpness of this geometry compared to the Berkovich tip. Fig. 5.8a shows a scan of a region with a high density fibre distribution, while Fig. 5.8b shows a scan of an isolated fibre. The surface of the fibres show clear evidence of damage due to the use of diamond suspensions as part of this procedure. This also leads to divots in the matrix pockets which adversely affects the ability of

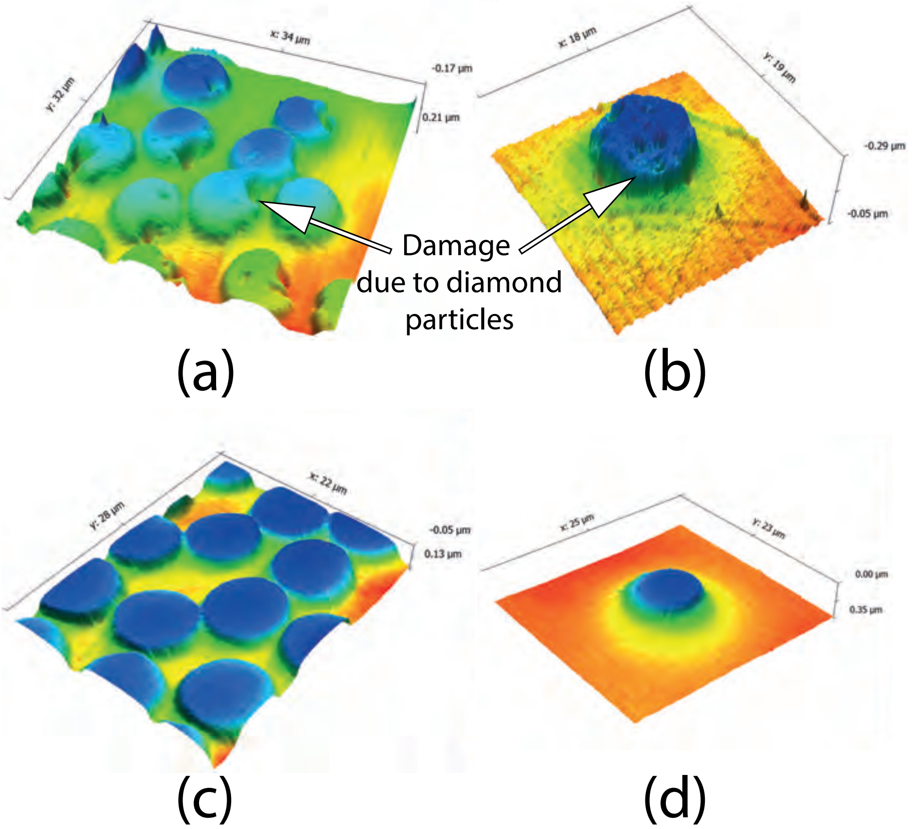
x: 34 µm
y: 32 µm
-0.17 µm
0.21 µm
x: 18 µm
y: 19 µm
-0.29 µm
-0.05 µm
Damage
due to diamond
particles
(a)
(b)
y: 28 µm
x: 22 µm
-0.05 µm
0.13 µm
x: 25 µm
y: 23 µm
0.00 µm
0.35 µm
(c)
(d)

Figure 5.8: 3D scan of composite regions, (a) high fibre volume region following surface preparation procedure A, (b) isolated fibre following surface preparation procedure A, (c) high fibre volume region following surface preparation procedure B, (d) isolated fibre following surface preparation procedure B

the nanoindentation method to characterise these regions accurately. The effects of preparation procedure B on the resulting microstructure is shown in Figs. 5.8c and 5.8d for the high density fibre distribution and isolated fibre regions, respectively. A clear improvement in surface quality can be seen using this procedure, where the fibre's circular shape remains intact and no significant damage visible on the surface of either constituent.

An important aspect of the resulting scans is the clear difference in height that exists between the fibre and matrix constituents following surface preparation. While this fibre-matrix relief is lessened by the less aggressive procedure and use of TexMet C cloths as part of procedure B, there still exists a significant height difference between the constituents as highlighted in Figs. 5.8c and 5.8d. The relief between the fibre and matrix is larger for the case with the isolated fibre, measuring approximately 300 nm, while the relief is reduced to 150 nm the regions with a high density of fibres. While the size of the relief is relatively small in comparison to the mean fibre diameter (6.6 µm), its effect on accurate microscale characterisation of the fibrous composite microstructure using the nanoindentation technique is considerable. The use of the indentation methods to characterise the 'interphase' region which surrounds the fibre-matrix interface is greatly affected. A simple analysis of the indentation geometry indicates that the thickness of material surrounding the fibre (th) which cannot be characterised by a conical or pyramidal indentation without contact between the indenter tip and fibre material is given by:

$$th = (R_{FM} + h_{max}) \tan \alpha \tag{5.1}$$

where R_{FM} is the fibre-matrix relief, h_{max} is the maximum indentation depth and α is the half-angle of the indenter. Consider the case of a Berkovich indentation with the flat side of the tip aligned closest to the fibre-matrix interface ($\alpha = 65.27°$), the lower detected fibre-matrix relief of 150 nm, and an extremely low indentation depth of just 50 nm. Even for this advantageous experimental scenario, the thickness of the material surrounding the fibre-matrix interface which cannot be indented without contact between the indenter and the fibre is 434 nm. The reported widths of the interphase region for CFRP materials measured using AFM phase imaging and Transmission Electron Microscopy (TEM) are in the order of 100–500 nm (Gu et al., 2010; Cech et al., 2013; Wu et al., 2014). Therefore, the measured fibre-matrix relief following surface preparation, combined with the effects of the sub-surface fibre-constraint characterised in Chapter 3, suggests an inherent difficulty when attempting to quantitatively determine the interphase properties of CFRP materials experimentally using the nanoindentation testing.

5.3 Testing and analysis procedures

The indentation experiments were carried out using a Nanoindenter G200 supplied by Agilent Technologies. The G200 is the updated version of the Nano

Indenter XP machine produced by MTS instruments. The G200 uses a Nanomechanical Actuating Transducer (NMAT) to apply loads and measure displacements during nanoindentation tests. The load and displacement resolutions are 50 nN and 0.01 nm respectively. A schematic showing the inner workings of the G200 is shown in Figure 5.9. The load is controlled by electromagnetic actuation and the displacement is measured using a capacitance gauge. The indenter shaft is held stiff by two leaf springs which ensure that there is no movement across the sample surface during indentation. The machine is capable of Continuous Stiffness Measurement (CSM) which allows measurement of the contact stiffness continuously throughout the indentation loading and not just at the point of initial unload. This continuous measure of contact stiffness allows the indentation hardness and modulus to be measured as a function of depth from a single indentation.

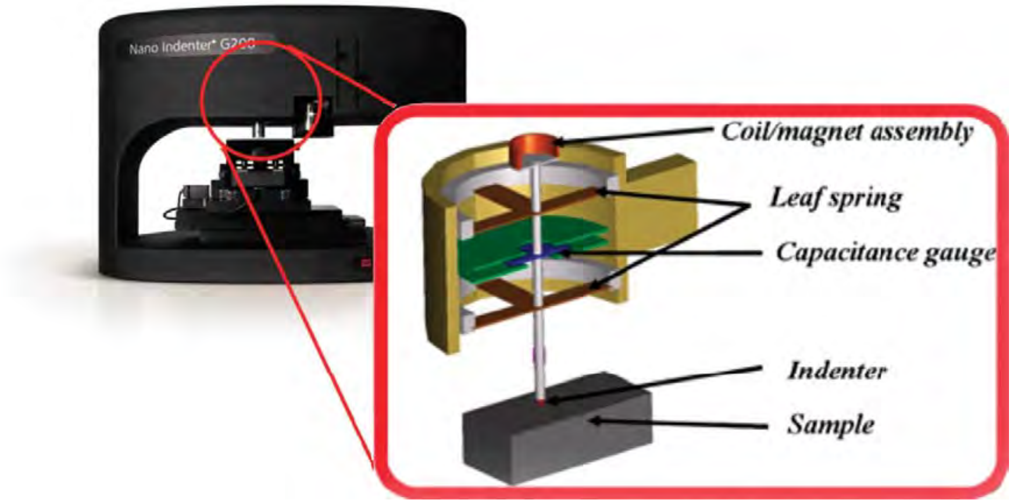

Figure 5.9: The Agilent Nano Indenter G200 and a cross-sectional diagram of the XP-NMAT (Agilent, 2009).

5.3.1 Express test property mapping[1]

In order to provide a general overview of the microscale properties of the HTA/6376 composite, the Express Test option of the Nanoindenter G200 was used. This method carries out an array of very fast (<2 s) shallow indentations in order to determine a high resolution map of the hardness and modulus properties of the sample surface. A DCM-II head was used in combination with a Nanovision stage to ensure the best accuracy and resolution of the resulting quantitative property maps. An area of the HTA/6376 composite microstructure surface measuring 12 × 12 µm was mapped using an array of 30 × 30 indentations. The maximum indentation depth target was set to 50 nm and the 900 indentations took approximately 28 minutes to complete. The region of microstructure mapped using the express tests is shown in Fig. 5.10.

---

[1] The express tests were carried out at Agilent Technologies in Frankfurt Germany, with the assistance of Dr. Holger Pfaff

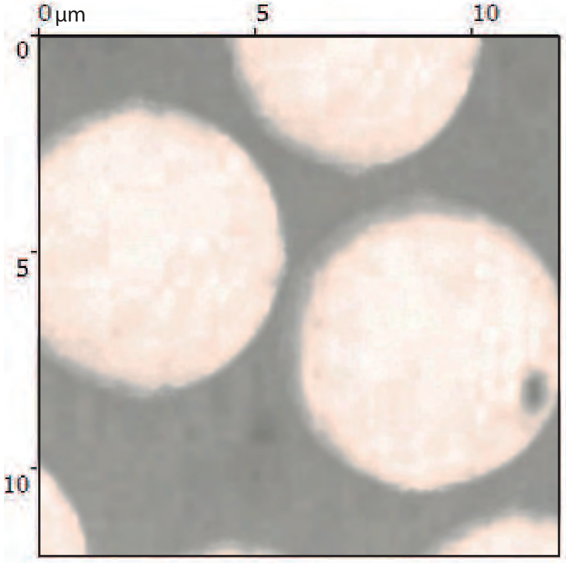

Figure 5.10: Micrograph of the 12 × 12 µm region of microstructure mapped using express testing

5.3.2 Characterisation of bulk 6376

In order to characterise the bulk 6376 epoxy material, indentation experiments were carried out into the bulk matrix regions of the hybrid specimens using both the unloading curve analysis (basic mode) and the dynamic CSM technique. Basic indentations were carried out to four different target indentation depths, namely, 250 nm, 500 nm, 1 µm and 2 µm, with a Berkovich indenter tip. A total of 30 indentations were carried out for each target depth. The indentation sites were targeted using an optical microscope and the spacing used between the indentations was equal to 50 times the maximum indentation depth to ensure no overlapping of deformation regions from neighbouring indentations. The indentations were positioned far from the composite and fibre migration sites of the hybrid specimens to ensure there was no influence from the composite on the bulk matrix indentations. The default settings of the G200 were used, which included a constant load hold segment at the maximum load of 10 seconds, and an indentation strain-rate target of 0.05 /s. The target strain rate was reached with a maximum deviation of ±0.01 /s for all depths deeper than 100 nm. Another 30 indentations were carried out into the bulk resin with the same settings using the CSM mode of the G200. The CSM indentations were assigned a maximum target displacement of 2 µm, and were programmed to apply a harmonic displacement of 2 nm and a frequency of 45 Hz.

5.3.3 Characterisation of in situ 6376

The hybrid specimens were also used to carry out nanoindentation tests on the in situ 6376 matrix material. To ensure comparability, the same nanoindentation CSM settings and Berkovich tip were used for both for the in situ resin pockets and bulk 6376 matrix. In total, 50 indentations were carried out into matrix pockets surrounded by fibres within the hybrid specimens. Matrix pockets which were surrounded by a circular array of fibres were preferred in order to make the experimental indentation results comparable to the previous finite element results from Chapter 3. The fibre migration regions of the hybrid specimens allowed for a wide variety of in situ resin pocket sizes to be indented. The radii of the 50 indented matrix pockets ranged from 3.86 to 23.9 µm. The indentations were located at the centre of the matrix pockets as the finite element models show that the stress field beneath the indenter is axisymmetric even though the Berkovich tip geometry is not. The CSM technique was again used when carrying out the indentations to highlight any change in mechanical properties with indentation depth.

5.4 Results and discussion

5.4.1 Express test results

The resulting indentation hardness and modulus property maps for the express tests are shown in Figs. 5.11a and 5.11b respectively. The distinct circular shapes of the fibre regions are obvious in these figures, as well as more compliant surrounding matrix regions. While there is a clear difference in mean properties of each of the constituent materials, the scatter in each region is relatively high. The quantitative property maps also reveal clear property gradients around the fibre-matrix interfaces which are observed as rings around the fibres measuring approximately 0.55 µm and 0.92 µm for the indentation hardness and modulus properties respectively.

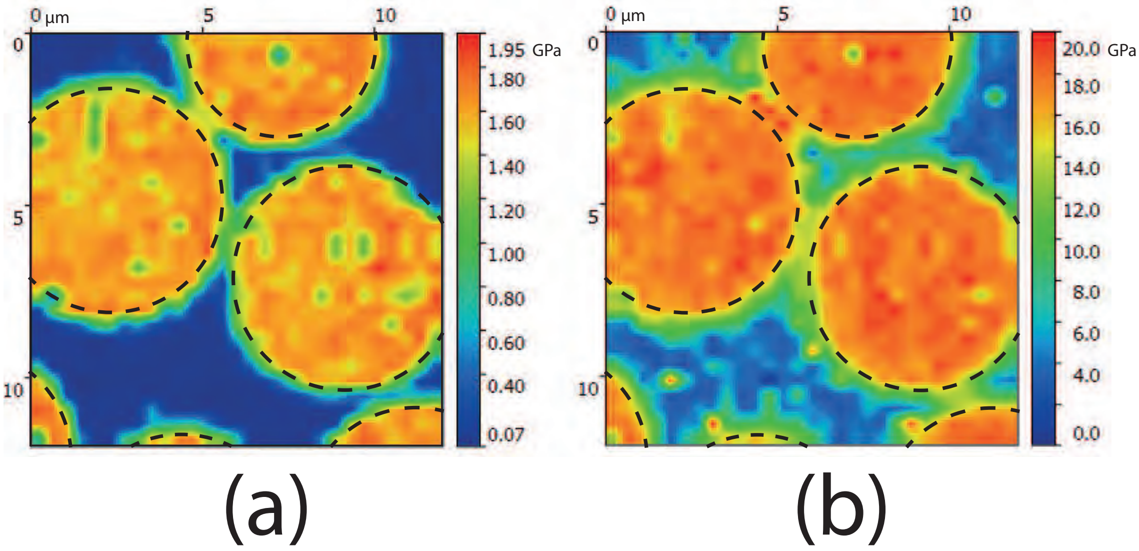

Figure 5.11: Express test quantitative property maps of indentation (a) hardness (b) modulus

While, the express tests provide a convenient quantitative map of the microstructural region of interest, the reliability of the measurements must be questioned. The low indentation depths (mean 52 nm) make the data susceptible to influence by indentation size effects and the fast indentation rate leads to relatively high scatter for the indentations carried out across each constituent. The high indentation rates also likely bias the matrix material data due to the inherent rate-dependence of the material. As shown in the finite element investigation of Chapter 3, the properties of the 'interphase' material can be overestimated by up 47% due to fibre constraint effects. The property gradients around the fibre matrix interfaces illustrated in Fig. 5.11 show that the measured properties of these regions increase by a greater magnitude than that likely to be due solely to fibre constraint effects. However, the post-preparation surface examination of Section 5.2.3 revealed significant fibre-matrix relief which shows that contact between the indenter and the fibre occurs if indentations are placed within at a few hundred nanometres of the fibre-matrix interface, even for very shallow indentations. This is the likely cause of the property gradient ‘rings’ around the fibres observed in Fig. 5.11.

5.4.2 Bulk 6376 matrix results

The load-displacement curves for the basic indentations are shown in Fig. 5.12a. The data for the 30 indentations carried out at each indentation depth is very consistent and reproducible as a result of the careful surface preparation processes. The maximum load reached by 2 µm target indentations only varies by 0.47 mN (27.15 to 27.62 mN) for all the indentations. Similar repeatability of measurements was observed for the CSM indentations. The use of the CSM technique allows the indentation modulus to be plotted against indenter displacement as shown in 5.12b for the 30 CSM indentations. The moduli calculated from the basic indentation tests have also been superimposed into Fig. 5.12b, where the calculated moduli from both methods show good agreement. For low values of indentation depth, there is significant scatter in the values for indentation modulus. As the indentations become deeper, the scatter converges and becomes relatively constant with indentation depth. The elastic modulus of the bulk material has been calculated by averaging data from the 30 CSM tests, using the data between the depths of 200 nm and 2 µm to minimize the effect of the low-depth scatter. The mean value of modulus for the bulk 6376 matrix material was calculated as 5.05 GPa with a standard deviation of 0.1 GPa.

As part of the Oliver and Pharr unloading curve analysis used for the basic indentations, Equation 5.2 is fit to the upper 50% (Agilent, 2013) of the unloading data measured from the indentation experiments:

$$P(h) = B\left(h - h_p\right)^m \tag{5.2}$$

where B, h_p and m are best fit constants. The application of this non-linear curve fitting procedure to the unloading data from indentations carried out on the 6376

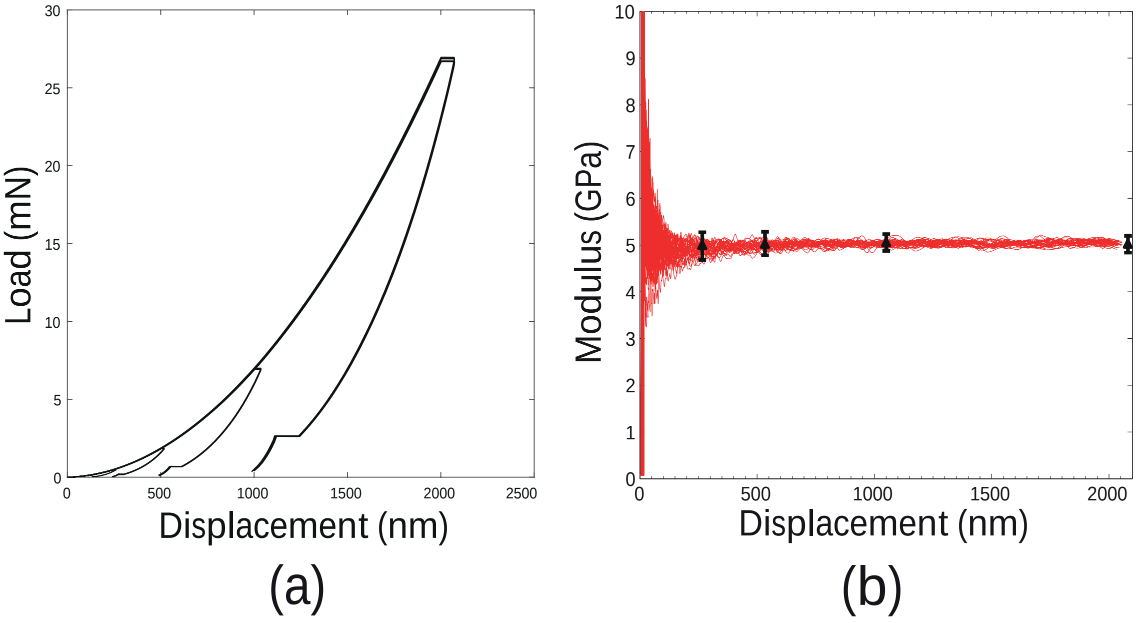

Figure 5.12: (a) Load displacement curves for 30 bulk 6376 matrix indentations (b) Young's modulus versus indentation depth for the basic and CSM indentations

epoxy resin proved to be problematic. The fits were found to be highly sensitive to the fitting constraints defined within the Matlab curve-fitting toolbox (Mathworks, 2010) used to apply the custom fits to the data. Poor fits to the data were produced if the fitting constraint weren't strictly defined. The startpoints and limits of the best fit constants B, h_p and m were varied to find the combination which consistently produced the best fits and indentation results. A parametrised load-displacement curve is shown in Fig. 5.13a, where the h_{SP} is the specified indentation depth target, h_{max} is the maximum measured indentation depth, h_{creep} is the amount of creep displacement which occurs during the maximum load hold segment and h_p represents the depth of the residual plastic impression left in the material after the indenter has been withdrawn from the specimen. The curve-fittings constraints which produced the best fits expressed in terms of these parameters are listed in Table 5.3. An example of a non-linear curve fit to the unloading data using these constraints is shown in Fig. 5.13b. A more detailed analysis of the non-linear curve-fitting procedure applied the bulk 6376 epoxy indentations is described in Chapter 6.

It is worth noting that the indentation moduli are significantly larger than the

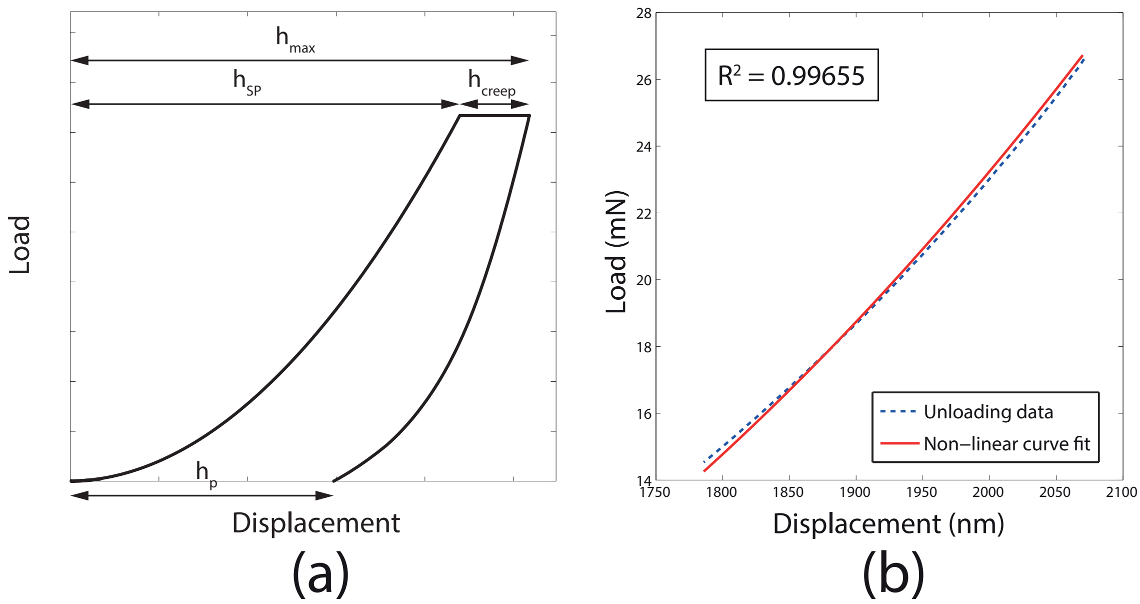

Figure 5.13: (a) Parametrised load-displacement curve (b) Resulting non-linear curve-fit

Table 5.3: The best choice of curve-fitting constraints for the best fit constants of the Oliver and Pharr non-linear curve-fit

Unknowns	StartPoint	Lower Limit	Upper Limit
B	0	0	5
h_p	$\frac{h_{SP}}{2} + h_{creep}$	0	h_{max}
m	2	0	Inf

value of elastic modulus taken from the 6376 data sheet (Hexcel, 2007) which was determined using conventional ISO 527-1 tensile testing of bulk epoxy material. The indentation modulus is approximately 40% greater than the expected value. This is a common observation in indentation testing of polymer materials (Tranchida et al., 2006; King et al., 2013). This error is often attributed to the viscous deformation associated of polymeric materials, pile-up of material around the indenter at maximum load and hydrostatic stress. These effects considered in more detail in Chapter 6. However, previous studies have examined the effects of temperature (Frontini et al., 2015), carbon nanotube composition (De Silva et al., 2013) and graphene platelet addition (King et al., 2013), on the tensile and indentation moduli of polymeric materials. In these comparative studies, the relative change in the tensile and indentation moduli values due to the investigated effects were similar, even if the quantitative values were different. As the bulk and in situ resins in this research are expected to be reasonably similar in nature, they are also assumed to have similar viscoelastic and pile-up properties for the purpose of this comparison. Therefore, a comparative study of the indentation moduli values determined using the Oliver and Pharr method for both in situ and bulk materials is still deemed valid.

5.4.3 Experimental investigation of fibre constraint

The mechanical constraining effect of the surrounding fibres was characterised using finite element models in Chapter 3. This study gave an insight into the subsurface stress transfer between the constituents when characterising matrix pockets using the nanoindentation technique and showed that the indentation modulus for the matrix material can be overestimated by up to 47% due to this phenomenon. The fibre constraint effect has also been characterised experimentally herein, by using the CSM data from the 50 indentations carried out into the resin pockets of the hybrid specimens. The pocket radii were measured after the indentations using the optical microscope of the G200 Nanoindenter at a magnification of 1000X. The pocket radius was measured from the point of initial indentation to the outer edges of the adjacent fibres. An example of a residual impression from an indentation in a matrix pocket is shown in Figure 5.14.

The CSM modulus data for 2 of the 50 indentations is compared with the CSM data for the 30 bulk resin indentations in Figure 5.15. For the lower depths, the values for in situ modulus remain relatively consistent with respect to depth. This is followed by a region of gradual increase in modulus values, with increasing indentation depth, due to the mechanical constraining effect of the surrounding fibres. At a certain point, the modulus increases rapidly due to the indenter coming in contact with one or more of the fibres that surround the indentation area. These observations are consistent for all the matrix pocket indentations, with the phenomena occurring at different indentation depths depending on the radius of the matrix pocket.

In order to characterise the effect of fibre constraint on the CSM modulus data from different matrix pocket sizes, the concept of a ‘fibre constraint factor’ is

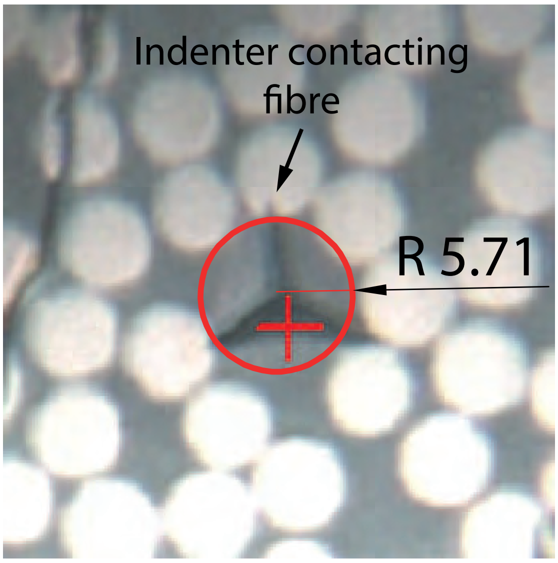

Figure 5.14: Optical microscope image (1000X) of a residual impression from an indentation carried out into a matrix pocket with a radius of 5.71 µm

introduced. The fibre constraint factor (FCF) at any point in the indentation has been defined as the radius of the matrix pocket being indented (R_p) divided by the instantaneous indentation depth (h) in Equation 5.3.

$$FCF = \frac{R_p}{h} \tag{5.3}$$

The FCF has been calculated using the CSM curves for each indentation by applying Equation 5.3 to each data point. The modulus data from the CSM plots was normalised by dividing it by the unconstrained value of modulus (E_{un}). The unconstrained modulus values were the values extracted from the CSM data at the unconstrained depth (h_{un}). From the finite element results of Chapter 3, it was determined that the indentations remain relatively unconstrained ($\frac{E}{E_{un}} < 1.05$) when the fibre constraint factor is approximately 20 or greater when a Berkovich tip is used. This value was indicative of the initiation of significant subsurface stress transfer across the fibre-matrix interface for the HTA/6376 material system. This implies, from Equation 5.3, that the unconstrained indentation depth is equal to the pocket radius divided by 20.

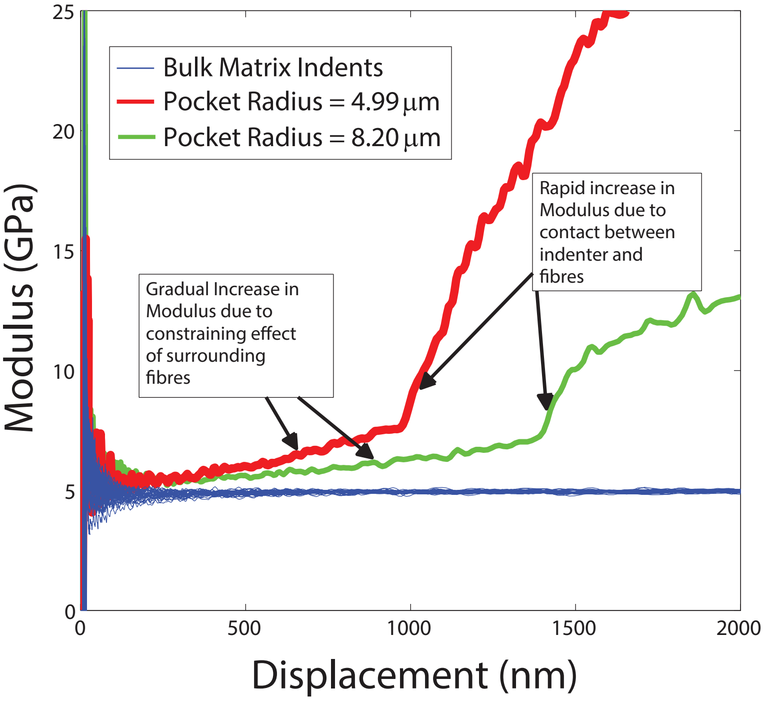

Figure 5.15: Modulus versus indenter displacement data for indentations into bulk 6376 resin and two resin pockets determined using the CSM Nanoindentation technique

$$h_{un} = \frac{R_p}{20} \tag{5.4}$$

The unconstrained indentation depth (h_{un}) has been calculated for each in situ indentation using Equation 5.4 once the pocket radius had been determined post-hoc. By applying these calculations to the CSM data, the fibre constraint effect on CSM data from indentations carried out in matrix pockets of varying size could be investigated. Figure 5.16 shows the normalised modulus values plotted against the fibre constraint factor for all 50 indentations carried out into the matrix pockets. The data for the 50 indentations converges nicely when the data is analysed in this way, with three regions of interest: (i) For large values of FCF there is some scatter in the data, which is caused by the experimental scatter observed at very low indentation depths (Figure 5.15) becoming significant for indentations carried out into the smaller-sized matrix pockets. As there is little or no fibre constraint at high values of fibre constraint factor, this scatter is not significant for this investigation. (ii) A gradual increase in the normalised modulus values is observed for all the indentations as the fibre constraint factor decreases. This is caused by mechanical constraint of the surrounding fibres which becomes more prevalent as the fibre constraint factor decreases. (iii) Following this gradual increase in normalised modulus, a rapid increase in normalised modulus is observed for a number of indentations for the lower values of FCF. This is due to the indenter tip contacting one or more of the neighbouring fibres while indenting to the maximum depth of 2 µm. The impression made by a Berkovich indenter at the maximum indentation depth of 2 µm will extend 6-9 µm out from the initial point of contact, depending on the orientation of the tip. Therefore, any indentations carried out into pockets of this radius size or smaller are likely to have contact between the indenter tip and the fibres as is clearly visible in the micrograph of Figure 5.14. The scatter observed for values of FCF where this steep increase in normalised modulus is observed is most likely due to the matrix pockets not being perfectly circular, the initial point of the indentations not being positioned directly at the centre of the pockets and the varying orientations of the Berkovich indenter tip relative to the closest neighbouring fibre.

The values of normalised modulus and FCF from the finite element investigation of Chapter 3 have also been superimposed onto Figure 5.16. The effect of the mechanical fibre constraint on the indentation modulus is similar for both the finite element models and the experimental CSM data. This is made evident in the middle portion of the figure where the gradual rates of increase in normalised modulus for the models and the experiments are very similar. The CSM experiments show that the indentation modulus of the matrix constituent can be increased by 40-50% by the neighbouring stiff fibre regions even when no contact has occurred between the indenter and the fibre material, and that care should be taken to avoid this phenomenon when attempting to determine accurate properties in these regions.

5.4.4 Bulk versus in situ matrix properties

Since the mechanical constraint effect of the fibres has been characterised both experimentally and numerically, the results can be used to investigate any real change in mechanical properties of the composite's matrix constituent following the

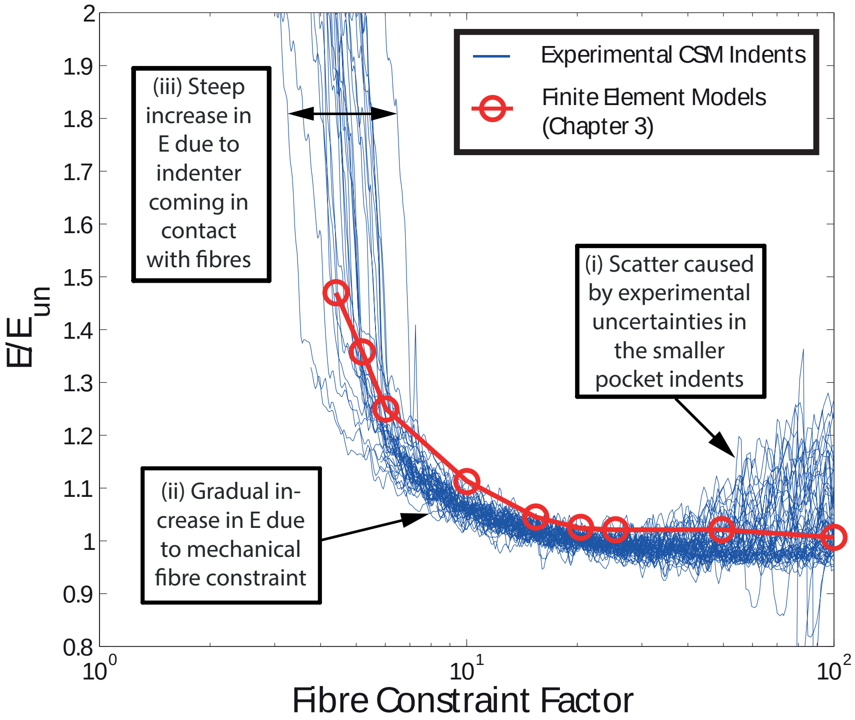

Figure 5.16: Normalised Modulus plotted against Fibre Constraint Factor (FCF) for all 50 pocket indentations and FE models

curing process, independently of this effect. The CSM technique can be used to determine the unconstrained modulus value for indentations constrained, or contacted by fibres, while approaching the maximum indentation depth. The unconstrained modulus (E_{un}) was determined from the CSM data at the unconstrained depth (h_{un}) that was defined using Equation 5.4. Once the unconstrained depth is known, the unconstrained value of modulus for the matrix in the pocket can be determined. The values of unconstrained modulus for the in situ indentations are plotted versus their corresponding matrix pocket radius values in Figure 5.17. The upper x-axis also indicates the unconstrained indentation depth at which the modulus values were measured. This is directly related to the radius of the matrix pocket by Equation 5.4. The unconstrained indentation depths for the 50 pockets ranged from 193-1265 nm.

The variation of the modulus with indentation depth for the 30 indentations carried out into bulk 6376 has been superimposed in Figure 5.17 to compare the in situ and bulk moduli over the range of indentation depths analysed for the in situ

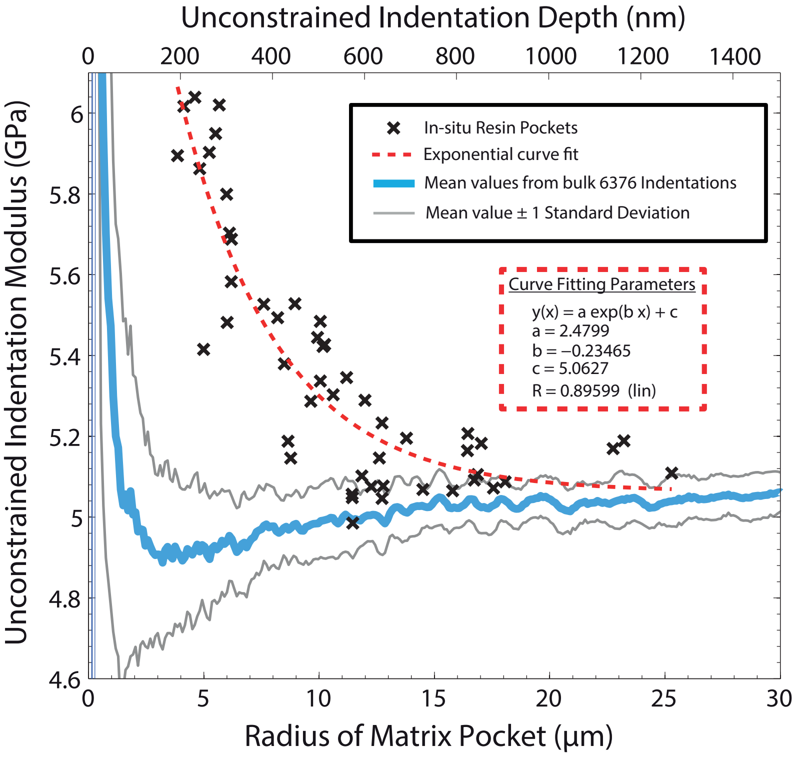

Figure 5.17: The unconstrained modulus for each matrix pocket indentation plotted versus the radius of the matrix pocket (lower x-axis) and the unconstrained depth of the indentation (upper x-axis). The bulk matrix mean and SD variance corresponding with the indentations depths on the upper x-axis are also shown.

indentations. For the larger matrix pockets (radius > 15 µm), the modulus values remain relatively constant and close to the mean value from the bulk 6376 indentations. The average indentation modulus in these large resin pockets is on average slightly larger than the mean value for the bulk resin material. For the smaller matrix pockets (radius < 15 µm), there is a clear increase in modulus with decreasing matrix pocket size. The curve fit added to Figure 5.17 shows that the modulus of the resin increases exponentially as the radius of the pocket decreases. The modulus is found to increase by up to 19% from that of the mean value determined for the bulk 6376 matrix.

Similarly, the values of the unconstrained hardness have been plotted against matrix pocket radii in Fig. 5.18. Unlike the values of in situ modulus, the values of hardness for the larger pockets (radius > 10 µm) are lower than that of the bulk matrix for the majority of in situ indentations. This is likely due to the existence of equibiaxial tensile residual stress in the matrix regions following thermal cooldown from the cure temperature. The reductions in hardness from that of the mean values for the bulk material are similar to the reductions predicted by the finite element models of Chapter 4, which characterised the effects of thermal residual stress on the calculated indentation properties. As the size of the matrix pockets get smaller, a similar to trend to that for modulus property is observed. An exponential increase in the hardness property is apparent as the pockets get smaller, with hardness increasing by up to 31% compared to that of the bulk 6376 material.

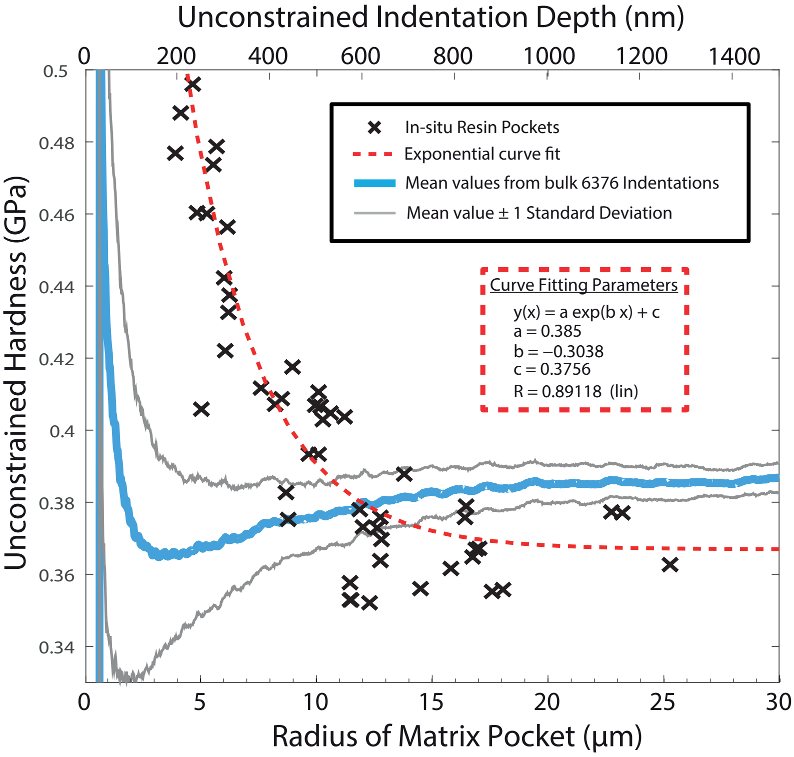

Figure 5.18: The unconstrained hardness for each matrix pocket indentation plotted versus the radius of the matrix pocket (lower x-axis) and the unconstrained depth of the indentation (upper x-axis). The bulk matrix mean and SD variance corresponding with the indentations depths on the upper x-axis are also shown.

The results suggest that the curing process has an effect on the in situ modulus and hardness of the composite's matrix constituent, causing a distinct increase in the properties compared to the material in its bulk form. The results also indicate that the magnitude of the property change is dependent on the distance of the matrix material to one or more fibre-matrix interfaces. The scatter in the data for indentations on pockets of similar size may be attributed to the assumption that all the pockets are perfectly circular, the indentations not being positioned directly at the centre of the pockets and varying densities of the fibre packing arrangements surrounding the matrix pockets.

5.4.5 Statistical analysis of nanoindentation results

Nanoindentation testing is notoriously susceptible to a large amount of experimental scatter, particularly at low indentation depths. Experimental factors such as tip blunting, poor tip area calibration procedures, insufficient sample preparation can all increase the experimental scatter in nanoindentation results. To determine whether the apparent property change observed in this study is significant and representative of a true change in the properties of the matrix material post-cure, a statistical analysis of the experimental scatter was carried out. The large number of indentations carried out in this study facilitates this analysis. The variation of the mean indentation modulus and hardness with depth from the 30 indentations carried out on the bulk 6376 matrix material are shown in Figs 5.17 and 5.18 respectively. The mean values are relatively consistent with indentation depth, except for extremely low indentation depths (<100nm). To illustrate the experimental scatter from the 30 bulk matrix indentations, the mean values ±1 Standard Deviation are also plotted against indentation depth on Figs 5.17 and 5.18, where the experimental scatter increases with decreasing indentation depth. To determine whether the variation between the bulk and in situ resin properties was representative of a true property change, or purely a consequence of experimental scatter, the student t-test was used (Livingston, 2004). The mean and standard deviation of both the bulk (X_B,σ_B) and in situ (X_I,σ_I) observation sets were determined over the range of unconstrained indentation depths for the in situ indentations, i.e. a depth range 193 - 1265nm. A confidence level of 99.9% was chosen and the degrees of freedom was calculated using Equation 5.5:

$$df = N_B + N_I - 2 \tag{5.5}$$

where df is the numbers of degrees of freedom, while N_B and N_I are the number of indentations carried out into the bulk and in situ resin materials respectively. The confidence level and degrees of freedom can be used to determine the critical value of the test statistic (Z_{crit}) by referring to the student-t test distribution table. The value for the test statistic (Z) for the observation sets of interest is determined using Equation 5.6. A summary of all the parameters used for the student-t test is shown in Table 5.4.

Table 5.4: Student-t test parameters

		Mean (X)	Standard Deviation (σ)	N	df	Z_{crit}	Z
Modulus	Bulk	4.89 GPa	0.107 GPa	30	78	3.4197	9.9094
	in situ	5.37 GPa	0.307 GPa	50			
Hardness	Bulk	381 MPa	11 MPa	30	78	3.4197	4.3464
	in situ	405 MPa	36 MPa	50			

$$Z = \frac{\|X_B - X_I\|}{\sqrt{\frac{\sigma_B^2}{N_B} + \frac{\sigma_I^2}{N_I}}} \tag{5.6}$$

For both the modulus and hardness data, the value of the calculated test statistic (Z) was greater than the critical value (Z_{crit}) indicating that there is a 99.9% probability that the observation sets are significantly different and drawn from different populations.

5.5 Concluding remarks

The micromechanical properties a fibrous composite microstructure has been investigated experimentally using the nanoindentation technique. The aerospace composite HTA/6376 was co-cured with bulk 6376 resin to create specimens ideal for micromechanical characterisation using the nanoindentation technique. The effect of different surface preparation techniques on the resulting microstructure and topography was investigated and highlighted the extent of the fibre-matrix relief which exists following the grinding and polishing processes. This phenomenon severely limits the usefulness of the nanoindentation technique to quantitatively characterise the ‘interphase’ region which surrounds the fibre-matrix interface.

Express test property mapping and Continuous Stiffness Measurement (CSM) experimental nanoindentation techniques have been used to characterise the microscale properties of the HTA/6376 composite. The express tests provided convenient quantitative map of the fibre and matrix properties, as well as highlighting the gradient in properties surrounding the fibre-matrix interface. However, the low indentation depths and high rates used by the technique limited the reliability of the results. In order to more accurately characterise the matrix constituent of the composite, indentations were carried out into a wide range of resin pocket sizes provided by the co-cured 'hybrid' specimens using the CSM technique. This allowed the effect of the mechanical fibre constraint to be characterised experimentally. The results were compared with those from the finite element investigation of Chapter 3. A similar increase in modulus versus 'fibre constraint factor' was evident for both finite element models and the experiments, therefore validating the previously outlined 3D finite element methodology for characterising fibre constraint. Characterising this effect allowed the unconstrained values of modulus and hardness for each matrix pocket to be compared with that of the bulk matrix material. The indentation modulus and hardness for many of the matrix pockets was found to deviate from the value for the bulk 6376 resin. It was found that the change in elastic modulus was dependant on the matrix pocket size and increased by up to 19% compared with the bulk matrix material value. The in situ values of hardness were found to decrease compared to the bulk material for the larger resin pockets. While, for the smaller pockets, an exponential increase in the property was apparent as the radius of the matrix pockets reduced. Importantly, it was found that the apparent changes in in situ properties was significantly different relative to the scatter from the bulk measurements, with a confidence level of 99.9%.

The experimental results indicate that the fibrous composite curing process has a significant effect on the properties of the matrix material in comparison to the properties of the material in its bulk form. The sample preparation procedures proposed in this study not only ensure that the bulk and in situ materials undergo the same curing process, but also allows the evolution of matrix property change to be observed as a function of the matrix pocket size. The results show that the increase in indentation properties for the in situ resin is considerable for matrix pockets with a radius of less than 15µm (Figure 5.17). While the increase in indentation properties reported here is not as large as the property changes reported for the interphase region by other authors (Hodzic et al., 2000; Lee et al., 2007), it is interesting that this property change still occurs at large distances from the fibre-matrix interfaces. The reported sizes of the interphase regions for CFRP materials are in the order of hundreds of nanometres, whereas none of the unconstrained indentation depths in this work begin to even approach this region surrounding the fibres. It is possible that the dependence of indentation modulus on the matrix pocket size could be due to a more far-field interphase effect, due to potential reactions between the fibre surface treatments and the matrix material at distances greater than previously assumed. However, it is also possible that the local curing conditions of the matrix material have been altered by the added confinement of the surrounding fibres, which does not exist for the bulk material. This local property change, independent of the small interphase region surrounding the fibres may be significant from a micromechanical point of view, depending on the loading scenario being analysed. The indentation protocols developed herein, thus provide a robust approach to determining the material properties of the matrix constituent in situ, taking into account the mechanisms associated with using the method on fibrous composite materials and the statistical scatter associated with the nanoindentation technique.

6 Investigation of Pile-Up, Viscoelasticity and Hydrostatic Stress Effects on Polymer Matrix Indentation

6.1 Introduction

Nanoindentation has proven itself to be an extremely useful technique for testing of composite material constituents at the microscale. The experimental comparison between the bulk and in situ indentation moduli in Chapter 5 is solid evidence of this. While this comparative analysis is interesting, it is clear that the quantitative values of the 6376 moduli do not compare well with those reported on the material data sheet. The indentation moduli are consistently larger than the reported macroscopic value, determined using conventional ISO 527-1 tensile testing of bulk epoxy material (Hexcel, 2007), by roughly 40%. Similar overestimations of polymer moduli by indentation methods have been noted in the literature (Tranchida et al., 2007; Kranenburg et al., 2009), and are often attributed to the effects of material pile-up, viscoelastic deformation and sub-surface hydrostatic stress. The overestimation of the true specimen elastic modulus using nanoindentation remains a predominant issue preventing the accurate quantitative characterisation of the in situ matrix properties of polymer matrix composites (PMCs) at the microscale.

The elastic theory on which the nanoindentation analysis technique is based assumes that “sink-in” behaviour has occurred in the region around the indentation, as this behaviour is characteristic of elastic conical indentations. However, depending on the substrate material, the behaviour can vary at the maximum indentation depth, as illustrated in Fig. 6.1. During pile-up, the contact depth (h_c) is greater than the maximum indentation depth (h_{max}). Fig. 6.1b shows the shapes of the projected contact areas at maximum depth in each case, for indentations carried out using a Berkovich indenter. For the case of pile-up, the flat sides of the indentation impression curve outwards as the material piles up mostly on the flat regions between the sharp edges of the indenter tip. During sink-in, the flat sides of the impression bow inward as the material sinks-in mostly in the same regions. While the assumption of sink-in behaviour is valid for most materials, there have been

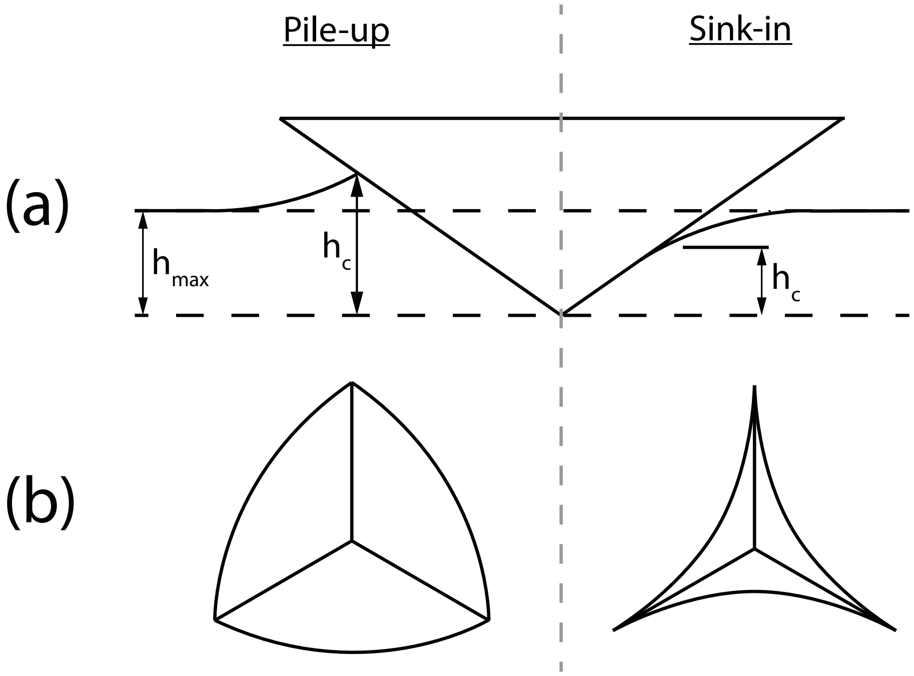

Figure 6.1: Pile-up and sink-in material behaviour at maximum indentation depth (a) side profile of indentation, (b) geometry of projected contact areas for each case

numerous reported cases where the theory has failed to correctly predict the true contact area for the elastic-plastic indentation, depending on the modulus to yield stress ratio of the material (Bolshakov and Pharr, 1998). This leads to overestimated indentation moduli values (McElhaney et al., 1998; Randall et al., 1998; Beegan et al., 2003, 2005; Zhou et al., 2008; Saha and Nix, 2001, 2002; Cao et al., 2006).

Studies have also indicated that the time-dependent behaviour of polymers affects the predictions of elastic moduli using the nanoindentation technique (Tranchida et al., 2007). In particular, it has been shown that the initial phase of the unloading curve is abnormal compared to the rest of the unloading curve, due to the notable effects of viscoelastic deformation (Beyaoui et al., 2009). These effects lead to an increase in the contact stiffness, poor non-linear curve fits of the unloading data, and theoretically invalid fitting exponents (Beyaoui et al., 2009; VanLandingham et al., 2001; Tranchida et al., 2007). In severe cases, indentation creep can actually lead to a negative slope at the initiation of indenter unloading, which makes analysis of the unloading curve impossible (Briscoe et al., 1998). However, even in the absence of this phenomenon, the unloading data can still be adversely affected by viscoelastic deformation, leading to overestimation of the sample modulus.

During indentation testing, the stressed material underneath the indentation tip becomes constrained by the surrounding unstressed material, leading to a build-up of large compressive hydrostatic stress (Atkins and Tabor, 1965). It has been postulated by a number of authors that, for polymers, the overestimation of the indentation modulus could be influenced by the existence of this hydrostatic stress state (De Silva et al., 2013; VanLandingham et al., 2001; Briscoe and Sebastian, 1996; Doerner and Nix, 1986), as the tensile modulus of polymers has been shown to increase with hydrostatic pressure when tensile tests were performed in a thick-walled cylindrical pressure chamber (Jones Parry and Tabor, 1973; Pae and Bhateja, 1975). However, the effect of the surrounding hydrostatic stress state on polymeric indentations has yet to be quantified.

In this chapter, the effects of material pile-up, time-dependent viscoelastic deformation and hydrostatic stress on the indentation modulus of the bulk 6376 epoxy using the Oliver and Pharr (1992) method is examined. Optical and Scanning Probe Microscopy (SPM) techniques have been used to investigate the residual impressions of indentations for evidence of pile-up, with area corrections applied to the nanoindentation results based on direct area measurement techniques. The effect of viscoelastic deformation has also been investigated by carrying out a large number of indentations using a wide range of experimental settings in order to determine the optimum configuration and analysis techniques to produce results free from the influence of time-dependent deformation effects. The effect of varying these experimental and analytical parameters on the curve-fitting procedure has been detailed. Finally, relations from the literature are used to quantify the value of the constraining hydrostatic stress, and characterise its influence on the calculated indentation modulus of the 6376 material.

6.2 Characterisation of 6376 matrix material

The nanoindentation experiments were carried out using the Nanoindenter G200 developed by Agilent Technologies, fit with a Berkovich indenter tip. Four

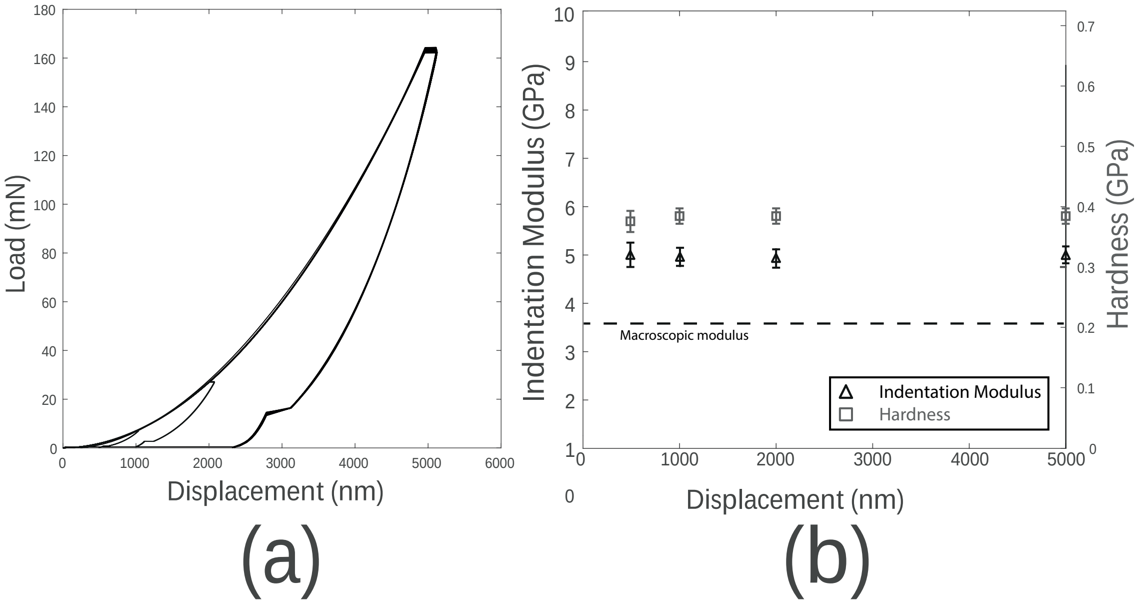

Figure 6.2: (a) load-displacement curves, (b) Indentation modulus and hardness versus target indentation depth

different target indentation depths, 500 nm, 1 µm, 2 µm and 5 µm, were used in order to characterise any depth dependency of the examined phenomena. The chosen indentation depths also ensure that the results are independent of experimental factors such as tip blunting, surface roughness and size-scale effects associated with low-depth indentation (Tranchida et al., 2007; Tatiraju et al., 2008; Tho et al., 2006; Voyiadjis and Peters, 2010; Han, 2010). In order to carry out an initial characterisation of the 6376 epoxy material, a total of 30 indentations were carried out for each depth. The default settings of the G200 were used, which included a constant load hold segment at the maximum load of 10 seconds, and an indentation strain-rate target of 0.05 /s.

The load-displacement data, indentation modulus and hardness for the indentations are shown in Fig. 6.2, and are consistent across the four depths investigated. The indentation moduli (mean 5.07 GPa) were consistently larger than the reported macroscopic value (3.63 GPa) determined using conventional ISO 527-1 tensile testing of bulk epoxy material (Hexcel, 2007), by approximately 40%.

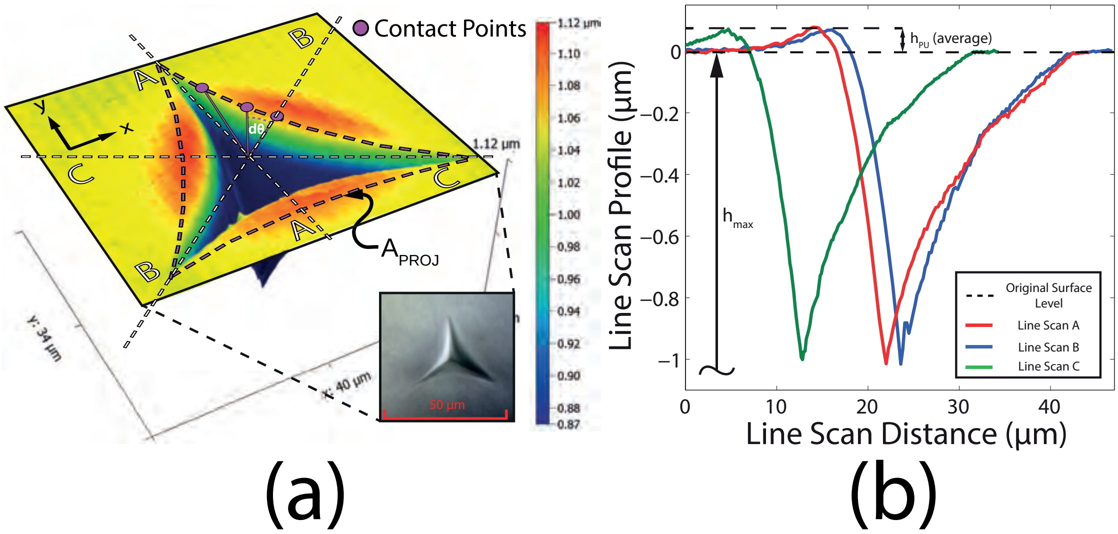

Figure 6.3: (a) Micrograph and SPM image of 5 µm indentation, highlighting locations of line scans, (b) Line scans A, B and C

6.3 Investigation of material pile-up

A residual impression for each indentation depth was investigated for pile-up using the optical microscope of the G200 (1000× magnification) and scanning probe microscopy (SPM). An example is shown in Fig. 6.3a, for a 5 µm indentation. The closed-loop nano-positioning (Nanovision) stage of the G200 was used in combination with the indenter head fit with a cube corner indenter tip to create high-resolution images of the residual impressions. This was accomplished by raster-scanning the tip over the area of interest under a force of 1 µN. The time between the test's unloading cycle and the SPM scans was roughly one hour for all the scans. The data from the scans was post-processed and plotted using the free and open source SPM data analysis software Gwyddion 2.30.

While the use of optical, electron and spanning probe microscopy to determine the true contact area is often recommended for cases where pile-up occurs during an indentation (ISO, 2015; Oliver and Pharr, 2004), there is no standard procedure or consensus regarding the method of measurement of the corrected contact area. Thus, two methods have been used to directly measure the contact area from the SPM scans. The first directly measures the projected contact area of the impression (A_{PROJ}) (Cabibbo et al., 2013; Beegan et al., 2003; Kese and Li, 2006; Saha and Nix, 2001; Zhou et al., 2008), while the second determines the depth-corrected contact area based on the measured pile-up profiles (A_{PU}) (Cao et al., 2006; Zhou et al., 2008). To determine A_{PROJ} from the residual impressions, line scans were examined which started at the centre of the impression and proceeded outwards towards the bulk non-indented surface, as illustrated in Fig. 6.3a. The highest points along these line scans were assumed to be the bounding points of contact between the indenter and the substrate material. The line scans were measured for the full 360° around the centre of the indentation at an angular increment ($d\Theta$ in Fig. 6.3a) of 2.5°. The analysis of the contact points leads to a projected contact area with inward curvature. The indentation modulus was recalculated using this new projected area, and is denoted as E_{PROJ}.

Material pile-up is clearly visible around the flat sides of the impression in Fig. 6.3a. To determine the corrected contact depth (h_c) from the SPM scans, the height of the material pile-up (h_{PU}) above the mean surface height was measured using the line scans A, B and C, illustrated in Fig. 6.3b. This height was then added to the maximum indentation depth (h_{max}) to determine the corrected contact depth (h_c) according to Equation 6.1:

$$h_c = h_{PU} + h_{max} \tag{6.1}$$

The depth-corrected contact area (A_{PU}) is then calculated using the indenter's area function and the corrected contact depth. The indentation modulus calculated using this new depth-corrected contact area is then denoted as E_{PU}. Both of the above methods of direct contact area determination were found to successfully correct the overestimated indentation modulus determined for indentations carried out on Aluminium 6082T6 alloy, where pile-up occurred during indentation. The results for the Aluminium sample are presented in Appendix B on page 179.

The corrected contact areas and moduli were normalised by dividing by the values determined using the Oliver and Pharr technique, and plotted in Fig. 6.4a and 6.4b, respectively. The values of area appear to be slightly dependent on the indentation depth, with larger normalised areas determined for smaller indentations. There is a clear disparity between the values calculated using the two techniques.

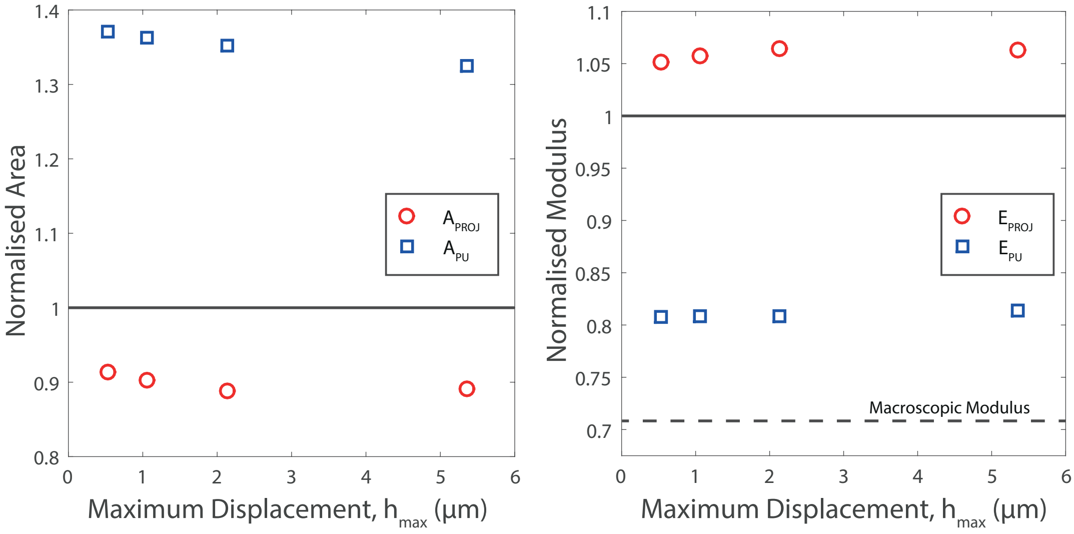

Figure 6.4: Normalised (a) Contact area and (b) Indentation modulus determined using each of the pile-up correction methods

The inward curvature of the projected contact area (A_{PROJ}) predicts sink-in behaviour, to an even greater degree than that predicted using the Oliver and Pharr prediction. This leads to an increase in the corresponding modulus value. The corrected area using the pile-up heights (A_{PU}) leads to roughly a 20% reduction in the indentation modulus, but is still 12% larger than the macroscopic modulus.

The observation of both inward curvature and material pile-up around the residual impression seems somewhat contradictory based on the expected impression geometry described in Fig. 6.1b. This behaviour is probably due to the recovery which the material undergoes on removal of the maximum indentation load. An interesting comparison can be made between the residual impression depth (h_p) extracted from the load-displacement data at zero load in Fig. 6.2a, and that observed post-hoc using the SPM line scans in Fig. 6.3b. These values are compared in Fig. 6.5, for both the aluminium alloy and 6376 epoxy material. Both measured values of residual indentation depth are quite similar for the aluminium material. However, for the 6376 material, it is clear that the depth of the residual impressions determined from the SPM scans is much lower than that extracted from the load-displacement curves at zero load. This is clear evidence of the significant viscoelastic recovery experienced by the material upon removal of the indentation load. This large amount of recovery makes direct measurement of the contact area prob-

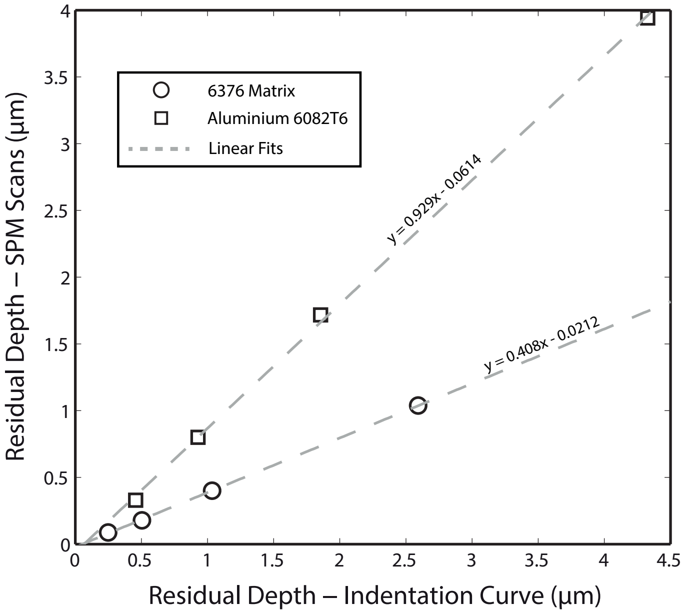

Figure 6.5: Comparison of residual depths calculated from load-displacement curves and scanning probe microscopy (SPM)

lematic. The indentations recover roughly 80% of the maximum indentation depth between the time the indenter is under its maximum load, and the time the surface was scanned. This excessive elastic and viscoelastic recovery makes it unlikely that the height of the measured pile-up (h_{PU}) is representative of the state of pile-up under the indenter at maximum indentation load. The surface recovery is more likely to occur predominantly upward based on the 80% recovery of the indentation depth and the recovery sequence observed in the numerical simulations of Chapter 3. In conclusion, the results of the SPM scans show that material pile-up does not provide a satisfactory explanation for the overestimation of the indentation modulus of the 6376 resin, while also providing further evidence of the significant viscoelastic deformation which occurs during and following the indentation of this material.

6.4 Investigation of viscoelastic effects

The experimental indentation settings were altered to determine the elastic modulus of the 6376 epoxy, independent of the viscous behaviour of the material. The parameters altered were the maximum load holding segment time (t_{hold}), the indentation strain-rate ($\dot{\varepsilon}$) and the point of contact stiffness evaluation ($h_{\frac{dP}{dh}}$), and these investigations are described in the subsections below.

6.4.1 Maximum load hold segment time (t_{hold})

To allow time-dependent deformation to diminish prior to the critical unloading segment of the test, a holding period is often applied to the nanoindentation test at maximum load. This hold period was first proposed by Hochstetter et al. (1999), and the default hold time for the G200 is 10 seconds. To investigate the effect of the hold time (t_{hold}) on the indentation modulus, tests were carried out using 6 different hold times for each target indentation depth. A wide range of hold times were investigated, namely, 0 s, 10 s, 60 s, 120 s, 600 s and 3600 s, with two indentations carried out for each combination of indentation depth and hold time.

The load-displacement data for indentations with a target depth of 2 µm is plotted in Fig. 6.6 for the range of hold times investigated. The increase in hold time leads to an increase in creep displacement which manifests as a shift in the unloading data along the displacement axis. A 'nose' was observed at the onset of unloading for the indentations carried out with no hold time and is highlighted in Fig. 6.6. This 'nose' is not present in the rest of the data where the hold segment was included. The long-term creep response of the 2 µm indentation with a hold time of 3600 s (1 hour) is shown in Fig. 6.7a, where t_{hold} has been plotted against the indenter displacement. The creep displacement during the hold period increases the total indentation displacement by 12% of the target indentation depth during the hold period. The holding time has also been plotted against the creep rate in Fig. 6.7b for the same indentation. It can be seen that the creep rate is very low after approximately 100 seconds, and is close to zero after approximately 1000 seconds. The indentation modulus values determined for the different hold times are plotted in Fig. 6.8, where a decrease in the modulus is observed as hold time increases, with the largest scatter in properties observed for the indentations with zero hold time. The values for $t_{hold} = 0$ have been plotted as $t_{hold} = 1$ for the purpose of illustration. The modulus decrease is somewhat dependent on the indentation depth, with the modulus for smaller indentations decreasing to a higher degree than larger ones. The long hold moduli are closer to macroscopic modulus, as indicated in Fig. 6.8.

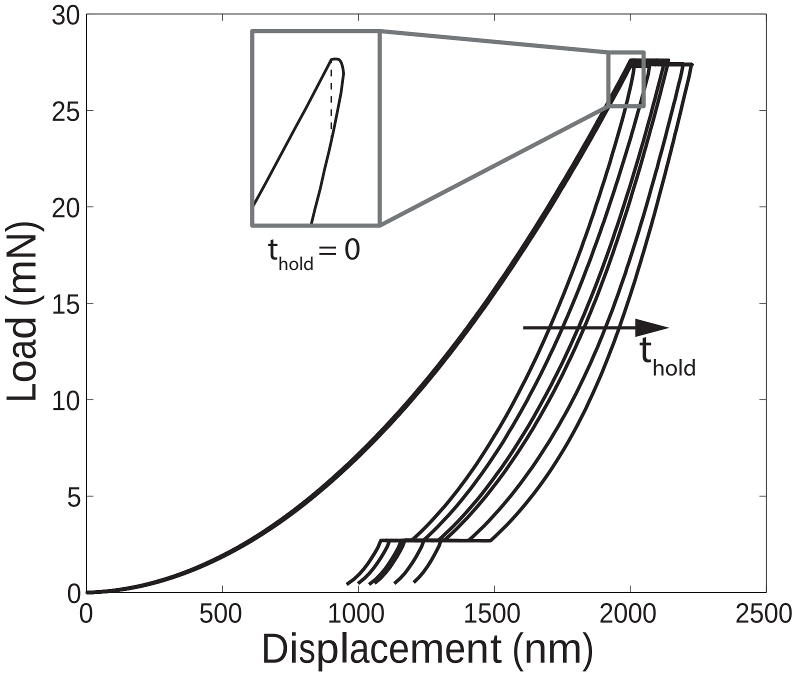

Figure 6.6: Comparison of load-displacement curves for a 2 µm displacement target and peak load hold times of 0, 10, 60, 120 600 and 3600 seconds.

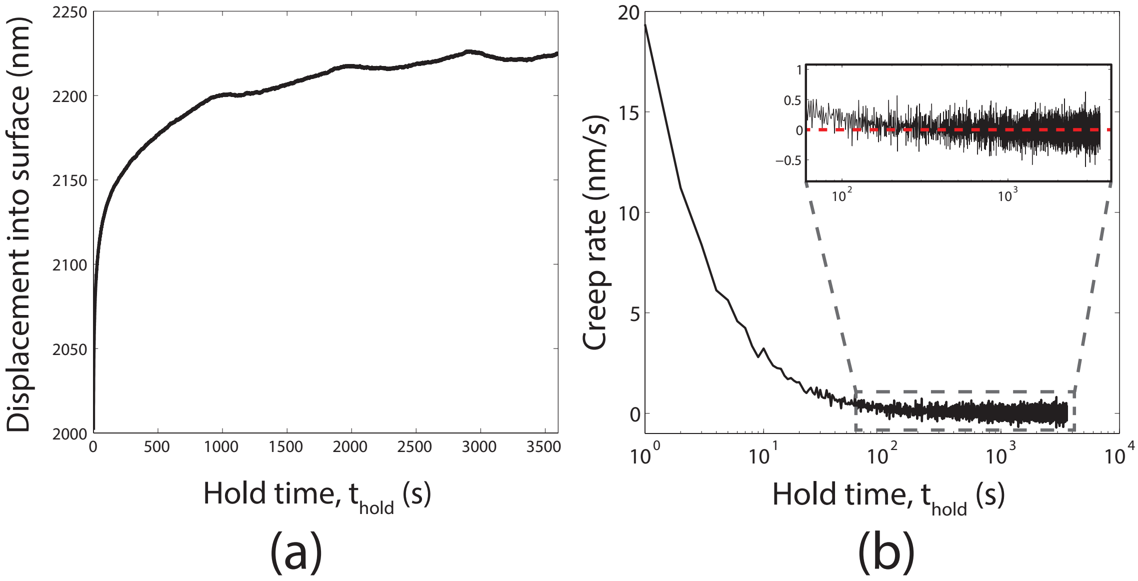

Figure 6.7: The long term creep response of the 2 µm indentation with a hold time of 3600 s: (a) Hold time versus indenter displacement, (b) Hold time versus creep rate.

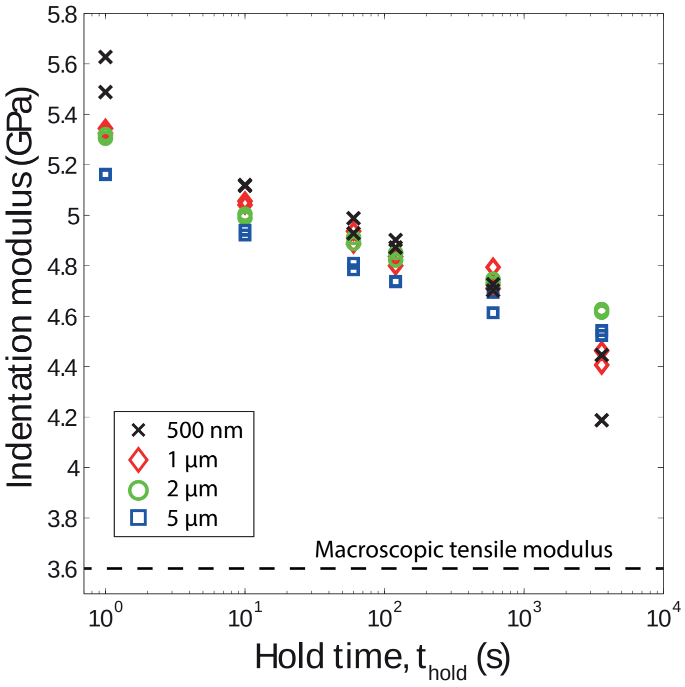

Figure 6.8: Indentation modulus versus hold time for the six hold times and four different indentation depths tested

6.4.2 Indentation strain-rate ($\dot{\varepsilon}$)

The 'indentation strain-rate' is defined as the loading rate divided by the instantaneous load ($\dot{P}/P$) and has a default value of 0.05 /s. The indentation strain-rate also affects the unloading rate for the indentation. The unload rate is calculated according to Equation 6.2 for the G200:

$$\dot{P} = \begin{cases} 0.1, & \text{if } P_{max}\dot{\varepsilon} < 0.1 \\ P_{max}\dot{\varepsilon}, & \text{if } P_{max}\dot{\varepsilon} \geq 0.1 \end{cases} \tag{6.2}$$

where $\dot{P}$ is the unload rate, P_{max} is the maximum load of the indentation and $\dot{\varepsilon}$ is the strain rate target defined for the test. A minimum unload rate of 0.1 mN/s was imposed. Tests were carried out over a range of strain-rates spanning four orders of magnitude, namely, 0.001, 0.01, 0.1 and 1 /s. The maximum indentation depth target was set to 2 µm, and a total of 10 indentations were carried out for each indentation strain-rate.

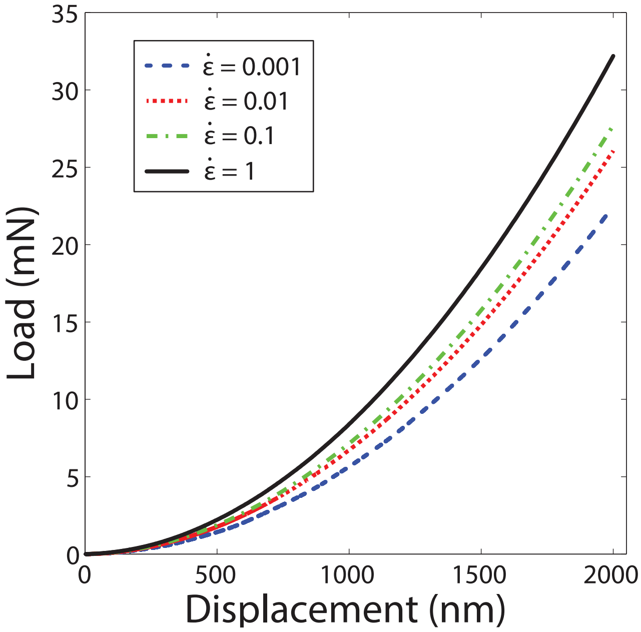

Figure 6.9: The effect of indentation strain rate on the 6376 epoxy loading curves

The loading curve behaviour of the 6376 epoxy was highly dependent on the strain rate target chosen as shown in Fig. 6.9. It is clear that as the strain rate is increased, the load required to reach the displacement target increased. The effect of the chosen indentation strain rate on the calculated indentation modulus is shown in Fig. 6.10, where an increase in modulus observed as the strain rate was increased. For strain-rates greater than 1, the increase in maximum load (P_{max}) and resulting properties was extreme and, therefore, deemed abnormal and omitted from the results. The lowest value of indentation modulus calculated was 4.5 ± 0.08 GPa, which was determined at the strain rate of 0.001 /s.

6.4.3 Point of contact stiffness evaluation ($h_{\frac{dP}{dh}}$)

An example load-displacement curve is shown in Fig. 6.11 where the regions of positive (first hold segment) and negative (second hold segment) displacement drift have been highlighted. It is reasonable to assume that a point of inflection must exist at some point on the load-displacement curve between these hold segments, where the effects of creep and relaxation are minimised. Here, it is proposed

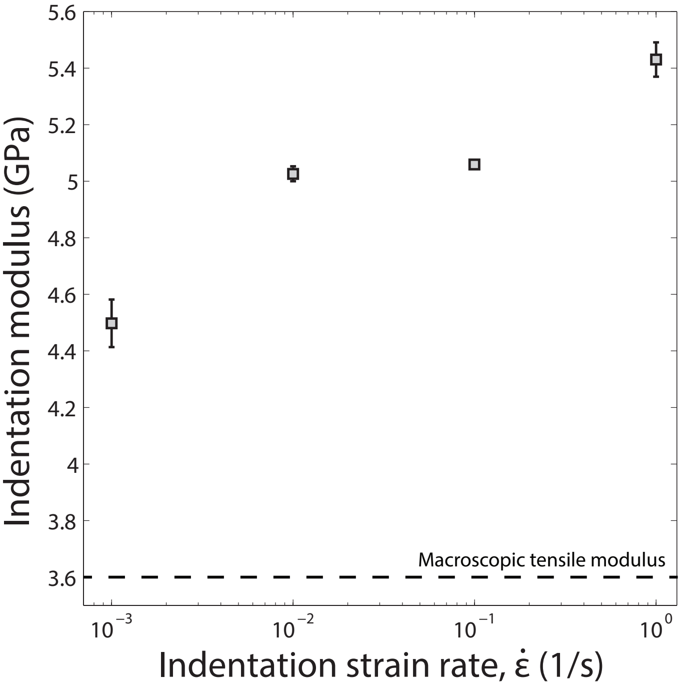

Figure 6.10: Indentation modulus versus strain rate for five repeats at four different strain rates

that the point of contact stiffness determination ($h_{\frac{dP}{dh}}$) be changed, based on the characterisation of a 'creep-relaxation profile' for the unloading curve. This allows the most drift-insensitive point along the unloading curve to be determined, and the contact stiffness calculated at this point, as opposed to fitting the drift-affected data from the early stages of unloading. To determine this optimum point, a series of indentations were held at a constant load at various stages along the unloading curve. Indentations were carried out using the default experimental settings ($t_{hold} =$ 10 s, $\dot{\varepsilon} = 0.05$ /s) across the four indentations depth under consideration. Holding segments were introduced during the unloading segments at increments of 10% of the maximum load, to ascertain the magnitude of the creep/relaxation at each stage. A total of 5 indentations were carried out for each combination of indentation depth and unloading curve load level, and the drift displacement from the first 10 seconds was measured. A time of 10 seconds was chosen because the total unloading takes 20 seconds and the upper 50% of the curve is used for fitting and the calculation of the indentation properties (Agilent, 2013).

The drift displacements during the unloading hold periods have been plotted

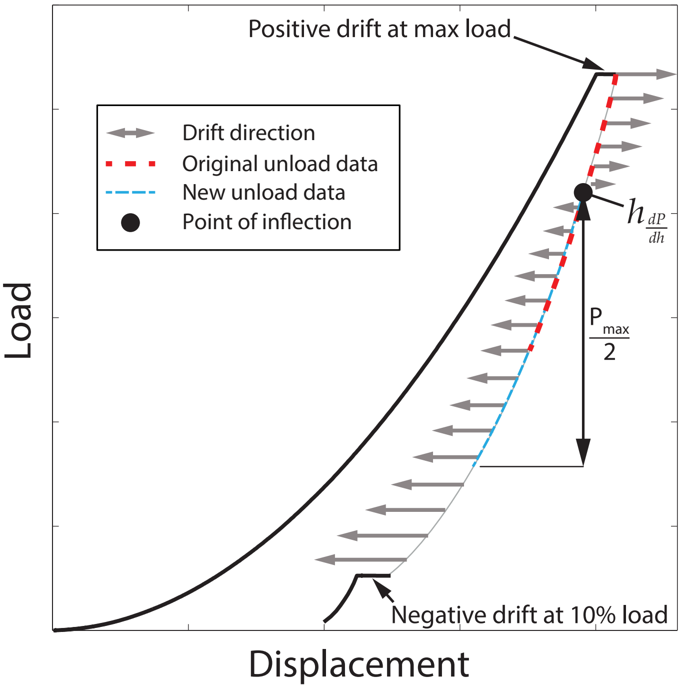
Positive drift at max load
Drift direction
Original unload data
New unload data
Point of inflection
$h_{\frac{dP}{dh}}$
$\frac{P_{max}}{2}$
Load
Negative drift at 10% load
Displacement

Figure 6.11: Schematic of load displacement data highlighting the areas of positive and negative unloading drift, the point of inflection for the drift, and the original and new unload data to be fitted

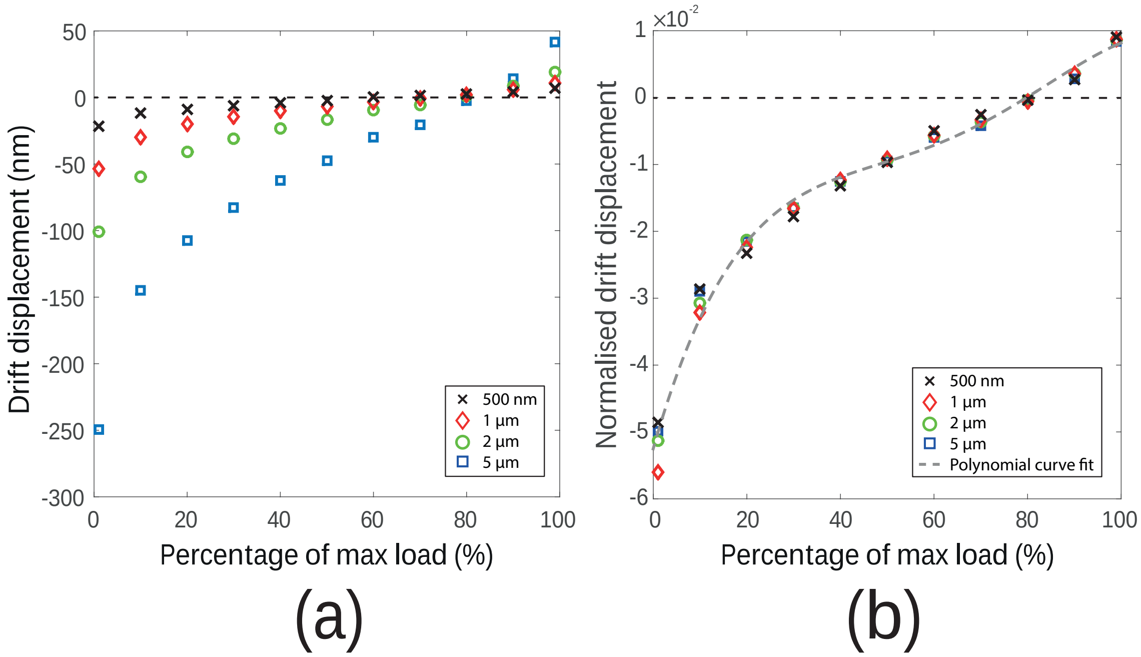

Figure 6.12: Unloading curve creep-relaxation profiles detailing the (a) Drift displacement and (b) Normalised drift displacement, measured from the unloading curves, plotted against the percentage of the maximum load

against the percentage of maximum load level, to produce the unloading curves' creep-relaxation profiles in Fig. 6.12a. The drift displacements were then normalised by dividing by their corresponding maximum indentation depth targets in Fig. 6.12b. It is clear from the creep-relaxation profile that the total drift is minimised at around 80% of the maximum load, and is insensitive to indentation depth. The indentation data from Fig. 6.2a was analysed firstly using the unloading data ranging from 100-50% of the maximum load (original) and again from 80-30% (new), as illustrated in Fig. 6.11, and the resulting indentation moduli are compared in Fig. 6.13. The data is very similar for all indentation depths, with only slightly higher values determined for the 500 nm indentations. The moduli calculated were 5.07 ± 0.08 GPa and 4.42 ± 0.02 GPa using the original and new unloading data, respectively, which is a similar decrease to that observed using long hold times and slow strain rates, but with much less time required on the sample. This is advantageous as high throughput experimentation (HTE) is often cited as one of the major advantages of nanoindentation experiments over conventional mechanical testing techniques (Kranenburg et al., 2009).

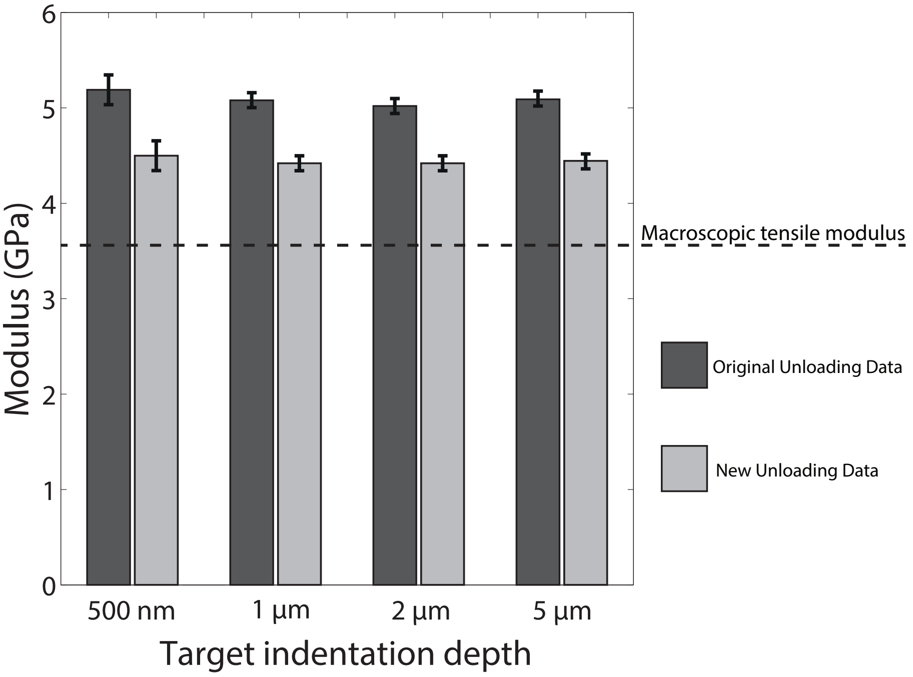

Figure 6.13: Indentation modulus results for the original and new unloading curves for the four indentation depths tested

6.4.4 Analysis of non-linear curve-fitting procedure

In order to calculate the indentation modulus of the sample, the upper 50% of the unloading data was fitted using Equation 6.3 (Agilent, 2013):

$$P(h) = B\left(h - h_p\right)^m \tag{6.3}$$

where B is a constant which depends on the indenter geometry and substrate properties, m is the curve-fitting exponent, and h_p is the residual depth of the indentation following complete unloading. The quality and exponents of this non-linear curve fit can provide insight into how well the data from a polymeric indentation, where time-dependent viscoelastic deformation is prevalent in the unloading data, adheres to the elastic nanoindentation theory. A selection of non-linear curve fits are compared with the corresponding unloading data in Fig. 6.14. Figs. 6.14a and 6.14b show that as the hold time is increased, the difference between the curve-fit and the

Table 6.1: Analysis of non-linear curve fitting parameters

		Coefficients of Determination (R^2)	Curve-fitting Exponent (m)
Hold Time, t_{hold} (s)	0	0.9952±0.006	2.93±0.18
	10	0.9980±0.005	2.82±0.05
	60	0.9982±0.006	2.74±0.06
	120	0.9982±0.004	2.60±0.03
	600	0.9989±0.003	2.48±0.06
	3600	0.9999±0.001	2.24±0.01
Strain Rate, $\dot{\varepsilon}$ (1/s)	0.001	0.9994±0.002	2.19±0.02
	0.01	0.9976±0.005	2.25±0.03
	0.1	0.9961±0.001	2.78±0.02
	1	0.9926±0.004	2.46±0.01
Point of contact stiffness ($h_{\frac{dP}{dh}}$)	Original	0.9966±0.005	2.75±0.06
	New	0.9999±0.004	2.23±0.02

unloading data decreases. This is probably due to an increase in creep deformation occurring prior to unloading. The curve-fits for the different strain-rates were all quite poor, especially for the data corresponding to the beginning of unloading. However, it clear from comparing the curves shown in Figs. 6.14c and 6.14d that slower strain rates led to a more accurate fit of the data. Interestingly, a significant improvement is noted for the fits where the point of contact stiffness determination was changed. The fit for the original unloading data, shown in Fig. 6.14e, is quite poor, while the fit for the new unloading data, shown in Fig. 6.14f, is much more accurate. The coefficients of variation (R^2) and curve-fitting exponents (m) for each indentation type are listed in Table 6.1. Despite the marked improvement in the non-linear fitting, the curve-fitting exponent (m) for all the indentations is still larger than the expected upper limit of 2, which is similar to previous observations from indentations carried out on polymeric materials (VanLandingham et al., 2001; Tranchida et al., 2007; Beyaoui et al., 2009). However, the value of m does appear to decrease for the indentations where the effects of viscoelastic deformation are nullified.

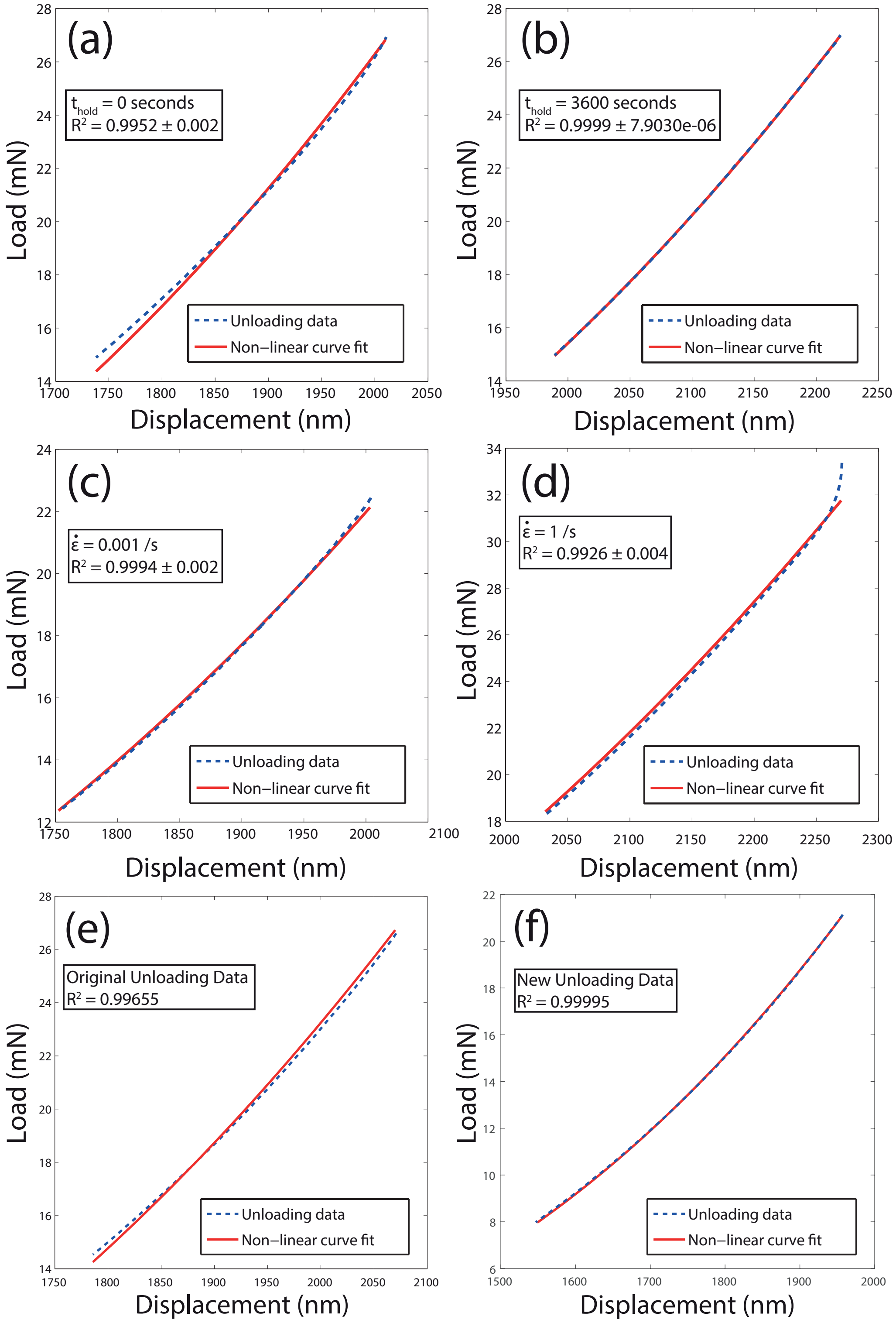

Figure 6.14: Comparison between the non-linear curve fits and unloading data: (a) Hold time of 0 seconds (b) Hold time of 3600 seconds (c) Strain rate of 0.001 /s (d) Strain rate of 1 /s (e) Original unloading data (f) New unloading data.

6.5 Influence of hydrostatic stress

It was proposed by Birch (1938) that the increase in the Young's modulus of isotropic solids due to the presence of hydrostatic pressure is described by Equation 6.4:

$$E = E(0) + 2\sigma_H(5 - 4\upsilon)(1 - \upsilon) \tag{6.4}$$

where $E(0)$ is the elastic modulus at atmospheric pressure, σ_H is the applied hydrostatic pressure, and υ is the Poisson's ratio of the material. It is clear from Equation 6.4, that the pressure dependence of the elastic modulus is greater for materials that have a lower modulus at atmospheric pressure, such as polymers. This expression was experimentally verified and shown to correctly predict the change in the tensile modulus of polymers with increasing hydrostatic pressure (Pae and Bhateja, 1975; Silano et al., 1974).

In an indentation test, the measured hardness of the material is equivalent to the mean contact pressure measured by the indenter tip. This measured pressure includes contributions from the stressed material's yield stress in compression (σ_{YC}) and the constraining hydrostatic stress (σ_H), as illustrated in Fig. 6.15. The ratio of the contributions from each of these effects on the total hardness value is determined by the constraint factor (C) for a given material, where the hardness (H) is related to the yield stress (σ_{YC}) by Equation 6.5 (Tabor, 1970).

$$H = C\sigma_{YC} \tag{6.5}$$

This relation can then be used to estimate the value of the constraining hydrostatic stress (σ_H), based on the value of hardness measured for the indentation, provided the constraint factor is known:

$$\sigma_H = H - \frac{H}{C} \tag{6.6}$$

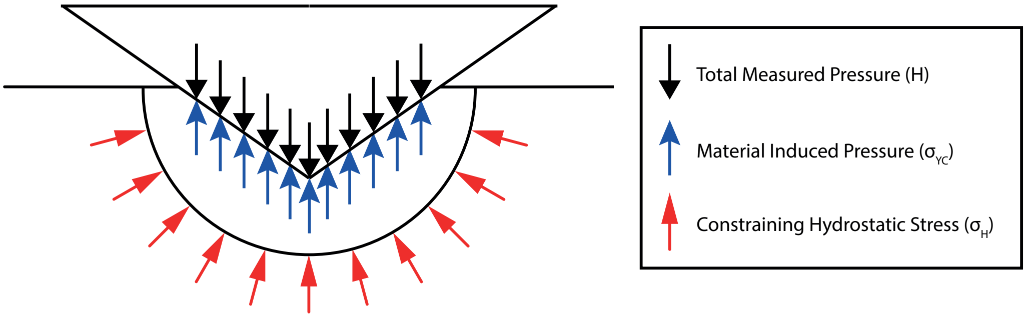
Total Measured Pressure (H)
Material Induced Pressure (σ_{YC})
Constraining Hydrostatic Stress (σ_H)

Figure 6.15: Schematic of an indentation, highlighting the contributions of the materials yield stress and the hydrostatic stress to the overall measured material hardness

Rearranging Equation 6.4 and substituting the relation from Equation 6.6 allows the true elastic modulus of the material ($E(0)$) to be calculated, where the indentation modulus and hardness are substituted for E and H respectively.

$$E(0) = E - 2(H - \frac{H}{C})(5 - 4\upsilon)(1 - \upsilon) \tag{6.7}$$

The mean values of indentation modulus and hardness, plotted in Fig. 6.2, have been used to determine the effect of hydrostatic stress on the indentation modulus of the 6376 material. Rodríguez et al. (2012) recently showed that the constraint factor (C) for pressure sensitive materials is dependent on the plasticity index (σ_{YC}/E) and the friction angle (ϕ) of the material. According to that numerical analysis, the constraint factor for materials with a high value of plasticity index, such as the 6376 epoxy, is approximately equal to 2. This allows the value of hydrostatic stress to be calculated using Equation 6.6. The value of hydrostatic stress (σ_H) inferred from these relations was 190.5 MPa. Equation 6.7 was then used to calculate $E(0)$, where the mean indentation modulus value from the experiments was substituted for E (the modulus influenced by hydrostatic stress). Removing the influence of the calculated hydrostatic stress reduces the mean indentation modulus from the experiments from 5.07 GPa to 4.24 GPa. This represents a 16% reduction in the property and shows that the constraining hydrostatic stress could have a significant influence on the values of indentation modulus calculated for the 6376 epoxy resin.

6.6 Concluding remarks

A comprehensive experimental study has been carried out to determine the effects of material pile-up, viscoelasticity and hydrostatic stress on the values of indentation modulus determined for 6376 epoxy material. Scanning probe microscopy (SPM) images of residual impressions showed regions of material pile-up adjacent to the impressions, but also highlighted the large amount of viscoelastic recovery which occurs following indenter unloading. This recovery makes the direct determination of the contact areas problematic. Based on the large recovery observed, and the relatively small heights of the pile-up measured, it was concluded that the pile-up did not provide an adequate explanation for the overestimation of the material's elastic modulus by indentation methods.

The indentation modulus was found to decrease for experimental configurations where viscoelastic deformation was allowed to diminish prior to unloading. The quality of the non-linear curve fits to the resulting unloading data also showed a marked improvement for these configurations. Similar reductions in modulus and improved curve-fits could also be produced by avoiding the abnormal unloading data present at the onset of unloading, requiring much less time on the sample. It was found that nullifying the effects of the viscoelastic deformation led to reductions of the modulus of the order of 10-12%. The effect of the sub-surface constraining hydrostatic stress on the indentation modulus was also investigated. A simple correction was proposed based on relations from literature, which allowed the constraining hydrostatic stress to be quantified. The resulting change in modulus due to the hydrostatic stress could then be approximated using experimental data. Correcting for the effects of hydrostatic stress lead to 16% reduction in the indentation modulus for the material, making it the most influential of the phenomena investigated.

It is clear from the above investigations that the overestimation of the elastic modulus of polymer materials by indentation methods could be a consequence of a combination of factors. Accounting for the effects of both viscoelasticity and hydrostatic stress results in a recalculated mean indentation modulus of 3.75 GPa, which compares well with the macroscopic elastic modulus of 3.63 GPa for the 6376 epoxy material, as highlighted in Table 6.2. The relative effect of the three investigated phenomena on the indentation modulus of various polymer materials is likely

Table 6.2: Summary of results

Elastic Modulus (GPa)	Tensile Test	Indentation	Viscoelastic Effects (-12%)	Hydrostatic Stress Effects (-16%)
Measured Value	3.63	5.07	4.46	3.75
Normalised Value	1.00	1.40	1.23	1.03

to vary depending on the properties of polymer being investigated. The methods described herein to find the drift-insensitive contact stiffness and to account for hydrostatic stress influence could be readily incorporated into the standard protocols for polymer material indentations, to ensure accurate calculation of the indentation modulus, independent of these effects.

7 Conclusions and Recommendations for Future Work

7.1 Conclusions

The work described in this thesis analyses the use the nanoindentation technique to determine the in situ properties of the carbon-fibre polymer matrix composite HTA/6376. This chapter provides a summary of the main points resulting from the numerical and experimental investigation. The objectives outlined in Section 1.3 are now concluded upon, and recommendations for further development of the completed work are proposed.

7.1.1 Fibre constraint

Finite element contact modelling of the nanoindentation process provided a useful insight into the mechanics of the indentation test applied to fibrous composite microstructures. A 3D indentation model of a matrix pocket surrounded by a circular array of fibres was analysed in Chapter 3 and highlighted the effect of fibre constraint on the resulting load-displacement data and indentation properties. It was shown that the fibre constraint affects indentations in pockets much larger than the area of the residual impression, in regions which could be considered suitable for in situ matrix characterisation upon visual inspection in an experimental scenario. The results show that the radius of the pocket must be at least 20 times larger than the maximum indentation depth if the indentation properties are to be representative of the in situ matrix material. The models also highlighted the sub-surface stress transfer between the composite constituent materials and the effect of increasing fibre constraint on the material pile-up behaviour. Analogous to the nanoindentation of soft films on hard substrates (Zhou et al., 2008), material pile-up is enhanced due to the fibre constraint imposed on the indentation's plastic deformation field. It was shown that when the contact areas are inferred directly from the finite element contact, the relative increase in the modulus is much less than that determined using the theoretically deduced areas. While the size of the indentation stress field was found to be similar for the axisymmetric 2D and full 3D models, the use of an encastre boundary condition to represent the surrounding fibre boundary led to a very conservative overestimation of the fibre constraint effect in experimental scenarios.

In order to validate the 3D finite element modelling approach, the fibre constraint effect was investigated experimentally in Chapter 5 using the Continuous Stiffness Measurement (CSM) technique, which allowed the indentation modulus to be measured as a function of depth. The experimentally observed increase in the indentation modulus with decreasing distance to the surrounding fibres was in good agreement with the modelling results, validating the finite element methodology. Thus, it is concluded that the fibre constraint effect can play a significant role in the characterisation of the in situ constituents of high fibre volume fraction composite materials. The numerical and experimental methods outlined can be used in future examinations of boundary bias effects on other multi-phase material systems.

7.1.2 Thermal residual stress

In Chapter 4, micromechanical finite element modelling of the thermal cooldown process applied to fibrous composites has been used to determine the wide range of residual stress states which exist in the composite microstructure post-cure. Three-dimensional finite element contact models were then used to determine the effect of the stress states on nanoindentation properties. It was shown that the equibiaxial tensile stress state in the matrix pockets was linearly dependent on pocket radius, leading a similar linear dependence of the indentation properties with radius. The hardness of the pockets decreased by up to 11.9% compared to that of the non-prestressed substrate, and thus could potentially be underestimated by experimental indentation studies. In Chapter 5, experimental indentations of the in situ 6376 matrix pockets revealed that the hardness of matrix pockets with radii greater than 10 µm was lower than that of the bulk material, which could be attributed to this residual stress effect. The finite element results also show that the stress in the interfacial regions was highly dependent on the vicinity of the surrounding fibres. Vaughan and McCarthy (2011*a*) previously showed that compressive interfacial stress plays a significant role in the micromechanical deformation and failure of composite materials. However, based on the results from Chapter 4 it can be concluded that the potential for this large compressive stress to artificially increase the indentation properties, and potentially bias to the experimental characterisation of the 'interphase' region, is nullified by perpendicularly acting tensile stresses in these regions. Interestingly, it is shown that an underestimation of the properties is more likely for the vast majority of experimentally viable interfacial regions. In conclusion, the study quantitatively characterised the effect of thermal stresses on the nanoindentation testing of fibrous composite microstructures, while also highlighting the microstructural areas where the effects of thermal stress are nullified, which will be useful for future experimental studies.

7.1.3 Bulk versus in situ properties

It has previously proven difficult to analyse the in situ properties of the matrix constituent in high fibre volume fraction composites using experimental nanoindentation due to the lack of large matrix pockets in the microstructure (Gregory and Spearing, 2005). In Chapter 5, a novel sample preparation procedure is described where the HTA/6376 composite and the bulk 6376 matrix were co-cured to produce specimens containing microstructural regions of fibre migration. The resulting sample was ideal for matrix characterisation using the nanoindentation technique, and can be applied to any high fibre volume composite. The Express Test technique developed by Agilent Technologies was used in order to develop a property map of the fibre and matrix properties and highlighted a gradient in the material properties surrounding the fibre-matrix interface. However, quantitative characterisation of the 'interphase' region surrounding the fibre-matrix interface was not possible due to the fibre constraint effect and fibre-matrix relief measured using Scanning Probe Microscopy following the grinding and polishing processes. The numerical and experimental characterisation of the fibre constraint described in the previous section allowed the properties of the in situ 6376 matrix to be determined using the CSM technique as a function of the matrix pocket size, and compared with the bulk material. An exponential increase in the hardness and modulus with decreasing matrix pocket radius was apparent for the pockets with radii less than 10 µm. Thus, it can be concluded that the composite manufacturing and processing had altered the post-cure properties of the in situ material. The sample preparation and experimental procedures described in Chapter 5 provide a robust approach for comparing the bulk and in situ properties of composite matrix materials by taking into account the mechanisms associated with using the method on the inhomogeneous fibrous composite microstructure and analysing the results relative to the statistical scatter associated with the nanoindentation technique.

7.1.4 Elastic characterisation of polymers

The results from nanoindentation experiments on polymers from both the literature and the current work highlight a disparity between the values of elastic modulus determined from nanoindentation, and those measured with traditional tensile tests. These results raise questions about the applicability of indentation testing and analysis methods outlined in ISO 14577 to polymer materials. In order to investigate the overestimation of the 6376 matrix elastic modulus by nanoindentation, the effects of pile-up, viscoelasticity and hydrostatic stress were investigated in Chapter 6. While SPM images highlighted regions of pile-up adjacent to the residual indentations, the observation of inward curvature on the impressions and the small ratio of residual indentation depth to maximum indentation depth appear to indicate that pile-up is not a significant attributing factor. The modulus was found to reduce for experimental scenarios where viscous deformation was allowed to diminish prior to unloading, similar to results from the literature. However, this increases the indentation time significantly so a method to determine the drift-insensitive contact stiffness using the default high throughput testing protocols was proposed, which produced similar reductions in modulus and improvements to the curve-fitting procedure. This method requires a small number of preliminary indentations to analyse the creep and relaxation of the unloading curve at various stages, but can easily be incorporated into the standard testing protocols. Relations from the literature were used to characterise the hydrostatic stress effect and it was shown that the modulus is significantly affected by the stress state. In conclusion, the methods proposed to account for viscous and hydrostatic stress effects on the indentation of polymers move towards addressing the well-known disparity between nanoindentation and macroscopic moduli.

7.2 Future work

It is clear from the above conclusions that nanoindentation provides a useful insight into the in situ properties of fibrous composite constituents. However, more work is required in order to standardise the experimental protocols and quantitatively analyse the microscale properties of inhomogeneous materials. Some direction for future studies is detailed in this section.

7.2.1 Matrix and interphase characterisation

There is a distinct lack of quantitative experimental comparisons between the bulk and in situ composite matrix properties in the current literature. Such comparisons provide critical input data to micromechanical simulations of composite materials since the vast majority of current simulations use the properties of the constituents in their bulk form. However, the experimental results presented in Chapter 5 show that the fundamental elastic behaviour of the in situ material has been altered by the manufacturer's recommended processing methods. Thus, the experimental methodology outlined herein could be used for future studies into the effects of different processing parameters such as curing temperature, curing pressure, curing time, matrix composition, and fibre treatments, in order to determine the parameters which produce the optimal microscale properties. The effects of environmental ageing on the microscale properties of fibrous composites is also not well understood. Composite materials in aircraft structures are subject operating temperatures ranging from -60 °C to 180 °C (Collard, 1999), while water absorption, or diffusion is an important parameter relating to the degradation of composites used in the marine industry. Bian et al. (2012) analysed the effect of submersing glass fibre reinforced epoxy test specimens in artificial sea water for 28 days and noted a significant degradation of the composite stiffness and strength. The nanoindentation methods outlined in this thesis could be used to assess the in situ degradation of the constituent properties due to such environmental effects during service.

While the existence and size of the 'interphase' region has been confirmed using AFM (Gao and Mäder, 2002; Cech et al., 2013), nanoscratch (Hodzic et al., 2001) and TEM (Wu et al., 2014) techniques, quantitative mechanical characterisation of the sub-micron sized region by indentation methods remains a challenge. Recently, Gu et al. (2010) characterised the interphase of a carbon-fibre epoxy composite using a dynamic mechanical property mapping technique. A Berkovich indenter was scanned across the surface with a constant normal load of 2 µN and a superimposed dynamic force of 1 µN at 200 Hz, to produce the storage modulus results shown in Fig. 7.1. While accurate quantitative characterisation is difficult using this technique due to the extremely low loads employed, modulus mapping techniques show promise for future indentation studies on composite microstructures if sharper tip geometries and low depths are employed. Future studies could examine the effect of composite processing and environmental ageing on the properties of the interphase region. As the resulting indentation depths from such studies are in the order of a few nanometres, Molecular Dynamics (MD) simulations could be used to analyse the experimental data as an alternative to using the nanoindentation theory or continuum based finite element methods. MD simulations would also provide a novel insight into the effects of fibre constraint and hydrostatic stress on shallow interphase region indentations, at the molecular level.

In Chapters 3 and 5 it was shown that quantitative characterisation of the interphase region at the depths required for reliable nanoindentation measurements is difficult due to fibre constraint effects. The fibre constraint problem is analogous to the substrate effect which is predominant during the indentation of thin film materials. The substrate effect is often investigated using analytical solutions (Bec et al., 2006). However, these solutions are often mathematically complex or for very limited cases. Finite element solutions allow more complex properties and geometries to be investigated. Fig. 7.2a shows a finite element model carried out on a thin film material by Pandure et al. (2014) investigating the substrate effect. Fig. 7.2b shows a finite element investigation carried out by Li et al. (2012) into the effect of fibre constraint on the characterisation of the interphase region of a fibrous composite. Reverse finite element modelling has been used to determine the properties of thin film materials when substrate effects are unavoidable. Knapp et al. (1999) used simulations of a thin film indentation to correct for the substrate effect. The known properties of the substrate and the indenter materials were fixed, while a series of simulations were performed varying the properties of the thin film material. The results were then linearly interpolated to predict the ‘best fit’ properties which produced force and stiffness responses that fit the experimental result. Recently,

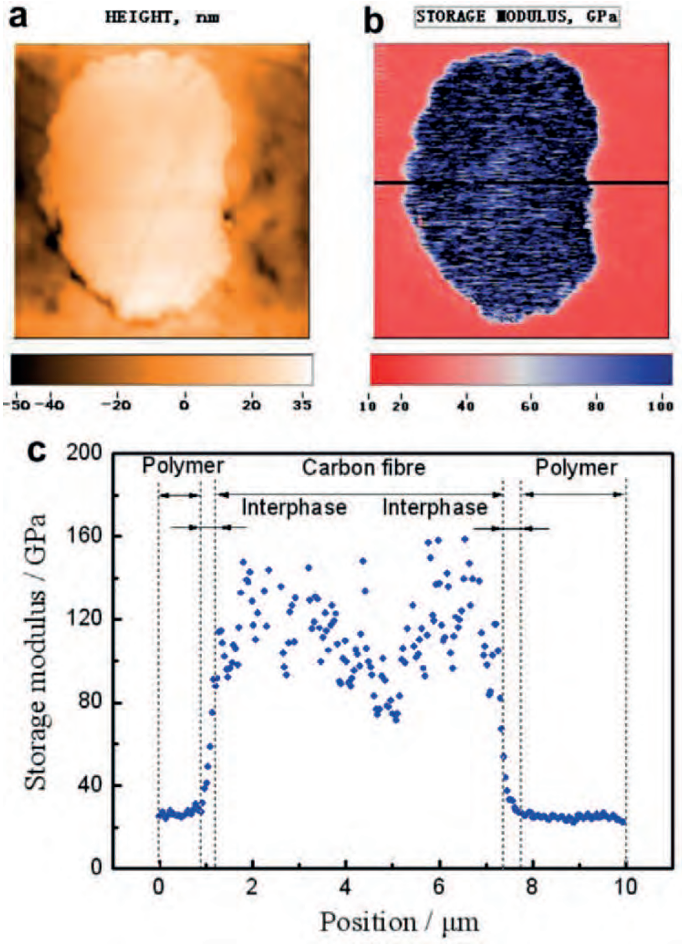

Figure 7.1: 10×10 µm dynamic mechanical map of CFRP using dynamic nanoscale imaging (a) fibre-matrix topography, (b) storage modulus map, (c) storage modulus variation across interface (Gu et al., 2010)

similar approaches have been used by Wang et al. (2010) and Zheng et al. (2011). A similar strategy could be employed to determine the properties of the interphase region in fibrous composite materials, where fibre constraint effects are unavoidable. A 3D finite element methodology, similar to that presented in Chapter 3, could be used to accurately model the geometry of the fibre and matrix constituents and facilitate the reverse analysis.

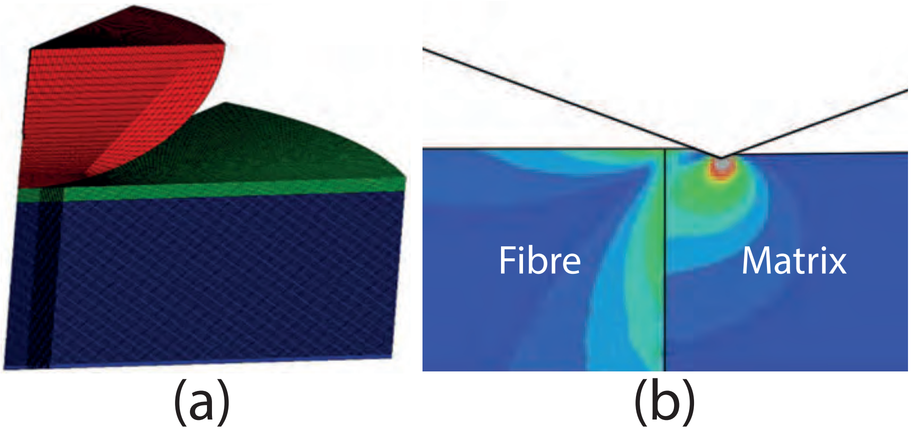

Figure 7.2: Finite element simulations of nanoindentation: (a) Thin film applied to substrate (adapted from Pandure et al. 2014) (b) Interphase region of fibrous composite (adapted from Li et al. 2012)

7.2.2 Residual stress effects

The HTA/6376 material, which was examined in this work, has a relatively low cure temperature in comparison to other composite material systems. The finite element modelling in Chapter 4 showed that the composite microstructure was in a state of elastic residual stress following thermal cooldown, with no matrix plasticity or interfacial damage resulting from the thermal step. Previous experimental (Gentz et al., 2004) and numerical (Yang et al., 2013) studies of residual stress effects in fibrous composites have shown that matrix plasticity and interfacial damage can occur due to the residual stress state induced during processing. Thus, the effect of these higher stress states on the nanoindentation test has still not been investigated. Material systems such as thermoplastic and metal matrix composites (MMCs) undergo large temperature changes following cure. Thus, the effect of the residual stress on the nanoindentation properties of these material systems warrants future investigation.

Thermal stress has been shown to significantly affect the transverse micromechanical behaviour of fibrous composites. While thermal cooldown modelling is useful for determining the stress state, the quantitative accuracy of these predictions may be influenced by other factors such as chemical shrinkage and local temperature gradients during curing. The nanoindentation technique has been successfully used by a number of authors to quantify equibiaxial stress states in thin copper foils (Dean et al., 2011), tungsten thin films (Qasmi et al., 2006) and aerospace aluminium alloys (Khan et al., 2011). A method could be developed to quantify the residual stress in the various regions of the fibrous composite microstructure, which would serve as a useful input to future micromechanical studies. By annealing specimens above the glass-transition temperature, the residual stress could be reduced and experimental indentation results could be compared with as-processed specimens.

7.2.3 Nanoindentation of polymers

The experimental and analytical methods presented in Chapter 6 moved toward addressing the well-known disparity between the indentation and macroscopic elastic characterisation of polymer materials using the standardised nanoindentation theory. However, further testing is required on a wide array of polymeric materials in order to validate the proposed methodology. The compressive modulus of the 6376 epoxy investigated in this study was unknown, and a disparity between the tensile and compressive modulus of the material may account somewhat for the difference between the macroscopic and indentation moduli. Also, the effect of material pile-up on polymer nanoindentation was not conclusively characterised. Recent advances of in situ indentation techniques have allowed the nanoindentation process to be observed with electron imagery (Nili et al., 2013). Fig. 7.3 shows an indentation observed inside the chamber of an SEM carried out by Rabe et al. (2004). The in situ images clearly show the material pile-up around the indenter tip, as well as the formation of a small crack during unloading in Figs. 7.3d and 7.3e. In situ indentation of polymer materials would provide a conclusive insight into the state of material pile-up at maximum indentation load, and allow observation of the elastic and viscoelastic surface recovery sequence for polymeric materials, during and following the indenter unloading process.

In micromechanical simulations of composite failure, the elastic behaviour of the matrix constituent is generally defined using the elastic modulus. However, as highlighted in Chapter 6, the elastic behaviour of polymeric materials is complicated by their viscoelastic time-dependent nature. Thus, nanoindentation testing and analysis procedures that account for viscoelastic and viscoplastic polymer behaviour are required. Fischer-Cripps (2004) proposed a simple phenomenological spring-dashpot model to characterise the creep compliance using nanoindentation. Dynamic nanoindentation techniques to measure the complex storage and loss moduli of time dependent materials have also been proposed by Odegard et al. (2003), and found to be in good agreement with values from dynamic mechanical analysis (DMA) of macroscopic samples. However, to date no comparisons have been made between the viscoelastic properties of bulk and in situ polymer composite matrix constituents.

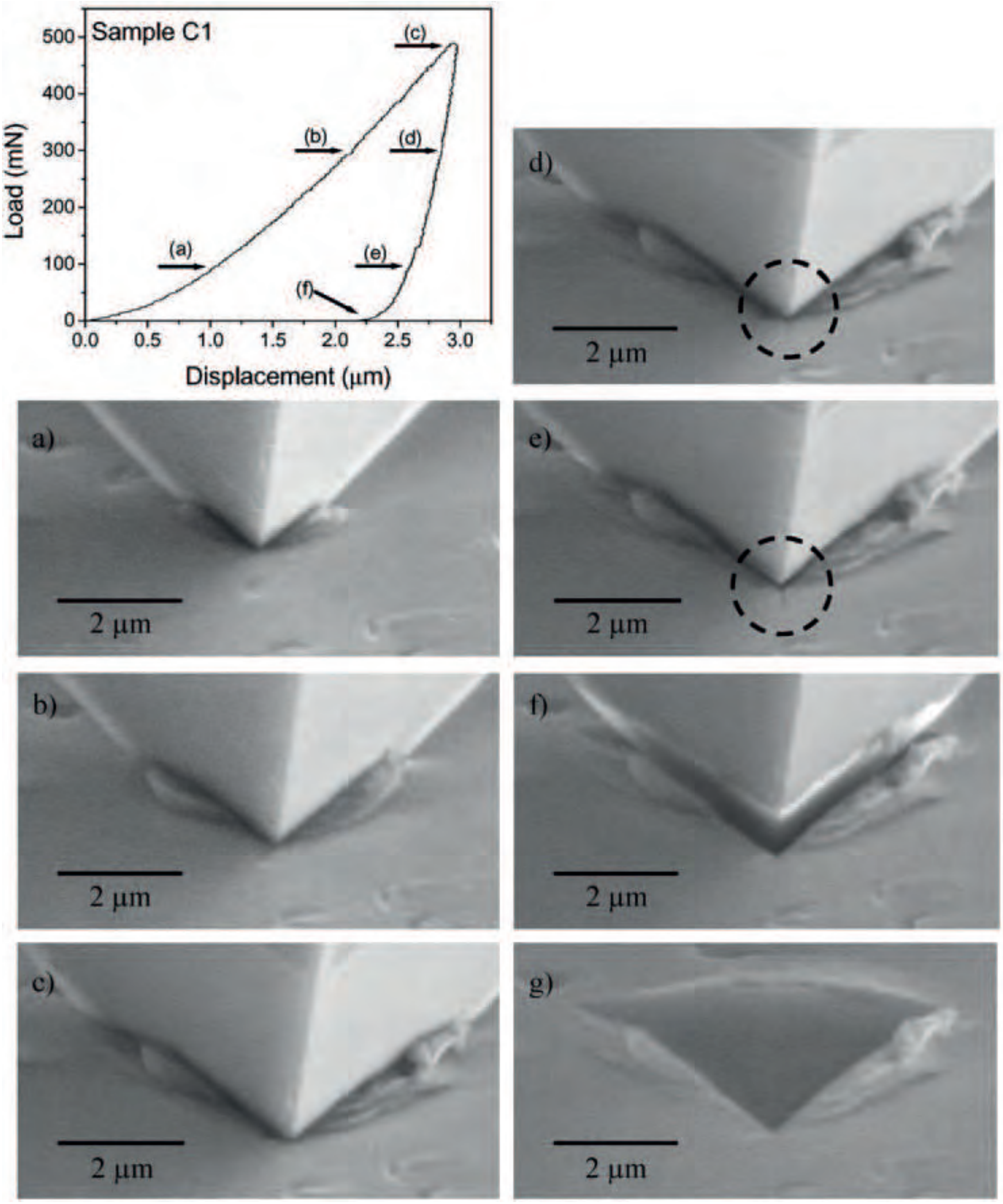

Figure 7.3: SEM indentation made on thin TiN/SiNx coating deposited on Si (Rabe et al., 2004).

7.2.4 Push-out testing

The strength and toughness of the fibre-matrix interface play a significant role in the micromechanical failure of fibrous composite materials under transverse (Vaughan and McCarthy, 2011a) and shear (Vaughan and McCarthy, 2011b) loadings. A number of experimental approaches to determine the interfacial properties have been attempted, such as the single-fibre fragmentation test, the single-fibre pull-out test, the single-fibre microbond test, and the push-out test. Single-fibre tests have proven useful in determining the effectiveness of various fibre treatments on the interfacial strength. However, single fibres are rarely isolated in high fibre volume fraction aerospace composite materials. Thus, in situ push-out testing provides a better representation of the interfacial properties in service, following composite material processing. First introduced by Marshall (1984), the push-out test can be used to determine the strength of the fibre-matrix interface by loading an individual fibre with a diamond indenter tip and increasing the load until interfacial debonding occurs. An SEM image of a pushed out fibre from testing carried out by Canal et al. (2012) on a glass fibre/epoxy composite is shown in in Fig. 7.4.

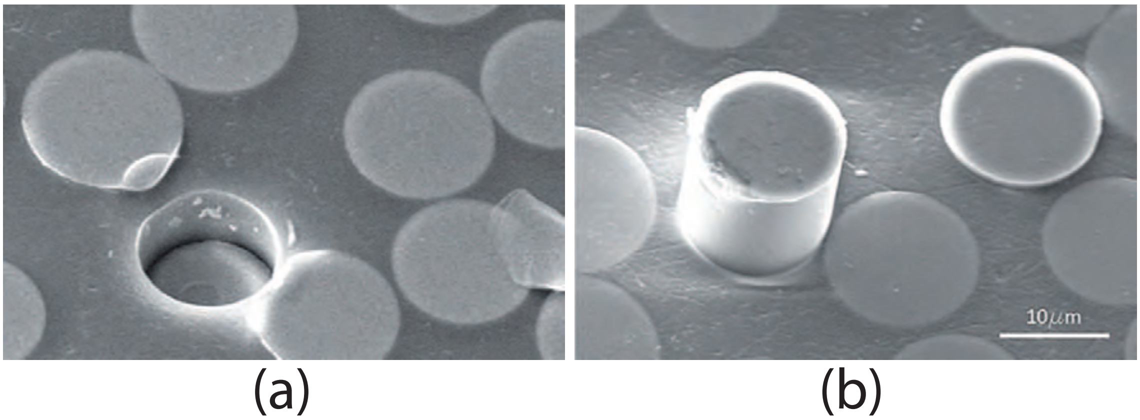

Figure 7.4: SEM image of (a) upper surface of the composite slice after the push-out test, (b) lower surface of the composite slice after the push-out test.(Canal et al., 2012)

Recently, Mueller et al. (2013) developed a new cyclic loading energy-based approach to the push-out test which allows the interfacial toughness to be determined. Push-out testing coupled with this new methodology could be used to evaluate the interfacial properties of the HTA/6376 composite, and provide directly determined values of interfacial strength and toughness to future micromechanical models. The effect of rate-dependence and environmental ageing on interfacial failure are also not well understood. Another important aspect of interfacial mechanics is the roll of thermal residual stress. Thomason and Yang (2011) measured the interfacial strength of glass fibre reinforced polypropylene across a temperature range of -40

°C to 100 °C using microbond testing and showed that approximately 70% of the apparent room temperature interfacial strength can be attributed to the residual compressive stress at the fibre-matrix interface. Greisel et al. (2014) recently investigated the influence of thermal stress on the push-out test and found that annealing the composite above the glass transition temperature of the matrix led to a significant increase in the interfacial toughness. Future experimental push-out studies could provide further insight into the effects of residual stress on the interfacial behaviour. The finite element results presented in Chapter 4 show that the interfacial thermal stress state is highly dependent on the fibre volume fraction and spacings. Thus, the interfacial strengths are also likely be a dependent on the fibre-matrix distribution. The various fibre packing arrangements provided by the 'hybrid' specimens (presented in Chapter 5) and recent developments in the analysis of push-out test data present the opportunity for future experimental studies into the effect of fibre distribution on the interfacial strength and toughness. The contact finite element methodology outlined in this work could also be useful in analysing the effect of thermal stress and surrounding fibre distribution on the push-out test.

Bibliography

Aalco (2016), Aluminium alloy 5754 - h22 sheet and plate, Technical report.

ABAQUS-Inc. (2013), *ABAQUS User Manual, Version 6.13*, Dassault Syst Systémes Simulia Corp., Providence, RI, USA.

Agilent (2009), Indentation rules of thumb: Applications and limits, Technical report, Agilent Technologies.

Agilent (2013), *Nanosuite 6.20.413*, Agilent Technologies.

Altenbach, H. and Tushtev, K. (2001), 'A New Static Failure Criterion for Isotropic Polymers', *Mechanics of Composite Materials* **37**(5), 475–482.

Asif, S. A. S., Wahl, K. J. and Colton, R. J. (1999), 'Nanoindentation and contact stiffness measurement using force modulation with a capacitive load-displacement transducer', *Review of Scientific Instruments* **70**(5).

Asp, L. E., Berglund, L. A. and Talreja, R. (1996), 'Prediction of matrix-initiated transverse failure in polymer composites', *Composites Science and Technology* **56**(9), 1089–1097.

ASTM (2007), 'Standard guide for preparation of flat composite panels with processing guidelines for specimen preparation'.

ASTM (2011), 'Standard guide for preparation of metallographic specimens'.

Atkins, A. and Tabor, D. (1965), 'Plastic indentation in metals with cones', *Journal of the Mechanics and Physics of Solids* **13**(3), 149–164.

Bai, M., Kato, K., Umehara, N. and Miyake, Y. (2000), 'Nanoindentation and fem study of the effect of internal stress on micro/nano mechanical property of thin cnx films', *Thin Solid Films* **377-378**(0), 138–147.

Beake, B. D. and Leggett, G. J. (2002), 'Nanoindentation and nanoscratch testing of uniaxially and biaxially drawn poly(ethylene terephthalate) film', *Polymer* **43**(2), 319–327.

Bec, S., Tonck, A. and Loubet, J. L. (2006), ‘A simple guide to determine elastic properties of films on substrate from nanoindentation experiments’, *Philosophical Magazine* **86**, 5347–5358.

Beegan, D., Chowdhury, S. and Laugier, M. T. (2003), ‘A nanoindentation study of copper films on oxidised silicon substrates’, *Surface and Coatings Technology* **176**(1), 124–130.

Beegan, D., Chowdhury, S. and Laugier, M. T. (2005), ‘Work of indentation methods for determining copper film hardness’, *Surface and Coatings Technology* **192**(1), 57–63.

Berkovich, E. S. (1950), ‘Three-Faceted Diamond Pyramid for Studying Microhardness by Indentation’, *Zavodskaia laboratoriia* **13**(3), 345–347.

Beyaoui, M., Mazeran, P.-E., Arvieu, M.-F., Bigerelle, M. and Guigon, M. (2009), ‘Analysis of nanoindentation curves in the case of bulk amorphous polymers’, *International Journal of Materials Research* **100**(7), 943–949.

Bhattacharya, A. K. and Nix, W. D. (1988), ‘Finite element simulation of indentation experiments’, *International Journal of Solids and Structures* **24**(9), 881–891.

Bian, L., Xiao, J., Zeng, J. and Xing, S. (2012), ‘Effects of seawater immersion on water absorption and mechanical properties of GFRP composites’, *Journal of Composite Materials* **46**(25), 3151–3162.

Birch, F. (1938), The Effect of Pressure Upon the Elastic Parameters of Isotropic Solids, According to Murnaghan’s Theory of Finite Strain, *in* ‘Elastic Properties and Equations of State’, American Geophysical Union, pp. 21–30.

Bolshakov, A., Oliver, W. C. and Pharr, G. M. (1996), ‘Influences of stress on the measurement of mechanical properties using nanoindentation: Part ii. finite element simulations’, *Journal of Materials Research* **11**(03), 760–768.

Bolshakov, A. and Pharr, G. M. (1998), ‘Influences of pileup on the measurement of mechanical properties by load and depth sensing indentation techniques’, *Journal of Materials Research* **13**(04), 1049–1058.

Boussinesq, J. (1885), *Applications des potentiels à l'étude de l'équilibre et du mouvement des solides élastiques*, Gauthier-Villars, Paris.

Bressan, J. D., Tramontin, A. and Rosa, C. (2005), 'Modeling of nanoindentation of bulk and thin film by finite element method', *Wear* **258**(1-4), 115–122.

Breuils, J., Krier, J., Pelletier, H. and Mille, P. (2011), 'Identification, using nanoindentation tests, of mechanical behaviour of a 2c22 steel presenting a residual stress state', *Procedia Engineering* **10**(0), 3528–3533.

Briscoe, B. J., Fiori, L. and Pelillo, E. (1998), 'Nano-indentation of polymeric surfaces', *Journal of Physics D: Applied Physics* **31**(19), 2395.

Briscoe, B. J. and Sebastian, K. S. (1996), *The Elastoplastic Response of Poly(Methyl Methacrylate) to Indentation*, Vol. 452.

Cabibbo, M., Ciccarelli, D. and Spigarelli, S. (2013), 'Nanoindentation Hardness Measurement in Piling up SiO2 Coating', *Physics Procedia* **40**, 100–112.

Canal, L. P., GonzÃ¡lez, C., Segurado, J. and Llorca, J. (2012), 'Intraply fracture of fiber-reinforced composites: Microscopic mechanisms and modeling', *Composites Science and Technology* **72**(11), 1223–1232.

Cao, Y., Allameh, S., Nankivil, D., Sethiaraj, S., Otiti, T. and Soboyejo, W. (2006), 'Nanoindentation measurements of the mechanical properties of polycrystalline au and ag thin films on silicon substrates: Effects of grain size and film thickness', *Materials Science and Engineering: A* **427**(1-2), 232–240.

Cech, V., Palesch, E. and Lukes, J. (2013), 'The glass fiber-polymer matrix interface/interphase characterized by nanoscale imaging techniques', *Composites Science and Technology* **83**(0), 22–26.

Chuang, C. T., Chao, C. K., Chang, R. C. and Chu, K. Y. (2008), 'Effects of internal stresses on the mechanical properties of deposition thin films', *Journal of Materials Processing Technology* **201**(1-3), 770–774.

Collard, D. (1999), Concorde airframe design and development, Technical report, Swiss Institution of Aeronautical Sciences.

De Silva, R., Pasbakhsh, P., Goh, K., Chai, S.-P. and Chen, J. (2013), ‘Synthesis and characterisation of poly (lactic acid)/halloysite bionanocomposite films’, *Journal of Composite Materials* .

Dean, J., Aldrich-Smith, G. and Clyne, T. W. (2011), ‘Use of nanoindentation to measure residual stresses in surface layers’, *Acta Materialia* **59**(7), 2749–2761.

Deuschle, J. (2008), Mechanics of Soft Polymer Indentation, PhD thesis, Max-Planck-Institut für Metallforschung, Universität Stuttgart.

Doerner, M. and Nix, W. (1986), ‘A method for interpreting the data from depth-sensing indentation instruments’, *Journal of Materials Research* **1**(04), 601–609.

Downing, T. D., Kumar, R., Cross, W. M., Kjerengtroen, L. and Kellar, J. J. (2000), ‘Determining the interphase thickness and properties in polymer matrix composites using phase imaging atomic force microscopy and nanoindentation’, *Journal of Adhesion Science and Technology* **14**(14), 1801–1812.

Fiedler, B., Hobbiebrunken, T., Hojo, M. and Schulte, K. (2005), ‘Influence of stress state and temperature on the strength of epoxy resins’.

Fiedler, B., Hojo, M., Ochiai, S., Schulte, K. and Ando, M. (2001), ‘Failure behavior of an epoxy matrix under different kinds of static loading’, *Composites Science and Technology* **61**(11), 1615–1624.

Fischer-Cripps, A. C. (2004), ‘A simple phenomenological approach to nanoindentation creep’, *Materials Science and Engineering A* **385**(1-2), 74–82.

Fischer-Cripps, A. C. (2009), *The IBIS Handbook of Nanoindentation*, Fischer-Cripps Laboratories Pty Ltd, P.O. Box 9, Forestville NSW 2087 Australia.

Fröhlich, F., Grau, P. and Grellmann, W. (1977), ‘Performance and analysis of recording microhardness tests’, *physica status solidi (a)* **42**(1), 79–89.

Frontini, P., Lotfian, S., Monclús, M. A. and Molina-Aldareguia, J. M. (2015), ‘High temperature nanoindentation response of rtm6 epoxy resin at different strain rates’, *Experimental Mechanics* pp. 1–12.

Gao, S.-L. and Mäder, E. (2002), ‘Characterisation of interphase nanoscale property variations in glass fibre reinforced polypropylene and epoxy resin composites’, *Composites Part A: Applied Science and Manufacturing* **33**(4), 559–576.

Gentz, M., Benedikt, B., Sutter, J. K. and Kumosa, M. (2004), ‘Residual stresses in unidirectional graphite fiber/polyimide composites as a function of aging’, *Composites Science and Technology* **64**(10-11), 1671–1677.

Gibson, R. F. (2014), ‘A review of recent research on nanoindentation of polymer composites and their constituents’, *Composites Science and Technology* **105**(0), 51–65.

Goel, S., Joshi, S. S., Abdelal, G. and Agrawal, A. (2014), ‘Molecular dynamics simulation of nanoindentation of Fe3C and Fe4C’, *Materials Science and Engineering: A* **597**, 331–341.

González, C. and Llorca, J. (2006), ‘Multiscale modeling of fracture in fiber-reinforced composites’, *Acta Materialia* **54**(16), 4171–4181.

González, C. and Llorca, J. (2007), ‘Mechanical behavior of unidirectional fiber-reinforced polymers under transverse compression: Microscopic mechanisms and modeling’, *Composites Science and Technology* **67**(13), 2795–2806.

Gregory, J. R. and Spearing, S. M. (2005), ‘Nanoindentation of neat and in situ polymers in polymer-matrix composites’, *Composites Science and Technology* **65**(3-4), 595–607.

Greisel, M., Jäger, J., Moosburger-Will, J., Sause, M., Mueller, W. and Horn, S. (2014), ‘Influence of residual thermal stress in carbon fiber-reinforced thermoplastic composites on interfacial fracture toughness evaluated by cyclic single-fiber push-out tests’, *Composites Part A: Applied Science and Manufacturing* **66**, 117–127.

Gu, Y., Li, M., Wang, J. and Zhang, Z. (2010), ‘Characterization of the interphase in carbon fiber/polymer composites using a nanoscale dynamic mechanical imaging technique’, *Carbon* **48**(11), 3229–3235.

Guicciardi, S., Melandri, C., Silvestroni, L. and Sciti, D. (2008), ‘Indentation grid analysis of nanoindentation bulk and inÂ situ properties of ceramic phases’, *Journal of Materials Science* **43**(12), 4348–4352.

Han, C.-S. (2010), ‘Influence of the molecular structure on indentation size effect in polymers’, *Materials Science and Engineering: A* **527**(3), 619–624.

Hay, J. C., Bolshakov, A. and Pharr, G. M. (1999), ‘A critical examination of the fundamental relations used in the analysis of nanoindentation data’, *Journal of Materials Research* **14**(06), 2296–2305.

Herakovich, C. T. (2012), ‘Mechanics of composites: A historical review’.

Hertz, H. (1881), ‘On the contact of elastic solids’, *J. Reine Angew. Math.* **92**(156).

Hexcel (2007), Hexply® 6376 product data, Technical report.

Hobbiebrunken, T., Hojo, M., Adachi, T., De Jong, C. and Fiedler, B. (2006), ‘Evaluation of interfacial strength in cf/epoxies using fem and in-situ experiments’, *Composites Part A: Applied Science and Manufacturing* **37**(12), 2248–2256.

Hochstetter, G., Jimenez, A. and Loubet, J. L. (1999), ‘Strain-rate effects on hardness of glassy polymers in the nanoscale range. comparison between quasi-static and continuous stiffness measurements’, *Journal of Macromolecular Science, Part B* **38**(5-6), 681–692.

Hodzic, A., Kim, J. K., Lowe, A. E. and Stachurski, Z. H. (2004), ‘The effects of water aging on the interphase region and interlaminar fracture toughness in polymer-glass composites’, *Composites Science and Technology* **64**(13-14), 2185–2195.

Hodzic, A., Kim, J. K. and Stachurski, Z. H. (2001), ‘Nano-indentation and nano-scratch of polymer/glass interfaces. ii: model of interphases in water aged composite materials’, *Polymer* **42**(13), 5701–5710.

Hodzic, A., Stachurski, Z. H. and Kim, J. K. (2000), ‘Nano-indentation of polymer-glass interfaces part i. experimental and mechanical analysis’, *Polymer* **41**(18), 6895–6905.

Hojo, M., Mizuno, M., Hobbiebrunken, T., Adachi, T., Tanaka, M. and Ha, S. K. (2009), ‘Effect of fiber array irregularities on microscopic interfacial normal stress states of transversely loaded ud-cfrp from viewpoint of failure initiation’, *Composites Science and Technology* **69**(11-12), 1726–1734.

Huang, Y.-C., Chang, S.-Y. and Chang, C.-H. (2009), ‘Effect of residual stresses on mechanical properties and interface adhesion strength of sin thin films’, *Thin Solid Films* **517**(17), 4857–4861.

ISO (2012), ‘527-1: Plastics - determination of tensile properties - part 1: General principles’.

ISO (2015), ‘14577: Metallic materials – instrumented indentation test for hardness and materials parameters’.

Jin, T., Niu, X., Xiao, G., Wang, Z., Zhou, Z., Yuan, G. and Shu, X. (2015), ‘Effects of experimental variables on pmma nano-indentation measurements’, *Polymer Testing* **41**(0), 1–6.

Jones, F. R. (2010), ‘A Review of Interphase Formation and Design in Fibre-Reinforced Composites’, *Journal of Adhesion Science and Technology* **24**(1), 171–202.

Jones Parry, E. and Tabor, D. (1973), ‘Effect of hydrostatic pressure on the mechanical properties of polymers: a brief review of published data’, *Journal of Materials Science* **8**(10), 1510–1516.

Kaddour, A. S. and Hinton, M. J. (2013), ‘Maturity of 3D failure criteria for fibre-reinforced composites: Comparison between theories and experiments: Part B of WWFE-II’, *Journal of Composite Materials* **47**(6-7), 925–966.

Kese, K. and Li, Z. C. (2006), ‘Semi-ellipse method for accounting for the pile-up contact area during nanoindentation with the Berkovich indenter’, *Scripta Materialia* **55**(8), 699–702.

Khan, M. K., Fitzpatrick, M. E., Hainsworth, S. V. and Edwards, L. (2011), ‘Effect of residual stress on the nanoindentation response of aerospace aluminium alloys’, *Computational Materials Science* **In Press, Corrected Proof**.

Khan, M. K., Hainsworth, S. V., Fitzpatrick, M. E. and Edwards, L. (2010), 'A combined experimental and finite element approach for determining mechanical properties of aluminium alloys by nanoindentation', *Computational Materials Science* **49**(4), 751–760.

Khanna, S. K., Ranganathan, P., Yedla, S. B., Winter, R. M. and Paruchuri, K. (2003a), 'Investigation of nanomechanical properties of the interphase in a glass fiber reinforced polyester composite using nanoindentation', *Journal of Engineering Materials and Technology* **125**(2), 90–96. 10.1115/1.1543966.

Khanna, S. K., Winter, R. M., Ranganathan, P., Yedla, S. B., Kalukanimuttam, M. and Paruchuri, K. (2003b), 'Sample preparation techniques for nano-mechanical characterization of glass fiber reinforced polyester matrix composites', *Composites Part A: Applied Science and Manufacturing* **34**(1), 53–65.

Kim, J.-K. and Hodzic, A. (2003), 'Nanoscale characterisation of thickness and properties of interphase in polymer matrix composites', *The Journal of Adhesion* **79**(4), 383 – 414.

Kim, J.-K., Sham, M.-L. and Wu, J. (2001), 'Nanoscale characterisation of interphase in silane treated glass fibre composites', *Composites Part A: Applied Science and Manufacturing* **32**(5), 607–618.

King, J. A., Klimek, D. R., Miskioglu, I. and Odegard, G. M. (2013), 'Mechanical properties of graphene nanoplatelet/epoxy composites', *Journal of Applied Polymer Science* **128**(6), 4217–4223.

Knapp, J. A., Follstaedt, D. M., Barbour, J. C. and Myers, S. M. (1997), 'Finite-element modeling of nanoindentation for determining the mechanical properties of implanted layers and thin films', *Nuclear Instruments and Methods in Physics Research Section B: Beam Interactions with Materials and Atoms* **127-128**, 935–939.

Knapp, J. A., Follstaedt, D. M., Myers, S. M., Barbour, J. C. and Friedmann, T. A. (1999), 'Finite-element modeling of nanoindentation', *Journal of Applied Physics* **85**(3), 1460–1474.

Kranenburg, J. M., Tweedie, C. A., van Vliet, K. J. and Schubert, U. S. (2009), 'Challenges and progress in high-throughput screening of polymer mechanical properties by indentation', *Advanced Materials* **21**(35), 3551–3561.

Lagoudas, D., Thakre, P. and Amine Benzerga, A. (2006), *Nanoindentation of CNT Reinforced Epoxy Nanocomposites*, Springer Netherlands, chapter 321, pp. 649–650.

Larsson, P. L., Giannakopoulos, A. E., SÖderlund, E., Rowcliffe, D. J. and Vestergaard, R. (1996), 'Analysis of berkovich indentation', *International Journal of Solids and Structures* **33**(2), 221–248.

Lee, S.-H., Wang, S., Pharr, G. M. and Xu, H. (2007), 'Evaluation of interphase properties in a cellulose fiber-reinforced polypropylene composite by nanoindentation and finite element analysis', *Composites Part A: Applied Science and Manufacturing* **38**(6), 1517–1524.

Li, Y., Li, M., Gu, Y., Zhang, Z. and Guan, P. (2012), 'Investigation of the nanoscale mechanical properties of carbon fiber/epoxy resin interphase. i. analysis of fiber-stiffening effect during the nanoindentation process based on numerical simulation', *Polymer Composites* **33**(8), 1387–1394.

Liao, Y., Zhou, Y., Huang, Y. and Jiang, L. (2009), 'Measuring elastic-plastic properties of thin films on elastic-plastic substrates by sharp indentation', *Mechanics of Materials* **41**(3), 308–318.

Lichinchi, M., Lenardi, C., Haupt, J. and Vitali, R. (1998), 'Simulation of berkovich nanoindentation experiments on thin films using finite element method', *Thin Solid Films* **312**(1-2), 240–248.

Ling, L., Long, S., Ma, Z. and Liang, X. (2010), 'Numerical study on the effects of equi-biaxial residual stress on mechanical properties of nickel film by means of nanoindentation', *Journal of Materials Science &amp; Technology* **26**(11), 1001–1005.

Livingston, E. H. (2004), 'Who was student and why do we care so much about his t-test?', *Journal of Surgical Research* **118**(1), 58–65.

Llorca, J., González, C., Molina-Aldareguía, J. M., Segurado, J., Seltzer, R., Sket, F., Rodríguez, M., Sádaba, S., Muñoz, R. and Canal, L. P. (2011), 'Multiscale modeling of composite materials: a roadmap towards virtual testing', *Advanced Materials* **23**(44), 5130–5147.

Love, A. E. H. (1939), 'BOUSSINESQ'S PROBLEM FOR A RIGID CONE', *The Quarterly Journal of Mathematics* **os-10**(1), 161–175.

Lu, H., Wang, B., Ma, J., Huang, G. and Viswanathan, H. (2003), 'Measurement of Creep Compliance of Solid Polymers by Nanoindentation', *Mechanics of Time-Dependent Materials* **7**(3-4), 189–207.

Maligno, A. R., Warrior, N. A. and Long, A. C. (2009), 'Effects of inter-fibre spacing on damage evolution in unidirectional (UD) fibre-reinforced composites', *European Journal of Mechanics - A/Solids* **28**(4), 768–776.

Mann, A. B. (2005), *Nanotribology and Nanomechanics: An Introduction*, Springer Berlin Heidelberg, Berlin, Heidelberg, chapter Nanomechanical Properties of Solid Surfaces and Thin Films, pp. 575–622.

Marshall, D. B. (1984), 'An Indentation Method for Measuring Matrix-Fiber Frictional Stresses in Ceramic Composites', *Journal of the American Ceramic Society* **67**(12), C–259–C–260.

Marteau, J., Bouvier, S. and Bigerelle, M. (2014), 'Review on Numerical Modeling of Instrumented Indentation Tests for Elastoplastic Material Behavior Identification', *Archives of Computational Methods in Engineering* **22**(4), 577–593.

Mata, M. and Alcalá, J. (2004), 'The role of friction on sharp indentation', *Journal of the Mechanics and Physics of Solids* **52**(1), 145–165.

Mathworks (2010), *Maltab R2010a (version 7.10)*, The Mathworks, Inc.

Mazumdar, S. (2015), 'What Will Drive Composites Growth in 2015?', *Composites Manufacturing Magazine* .

McElhaney, K. W., Vlassak, J. J. and Nix, W. D. (1998), 'Determination of indenter tip geometry and indentation contact area for depth-sensing indentation experiments', *Journal of Materials Research* **13**(05), 1300–1306.

Mike Keeble, B. L. (2013), 'Personnal communication'.

Moharrami, N. and Bull, S. (2014), 'A comparison of nanoindentation pile-up in bulk materials and thin films', *Thin Solid Films* **572**, 189–199.

Mueller, W., Moosburger-Will, J., Sause, M. and Horn, S. (2013), 'Microscopic analysis of single-fiber push-out tests on ceramic matrix composites performed with Berkovich and flat-end indenter and evaluation of interfacial fracture toughness', *Journal of the European Ceramic Society* **33**(2), 441–451.

Nili, H., Kalantar-zadeh, K., Bhaskaran, M. and Sriram, S. (2013), 'In situ nanoindentation: Probing nanoscale multifunctionality', *Progress in Materials Science* **58**(1), 1–29.

Odegard, G. M., Herring, H. M. and Gates, T. S. (2003), T.s.: Characterization of viscoelastic properties of polymeric materials through nanoindentation, *in* '2003 SEM Annual Conference and Exposition on Experimental and Applied Mechanics. Charlotte, NC; Society of Experimental Mechanics'.

O'Higgins, R. M., McCarthy, M. A. and McCarthy, C. T. (2008), 'Comparison of open hole tension characteristics of high strength glass and carbon fibre-reinforced composite materials', *Composites Science and Technology* **68**(13), 2770–2778.

Oliver, W. C. and Pharr, M. G. (2004), *Measurement of hardness and elastic modulus by instrumented indentation: Advances in understanding and refinements to methodology*, Vol. 19, Cambridge University Press, Cambridge, Royaume-Uni.

Oliver, W. and Pharr, G. (1992), 'An improved technique for determining hardness and elastic modulus using load and displacement sensing indentation experiments', *Journal of Materials Research* **7**(06), 1564–1583.

Oyen, M. L. (2005), Ultrastructural Characterization of Time-Dependent, Inhomogeneous Materials and Tissues, PhD thesis, University of Minnesota.

Oyen, M. L. (2007), 'Sensitivity of polymer nanoindentation creep measurements to experimental variables', *Acta Materialia* **55**(11), 3633–3639.

Pae, K. D. and Bhateja, S. K. (1975), 'The Effects of Hydrostatic Pressure on the Mechanical Behavior of Polymers', *Journal of Macromolecular Science, Part C* **13**(1), 1–75.

Pandure, P. S., Jatti, V. S. and Singh, T. (2014), 'Finite Element Simulation of Nano-indentation of DLC Coated HSS Substrate', *Procedia Materials Science* **6**, 1619–1624.
URL: *http://www.sciencedirect.com/science/article/pii/S2211812814005100*

Panich, N. and Sun, Y. (2004), 'Effect of penetration depth on indentation response of soft coatings on hard substrates: a finite element analysis', *Surface and Coatings Technology* **182**(2-3), 342–350.

Pelegri, A. A. and Huang, X. (2008), 'Nanoindentation on soft film/hard substrate and hard film/soft substrate material systems with finite element analysis', *Composites Science and Technology* **68**(1), 147–155.

Pelletier, C. G. N., Den Toonder, J. M. J., Govaert, L. E., Hakiri, N. and Sakai, M. (2008), 'Quantitative assessment and prediction of contact area development during spherical tip indentation of glassy polymers', *Philosophical Magazine* **88**(9), 1291–1306.

Pharr, G. M. and Bolshakov, A. (2002), 'Understanding nanoindentation unloading curves', *Journal of Materials Research* **17**(10), 2660–2671.

Pharr, G. M., Oliver, W. C. and Brotzen, F. R. (1992), 'On the generality of the relationship among contact stiffness, contact area, and elastic modulus during indentation', *Journal of Materials Research* **7**(03), 613–617.

Philip, A. (2009), Instrumented indentation testing with the agilent nano indenter g200, Technical report, Agilent Technologies.

Qasmi, M., Delobelle, P., Richard, F. and Bosseboeuf, A. (2006), 'Effect of the residual stress on the determination through nanoindentation technique of the young's modulus of w thin film deposit on sio2/si substrate', *Surface and Coatings Technology* **200**(14-15), 4185–4194.

Rabe, R., Breguet, J.-M., Schwaller, P., Stauss, S., Haug, F.-J., Patscheider, J. and Michler, J. (2004), 'Observation of fracture and plastic deformation during indentation and scratching inside the scanning electron microscope', *Thin Solid Films* **469-470**, 206–213.

Randall, N. X., Julia-Schmutz, C. and Soro, J. M. (1998), ‘Combining scanning force microscopy with nanoindentation for more complete characterisation of bulk and coated materials’, *Surface and Coatings Technology* **108-109**(0), 489–495.

Rodríguez, J., Garrido-Maneiro, M. A., Poza, P. and Gómez-del Río, M. T. (2006), ‘Determination of mechanical properties of aluminium matrix composites constituents’, *Materials Science and Engineering: A* **437**(2), 406–412.

Rodríguez, M., Molina-Aldareguía, J. M., González, C. and Llorca, J. (2012), ‘Determination of the mechanical properties of amorphous materials through instrumented nanoindentation’, *Acta Materialia* **60**(9), 3953–3964.

Romanowicz, M. (2010), ‘Progressive failure analysis of unidirectional fiber-reinforced polymers with inhomogeneous interphase and randomly distributed fibers under transverse tensile loading’, *Composites Part A: Applied Science and Manufacturing* **41**(12), 1829–1838.

Ruan, H., Chen, A. and Lu, J. (2010), ‘Characterization of plastically graded nanostructured material: Part I. The theories and the inverse algorithm of nanoindentation’, *Mechanics of Materials* **42**(5), 559–569.

Saha, R. and Nix, W. D. (2001), ‘Soft films on hard substrates - nanoindentation of tungsten films on sapphire substrates’, *Materials Science and Engineering: A* **319-321**(0), 898–901.

Saha, R. and Nix, W. D. (2002), ‘Effects of the substrate on the determination of thin film mechanical properties by nanoindentation’, *Acta Materialia* **50**(1), 23–38.

Silano, A. A., Bhateja, S. K. and Pae, K. D. (1974), ‘Effects of Hydrostatic Pressure on the Mechanical Behavior of Polymers: Polyurethane, Polyoxymethylene, and Branched Polyethylene’, *International Journal of Polymeric Materials and Polymeric Biomaterials* **3**(2), 117–131.

Sneddon, I. N. (1948), ‘Boussinesq’s problem for a rigid cone’, *Mathematical Proceedings of the Cambridge Philosophical Society* **44**(04), 492–507.

Sneddon, I. N. (1965), ‘The relation between load and penetration in the axisymmetric boussinesq problem for a punch of arbitrary profile’, *International Journal of Engineering Science* **3**(1), 47–57.

Tabor, D. (1970), 'The hardness of solids', *Review of Physics in Technology* **1**(3), 145.

Tatiraju, V. S., Han, C. S. and Nikolov, S. (2008), 'Size dependent hardness of polyamide/imide', *The Open Mechanics Journal* **2**, 89–92.

Telford, R., Katnam, K. B. and Young, T. M. (2014), 'The effect of moisture ingress on through-thickness residual stresses in unsymmetric composite laminates: A combined experimental-numerical analysis', *Composite Structures* **107**(0), 502–511.

Tho, K. K., Swaddiwudhipong, S., Hua, J. and Liu, Z. S. (2006), 'Numerical simulation of indentation with size effect', *Materials Science and Engineering: A* **421**(1-2), 268–275.

Thomason, J. L. and Yang, L. (2011), 'Temperature dependence of the interfacial shear strength in glass-fibre polypropylene composites', *Composites Science and Technology* **71**(13), 1600–1605.

Totry, E., González, C. and Llorca, J. (2008), 'Failure locus of fiber-reinforced composites under transverse compression and out-of-plane shear', *Composites Science and Technology* **68**(3-4), 829–839.

Tranchida, D., Piccarolo, S., Loos, J. and Alexeev, A. (2006), 'Accurately evaluating young's modulus of polymers through nanoindentations: A phenomenological correction factor to the oliver and pharr procedure', *Applied Physics Letters* **89**(17), 171905–3.

Tranchida, D., Piccarolo, S., Loos, J. and Alexeev, A. (2007), 'Mechanical characterization of polymers on a nanometer scale through nanoindentation. a study on pile-up and viscoelasticity', *Macromolecules* **40**(4), 1259–1267.

Tseng, S.-C. and Osswald, T. A. (1994), 'Predicting shrinkage and warpage of fiber-reinforced composite parts', *Polymer Composites* **15**(4), 270–277.

van der Sluis, O., Schreurs, P. J. G., Brekelmans, W. A. M. and Meijer, H. E. H. (2000), 'Overall behaviour of heterogeneous elastoviscoplastic materials: effect of microstructural modelling', *Mechanics of Materials* **32**(8), 449–462.

VanLandingham, M. R., Dagastine, R. R., Eduljee, R. F., McCullough, R. L. and GillespieJr, J. W. (1999), 'Characterization of nanoscale property variations in polymer composite systems: 1. experimental results', *Composites Part A: Applied Science and Manufacturing* **30**(1), 75–83.

VanLandingham, M. R., Villarrubia, J. S., Guthrie, W. F. and Meyers, G. F. (2001), 'Nanoindentation of polymers: An overview', *Advances in Scanning Probe Microscopy of Polymers. Macromolecular Symposia* **167**.

Vaughan, T. J. and McCarthy, C. T. (2010), 'A combined experimental-numerical approach for generating statistically equivalent fibre distributions for high strength laminated composite materials', *Composites Science and Technology* **70**(2), 291–297.

Vaughan, T. J. and McCarthy, C. T. (2011*a*), 'Micromechanical modelling of the transverse damage behaviour in fibre reinforced composites', *Composites Science and Technology* **71**(3), 388–396.

Vaughan, T. J. and McCarthy, C. T. (2011*b*), 'A micromechanical study on the effect of intra-ply properties on transverse shear fracture in fibre reinforced composites', *Composites Part A: Applied Science and Manufacturing* **42**(9), 1217–1228.

Verkhovtsev, A. V., Yakubovich, A. V., Sushko, G. B., Hanauske, M. and Solovyov, A. V. (2013), 'Molecular dynamics simulations of the nanoindentation process of titanium crystal', *Computational Materials Science* **76**, 20–26.

Voyiadjis, G. and Peters, R. (2010), 'Size effects in nanoindentation: an experimental and analytical study', *Acta Mechanica* **211**(1), 131–153.

Wang, J., Zheng, X., Zheng, H., Song, S. and Zhu, Z. (2010), 'Identification of elastic parameters of transversely isotropic thin films by combining nanoindentation and FEM analysis', *Computational Materials Science* **49**(2), 378–385.

Wang, T. H., Fang, T.-H. and Lin, Y.-C. (2007), 'A numerical study of factors affecting the characterization of nanoindentation on silicon', *Materials Science and Engineering: A* **447**(1-2), 244–253.

Warren, A. and Guo, Y. (2006), 'Machined surface properties determined by nanoindentation: Experimental and FEA studies on the effects of surface integrity and tip geometry', *Surface and Coatings Technology* **201**(1-2), 423–433.

Wei, C. and Yang, J.-F. (2011), 'A finite element analysis of the effects of residual stress, substrate roughness and non-uniform stress distribution on the mechanical properties of diamond-like carbon films', *Diamond and Related Materials* **20**(5-6), 839–844.

Wu, Q., Li, M., Gu, Y., Li, Y. and Zhang, Z. (2014), 'Nano-analysis on the structure and chemical composition of the interphase region in carbon fiber composite', *Composites Part A: Applied Science and Manufacturing* **56**(0), 143–149.

Xu, Z.-H. and Li, X. (2005), 'Influence of equi-biaxial residual stress on unloading behaviour of nanoindentation', *Acta Materialia* **53**(7), 1913–1919.

Yang, L., Yan, Y., Ma, J. and Liu, B. (2013), 'Effects of inter-fiber spacing and thermal residual stress on transverse failure of fiber-reinforced polymer-matrix composites', *Computational Materials Science* **68**(0), 255–262.

Yedla, S. B., Kalukanimuttam, M., Winter, R. M. and Khanna, S. K. (2008), 'Effect of shape of the tip in determining interphase properties in fiber reinforced plastic composites using nanoindentation', *Journal of Engineering Materials and Technology* **130**(4), 041010–15.

Zhang, B., Yang, Z., Sun, X. and Tang, Z. (2010), 'A virtual experimental approach to estimate composite mechanical properties: Modeling with an explicit finite element method', *Computational Materials Science* **49**(3), 645–651.

Zhang, Y., Shi, T., Tang, Z. and Liao, G. (2015), 'An improved method to estimate Young's modulus of Zr-based BMGs accounting for pile-up during nanoindentation', *Journal of Non-Crystalline Solids* **427**, 20–25.

Zhao, L. G., Warrior, N. A. and Long, A. C. (2006), 'A micromechanical study of residual stress and its effect on transverse failure in polymer-matrix composites', *International Journal of Solids and Structures* **43**(18-19), 5449–5467.

Zheng, H., Zheng, X.-J., Song, S.-T., Sun, J., Jiao, F., Liu, W. and Wang, G.-Y. (2011), 'Evaluation of the elastic modulus of thin film considering the substrate effect and geometry effect of indenter tip', *Computational Materials Science* **50**(10), 3026–3031.

Zhou, X., Jiang, Z., Wang, H. and Yu, R. (2008), 'Investigation on methods for dealing with pile-up errors in evaluating the mechanical properties of thin metal films at sub-micron scale on hard substrates by nanoindentation technique', *Materials Science and Engineering: A* **488**(1-2), 318–332.

Appendices

A Publication Summary

Peer Reviewed Journal Papers

1. Hardiman, M., Vaughan, T. J. and McCarthy, C. T. (2012), 'The effect of fibre constraint in the nanoindentation of fibrous composite microstructures: A finite element investigation', Computational Materials Science 64(0), 162–167.

2. Hardiman, M., Vaughan, T. J. and McCarthy, C. T. (2015), 'Fibrous composite matrix characterisation using nanoindentation: The effect of fibre constraint and the evolution from bulk to in-situ matrix properties', Composites Part A: Applied Science and Manufacturing 68(0), 296–303.

3. Hardiman, M., Vaughan, T. J. and McCarthy, C. T. (2016), 'The effect of microscale residual stress from thermal cooldown on the nanoindentation properties of fibre-reinforced composites', Journal of Composite Materials.

4. Hardiman, M., Vaughan, T. J. and McCarthy, C. T., 'The Effects of Pile-Up, Viscoelasticity and Hydrostatic Stress on Polymer Matrix Nanoindentation', Polymer Testing.

Conference Proceedings

1. Hardiman M., McCarthy, C. Nanoindentation of Fibrous Composites. 21st International Workshop on Computational Mechanics of Materials (IWCMM 21), University of Limerick, Ireland, 21-24 August, 2010.

2. Hardiman M., McCarthy, C. Finite Element Modelling of Nanoindentation Applied to Fibrous Composites. 15th European Conference on Composite Materials (ECCM 15), Venice Congress Centre, Italy, 24-28 June, 2012.

3. Hardiman M., McCarthy, C. Nanoindentation of a Carbon-Fibre Composite Microstructure: Matrix Characterisation. 19th International Conference on Composite Materials (ICCM19), Palais des congress, Montreal, July 28 – August 2, 2013.

B Aluminium pile-up correction

B.1 Experimental setup

To investigate the effects of pile-up on the nanoindentation characterisation of the Aluminium Alloy 6082T6 alloy, residual indentations spanning four different indentation target depths (500 nm, 1 µm, 2 µm and 5µm) were investigated for evidence of the phenomenon. A total of 30 indentations were carried out for each depth. Following the experiments, a residual impression for each indentation depth was investigated using the optical microscope of the G200 (1000X magnification) and scanning probe microscopy (SPM). The nanovision stage was used to scan the surface and the time between the test's unloading cycle and the SPM scans was roughly one hour for all the scans. The tip was raster scanned the surface by moving the tip in the Y direction, and incrementing the lines in the X direction. A total of 100 data points were taken in the X direction while 250 points were taken in the Y direction for each line scan. Each line in the Y-direction took 2 seconds to scan and the scanning load was set to 1 µN. The cube corner indenter tip geometry was used as the probe for scanning, as the steeper face angle allows for more accurate scanning of the residual impressions created with the Berkovich indenter tip. The data from the scans was post-processed and plotted using the free and open source SPM data analysis software Gwyddion 2.30.

B.2 Results

The load-displacement data and indentation modulus results for the indentations carried out on the Aluminium Alloy 6082 are shown in Figs. B.1a and B.1b respectively. Fig. B.1b shows that the indentation moduli were consistent with indentation depth, but were larger than mean modulus determined from macroscopic testing (Aalco, 2016). According to finite element work carried out by Bolshakov and Pharr (1998), the ratio of residual indentation depth (h_p) to maximum indentation depth (h_{max}) can be used as in indicator for when pile-up is prevalent in an indentation. It was shown if $h_p/h_{max} > 0.7$, pile-up is likely, provided that the material does not work harden. This is clearly the case for the aluminium alloy tested, where the h_p/h_{max} is around equal to 0.9, as can be seen in the load displacement data in Fig. B.1a.

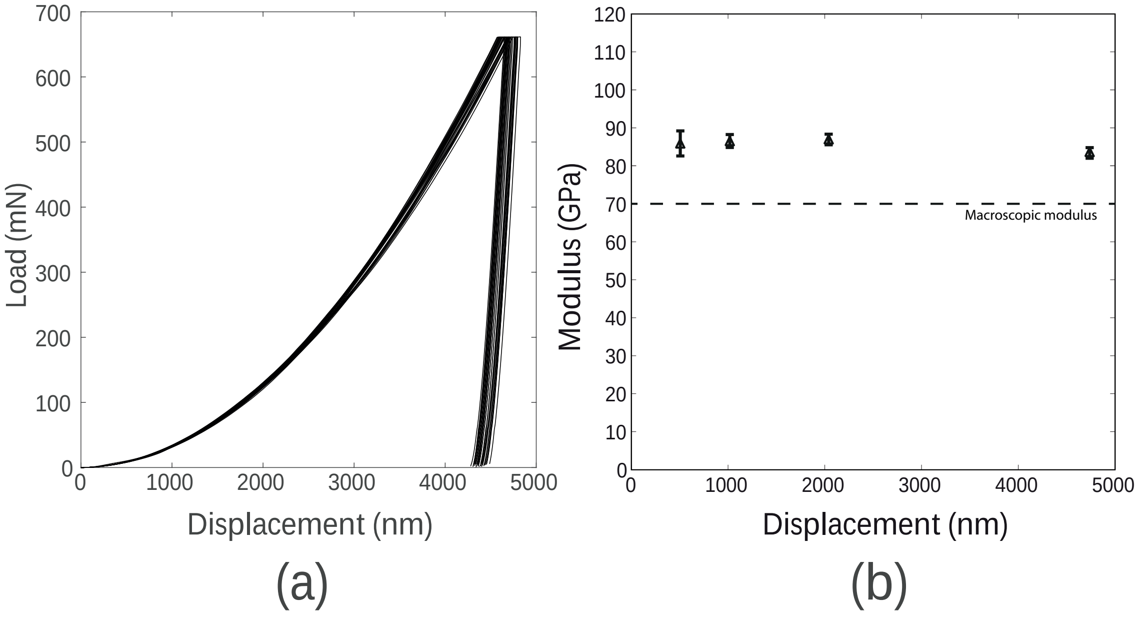

Figure B.1: Results from indentations carried out on Aluminium Alloy 6082T6: (a) load-displacement curves for 5 µm indentations (b) modulus results from CSM and basic indentations

The residual impression from a 5 µm indentation carried out into the Aluminium Alloy is shown in Fig. B.2. The optical micrograph of the impression is shown in Fig. B.2a, and the 3D SPM image is shown in Fig. B.2b. The outward curvature associated with material pile-up can clearly be seen in both images. The SPM image also shows that the material piles up around the outside of the edges of the indentation, as opposed to around the sharp corners. This is expected due to the high stress concentrations underneath the sharp corners of the indenter, and is similar to previous observations from AFM and SPM scans (Zhang et al., 2015; Moharrami and Bull, 2014).

The scanning probe micrographs were used to correct the contact area of the indentations by directly measuring the projected contact area (A_{PROJ}), and alternatively by correcting the contact depth based on the observed pile-up height (A_{PU}), as described in Chapter 6. The top view of the SPM image for the aluminium sample is illustrated in Fig. B.3a, where line scans A, B and C have been defined. The cross-sections of the line scans are shown in Fig. B.3b, which shows the extent of

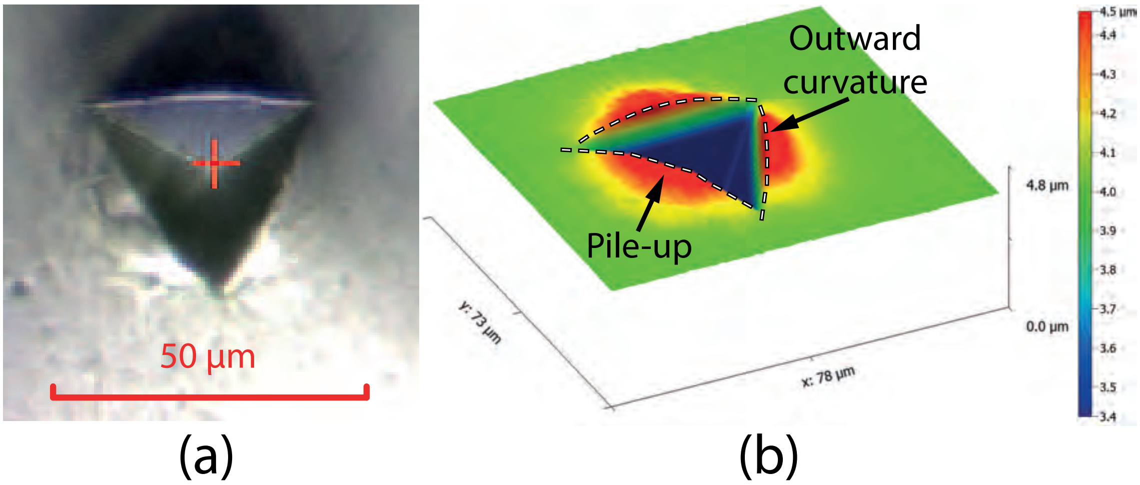

Figure B.2: The residual impression of a 5 µm indentation carried out on Aluminium Alloy 6082: (a) Optical microscope image (1000X), (b) SPM image

the material pile-up more clearly. The three line scans display very similar profiles, showing that the effect of sample tilt on the scans was minimal.

The corrected contact areas and moduli for the aluminium alloy have been normalised by dividing by the same parameters determined using the Oliver and Pharr method, and are plotted in Figs. B.4a and B.4b respectively. It is clear that similar measurements of the pile-up contact area have been measured using both methods based on the normalised areas plotted in Fig. B.4a. This in turn leads to similar reductions in the calculated moduli plotted in Fig. B.4b. The corrected indentation moduli show better correlation with the macroscopic value of 70 GPa, determined using BS EN 485-2:2008. The correlation between the macroscopic modulus and the corrected indentation moduli verifies the validity of both post-hoc correction methods for a material where the effect of material pile-up was prevalent.

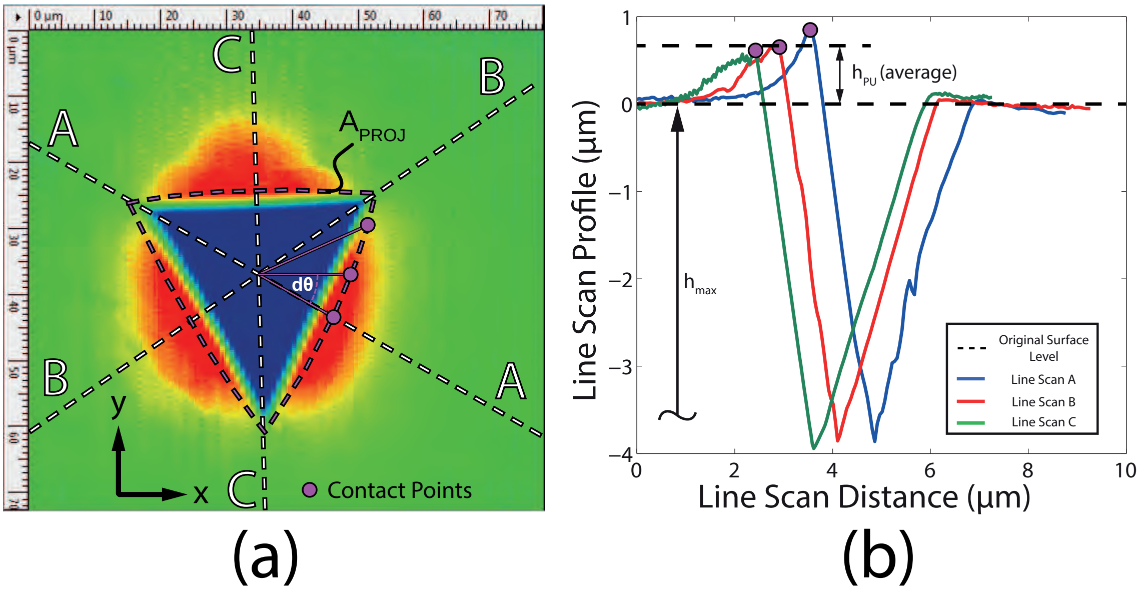

(a) (b)

Figure B.3: (a) Top view of Aluminium Alloy 6082 SPM image, highlighting locations of line scans, (b) Line scans A, B and C

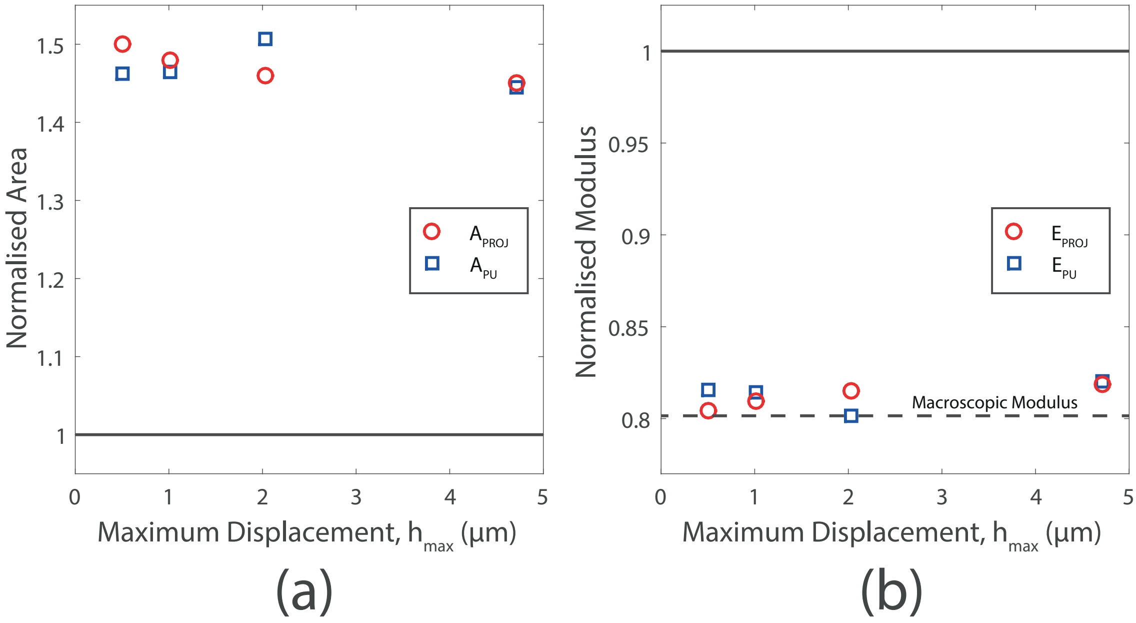

(a) (b)

Figure B.4: Normalised (a) Contact area and (b) Indentation modulus determined using each of the pile-up correction methods for Aluminium alloy 6082